



**Top-Quark Mass Determinations
in the $e\mu$ Dilepton Channel**

and

**Top-Quark Mass Effects in
Higgs Boson Pair Production**

Ludovic M. Scyboz



Top-Quark Mass Determinations in the $e\mu$ Dilepton Channel

and

Top-Quark Mass Effects in Higgs Boson Pair Production

Ludovic M. Scyboz

Vollständiger Abdruck der von der Fakultät für Physik der Technischen Universität München zur Erlangung des akademischen Grades eines

Doktors der Naturwissenschaften (Dr. rer. nat.)

genehmigten Dissertation.

Vorsitzender:

Prof. Dr. Andreas Weiler

Prüfende der Dissertation:

1. Dr. Stefan Kluth
2. Prof. Dr. Wolfgang Hollik,
Technische Universität München

Die Dissertation wurde am 16.05.2019 bei der Technischen Universität München eingereicht und durch die Fakultät für Physik angenommen.

⁵ Abstract

⁶ The top quark is a centrepiece of the Standard Model (SM) of Particle Physics. It
⁷ interacts across all sectors and with all gauge fields, and has been successfully used as a
⁸ portal to precision measurements of the SM parameters. Top quarks are also indirectly
⁹ related to other SM sectors, for example to Higgs boson production processes which
¹⁰ are induced predominantly by top-quark loops at the Large Hadron Collider (LHC).
¹¹ During Runs I and II of the LHC, a large number of top-quark pair ($t\bar{t}$) and single-top
¹² events were recorded. They allow to reduce the experimental uncertainty on top-quark
¹³ properties, like the top-quark mass, spin correlations and W -boson polarization in $t\bar{t}$
¹⁴ events, the Wtb coupling, or flavor-changing neutral currents. In the case of the top-
¹⁵ quark mass, the experimental uncertainties of the latest ATLAS and CMS combination
¹⁶ are now competing with theoretical uncertainties: approximations that were previously
¹⁷ thought to be appropriate must be reevaluated.

¹⁸ In particular, the narrow-width approximation (NWA) for top-quark pair processes
¹⁹ assumes the production of an on-shell top and anti-top quark, and is used in Monte-Carlo
²⁰ (MC) predictions for most experimental measurements. Since the actual final-state is
²¹ composed of the top-quark pair decay products, a more accurate description of the signal
²² should consider $W^+W^-b\bar{b}$ final-states instead. The full final-state includes contributions
²³ that cannot be factorized in both top-quark decay legs, or that do not contain a top-quark
²⁴ pair to begin with. These diagrams are called non-factorizing, respectively non-doubly
²⁵ resonant. In cases where measurements rely on phase-space regions sensitive to these
²⁶ contributions, the extracted top-quark mass will be biased.

²⁷ In this work, the ATLAS top-quark mass analysis in the $e\mu$ dilepton channel is taken
²⁸ as an example. Based on simulated templates, the MC top-quark mass is extracted via
²⁹ an unbinned likelihood fit. In a setup similar to the experimental analysis, the extracted
³⁰ top-quark mass is compared at parton level in different theoretical descriptions of the $t\bar{t}$
³¹ final-state at next-to-leading order (NLO) in production. MC events are produced for
³² different descriptions of the top-quark decay in the NWA, as well as for the full $W^+W^-b\bar{b}$
³³ process at NLO in production. The top-quark mass m_t^{MC} extracted by the template fit
³⁴ method is compared for each of these theoretical descriptions, and important offsets of up
³⁵ to $\Delta m_t^{\text{MC}} \sim 1$ GeV are underlined. A more realistic assessment, where these predictions
³⁶ are folded to detector level, is also presented.

³⁷ As mentioned, the top-quark mass also plays an important role in other sectors of
³⁸ the SM. In di-Higgs production with non-SM values of the Higgs couplings, it is shown
³⁹ that the m_t -dependence of QCD NLO corrections introduces sizeable differences with
⁴⁰ respect to predictions where the top-quark degrees of freedom are integrated out. A
⁴¹ full-fledged MC event generator (with the possibility of varying the Higgs self-coupling
⁴² and the Higgs-top Yukawa coupling) is introduced.

⁴³ Zusammenfassung

⁴⁴ Im Standard-Modell (SM) der Teilchenphysik spielt das Top-Quark eine zentrale Rolle.
⁴⁵ Es wechselwirkt mit Teilchen aller Sektoren sowie mit allen quantentheoretischen Eich-
⁴⁶ feldern, und wurde in verschiedenen Zusammenhängen als Grundpfeiler für Präzisions-
⁴⁷ messungen des SM verwendet. Top-Quarks sind auch indirekt eng mit anderen Sek-
⁴⁸ toren des SM verbunden: Higgs-Bosonen zum Beispiel werden am Large Hadron Col-
⁴⁹ llider (LHC) überwiegend durch Top-Quark-Schleifen erzeugt. Während Run I und II
⁵⁰ des LHC wurde eine große Anzahl an Top-Quark-Paar ($t\bar{t}$) und Einzel-Top-Events er-
⁵¹ mittelt. Diese ermöglichen es, Messungen von Top-Quark-Eigenschaften bedeutend zu
⁵² verbessern, beispielsweise die der Top-Quark-Masse. In diesem Fall sind die von ATLAS
⁵³ und CMS angegebenen experimentellen Unsicherheiten zu dem Punkt gekommen, wo sie
⁵⁴ mit den aktuellen theoretischen Unsicherheiten konkurrieren: das heisst insbesondere,
⁵⁵ dass früher verwendete Näherungen neu evaluiert werden müssen.

⁵⁶ Die sogenannte Schmal-Breite-Näherung (NWA), bei der ein Top-Quark-Paar on-shell
⁵⁷ produziert wird, wird üblicherweise in den meisten Monte-Carlo (MC) Generatoren ver-
⁵⁸ wendet. Weil der gemessene $t\bar{t}$ -Endzustand aber von den Top-Zerfallsprodukten gebildet
⁵⁹ wird, sollte eine konsistente Beschreibung des Signals eher auf dem intermediären
⁶⁰ $W^+W^-b\bar{b}$ Zustand beruhen. Letzerer beinhaltet Feynman-Diagramme, die entweder
⁶¹ nicht in zwei Top-Zerfall-Kanälen faktorisieren, oder überhaupt keine zwei Top-Propa-
⁶² gatoren aufweisen. Diese Diagramme heissen nicht-faktorisierend, bzw. nicht-doppelt-
⁶³ resonant. Wenn Messungen durchgeführt werden, welche sensitiv auf solche Beiträge
⁶⁴ sind, kann es zu einer Verzerrung der extrahierten Top-Quark-Masse kommen.

⁶⁵ Wir nehmen als Beispiel die ATLAS Top-Quark-Massenanalyse im $e\mu$ -Dileptonkanal,
⁶⁶ welche simulierte Templates zur Bestimmung der Top-Quark-Masse verwendet. In einem
⁶⁷ ähnlichen Setup wird die extrahierte Top-Masse verglichen, wo unterschiedliche $t\bar{t}$ - Endzu-
⁶⁸ standsbeschreibungen in nächstführender Ordnung der Störungstheorie (NLO) in Pro-
⁶⁹ duktion eingesetzt werden. Genauer werden für drei verschiedene Beschreibungen des
⁷⁰ Top-Quark-Zerfalls, sowie für die volle NLO $W^+W^-b\bar{b}$ -Rechnung, Verteilungen erzeugt.
⁷¹ Die mithilfe der Template-Fit-Methode extrahierte Top-Quark-Masse m_t^{MC} zeigt erhe-
⁷² bliche Unterschiede bis zu $\Delta m_t^{\text{MC}} \sim 1 \text{ GeV}$. Eine realistischere Studie wird eingeführt,
⁷³ in welcher Particle-Level-Vorhersagen auf Detektor-Level gefaltet werden.

⁷⁴ Außerdem wirken Top-Quark-Effekte auch im Higgs-Sektor. Anhand des Beispiels
⁷⁵ von Higgs-Paar-Produktion (hh) beim LHC wird gezeigt, dass die m_t -Abhängigkeit
⁷⁶ von hh Produktion auf NLO QCD zu Unterschieden in differentiellen Verteilungen
⁷⁷ führt im Vergleich zu Vorhersagen, wo die Top-Quark-Freiheitsgrade ausintegriert wer-
⁷⁸ den. Ein vollständiges MC-Programm zur Erzeugung von Higgs-Paar-Events (wo die
⁷⁹ trilineare Higgs-Selbstkopplung sowie die Higgs-Top-Yukawakopplung variiert werden
⁸⁰ können) wird präsentiert.

81 **Contents**

| | | |
|-----|---|-----|
| 82 | Abstract | v |
| 83 | Zusammenfassung | vii |
| 84 | Contents | ix |
| 85 | 1 Introduction | 1 |
| 86 | I Theoretical and Experimental Setup | 5 |
| 87 | 2 The Standard Model | 7 |
| 88 | 2.1 Matter content and gauge interactions | 7 |
| 89 | 2.2 The Higgs mechanism | 10 |
| 90 | 2.3 Top-Higgs interactions | 13 |
| 91 | 2.4 Outstanding issues with the Standard Model | 16 |
| 92 | 3 Higher-order perturbative calculations in hadron-hadron collisions | 17 |
| 93 | 3.1 Divergences in Quantum-Field Theory | 17 |
| 94 | 3.1.1 Regularization | 18 |
| 95 | 3.1.2 Renormalization | 20 |
| 96 | 3.1.3 Perturbative expansion of Quantum Chromodynamics | 20 |
| 97 | 3.2 Infrared divergences | 22 |
| 98 | 3.3 The factorization theorem | 23 |
| 99 | 4 Monte-Carlo (MC) event generators | 25 |
| 100 | 4.1 Matrix-element providers | 27 |
| 101 | 4.1.1 GoSAM: MC interfacing of one-loop amplitudes | 28 |
| 102 | 4.1.2 Infrared divergence cancellation | 29 |
| 103 | 4.2 Parton-shower models | 31 |
| 104 | 4.2.1 The Altarelli-Parisi splitting functions | 31 |
| 105 | 4.2.2 The Sudakov form factor | 32 |
| 106 | 4.2.3 Parton-shower matching | 32 |
| 107 | 4.3 Hadronization | 34 |
| 108 | 4.3.1 The Lund hadronization string model | 34 |
| 109 | 4.3.2 The cluster hadronization model | 34 |

| | | |
|-----|---|-----------|
| 110 | 5 The LHC and the ATLAS detector | 37 |
| 111 | 5.1 The Large Hadron Collider | 37 |
| 112 | 5.2 The ATLAS detector | 38 |
| 113 | 5.2.1 The Inner Detector | 39 |
| 114 | 5.2.2 Calorimeters | 41 |
| 115 | 5.2.2.1 The Liquid Argon (LAr) Calorimeter | 42 |
| 116 | 5.2.2.2 The Tile Calorimeter (TileCal) | 42 |
| 117 | 5.2.3 The Muon Spectrometer | 43 |
| 118 | 5.2.4 Trigger and Data acquisition | 43 |
| 119 | 5.2.4.1 Data formats | 44 |
| 120 | 5.2.4.2 MC simulation in ATLAS | 45 |
| 121 | II Top-Quark Mass Determinations | 47 |
| 122 | 6 Theoretical predictions for $t\bar{t}$ final-states | 49 |
| 123 | 6.1 The narrow-width approximation (NWA) | 50 |
| 124 | 6.2 $W^+W^-b\bar{b}$ production: review of existing calculations | 52 |
| 125 | 6.3 $W^+W^-b\bar{b}$ calculation setup at NLO QCD | 53 |
| 126 | 6.4 Event requirements | 55 |
| 127 | 6.5 Total cross-section results | 56 |
| 128 | 7 NWA versus $W^+W^-b\bar{b}$: Top-quark mass uncertainties at parton level | 57 |
| 129 | 7.1 The template fit method | 57 |
| 130 | 7.2 Definition of the observables | 58 |
| 131 | 7.3 Comparison of the different theoretical descriptions | 60 |
| 132 | 7.4 Template fit results | 65 |
| 133 | 8 Folding of predictions to detector level | 71 |
| 134 | 8.1 Inverse problems | 71 |
| 135 | 8.2 Folding setup in ATLAS | 72 |
| 136 | 8.3 Theoretical descriptions of the signal | 74 |
| 137 | 8.4 Object definition | 75 |
| 138 | 8.4.1 Electrons | 75 |
| 139 | 8.4.2 Muons | 76 |
| 140 | 8.4.3 Jets | 76 |
| 141 | 8.5 Event requirements | 77 |
| 142 | 9 Determination of the top-quark mass at detector level | 79 |
| 143 | 9.1 Differential results at particle and detector level | 79 |
| 144 | 9.2 Statistical and systematic cross-checks | 84 |
| 145 | 9.3 Folded results and template parametrization | 86 |
| 146 | 9.4 Numerical results for top-quark mass uncertainties | 87 |

| | | |
|-----|---|------------|
| 147 | III Top-Quark Mass Effects in Higgs Pair Production | 91 |
| 148 | 10 Top-mass dependence in Higgs pair production at NLO | 93 |
| 149 | 10.1 Theoretical descriptions of hh production | 94 |
| 150 | 10.1.1 Approximations in the heavy-top limit ($m_t \rightarrow \infty$) | 95 |
| 151 | 10.1.2 Two-loop contribution in the SM | 96 |
| 152 | 10.2 The Electroweak Chiral Lagrangian | 96 |
| 153 | 10.3 Total cross-sections for BSM benchmark points | 98 |
| 154 | 10.4 Differential cross-sections and HTL approximations | 104 |
| 155 | 11 Variations of the triple Higgs coupling and parton-shower effects | 107 |
| 156 | 11.1 The Powheg-BOX framework | 107 |
| 157 | 11.2 Interfacing two-loop contributions | 108 |
| 158 | 11.3 Total and differential cross-sections at fixed-order | 109 |
| 159 | 11.4 Parton-shower matched predictions at NLO | 111 |
| 160 | 12 Conclusion and Outlook | 115 |
| 161 | Bibliography | 119 |
| 162 | A Further template fit plots | 139 |
| 163 | B Monte-Carlo samples at detector level | 143 |
| 164 | C Template fit parameters at detector level | 144 |
| 165 | D BSM benchmark points in hh production | 145 |
| 166 | E Hardness definitions in parton-shower matching | 148 |
| 167 | Acknowledgments | 149 |

¹⁶⁸ 1 Introduction

¹⁶⁹ The Standard Model (SM) of Particle Physics is one of the most successful physical
¹⁷⁰ theories to date. While it still raises some unanswered questions that are outlined in
¹⁷¹ Chapter 2, the precision to which its predictions were tested by high-energy colliders,
¹⁷² but also in low-energy experiments, large-scale universe phenomena, neutrino and other
¹⁷³ experiments is extremely convincing. In particular, the SM bases on mathematical
¹⁷⁴ concepts that allow for a significant predictive power. Considering that physicists tend
¹⁷⁵ to like a theory with the least amount of free parameters and a maximal predictive
¹⁷⁶ power, the SM fares rather well: it contains only 19 parameters, namely the angles
¹⁷⁷ of the Cabibbo-Kobayashi-Maskawa mixing matrix and its CP-violating phase (3 + 1),
¹⁷⁸ the gauge couplings corresponding to the model’s underlying symmetries (3), the lepton
¹⁷⁹ and quark masses (9), the QCD vacuum angle (1), and the Higgs mass and vacuum
¹⁸⁰ expectation value (2). Since most of these parameters have been measured to an excellent
¹⁸¹ precision, efforts have largely concentrated on the less well-measured parameters, one of
¹⁸² these being the top-quark mass.

¹⁸³ Because the top quark is the heaviest known elementary particle, with a mass from
¹⁸⁴ the world combination measured at $m_t = 173.0 \pm 0.4$ GeV [1], physicists had to wait
¹⁸⁵ until 1995 for its observation by the CDF [2] and DØ [3] experiments at Fermilab, 23
¹⁸⁶ years after it was predicted. Only then did the last missing piece of the three quark
¹⁸⁷ generations fall into place. Nowadays, abundant production of top quarks with the
¹⁸⁸ Large Hadron Collider (LHC) at CERN allows for a variety of accurate measurements
¹⁸⁹ of its properties. Of particular interest, the precise determination of its mass is a key
¹⁹⁰ to a deeper understanding of modern quantum-field theory (QFT). Most notably, the
¹⁹¹ top-quark mass enters global electroweak fits which are important for consistency testing
¹⁹² of the SM; it also strongly affects corrections to the Higgs quartic coupling, thus having
¹⁹³ a large impact on the stability of the SM vacuum. Finally, being the only quark with a
¹⁹⁴ lifetime surpassing the hadronization scale, it is the only *bare* colored particle produced
¹⁹⁵ in SM processes. In general, one has to choose an appropriate mass definition, be it a
¹⁹⁶ QFT-consistent definition like the pole mass (on-shell renormalized) and the $\overline{\text{MS}}$ mass
¹⁹⁷ (renormalized after the short-distance $\overline{\text{MS}}$ scheme), or the so-called Monte-Carlo (MC)
¹⁹⁸ mass.

¹⁹⁹ Recently, the ATLAS and CMS experiments, using innovative approaches and analysis
²⁰⁰ techniques, have been able to reduce the uncertainty of the measured MC top-quark
²⁰¹ mass to about $\Delta m_t \approx 0.5$ GeV in their respective combinations [5, 6] (see Fig. 1.1 for
²⁰² measurements at the LHC). Achieving a more precise determination of m_t constitutes
²⁰³ a significant challenge for both the experimental and theoretical communities. While
²⁰⁴ on the one hand, experimentalists have to find new ideas to drive down the mostly
²⁰⁵ systematics-dominated uncertainties, theorists need to improve precision calculations by

1 Introduction

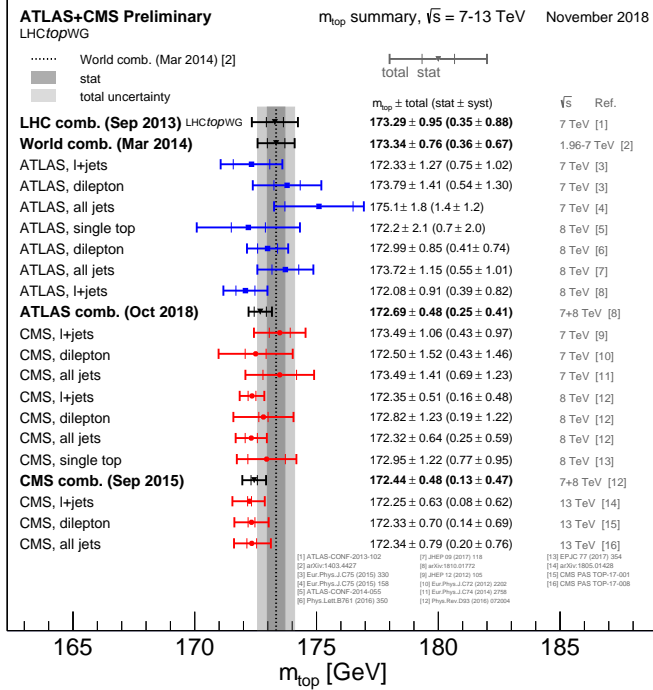


Figure 1.1: ATLAS and CMS combination of $\sqrt{s} = 7, 8, 13$ TeV data for measurements of the top-quark mass m_t . Figure taken from Ref. [4].

going to higher-order predictions and beyond formerly accepted approximations. The computation of higher-order corrections for on-shell top-quark pair ($t\bar{t}$) production has been a major success during the LHC era. The production of a pair of on-shell top quarks is referred to as the narrow-width approximation (NWA). Because the corrections to NWA calculations are expected to be small, of order $\mathcal{O}(\Gamma_t/m_t) < 1\%$ for inclusive cross-sections, most fixed-order predictions aim at computing higher-order QCD and EW corrections to top-quark pair production in this approximation.

The experimentalists, though, reconstruct the top-quark pair from their decay products, either from the dilepton, lepton+jets or all-hadronic final-states, depending on the decay channel of the top and anti-top quarks. The fixed-order prediction of a fully-decayed $t\bar{t}$ final-state is computationally demanding: instead of a $2 \rightarrow 2$ process, the final-state phase-space becomes that of a $2 \rightarrow 4$ (for $pp \rightarrow W^+W^-b\bar{b}$) or a $2 \rightarrow 6$ process (including W -boson decay products). The full final-state prediction at next-to-leading order (NLO) comprises Feynman diagrams that are not present in the NWA: some do not contain doubly-resonant top quarks, and others include internal lines between the top-quark decay legs, which means the latter do not factorize. In fact, the additional interference terms can be of importance to distributions that are sensitive to higher-order and off-shell effects, for example in phase-space regions populated first at higher-order in QCD. The qualitative differences between NWA and full $W^+W^-b\bar{b}$ predictions shall be investigated later on.

Another issue concerns the theoretical definition of the top-quark mass in different renormalization schemes. Indeed, relations between schemes are known at 4-loop order [7]. This relation suffers from an infrared (IR) so-called renormalon singularity, which is associated with an intrinsically non-perturbative ambiguity in the definition of the top-quark pole mass. This inherent uncertainty was estimated to be of the order $\mathcal{O}(250 \text{ MeV})$ [8–11]. Moreover, analyses that rely on simulated distributions (like the template fit method studied in the next chapters) measure the MC top-quark mass, not the pole mass. Although the discussion on the exact relation of the MC to the pole top-quark mass is still ongoing, the difference between both values is expected to be of the order $\mathcal{O}(300 - 500 \text{ MeV})$ [12, 13].

In this work, the foundations of the SM are briefly presented, including the Higgs mechanism and the relation between the Higgs sector and the top quark, in Chapter 2. In Chapter 3, the basics of higher-order calculations are summarized: the appearance of UV and IR divergences in loop corrections and the way to deal with them, the perturbative expansion for QCD at high energies from the running of the strong coupling α_s , and the factorization theorem for hadron-hadron collisions are laid out in some detail. Finally, the focus point is set on MC event generators in Chapter 4 and the ingredients needed for particle-level event generation are explained. Switching to the experimental side, the LHC and in particular the ATLAS detector are presented in Chapter 5. After having sketched out these fundaments, the different theoretical descriptions of top-quark pair production are discussed in Chapter 6. With the example of top-quark pair predictions in the $e\mu$ dilepton channel, it is shown how higher-order and off-shell effects can have a sizeable impact on an experimental MC top-quark mass extraction in Chapter 7. There, four different theoretical descriptions are compared with respect to an experimentally realistic top-quark mass extraction for $pp \rightarrow W^+(\rightarrow e^+\nu_e)W^-(\rightarrow \mu^-\bar{\nu}_\mu)b\bar{b}$. In the NWA, top-quark pair production is described at NLO QCD, where the top-decay is described at different accuracies: LO, respectively NLO QCD, as well as operated by a parton-shower. The NWA results are compared to a full $W^+W^-b\bar{b}$ computation at NLO QCD. Taking into account detector reconstruction efficiencies and bin migration effects, which is the subject of Chapter 8, the shift in the extracted top-quark mass is quantified in an exact ATLAS framework in Chapter 9, where distributions are folded up to detector level.

Looking at another sector entirely, top quarks also play an important role in calculations for the production of one or several Higgs bosons at the LHC. Because the top quark is the heaviest SM particle and since the Higgs boson's coupling to fermions is proportional to their mass, higher-order corrections to Higgs processes mainly happen through top-quark loops. For instance, single Higgs production at the LHC is dominated by gluon-fusion with a top-quark loop intermediate state (so-called loop-induced production), i.e. higher-order corrections to $gg \rightarrow h$ start at two-loop level already. The same holds for the production of a pair of Higgs bosons: this process is of particular interest, since di-Higgs production is the main channel for probing the trilinear Higgs self-coupling. Although the Higgs couplings to heavy fermions and gauge bosons are currently reasonably constrained, as shown in Fig. 1.2, the best limit set on the Higgs self-coupling's ratio κ_λ to the SM-predicted value is given by ATLAS at

1 Introduction

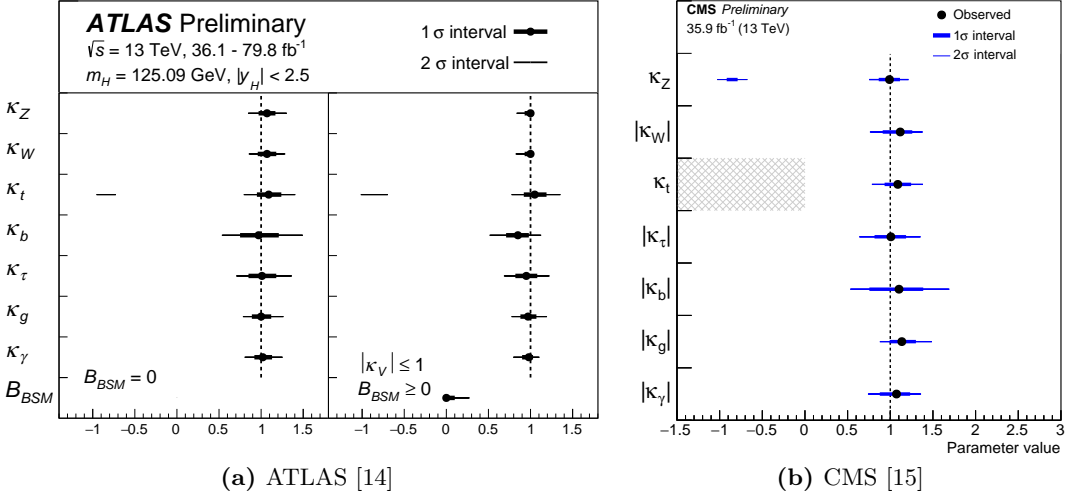


Figure 1.2: Fit values of the Higgs coupling modifiers with respect to the SM-predicted coupling strength (in the κ -framework).

270 $-5.0 \leq \kappa_\lambda \leq 12.1$ [16]. In general, the Higgs sector is one of the more poorly explored
 271 experimentally, and it is important to have precise (at best model-independent) theo-
 272 retical predictions for the case where the Higgs couplings are not SM-like. It is shown,
 273 within a non-linear Effective Field Theory (EFT) framework allowing to vary the Higgs
 274 couplings, that the full m_t -dependence of di-Higgs production at NLO QCD has impor-
 275 tant effects, especially on differential cross-section predictions. In Chapter 10, the EFT
 276 framework is introduced under the form of the electroweak chiral Lagrangian (EWChL).
 277 The results for NLO di-Higgs cross-sections and differential distributions with variations
 278 of the Higgs couplings are presented at a center-of-mass energy of 14 TeV for several
 279 benchmark points. Finally, the implementation of the full m_t -dependent NLO correc-
 280 tions for di-Higgs production into the POWHEG-BOX-V2 [17–19] event generator is the
 281 subject of Chapter 11. In this package, variations of the trilinear Higgs self-coupling
 282 and the top-Higgs Yukawa coupling are now possible. Studies comparing differential
 283 distributions for fixed-order NLO to parton-shower matched predictions are presented.
 284 Parton-shower related uncertainties are also discussed. Finally, the current state of the
 285 SM is summarized and future, potentially interesting developments in both top quark
 286 and Higgs physics are outlined.

287

Part I

288 **Theoretical and Experimental Setup**

²⁸⁹ 2 The Standard Model

²⁹⁰ The SM was developed and supplemented over five decades, and describes all elementary
²⁹¹ particles and their interactions via three of the four fundamental forces in a quantum-field
²⁹² theoretical framework: the electromagnetic, weak and strong interactions. Although it
²⁹³ is known that the SM suffers from some theoretical shortfalls that are briefly described
²⁹⁴ at the end of this chapter (like non-zero neutrino mass measurements [20]), there is, to
²⁹⁵ date, no experimental evidence that directly contradicts it.

²⁹⁶ At the core, the discovery by Glashow, Salam and Weinberg [21–23] that the electro-
²⁹⁷ magnetic and weak interactions could be embedded in a unified theory constitutes the
²⁹⁸ first stone of the SM edifice. What if all known forces and particles could be described
²⁹⁹ by the same, unique theory? Later, the quantum chromodynamics (QCD) sector, which
³⁰⁰ describes the strong interaction, was correctly theorized to rely on a (non-Abelian) gauge
³⁰¹ symmetry group by Wilczek, Gross and Politzer [24, 25], which leads to asymptotic free-
³⁰² dom of color-charged particles. The addition of the Higgs mechanism, that generates
³⁰³ mass terms for the fermions and gauge bosons, culminated in what is known today as the
³⁰⁴ SM Lagrangian. The SM is one of the most successful theories up-to-date, and has been
³⁰⁵ extensively tested against experimental data. A comprehensive comparison of computed
³⁰⁶ cross-sections for SM processes to values measured by ATLAS, shown in Fig. 2.1, makes
³⁰⁷ for a compelling argument in favor of the SM’s predictive power.

³⁰⁸ 2.1 Matter content and gauge interactions

³⁰⁹ The SM is a quantum-field gauge theory: the known elementary particles are interpreted
³¹⁰ as the excitations of quantized fields, and their interactions are described by the exchange
³¹¹ of gauge bosons. Both matter and gauge fields obey certain rules under the corresponding
³¹² gauge transformations: that is, they transform according to different representations of
³¹³ the underlying gauge group. The SM builds on the

$$SU(3)_C \times SU(2)_L \times U(1)_Y$$

³¹⁴ gauge group. It is the product group of the QCD group $SU(3)_C$, and its corresponding
³¹⁵ color quantum number C , and the electroweak group $SU(2)_L \times U(1)_Y$, that distinguishes
³¹⁶ left- from right-handed particles as doublets, respectively singlets under the group trans-
³¹⁷ formation. The $U(1)_Y$ group’s quantum number is the so-called hypercharge Y . The
³¹⁸ fermionic matter fields are classified into left-handed leptons and quarks, both transform-
³¹⁹ ing as doublets under the $SU(2)_L$ group, and their singlet right-handed counterparts.
³²⁰ There are furthermore three distinct copies, called generations, or families:

2 The Standard Model

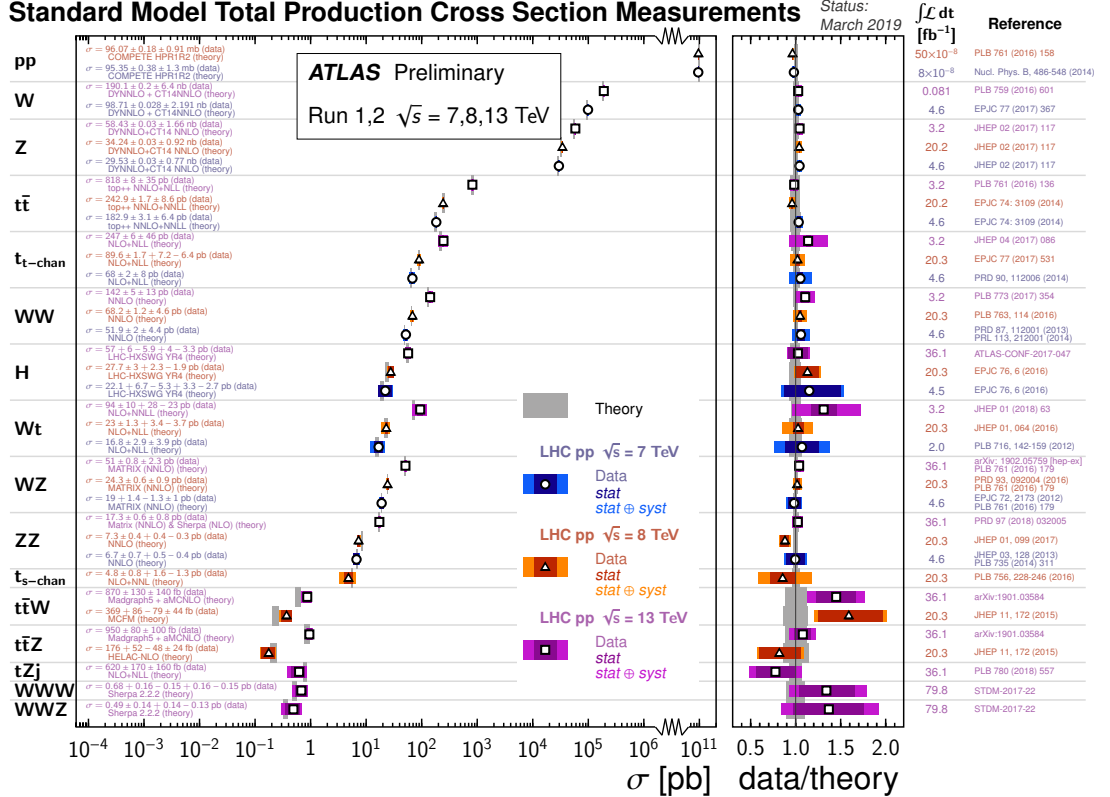


Figure 2.1: The predicted cross-sections (in gray, where bands represent the theoretical uncertainty) for SM production processes at LHC center-of-mass energies of $\sqrt{s} = 7, 8, 13$ TeV are compared to their measured values at the ATLAS experiment (in color) [26]. The ratio of data to theory is shown to be compatible with 1.

$$\begin{pmatrix} \nu_e \\ e^- \end{pmatrix}_L, \quad \begin{pmatrix} u \\ d' \end{pmatrix}_L, \quad \begin{pmatrix} \nu_\mu \\ \mu^- \end{pmatrix}_L, \quad \begin{pmatrix} c \\ s' \end{pmatrix}_L, \quad \begin{pmatrix} \nu_\tau \\ \tau^- \end{pmatrix}_L, \quad \begin{pmatrix} t \\ b' \end{pmatrix}_L,$$

$$e_R^-, \quad u_R, \quad d'_R, \quad \mu_R^-, \quad c_R, \quad s'_R, \quad \tau_R^-, \quad t_R, \quad b'_R,$$

and their corresponding antiparticles. Here, e, μ, τ are the three lepton (ℓ) generations and their corresponding neutrinos ν_ℓ . The particles u, c, t , and d', s', b' are the up-type, respectively down-type quark weak eigenstates. The down-type eigenstates mix via the unitary Cabibbo-Kobayashi-Maskawa (CKM) matrix to give the physical mass eigenstates d, s, b :

$$\begin{pmatrix} d' \\ s' \\ b' \end{pmatrix} = \begin{pmatrix} V_{ud} & V_{us} & V_{ub} \\ V_{cd} & V_{cs} & V_{cb} \\ V_{td} & V_{ts} & V_{tb} \end{pmatrix} \begin{pmatrix} d \\ s \\ b \end{pmatrix}.$$

2.1 Matter content and gauge interactions

326 The quarks are the only matter fields carrying color charge, and live in the triplet **(3)**,
 327 respectively anti-triplet **(̄3)** representations of the $SU(3)_C$ group. The color quantum
 328 numbers are defined as red, blue and green, respectively anti-red, anti-blue and anti-
 329 green. That is, for the up- and down-quark:

$$\begin{pmatrix} u_r \\ u_b \\ u_g \end{pmatrix}, \quad \begin{pmatrix} d_r \\ d_b \\ d_g \end{pmatrix} \in SU(3)_C .$$

330 Governing the interactions, the gauge bosons corresponding to each subgroup couple
 331 with a separate strength to the matter fields. There are:

- 332 • three W_μ^a , $a = (1, 2, 3)$, bosons belonging to $SU(2)_L$, coupling with strength $\propto g$,
- 333 • one B_μ boson belonging to $U(1)_Y$, coupling with strength $\propto g'$,
- 334 • eight gluon fields G_μ^a , $a = (1, \dots, 8)$, belonging to $SU(3)_C$, with coupling $\propto g_s$.

335 By the principle of gauge covariance, the interaction terms between gauge bosons and
 336 the rest of the particle fields are given by promoting the 4-derivatives in the kinetic terms
 337 of the corresponding sector to covariant derivatives:

$$\partial_\mu \rightarrow D_\mu = \left[\partial_\mu + ig \frac{\sigma_a}{2} W_\mu^a + ig' \frac{Y}{2} B_\mu \right] \quad (\text{EW}) , \quad (2.1)$$

338

$$\partial_\mu \rightarrow D_\mu = \left[\partial_\mu + ig_s T_a G_\mu^a \right] \quad (\text{QCD}) , \quad (2.2)$$

339 where σ_a are the three Pauli matrices (the generators of the Lie algebra of $SU(2)_L$),
 340 and T_a are the eight generators of the Lie algebra of $SU(3)_C$. The replacement by a
 341 covariant derivative also induces gauge boson self-coupling interactions.

342 Finally, analogously to the quarks, the electroweak gauge bosons mix to give rise to
 343 the physical charged- and neutral-current interaction bosons:

$$W^\pm = \frac{1}{\sqrt{2}} (W^1 \mp iW^2) , \quad (2.3)$$

$$\begin{pmatrix} \gamma \\ Z \end{pmatrix} = \begin{pmatrix} \cos(\theta_W) & \sin(\theta_W) \\ -\sin(\theta_W) & \cos(\theta_W) \end{pmatrix} \begin{pmatrix} B \\ W^3 \end{pmatrix} , \quad (2.4)$$

344 where θ_W is the Weinberg angle.

345 2.2 The Higgs mechanism

346 If one writes down the most general, renormalizable Lagrangian for the model above,
 347 two problems appear:

- 348 • the usual Dirac mass terms one can introduce in the fermionic sector are not
 349 invariant under $SU(2)_L$,
- 350 • mass terms for the W^\pm, Z bosons are not gauge-invariant.

351 So, in order to generate masses for the aforementioned particles, an external contrap-
 352 tion is needed. The Brout-Englert-Higgs [27–29] mechanism proposed in 1964 introduces
 353 a new spin-0 fundamental $SU(2)_L$ doublet, called the Higgs field:

$$\phi(x) = \begin{pmatrix} \phi^+(x) \\ \phi^0(x) \end{pmatrix}. \quad (2.5)$$

354 It is colorless, and is charged under the electroweak $U(1)_Y$ symmetry. The $SU(3)_C \times$
 355 $SU(2)_L \times U(1)_Y$ Lagrangian gets completed by a (gauged) Higgs sector, where the
 356 covariant derivative D_μ is given by Eq. (2.1):

$$\mathcal{L}_h = (D_\mu \phi)^\dagger (D^\mu \phi) + V(\phi) \quad (2.6)$$

$$= (D_\mu \phi)^\dagger (D^\mu \phi) + \mu^2 \phi^\dagger \phi - \lambda (\phi^\dagger \phi)^2, \quad \lambda > 0. \quad (2.7)$$

357 Similarly to the case of superconductivity [30], the underlying $SU(2)_L \times U(1)_Y$ sym-
 358 metry can be spontaneously broken if the Higgs potential $V(\phi)$ has a non-zero ground
 359 state. This is the case for the *Mexican-hat* potential given above, which is pictured in
 360 Fig. 2.2. When the Higgs field assumes one of the degenerate ground states with a vac-
 361 uum expectation value at the minimum of the potential around $v = \mu/\sqrt{\lambda} \sim 246$ GeV,
 362 it spontaneously breaks the $SU(2)_L \times U(1)_Y$ symmetry of the Lagrangian.

363 Expanding the Higgs field from Eq. (2.5) around the vacuum and taking the EW
 364 covariant derivative from Eq. (2.1),

$$\phi(x) = \frac{1}{\sqrt{2}} \begin{pmatrix} 0 \\ v + h(x) \end{pmatrix}, \quad (2.8)$$

$$D_\mu \phi(x) = \frac{1}{\sqrt{2}} \begin{pmatrix} -\frac{ig}{2} (W_\mu^1 - iW_\mu^2) (v + h(x)) \\ \partial_\mu h(x) - \frac{i}{2} (g'B_\mu - gW_\mu^3) (v + h(x)) \end{pmatrix}, \quad (2.9)$$

365 the Higgs field naturally couples to the gauge bosons. Then, computing the squared
 366 gauged kinematic term of the spontaneously broken Higgs field from Eq. (2.7), and
 367 replacing the gauge fields with their physical rotated states from Eqs. (2.3), (2.4) gives:

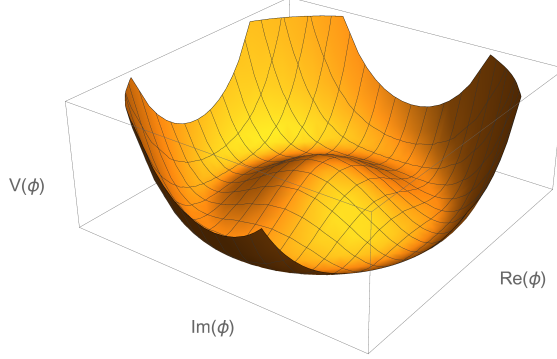


Figure 2.2: The $SU(2) \times U(1)$ symmetric Higgs Mexican-hat potential has a degenerate non-zero ground state at $v^2 = \langle \phi_0^\dagger \phi_0 \rangle \sim (246 \text{ GeV})^2$.

$$\begin{aligned} \mathcal{L} \supset & \frac{1}{2} (\partial_\mu h)(\partial^\mu h) + \underbrace{\frac{g^2 v^2}{4}}_{m_W^2} W_\mu^+ W^{-\mu} + \frac{1}{2} \underbrace{\left(\frac{(g^2 + g'^2)v^2}{4} \right)}_{m_Z^2} Z_\mu Z^\mu \\ & + \underbrace{\frac{1}{2} (2\lambda v^2)}_{m_h^2} h^2 + \lambda v h^3 + \frac{\lambda}{8} h^4. \end{aligned} \quad (2.10)$$

368 So, the dynamic EW spontaneous symmetry breaking (EWSB) of the Higgs potential
 369 generates masses for the W^\pm , Z gauge bosons and identifying the mass terms in the
 370 Lagrangian leads to the following leading-order boson mass relations¹:

$$\begin{aligned} m_H &= \sqrt{2\lambda}v, \\ m_W &= \frac{gv}{2}, & \cos(\theta_W) &= \frac{g}{\sqrt{g^2 + g'^2}}, \\ m_Z &= \frac{\sqrt{g^2 + g'^2}v}{2}, & \sin(\theta_W) &= \frac{g'}{\sqrt{g^2 + g'^2}}. \\ m_\gamma &= 0, \end{aligned}$$

372 The W and Z boson masses are related (at tree-level):

$$m_W = m_Z \cos(\theta_W),$$

373 with the experimentally measured values $m_W = 80.385 \text{ GeV}$, $m_Z = 91.1876 \text{ GeV}$ and
 374 the Weinberg angle $\theta_W = 0.2223$. Finally, considering the last two terms in Eq. (2.10),
 375 the Higgs couples to itself to produce the Feynman diagrams shown in Fig. 2.3.

¹The introduction of the Higgs mechanism also allows for a fermionic gauge-invariant mass term, e.g. by the Yukawa coupling of fermions to the Higgs boson $\mathcal{L} \supset \frac{m_f}{2v} \bar{\psi}_f \psi_f h \xrightarrow{(h \rightarrow v)} \frac{1}{2} m_f \bar{\psi}_f \psi_f$.

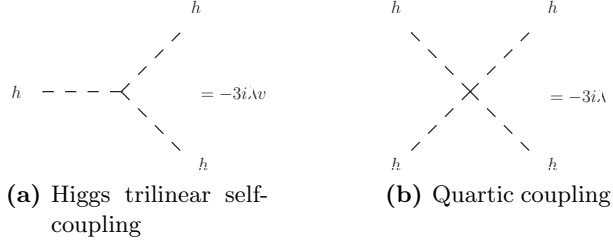


Figure 2.3: The physical Higgs field couples to itself after EWSB. The Feynman rules are given for (a) the triple vertex and (b) the quartic vertex.

As a side note, expressing Eq. (2.5) with all available degrees of freedom would give, in polar coordinates,

$$\phi(x) = \frac{1}{\sqrt{2}} e^{\frac{i}{v} \chi_a(x) \sigma^a} \begin{pmatrix} 0 \\ v + h(x) \end{pmatrix}, \quad (2.11)$$

where the three real fields χ_a are the massless Goldstone bosons associated with the EWSB of $SU(2) \times U(1)$. Because they will anyhow disappear from the theory (their respective degrees of freedom are sacrificed to the W - and Z -boson longitudinal polarizations), they are not explicitly considered in the following. Combining the matter and gauge terms with the Higgs sector yields the final form of the SM Lagrangian:

$$\begin{aligned} \mathcal{L}_{\text{SM}} = & -\frac{1}{2} \langle G_{\mu\nu} G^{\mu\nu} \rangle - \frac{1}{2} \langle W_{\mu\nu} W^{\mu\nu} \rangle - \frac{1}{4} B_{\mu\nu} B^{\mu\nu} \\ & + \sum_{\psi=q_L,l_L,q_R,l_R} \bar{\psi} i \not{D} \psi + \text{h.c.} \\ & + Y_l \bar{\psi}_L \phi \psi_R + Y_d \bar{q}_L \phi d_R + Y_u \bar{q}_L \phi u_R + \text{h.c.} \\ & + (D_\mu \phi)^\dagger (D^\mu \phi) + \mu^2 \phi^\dagger \phi - \lambda (\phi^\dagger \phi)^2, \end{aligned} \quad (2.12)$$

where $\langle \cdot \rangle$ represents the trace and $\not{D} = \gamma^\mu \partial_\mu$. The first line contains the field-strength tensors of the corresponding gauge bosons, e.g. for a gauge group with structure functions f^{abc} defined by the generators $[T_a, T_b] =: i f^{abc} T_c$ of the corresponding Lie algebra, and general coupling strength \tilde{g} :

$$F_{\mu\nu}^a = \partial_\mu A_\nu^a - \partial_\nu A_\mu^a + \tilde{g} f^{abc} A_\mu^b A_\nu^c.$$

387 For the three SM subgroups:

- $SU(3)_C$
 - $A_\mu^a := G_\mu^a$ the gluon fields in the adjoint representation,
 - $\tilde{g} := g_s$ the strong coupling constant,
 - $[T_a, T_b] =: if^{abc}T_c$ with the generators given in Eq. (2.2).

- $SU(2)_L$
 - $A_\mu^a := W_\mu^a$ the gauge fields defined in Eq. (2.1),
 - $\tilde{g} := g$ the $SU(2)_L$ coupling constant,
 - $[\sigma_a, \sigma_b] =: 2i\epsilon_{abc}\sigma_c$ with the Pauli matrices σ_i and the Levi-Civita symbol ϵ_{abc} .

- $U(1)_Y$
 - $A_\mu^a := B_\mu$ the last gauge field appearing in Eq. (2.1),
 - $\tilde{g} := g'$ the $U(1)_Y$ coupling constant,
 - $f^{abc} = 0$ since the group is Abelian.

390 The second line of the SM Lagrangian in Eq. (2.12) contains the kinetic and interaction terms for the fermion fields. The third line contains the Yukawa interaction of all fermions 391 with the Higgs boson for mass generation, and the last line is the unbroken SM Higgs 392 boson sector. 393

394 The addition of just one Higgs doublet to the SM, like in Eq. (2.5), is a minimal 395 choice. One could legitimately introduce further Higgs fields, as in the two-Higgs doublet 396 model (2HDM) [31] or the Minimal Supersymmetric SM (MSSM) [32], which predict 397 five physical scalar Higgs particles and which can assimilate the discovered Higgs boson 398 at $m_h = 125$ GeV. These extensions of the SM predict in general different coupling 399 strengths of the Higgs boson(s) to other particles and to itself, and precise experimental 400 measurements of these couplings (and of the Higgs decay branching ratios) are needed 401 in order to differentiate between models.

402 2.3 Top-Higgs interactions

403 Intrinsically, the top quark is tightly linked to the Higgs boson properties and has generally 404 strong phenomenological implications for the Higgs sector. Because it is the heaviest 405 SM elementary particle, and since the Yukawa coupling of the Higgs boson to fermions is 406 proportional to their masses, the Higgs couples strongest to the top quark (in comparison, 407 bottom-quark effects in inclusive Higgs observables are of the order of $m_b/m_t = 2.8\%$). 408 It is especially important for Higgs production at the LHC: the predominant production 409 mechanism is gluon-fusion via a triangle top-quark loop, as shown in Fig. 2.4. In comparison, 410 other associated production modes have cross-sections that are more than one 411 order of magnitude smaller. Representative Feynman diagrams for the main production 412 channels at LHC are also depicted in Fig. 2.5.

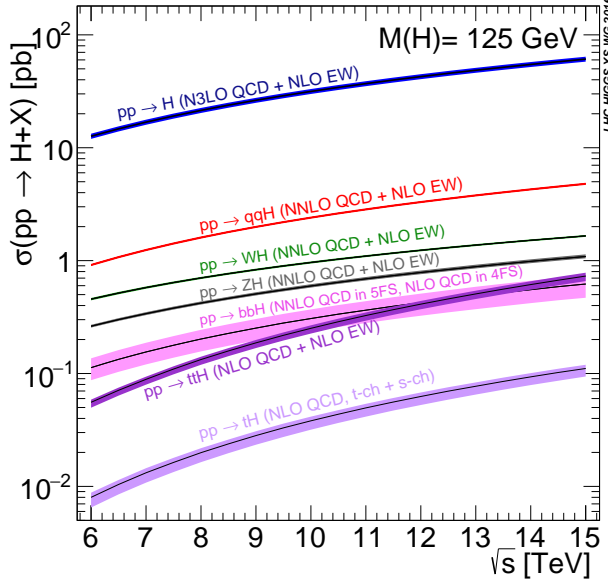


Figure 2.4: Theory prediction for $pp \rightarrow h + X$ production cross-sections as a function of the center-of-mass energy \sqrt{s} . Single Higgs production at the LHC is dominated by gluon fusion mediated by a top-quark loop. Figure taken from Ref. [33].

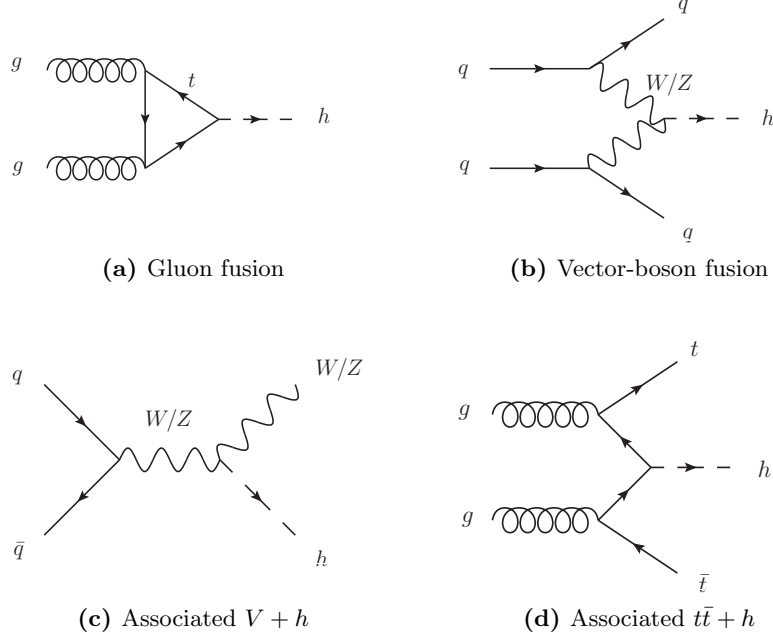


Figure 2.5: Leading-order diagrams for Higgs production by (a) gluon fusion, (b) vector-boson fusion, (c) associated vector production and (d) associated $t\bar{t}$ production.

2.3 Top-Higgs interactions

In relation to both the measurement of the Higgs triple self-coupling and the importance of top-mass effects in Higgs production, the reader is referred to the extensive discussion laid out in Chapter 10. Not only do top quarks influence Higgs process cross-sections at collider experiments, but they also have a deeper connection to the Higgs potential. Indeed, the β -function of the Higgs quartic coupling (which governs the evolution of the coupling’s value at different resolution scales, see Chapter 3) is sensitive to renormalization counterterms stemming from top-quark loops.

Eq. (2.13) gives the one-loop β -function for the Higgs quartic coupling [34]:

$$\mu^2 \frac{d\lambda}{d\mu^2} = \beta_\lambda(\lambda, y_t, g_s, \dots) = \frac{1}{16\pi^2} (12\lambda^2 + 6\lambda y_t^2 - 3y_t^4), \quad y_t = \sqrt{2} \frac{m_t}{v} \sim 1 \quad (2.13)$$

where y_t is the top-Yukawa coupling and is proportional to the top-quark mass m_t .

Because the top-Yukawa coupling is of order $\mathcal{O}(1)$, small variations in the value of the top-quark mass modify the evolution of the Higgs quartic coupling λ in a non-trivial way. If $\lambda(\mu)$ was to become negative at scales much below the Planck scale, $M_P \sim 10^{18} - 10^{19}$ GeV (see Fig. 2.6a), the Higgs field could tunnel from the current false vacuum state to the true, absolutely stable vacuum ground state. Current measurements seem to support the fact that the SM is in a metastable state, as shown in Fig. 2.6b. For the existentially anxious reader, a state-of-the art calculation of the EW vacuum decay rate can be found in Ref. [35].

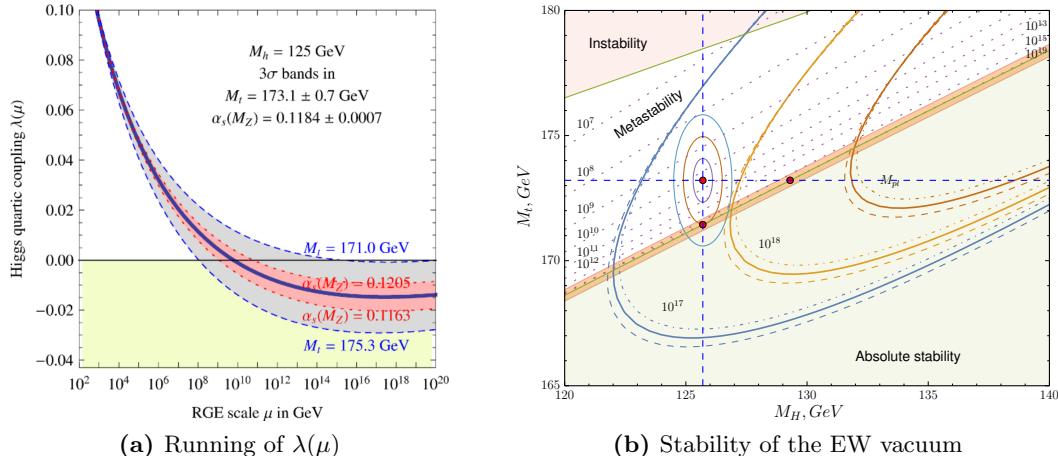


Figure 2.6: (a) The evolution of the Higgs quartic coupling λ can lead to negative values at high energy scales (below the Planck scale M_P). This in turn makes the EW vacuum potentially unstable. The running is highly dependent on the top-quark mass and α_s values [36]. (b) The SM point, in red, is plotted in the (m_h, m_t) phase-space with $1-, 2-$ and 3σ uncertainties. The pink dotted lines indicate contours where $\lambda(\mu) = 0$ for the indicated values of μ , and the parabolic curves where the beta-function $\beta_\lambda(\mu) = 0$ for chosen values of μ . The measured Higgs and top-quark masses point to a SM universe close to the metastable region [37].

430 2.4 Outstanding issues with the Standard Model

431 For all its successes, the SM is known to have some theoretical flaws. Below is a list of
 432 familiar shortcomings:

- 433 • **Massless neutrinos:** In the SM, neutrinos are naturally massless. Experi-
 434 ments [20] have shown that neutrinos can oscillate between the different fami-
 435 lies, and this requires a mixing of flavor states into mass eigenstates, similarly
 436 to the CKM mixing. Different mechanisms [38–40] were introduced to generate
 437 neutrino masses: a right-handed (so-called *sterile*) neutrino could exist, and not
 438 interact with matter (since no right-handed neutrino was ever observed), or neu-
 439 trinos could acquire a Majorana mass. Some R-parity violating supersymmetric
 440 (SUSY) models also produce neutrino masses [41, 42].
- 441 • **Gravity:** General relativity has yet to be quantized and incorporated into the SM
 442 under its current form, and a unified theory of all four interactions is still missing.
 443 As a first attempt, an exchange gravitational gauge boson can be introduced under
 444 the form of a spin-2 particle, called the graviton. The addition of corresponding
 445 terms to the SM Lagrangian spawns the apparition of UV divergences that cannot
 446 be handled by a finite number of counterterms [43–45], though, and the theory is
 447 not perturbatively renormalizable.
- 448 • **Dark matter:** The presence of dark matter in the Universe has been suggested
 449 from multiple cosmological observations [46–50]. Yet, the SM does not contain a
 450 good dark matter candidate particle. Some extensions of the SM, in particular
 451 SUSY, provide a heavy non-decaying particle (the lightest in the SUSY spectrum,
 452 called lightest supersymmetric particle) that turns out to be a good candidate.
- 453 • **Baryon asymmetry:** The SM predicts that matter and antimatter should have
 454 been produced almost symmetrically at the Big Bang. Yet baryons are observed
 455 to be in overwhelming excess over antibaryons in our part of the Universe [51, 52].
- 456 • **Hierarchy problem:** There is a manifest imbalance between the three unified
 457 forces of the SM and gravity, or between their respective mass scales. In particular,
 458 it is not clear why the Higgs boson mass is so small with respect to the Planck scale:
 459 basically, radiative corrections to the Higgs self-energy should blow up its mass, and
 460 the observed value of $m_h = 125$ GeV requires an incredible amount of fine-tuning to
 461 cancel radiative corrections. Again, SUSY models solve this problem by requiring
 462 every SM particle to have a supersymmetric partner which has the opposite spin-
 463 statistics: their contributions to the Higgs mass then cancel naturally [53].

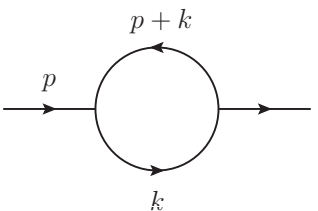
464 Although all model extensions of the SM have respective advantages over the current
 465 theory, none of the particles predicted by them has been observed at the LHC or any
 466 other experiment yet.

467 **3 Higher-order perturbative calculations in
468 hadron-hadron collisions**

469 The SM Lagrangian presented in the last chapter provides the Feynman rules to compute
470 theoretical cross-sections. As will be explained in Section 3.1.3, the scattering amplitudes
471 (at high-energies, for QCD) can be expanded to a perturbative series in the coupling
472 constant: the interactions are represented by Feynman diagrams, and higher-order cor-
473 rections generate loop diagrams that are most of the time divergent. Since the first
474 successes of QFT in predicting basic energy spectrum properties and leading-order (LO)
475 scattering amplitudes, there has always been a need for a more consistent framework in
476 which higher-order corrections could be worked out. In this chapter, the important in-
477 gredients used in most theoretical computations nowadays are summarized, in particular
478 in the context of high-energy hadron-hadron collisions. Most of the standard textbook
479 content presented here is adapted from Refs. [54–58].

480 **3.1 Divergences in Quantum-Field Theory**

481 Going beyond Feynman tree diagrams in the computation of scattering matrix-elements,
482 one encounters two classes of divergences. Consider a one-loop scalar massless two-point
483 function, where the internal loop-momentum is integrated over:

484 

$$I_2(p^2; 0, 0) = \int_{-\infty}^{\infty} \frac{d^4 k}{(2\pi)^4} \frac{1}{(k^2 + i\delta)((p+k)^2 + i\delta)} . \quad (3.1)$$

485 In the limit $\lambda \rightarrow \infty$ for $k = \lambda \cdot \tilde{k}$, the integral behaves as $I \propto \int \frac{d\lambda \lambda^3}{\lambda^2 \cdot \lambda^2} = \int \frac{d\lambda}{\lambda}$ which
486 is logarithmically divergent. This is called an *ultraviolet* (UV) divergence. The above
487 integral is also divergent when taking the limit $\lambda \rightarrow 0$, which is symptomatic of an
488 *infrared* (IR) divergence.

489 As a solution to the infinities conundrum, the above integral has to be treated by the
490 introduction of a UV regulator of some kind – this is a method called *regularization*.
491 Then, the regularized infinities are absorbed in a consistent way through the *renormal-
492* ization of the Lagrangian bare couplings and masses.

493 3.1.1 Regularization

494 A first attempt at controlling UV divergences consists in the introduction of a high-
495 momentum regulator $k^2 < \Lambda^2$. Then, the loop integral given in Eq. (3.1) behaves as

$$I_2(p^2; 0, 0) \propto \int_{\epsilon}^{\Lambda} \frac{dk}{k} \sim \log(\Lambda), \quad (3.2)$$

496 and the integral diverges logarithmically in the cutoff Λ . This is typical of renormal-
497 izable theories. Now, obviously, any physical observable should not depend on the value
498 of the arbitrary cutoff, and in practice it does not.¹ As a theoretical downside, the in-
499 troduction of the cutoff breaks gauge-invariance. It also breaks translational invariance.

500 A possible gauge-invariant regularization method is the so-called Pauli-Villars regu-
501 larization: a much more massive particle is introduced and its contribution subtracted
502 from the ordinary propagator, that is:

$$\int \frac{d^4 k}{(2\pi)^4} \frac{1}{k^2 + i\delta} \rightarrow \int \frac{d^4 k}{(2\pi)^4} \left(\frac{1}{k^2 + i\delta} - \frac{1}{k^2 - M^2 + i\delta} \right). \quad (3.3)$$

503 The Pauli-Villars technique cannot be applied to QCD because it is not gauge-covariant,
504 though. On the same stance, it introduces an unphysical field that violates the spin-
505 statistics theorem (it amounts to a spurious scalar field with Fermi statistics). One of the
506 preferred regularization methods nowadays is dimensional regularization. It was worked
507 out by 't Hooft and Veltman [60] to regularize any integral, is gauge-invariant and works
508 for non-Abelian theories as well. The governing idea is that quantum-field theories in
509 a smaller number of dimensions have a lower degree of divergence in the UV. The four
510 dimensions of space-time are therefore analytically continued to $d = 4 - 2\epsilon$ dimensions,
511 and the integral in Eq. (3.1) can be cast into the following form:

$$I_2(p^2; 0, 0) = \mu^{2\epsilon} \int \frac{d^d k}{(2\pi)^d} \frac{1}{(k^2 + i\delta)((p+k)^2 + i\delta)}, \quad (3.4)$$

512 where the renormalization scale μ is a dimensionful parameter introduced to keep the
513 integral dimensionless. Then the integral can be worked out by introducing Feynman
514 parameters and Wick-rotating to give the analytical result

$$I_2(p^2; 0, 0) = \frac{1}{\epsilon} + \ln \frac{\mu^2}{-p^2 - i\delta} + 2 + \mathcal{O}(\epsilon), \quad (3.5)$$

515 where the UV divergences now appear as (at most single, at one-loop) poles in the
516 dimensional regulator ϵ . A general dimensionally-regularized one-loop scalar integral
517 with n external legs has the form:

¹For a fun exercise of trying out different forms of cutoff (Gaussian, Dirac-delta,...), see Ref. [54] for the case of the vacuum polarization in the Casimir effect [59].

3.1 Divergences in Quantum-Field Theory

518

$$I = \mu^{n-d/2} \int \frac{d^d k}{(2\pi)^d} \prod_{j=1}^n \frac{1}{(q_j^2 - m_j^2 + i\delta)} , \quad (3.6)$$

519 where the internal momenta $q_j = k + \sum_{i=1}^j p_i$ are expressed as a linear combination
 520 of the loop momentum k and the external momenta p_i . Feynman parameters can be
 521 introduced for the integral above, and generally it can be recast into the form

$$I = \Gamma(n - d/2) \prod_{i=1}^n \int_{0 \leq x_i \leq 1} dx_i \delta \left(1 - \sum_{j=1}^n x_j \right) \frac{\mathcal{U}^{n-d}(\vec{x})}{\mathcal{F}^{n-d/2}(\vec{x}, p_i \cdot p_j, m_i^2)} . \quad (3.7)$$

522 The x_1, \dots, x_n are the Feynman parameters, and \mathcal{U} , \mathcal{F} are the first, respectively
 523 second Symanzik polynomials.² Then, one needs only perform the integration over the
 524 Feynman parameters. For tensor integrals where the numerator of Eq. (3.6) contains
 525 Lorentz indices, there exist methods for their reduction to a set of scalar integrals, like
 526 the systematic Passarino-Veltman method [61] which uses a form factor expansion to
 527 factorize the indices. Most importantly, all one-loop integrals can be reduced to a linear
 528 combination of a set of *master integrals* that are at most box-diagrams, which are all
 529 known analytically and implemented in integral libraries. For the interested reader,
 530 Refs. [62–67] supply a comprehensive examination of various techniques for reducing
 531 and evaluating Feynman integrals.

532 Dimensional regularization has lots of benefits, and the algebra is quite straightforward.
 533 Its major disadvantage is that the Dirac algebra for fermions has to be analytically
 534 extended to $d = 4 - 2\epsilon$ space-time dimensions as well, which is not trivial. The Dirac
 535 matrices can be made to obey an analytically continued Clifford algebra

$$\{\gamma^\mu, \gamma^\nu\} = 2g^{\mu\nu} , \quad (3.8)$$

536 with a d -dimensional metric, $g^{\mu\nu}g_{\mu\nu} = d$, where it is unclear what happens to the
 537 Dirac matrix $\gamma_5 = i\gamma_0\gamma_1\gamma_2\gamma_3$. The different ways of treating γ_5 and the helicities of
 538 external and internal particle fields lead to different regularization schemes. Note that
 539 physical observables do not depend on the chosen scheme. In the dimensional reduction
 540 scheme (DRED) which is used for the predictions given in Chapters 6–11, the Dirac
 541 algebra is left to $d = 4$ dimensions, and the same holds for all external momenta and
 542 helicities. Only the internal momenta are analytically continued to d -dimensions.

²Eq. (3.7) can also be generalized to a Feynman integral for l loops and n external momenta.

543 3.1.2 Renormalization

544 As a way to treat the infinities arising from the UV region of integration, the bare
 545 parameters of the Lagrangian are redefined to absorb the divergent contributions. Al-
 546 though this seems mathematically inconspicuous, it is remarkable that the redefinition
 547 of a finite number of parameters allows for the treatment of divergences order-by-order
 548 and for all Feynman diagrams contributing to the amplitude of a renormalizable theory.
 549 In practice, renormalization of the Lagrangian is achieved by rewriting the bare masses
 550 and couplings m_0 and g_0 as a physical (measurable) parameter and a counterterm, as
 551 well as the fields themselves ψ_0 , as

$$\begin{aligned} m_0 &= Z_m m = m + \delta m , \\ g_0 &= Z_g g = g + \delta g , \\ \psi_0 &= \sqrt{Z} \psi . \end{aligned} \tag{3.9}$$

552 The only requirement is that diagrams corresponding to the counterterms should can-
 553 cel UV divergences stemming from the bare Lagrangian. In principle, the procedure does
 554 not define how to handle the finite terms accompanying these diagrams: depending on
 555 the additional criteria, several renormalization schemes can be chosen (on-shell, MS, $\overline{\text{MS}}$,
 556 or others). Here as well, the physical observables should be independent of the choice
 557 of scheme (the top-quark mass is a fringe example and will be discussed summarily in
 558 Chapter 6).

559 The physical parameters entering the Lagrangian, e.g. the masses and couplings m, g ,
 560 have to be determined by experiment. By definition, they are measured at a given energy
 561 scale. Colloquially, a renormalization starting point is chosen: the couplings/masses can
 562 then be evolved to a different scale in a well-defined way. Notably, the parameters of the
 563 renormalized field theory run according to the Callan-Symanzik [68–70] equation, which
 564 governs the dependence of the n -point correlation functions $G_0^{(n)}(x_1, \dots, x_n; m_0, g_0)$ on
 565 the model's parameters:

$$\left(m \frac{\partial}{\partial m} + \beta(g) \frac{\partial}{\partial g} + n\gamma \right) G^{(n)}(x_1, \dots, x_n; m, g) = 0 , \tag{3.10}$$

566 where the β -function of the theory is defined as $\beta(g) = \frac{m}{\delta m} \delta g$, and the anomalous
 567 dimension is given by $\gamma = \frac{m}{\delta m} \frac{\delta \sqrt{Z}}{\sqrt{Z}}$. Eq. (3.10) is an example of a broad class of evolution
 568 equations called renormalization group equations (RGE).

569 3.1.3 Perturbative expansion of Quantum Chromodynamics

570 From the running of the strong coupling constant given by the QCD β -function,

$$\mu_R^2 \frac{\partial \alpha_s}{\partial \mu_R^2} = \beta(\alpha_s) = - (b_0 \alpha_s^2 + b_1 \alpha_s^3 + \dots) , \tag{3.11}$$

3.1 Divergences in Quantum-Field Theory

one sees that because of the negative sign in Eq. (3.11), the strong coupling $\alpha_s(\mu_R^2)$ becomes smaller at higher scales μ_R^2 . This running is manifest in Fig. 3.1, which shows measurements of the strong coupling α_s at different energy scales Q , in agreement with the QCD theory prediction. Thus, with the measured value of the strong coupling at intermediate scales $\alpha_s(M_Z) \approx 0.118$, the interactions at high-energy hadron colliders can be treated perturbatively in α_s . For any partonic cross-section $\sigma_{ab \rightarrow X}$, where a, b , and X are freely propagating initial-, respectively final-states, one can expand the cross-section in a Taylor series,

$$\hat{\sigma}_{ab \rightarrow X} = \alpha_s^k(\mu_R^2) (\hat{\sigma}_{\text{LO}}(p_i, p_f; \mu_R^2) + \alpha_s(\mu_R^2) \hat{\sigma}_{\text{NLO}}(p_i, p_f; \mu_R^2) + \mathcal{O}(\alpha_s^2(\mu_R^2))) . \quad (3.12)$$

At each order in the strong coupling α_s , the cross-section can be computed and will depend on the choice of the renormalization scale. In general, it is chosen close to the expected momentum exchange Q^2 . The systematic uncertainty related to the arbitrary choice of the scale is then usually estimated by varying the renormalization scale by factors of $\frac{1}{2}$ and 2.

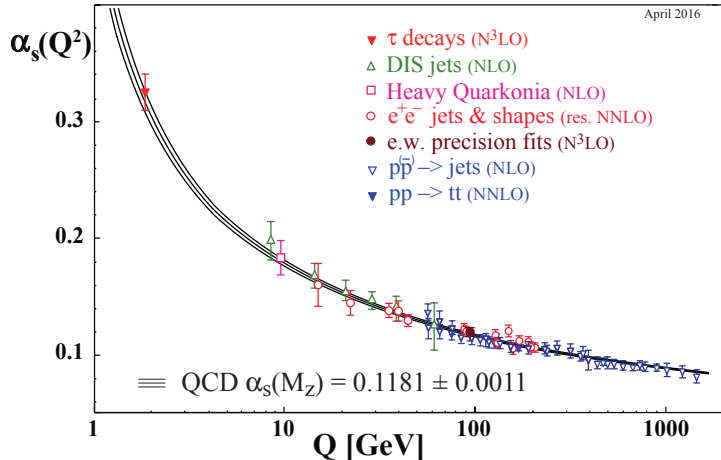


Figure 3.1: Various measurements of the strong coupling $\alpha_s(Q^2)$ at different energy scales Q show the running behavior typical of QCD, with a coupling strength that becomes smaller at higher energies, and a Landau pole at the hadronization scale $Q = \Lambda \sim 1 \text{ GeV}$. Figure taken from Ref. [1].

The accuracy of a computation is given by the truncation order of the perturbative series in Eq. (3.12). In certain regions of phase-space, though, large prefactors can be introduced at all orders, when two far-away scales Q and q are involved. This usually spawns the appearance of large logarithms of the form $\ln^n(Q^2/q^2)$, which have to be resummed to a given *logarithmic* accuracy across all orders. Some details will be given in Section 4.2.

3.2 Infrared divergences

Starting from an example, let us consider the case of QED higher-order corrections to $e^+e^- \rightarrow \mu^+\mu^-$ annihilation, where $m_e = m_\mu = 0$. Feynman diagrams contributing up to $\mathcal{O}(\alpha^3)$ at cross-section level are shown in Fig. 3.2.

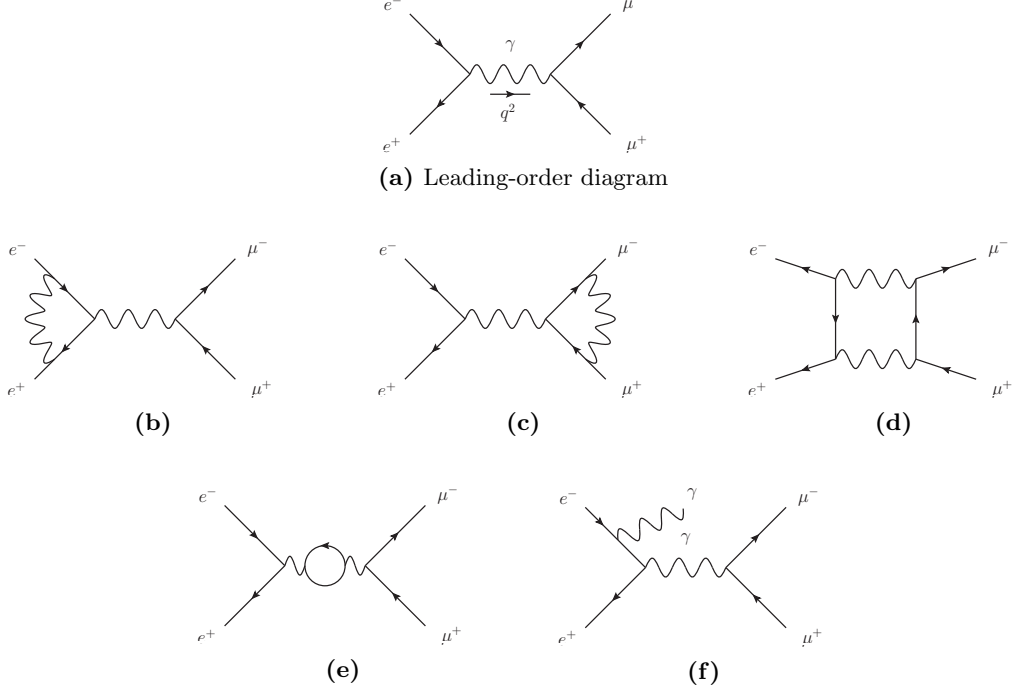


Figure 3.2: Feynman diagrams for $e^+e^- \rightarrow \mu^+\mu^-$. (a) The only leading-order diagram, with a photon in the s -channel, (b-e) virtual one-loop corrections and (f) a real-emission diagram.

At leading-order, the cross-section is given by

$$\sigma_{\text{LO}} = \int_{\Phi} d\Phi |\mathcal{M}_0|^2 = \frac{4\pi\alpha^2}{3q^2}, \quad (3.13)$$

where the squared amplitude $|\mathcal{M}_0|^2$ has to be integrated over the phase-space Φ , and q^2 is the momentum carried by the exchanged photon. Let us assume the UV divergences have been handled by the introduction of appropriate counterterms.³ Computing the amplitude, one realizes there is also an IR divergence coming from the massless photon propagator in the loops, and from the soft photon radiation.

First, the IR divergence needs regularizing. The simplest way to do that is to give the photon a small, non-zero mass, $m_\gamma > 0$, and to take the limit $m_\gamma \rightarrow 0$ at the end of

³The Ward identity [71, 72] in QED relates the renormalization terms together and ensures the cancellation of UV divergences.

3.3 The factorization theorem

the calculation. In this way, the nature of the IR pole is made explicit. Computing the virtual contribution, $\sigma_V \propto (\mathcal{M}_V^\dagger \mathcal{M}_0 + \text{h.c.})$, one arrives at the result

$$\sigma_V = \frac{2}{3} \pi^2 \frac{\alpha^3}{q^2} \left(\frac{\pi^2}{5} - \frac{7}{2} - \ln^2 \left(\frac{m_\gamma^2}{q^2} \right) - 3 \ln \left(\frac{m_\gamma^2}{q^2} \right) \right). \quad (3.14)$$

The IR divergence is still present but it is explicit in $\ln(m_\gamma)$.⁴ For the perturbative expansion to be consistent, real-emission diagrams contributing to $\mathcal{O}(\alpha^3)$ at cross-section level have to be included, that is diagrams of the sort pictured in Fig. 3.2f, where a photon is radiated either from the initial- or the final-state. Doing so, one gets a contribution of the form $\sigma_R \propto |\mathcal{M}_R|^2$:

$$\sigma_R = \frac{2}{3} \pi^2 \frac{\alpha^3}{q^2} \left(-\frac{\pi^2}{5} + 5 + \ln^2 \left(\frac{m_\gamma^2}{q^2} \right) + 3 \ln \left(\frac{m_\gamma^2}{q^2} \right) \right). \quad (3.15)$$

Combining the different contributions to the cross-section, the IR divergences cancel between the virtual one-loop and the real-emission matrix-elements to give a finite correction to the leading-order cross-section:

$$\sigma_{\text{NLO}} = \sigma_{\text{LO}} + \sigma_V + \sigma_R = \sigma_{\text{LO}} \left(1 + \frac{3}{4\pi} \alpha \right). \quad (3.16)$$

This behavior is symptomatic of IR divergences and falls under the purview of the Kinoshita–Lee–Nauenberg (KLN) theorem, which states that sufficiently inclusive observables are always IR-finite.

Although the cancellation of IR divergences is ensured by the KLN theorem, it is non-trivial to realize it numerically (for example in the context of a Monte-Carlo event generator). Section 4.1.2 will briefly develop this point.

3.3 The factorization theorem

The collision of composite states like the protons used at LHC implies interactions of highly non-perturbative objects. It is not clear at first how to handle these theoretically: color confinement does not allow for free quarks or gluons to be observed, thus the initial-state in hadron colliders cannot *a priori* be defined perturbatively. At high-energy, though, the interaction with the highest momentum exchange takes place over time scales that are far smaller than the typical time scale at which the proton's constituents interact among themselves. The description of such a collision can therefore be *factorized* in long- and short-distance (or short- and long-time scale) physics: a hard collision of two freely propagating partons, and non-perturbative interactions within hadrons.

⁴The divergent terms are called Sudakov double logarithms and are systemic of collinear/soft emission (see Chapter 4).

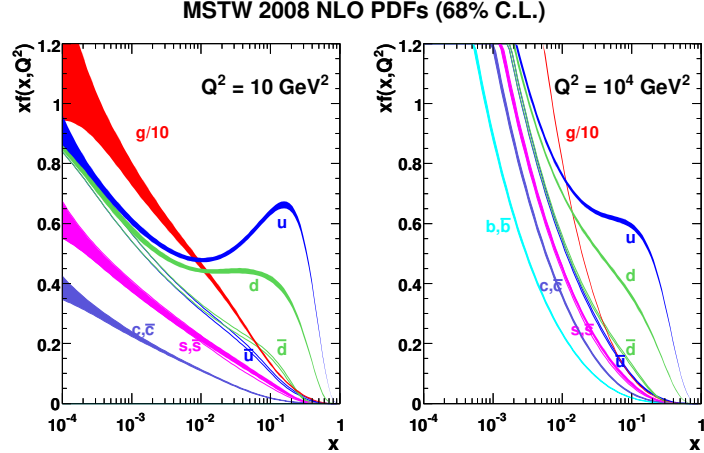


Figure 3.3: The MSTW 2008 NLO proton PDFs [73] as a function of the parent proton's momentum fraction x at resolution scales $Q^2 = 10 \text{ GeV}^2$ (left), $Q^2 = 10^4 \text{ GeV}^2$ (right).

Mathematically, the cross-section $\sigma_{pp \rightarrow X}$ for the production of a state X from the collision of two protons can be written in this approach as

$$\sigma_{pp \rightarrow X} = \sum_{ab} \int dx_a f_{a/p}(x_a, \mu_F^2) \int dx_b f_{b/p}(x_b, \mu_F^2) \cdot \hat{\sigma}_{ab \rightarrow X}(x_a p_1, x_b p_2; \mu_F^2), \quad (3.17)$$

where a and b are possible constituents of the parent protons (sea or valence quarks and gluons), $f_{a/p}$, $f_{b/p}$ are encoding the non-perturbative origin of the partons in the parent protons, and $\hat{\sigma}_{ab \rightarrow X}$ is the cross-section for the production of the final-state X from the collision of the free partons a and b , which can now be computed perturbatively in QCD. Eq. (3.17) is called the *QCD factorization theorem*, and sets the basis for all cross-section predictions at LHC. The functions $f_{a/p}$, $f_{b/p}$, which are called *parton distribution functions* (PDF), depend on the momentum fraction x_a , x_b carried away by the parton from the parent proton, and on the resolution scale Q^2 . Crudely said, the partonic content of the protons depends on the scale at which they are resolved.⁵ The PDFs by definition cannot be computed perturbatively in QCD, but they can be measured from experimental data. As a matter of fact, a precise measurement of the proton's PDF is crucial, and constitutes one of the main sources of uncertainty in theoretical predictions at the LHC. Fig. 3.3 depicts the measurement of the proton PDFs by the MSTW collaboration from a global fit of hard-scattering data [73].

⁵The PDFs also obey an evolution equation similar to the RGE called DGLAP equation: this evolution runs from a central scale choice, namely the *factorization scale* μ_F .

644 4 Monte-Carlo (MC) event generators

645 To be able to compare a theory prediction for hadron colliders to an experimental mea-
646 surement released by e.g. the ATLAS experiment, theorists and experimentalists meet
647 on a common ground: the cross-section σ . The cross-section can be inclusive, and re-
648 presents the total number of events for a given process after applying cuts and correcting
649 for the detector acceptance, or it can be a differential cross-section $d\sigma/d\mathcal{O}$ with respect
650 to some kinematic variable, where \mathcal{O} is any event observable. On one side, the theorists
651 need to compute a cross-section from a QFT starting point, namely from the Lagrangian:
652 at the most basic level, this means implementing Fermi's golden rule:

$$\sigma = \frac{1}{4E_a E_b v} \int \prod_f \left(\frac{d^3 p_f}{(2\pi)^3} \frac{1}{2E_f} \right) |\mathcal{M}_{fi}|^2 (2\pi)^4 \delta^4(p_a + p_b - \sum_f p_f), \quad (4.1)$$

653 On the other side, experimentalists have to count events and correct for detector
654 acceptance and resolution:

$$\sigma = \frac{N_{\text{events}}}{\epsilon \cdot \mathcal{L}_{\text{int}}}, \quad (4.2)$$

655 where E_a and E_b are the energies of the incoming particles a and b , the constant
656 $v = |\vec{v}_a - \vec{v}_b|$ is given by the relative 3-velocities of the particles in the beam and p_f , E_f
657 are the 3-momenta and energies of all final states. As a matter of fact, the infinitesimal
658 volume element above is relativistically invariant. Ultimately, the relativistic matrix-
659 element squared $|\mathcal{M}_{fi}|^2$ has to be integrated over the whole phase-space while enforcing
660 4-momentum conservation. Experimentally, in Eq. (4.2), the cross-section is equal to
661 the event count, corrected for phase-space acceptance, detector resolution and normal-
662 ized by the integrated luminosity \mathcal{L}_{int} . For the case of differential distributions, the
663 formula becomes more complicated, as binned events migrate depending on the detector
664 resolution. The discussion of this case is postponed to Chapter 8.

665 There are two issues with the picture at hand. First, the matrix-element for a given
666 process can typically be computed only up to $\mathcal{O}(\text{few})$ external legs. Because the mul-
667 tiplicity of final-state particles in a collider experiment like the LHC is of the order
668 $\mathcal{O}(10^2 - 10^3)$, it is in practice impossible to calculate such amplitudes. Second, the
669 perturbative expansion and the factorization presented in Chapter 3 break down when
670 colored particles are produced with small energies. In particular, around energy scales
671 where free final-state partons fall in the realm of non-perturbative interactions, they
672 hadronize to form the observable colorless bound states demanded by color confinement.
673 Therefore, the structure of the whole collision has to be broken down into pieces across
674 the several scales involved, and the theoretical treatment of each piece is valid only in

4 Monte-Carlo (MC) event generators

these subdomains and subjected to different levels of approximation. The theory community developed the necessary ingredients to improve the description of each stage and assembled them into mostly-automated programs called *Monte-Carlo (MC) event generators*.

MC event generators basically simulate the particle collisions as they would happen at the interaction points of an experiment like ATLAS or CMS. The MC program has to match multi-scale physics to simulate a collision, taking into account non-perturbative (PDF and quark fragmentation, hadron decay, underlying event, proton beam remnants) as well as perturbative (matrix-element and parton-shower matching) phenomena, as shown in Fig. 4.1.

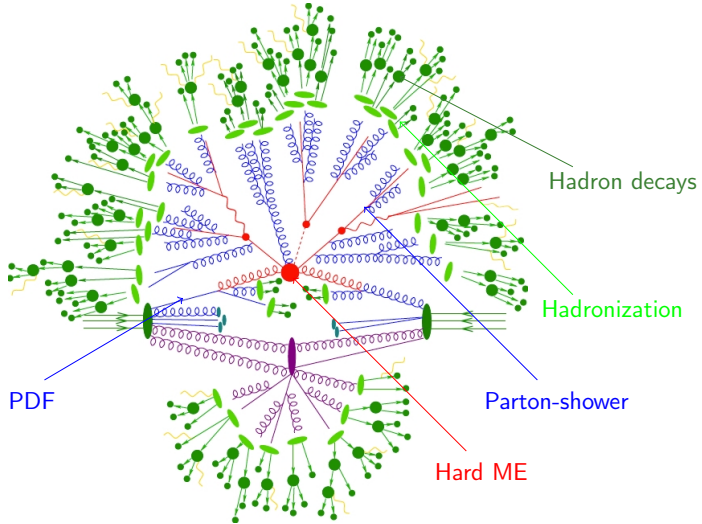


Figure 4.1: A typical MC event. Figure adapted from Ref. [74].

Under the hood of any Monte-Carlo program, the ingredients are essentially the same:

- **Monte-Carlo integrator:** The phase-space is sampled, usually with the help of an adaptive Monte-Carlo integration algorithm, to numerically perform the integral given in Eq. (4.1). As a notable example, the `Cuba` library [75] implements four multi-dimensional integration algorithms: `Vegas` [76], `Divonne` [77], `Suave` [75, 78] and `Cuhre` [79] (although `Cuhre` is deterministic and not properly a MC integrator).
- **PDFs:** There is an extensive amount of PDF measurements varying in the used datasets, theoretical precision, combination strategy, handling of α_s , or flavor thresholds. The `LHAPDF6` package [80] interpolates PDF values from discrete measurement points in the (x, Q^2) phase-space and can be interfaced to the MC generator.

- **Hard matrix-element:** The core of the calculation is the computation of the matrix-element \mathcal{M}_{fi} . It determines the theoretical accuracy of the prediction to a given order in the corresponding couplings. More details are given in Section 4.1.
- **Parton shower:** As stated above, the high-multiplicity final-state is evolved from the few-parton hard matrix-element through subsequent radiative emission by a parton-shower algorithm. These routines base on first-principles QCD (and QED), but contain inherent approximations and parametric degrees of freedom that generate an uncertainty associated with the choice of algorithm. Section 4.2 will expand on the topic.
- **Hadronization and hadron decay:** Once the shower evolution is brought down to energies of the order of the hadronization scale (of order $\mathcal{O}(1 \text{ GeV})$), the free partons bind to form colorless states. This is handled by a model on the only assumption that it should describe data to the best possible extent. Commonly, these models have a certain number of free parameters that are *tuned* to data. In Section 4.3, the Lund string and the cluster model are briefly detailed.
- **Multiple partonic interaction and underlying event:** Especially at small momentum fractions, it is possible that more than one parton from the same parent proton contribute to the interaction. The description of this phenomenon is also mostly based on MC modeling and has to be tuned to experimental data.

4.1 Matrix-element providers

The first programs for generating the matrix-element \mathcal{M}_{fi} needed in Eq. (4.1) were highly specialized. They would handle one specific process and would be mostly analytically hard-coded. At some point, authors from the theory community started to make their code available and the corresponding libraries would be assembled into multi-processes packages. This is the example of the MCFM [81], VBFNLO [82–84] and BlackHat [85] packages. Nowadays, after a paradigm shift, the computation of the hard process matrix-element is decidedly automatized at one-loop level: programs like MADLOOP [86–89], OPENLOOPS [90, 91], GoSAM [92, 93], RECOLA [94, 95] and HELAC-NLO [96] can be interfaced directly to most MC generators and provide the amplitude given any phase-space point, while other programs focus on specific processes, as for example NJET [97], which calculates multijet amplitudes at NLO in massless QCD, VBFNLO for vector-boson fusion in a number of processes, or HJETS++ [98] for Higgs boson production in association with one or more jets in the high-energy limit. The program GoSAM-2.0 is used in all subsequent NLO computations, thus its mode of operation is detailed in the next section.

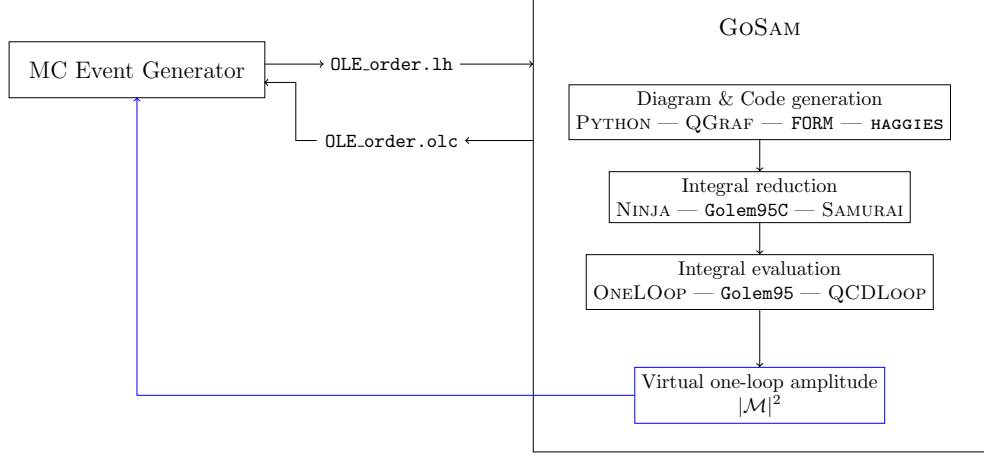


Figure 4.2: GoSAM relies on external packages to compute virtual one-loop amplitudes. Feynman diagrams are generated by QGRAF, and fortran code containing the terms relevant to each diagram is automatically written out by FORM. The various integral families are then reduced and the basis integrals evaluated using external libraries.

731 4.1.1 GoSam: MC interfacing of one-loop amplitudes

732 GoSAM is a general-purpose package that computes one-loop amplitudes automatically
 733 and interfaces to any MC generator, provided it supports the Bineth-Les Houches Accord
 734 (BLHA1 [99] or BLHA2 [100]) format. The workflow of GoSAM is shown in Fig. 4.2.

735 Any process can be defined in the GoSAM input card, where only incoming and
 736 outgoing particles as well as the desired order in α, α_s for the generation of the Feynman
 737 diagrams have to be given. The PYTHON `gosam.py` executable is then called and a
 738 series of external packages handle the different steps of the computation: QGRAF [101]
 739 generates the Feynman diagrams, and filters for vertices or propagators can be applied,
 740 as well as manual removal of diagrams. Then, FORM [102] code containing the relevant
 741 expressions is generated automatically for all diagrams and helicities. Integral reduction
 742 is operated by any of three programs, namely NINJA [103], Golem95C [104, 105] or
 743 SAMURAI [106]. Finally, the evaluation of the set of basis integrals is performed using one
 744 of the three external integral libraries QCDLOOP [107], ONELOOP [108] or Golem95C.

745 On a higher level, in compliance with BLHA, the MC generator produces an order
 746 file `OLE.order.1h` containing the subprocesses to be computed by GoSAM. The latter is
 747 called and generates routines for all subprocesses. After checking the order file, GoSAM
 748 validates the order and returns a contract file `OLE.order.olc`. The generated libraries
 749 for all helicities are linked, and common functions are written in a `matrix.f90` file to be
 750 called by the MC generator. The physics parameters, like particle masses and couplings,
 751 can be set by an external call to the `OLP_Option` function. Then, for a set of 4-momenta
 752 $(p_i)_{i=1,\dots,n}$, the matrix-element is provided by calling the `OLP_EvalSubProcess({p_i})`
 753 function, which returns the full one-loop amplitude coefficients $c_{(-2)}, c_{(-1)}$ and c_0 (double,
 754 single pole and finite terms) as given in the Laurent series

$$\text{Re}\{\mathcal{M}^{(0)}\mathcal{M}_{\text{virt}}^{(1)}\} = g_1^{n_1} \dots g_q^{n_q} \frac{\alpha_s}{2\pi} \frac{(4\pi)^\epsilon}{\Gamma(1-\epsilon)} \left(\frac{c_{(-2)}}{\epsilon^2} + \frac{c_{(-1)}}{\epsilon} + c_0 + \mathcal{O}(\epsilon) \right), \quad (4.3)$$

where $g_i^{n_i}$ are the coupling constants appearing in the tree-level matrix-element. GoSAM is a very flexible package, and allows high-level control over the various subtleties of higher-order computations (e.g. choice of regularization scheme, renormalization counterterms, and so on). A rescue system for phase-space points that are numerically badly behaved can be activated, and the amplitude for these is recomputed either in quadruple precision or with a different method.

4.1.2 Infrared divergence cancellation

Having acquired the virtual contribution to the amplitude, one has to combine the Born, virtual and real-emission contributions together. As was shown in Section 3.2, the singularities appearing in both virtual loop calculations and in soft/collinear configurations of real emissions should combine to give finite quantities for any IR-safe observable.¹ Although this is analytically true, in the case of MC computations, the different contributions are first sampled over different phase-spaces, and only then combined. Symbolically, for the NLO cross-section σ^{NLO} :

$$\sigma^{\text{NLO}} = \int_{\Phi_m} d\sigma^B + \int_{\Phi_m} d\sigma^V + \int_{\Phi_{m+1}} d\sigma^R, \quad (4.4)$$

where $d\sigma^B$, $d\sigma^V$ and $d\sigma^R$ are the Born, virtual and real contributions. Note that the singularities in virtual and real contributions only cancel after integration. Numerically, the cancellation of IR divergences is thus non-trivial. At NLO, there are two kinds of algorithms to implement IR divergence cancellation: phase-space slicing and subtraction methods. The Catani-Seymour (CS) [109] and Frixione-Kunzst-Signer (FKS) [110, 111] automatized subtraction of IR divergences are mostly used nowadays in NLO MC generators. The CS algorithm is outlined below and is used in all calculations present in Chapters 6–10, while the PowHEG framework in Chapter 11 uses the FKS scheme.

Consider the addition of a subtraction term $d\sigma^S$ which approximates the ($d = 4 - 2\epsilon$ regularized) real contribution and reproduces its IR singularity pattern in d dimensions:

$$d\sigma^V + d\sigma^R = d\sigma^V + d\sigma^S + (d\sigma^R - d\sigma^S). \quad (4.5)$$

Then, the ($d = 4$)-dimension limit can be taken directly for the integration of the real-emission and the local counterterm cancels the divergence in the phase-space integrand. The total NLO cross-section then takes the form:

$$\sigma^{\text{NLO}} = \int_{\Phi_m} d\sigma^B + \int_{\Phi_m} \left(d\sigma^V + \int_{\Phi_1} d\sigma^S \right)_{\epsilon=0} + \int_{\Phi_{m+1}} (d\sigma^R|_{\epsilon=0} - d\sigma^S|_{\epsilon=0}), \quad (4.6)$$

¹Generally, at NLO, regularized poles appear either as double poles (soft and collinear), or single poles (soft, collinear, or UV).

4 Monte-Carlo (MC) event generators

782 where all integrals are now separately finite. The CS dipole formalism is a factorization
 783 framework that allows the automatic generation of the subtraction term $d\sigma^S$. Universal
 784 dipole factors are introduced for any process, and setting the subtraction term to

$$d\sigma^S = \sum_{\text{dipoles}} d\sigma^B \otimes dV_{\text{dip}}, \quad (4.7)$$

$$\int_{\Phi_{m+1}} d\sigma^S = \sum_{\text{dipoles}} \int_{\Phi_m} d\sigma^B \otimes \int_{\Phi_1} dV_{\text{dip}} =: \int_{\Phi_m} d\sigma^B \otimes \mathbf{I} \quad (4.8)$$

785 allows one to compute the cross-section σ^{NLO} of any process:

$$\int_{\Phi_m} d\sigma^B + \int_{\Phi_m} (d\sigma^V + d\sigma^B \otimes \mathbf{I})|_{\epsilon=0} + \int_{\Phi_{m+1}} \left(d\sigma^R|_{\epsilon=0} - \sum_{\text{dipoles}} d\sigma^B \otimes dV_{\text{dip}}|_{\epsilon=0} \right) \quad (4.9)$$

786 with \mathbf{I} the integrated CS insertion operator. The universal dipole factors are obtained
 787 by considering the soft/collinear limits of a one-emission matrix-element with respect to
 788 the Born configuration:

$$|\mathcal{M}_{m+1}|^2 = \sum_{k \neq i,j} \mathcal{D}_{ij,k}(p_1, \dots, p_{m+1}) + (\text{regular in } p_i \cdot p_j \rightarrow 0) \quad (4.10)$$

$$= - \sum_{k \neq i,j} \frac{1}{2p_i \cdot p_j} \mathcal{M}_m^\dagger(i, j \rightarrow \tilde{i}\tilde{j}, \tilde{k}) \left(\frac{\mathbf{T}_k \cdot \mathbf{T}_{ij}}{\mathbf{T}_{ij}^2} \mathbf{V}_{ij,k} \right) \mathcal{M}_m(i, j \rightarrow \tilde{i}\tilde{j}, \tilde{k}) \\ + (\text{regular in } p_i \cdot p_j \rightarrow 0) \quad (4.11)$$

789 where the singular terms are collected in the dipoles $D_{ij,k}$. The \mathbf{T}_i are the generators of
 790 the color algebra and \mathcal{M}_m is a general matrix-element corresponding to an m -particle
 791 final-state, $\mathcal{M}_m = |1, \dots, m\rangle$. Then Eq. (4.11) states that the matrix-element corre-
 792 sponding to an $(m+1)$ -particle final-state factorizes into dipole factors $\mathbf{V}_{ij,k}$ convo-
 793 luted with an underlying Born configuration where partons i and j are assembled into
 794 one parton $(\tilde{i}\tilde{j})$ (the so-called *emitter*), and parton \tilde{k} (the *spectator*) absorbs the residual
 795 4-momentum. The formulae for the universal dipoles $\mathbf{V}_{ij,k}$ are very closely related to
 796 the Altarelli-Parisi splitting functions, see Section 4.2.

797 In the case of the presence of initial-state hadrons like at the LHC, Eq. (4.11) is
 798 modified and an additional dipole term has to be added in Eq. (4.8), $dV_{\text{dip}} \rightarrow dV_{\text{dip}} +$
 799 dV'_{dip} . Eq. (4.8) then becomes

$$\int_{\Phi_{m+1}} d\sigma^S = \int_{\Phi_m} d\sigma^B \otimes \mathbf{I} + \int_0^1 dx \int_{\Phi_m} d\sigma_B(xp) \otimes (\mathbf{P} + \mathbf{K})(x), \quad (4.12)$$

800 where xp is the proton momentum fraction carried away by the parton, and \mathbf{P}, \mathbf{K} are
 801 insertion operators appearing from the convolution with the PDF.

4.2 Parton-shower models

4.2.1 The Altarelli-Parisi splitting functions

Parts of the following section are adapted from Ref. [112]. Inherently, the few-parton, high-energy final-state generated by the hard process matrix-element further produces both QCD and QED radiation. The parton-shower algorithm evolves partons from the collision scale Q^2 , letting them radiate new partons (quarks and gluons), to a cutoff scale Q_{\min}^2 that is set around the hadronization scale. At that point, the shower terminates and the final-state is passed on to the hadronization model. Schematically, the simplest shower algorithms are based on the so-called Dokshitzer–Gribov–Lipatov–Altarelli–Parisi (DGLAP) kernels [113–115] for $1 \rightarrow 2$ collinear particle splitting $P_{a \rightarrow bc}$, as given in Fig. 4.3.

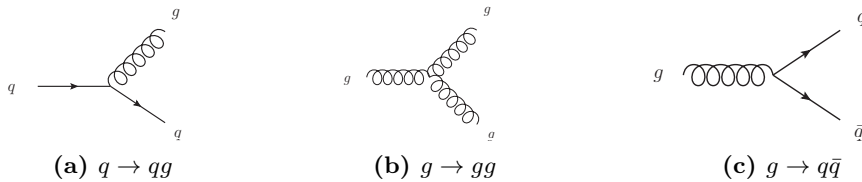


Figure 4.3: The QCD vertices for $1 \rightarrow 2$ splittings allow to calculate the leading-order kernels appearing in the DGLAP evolution equation.

The (unregularized) LO kernels can be computed from the QCD interaction vertices as:

$$P_{q \rightarrow qg}(z) = C_F \frac{1+z^2}{1-z}, \quad (4.13)$$

$$P_{g \rightarrow gg}(z) = 2C_A \left(\frac{1-z}{z} + z(1-z) + \frac{z}{1-z} \right), \quad (4.14)$$

$$P_{g \rightarrow q\bar{q}}(z) = T_R(1 - 2z(1-z)). \quad (4.15)$$

with z , $0 \leq z \leq 1$, the longitudinal momentum fraction of the parent parton a . Notice the undefined behavior of $P_{q \rightarrow qg}$ and $P_{g \rightarrow gg}$ for $z \rightarrow 1$: the splitting functions can be regularized from general constraints to:

$$P_{q \rightarrow qg}(z) = C_F \left(\frac{1+z^2}{(1-z)_+} + \frac{3}{2} \delta(z-1) \right), \quad (4.16)$$

$$P_{g \rightarrow gg}(z) = 2C_A \left(\frac{1-z}{z} + z(1-z) + \frac{z}{(1-z)_+} + \left(\frac{11}{12} - \frac{1}{3} \frac{T_R}{C_A} \right) \delta(z-1) \right), \quad (4.17)$$

$$P_{g \rightarrow q\bar{q}}(z) = T_R(1 - 2z(1-z)). \quad (4.18)$$

The factor $(1-z)^{-1}$ is regularized in being interpreted as a plus-distribution $(1-z)_+^{-1}$ such that for any test function $f(z)$ sufficiently regular at $z=0, z=1$,

4 Monte-Carlo (MC) event generators

$$\int_0^1 \frac{dz f(z)}{(1-z)_+} = \int_0^1 \frac{f(z) - f(1)}{1-z} . \quad (4.19)$$

820 The master equation governing the evolution of the collinear splitting of a parton a
 821 from a scale q^2 to a scale $q^2 + dq^2$ is then given by

$$dP_{a \rightarrow bc} = \frac{dq^2}{q^2} \frac{\alpha_s}{2\pi} P_{a \rightarrow bc}(z) dz , \quad (4.20)$$

822 where q^2 is an arbitrary strong-ordered evolution variable. It can be the azimuthal
 823 angle of emission $E_a^2 \theta^2$, or the particle's virtuality m^2 , or the transverse momentum
 824 p_T^2 . Different shower algorithms implement different choices of the evolution variable.
 825 This will be of importance when considering parton-shower related uncertainties, see
 826 Chapters 7 and 11.

827 4.2.2 The Sudakov form factor

828 Going from the one-emission to the multiple-emission case, and using broad assump-
 829 tions², the probability of no-emission between scales Q^2 and Q_{\max}^2 is given by the *Sudakov*
 830 *form factor*:

$$dP_{a \rightarrow bc}(z) = \frac{dq^2}{q^2} \frac{\alpha_s}{2\pi} P_{a \rightarrow bc}(z) dz \times \exp \left(- \sum_b \int_{Q^2}^{Q_{\max}^2} \frac{dq'^2}{q'^2} \int \frac{\alpha_s}{2\pi} P_{a \rightarrow bc}(z') dz' \right) . \quad (4.21)$$

831 As explained in Section 3.1.3, the perturbative expansion of the cross-section in α_s can
 832 suffer from large enhancements in the soft/collinear regions of phase-space. In general,
 833 double logarithms of the form $\alpha_s^n \log^{2n}(Q^2/q^2)$ appear when a soft particle is emitted, or
 834 when it becomes collinear to one of the incoming partons. Here, q^2 is the scale describing
 835 the soft/collinear emission, and Q^2 is the global scale of the process. Generally, this tower
 836 of large logarithms can be analytically resummed to all orders in α_s . Instead, the parton
 837 shower algorithm offers the possibility of resumming soft and collinear contributions
 838 within the Monte-Carlo framework. Nowadays, most parton showers only guarantee
 839 leading-logarithmic (LL) accuracy, although recent studies [116] have found differences
 840 at LL (subleading number of colors N_C), and NLL (leading- N_C) between parton-showers
 841 and analytic resummations.

842 4.2.3 Parton-shower matching

843 The shower algorithm should respect the theoretical accuracy of the hard matrix-element,
 844 and at the same time conserve the logarithmic accuracy of the parton-shower resumma-
 845 tion in their respective limits. In particular, the cross-section after showering should

²Namely that the time between emissions can be sliced, and unitarity as well as multiplicativity (meaning the shower has no memory of past emissions) hold.

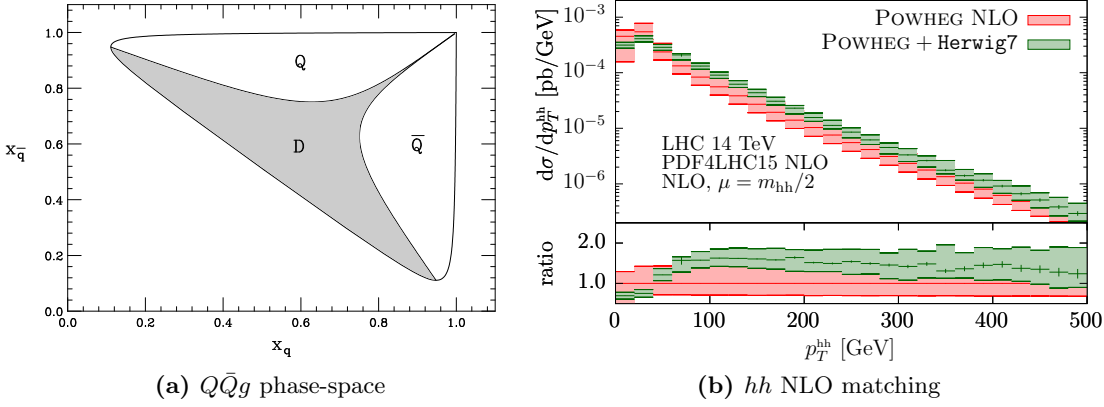


Figure 4.4: (a) Phase-space for a heavy-quark pair emitting a gluon, depicted as a function of the Dalitz plot variables ($x_Q, x_{\bar{Q}}$). Figure adapted from Ref. [121]. (b) The transverse momentum p_T^{hh} of the Higgs pair system in di-Higgs production is compared for the fixed-order NLO prediction to a parton-shower matched calculation.

be identical to the fixed-order cross-section. Also, kinematic configurations that belong both to the hard matrix-element and the parton-shower final-states should not be double-counted. This whole procedure is called *matching*.

At NLO, the matching of the parton-shower algorithm to the fixed-order matrix-element handles both these issues. Roughly said, it interpolates between the two kinematic regions where the hard matrix-element, respectively the parton-shower, generate their respective dominant contributions. As an example, the phase-space for the production of two heavy quarks and one gluon-emission $Q\bar{Q}g$ is given in Fig. 4.4a. The soft/collinear emission regions (where $x_Q \rightarrow 1$ or $x_{\bar{Q}} \rightarrow 1$, with $x_j = 2p \cdot q_j/p^2$, and p is the initial center-of-mass 4-momentum) can be covered by the parton-shower while the dead region (shaded) describes a hard gluon-emission (matrix-element). In a correct matching, these regions should not overlap. An illustration of this fact is shown in Fig. 4.4b for the case of $gg \rightarrow hh$ production, where a fixed-order NLO calculation is matched to the HERWIG7 [117, 118] parton-shower. There, the parton-shower correctly reproduces the NLO computation at high-transverse momentum and softens the low-momentum region (Sudakov suppression). Among the various matching procedures that keep in line with the above criteria, the subtractive MC@NLO [119] and the multiplicative Powheg [120] schemes are among the most used ones.

As examples of available parton-shower algorithms mostly used by the physics community, the PYTHIA8 [122, 123] and HERWIG7 codes implement a p_T -ordering, respectively an angular-ordering in the choice of the evolution variable. HERWIG also uses a dipole shower as an alternative algorithm (which is based on a Catani-Seymour dipole formulation of $2 \rightarrow 3$ splitting kernels). The Sherpa [124] generator implements two alternative parton-shower algorithms based on variations of the CS dipoles.

870 4.3 Hadronization

871 Once particles have been showered down to the hadronization scale, the hadronization
 872 model takes over. By far, the two most used hadronization models are the Lund string
 873 model and the cluster model.

874 4.3.1 The Lund hadronization string model

875 The Lund string model [125] is based on the principle of quark color confinement. When
 876 two quarks are separated by a distance r , the potential takes the form:

$$U(r) = -\frac{4}{3} \frac{\alpha_s}{r} + \kappa r, \quad (4.22)$$

877 and the linear confinement contribution dominates for larger distances, with $\kappa \sim$
 878 1 GeV/fm. In analogy to a classical elastic potential, the field lines build up a stretched
 879 *string*. When the distance between a quark-pair increases, the string tension grows
 880 until the string breaks: the freed energy creates another quark-antiquark pair appearing
 881 from the vacuum. The creation of the quark-pair happens with a Gaussian probability
 882 (similarly to quantum tunnelling) in the quark transverse mass $m_T^2 = m^2 + p_T^2$. From
 883 Lorentz invariance, causality and left-right symmetry, the fragmentation function $f(z)$
 884 can be constrained and fixes the longitudinal momentum fraction z carried away by the
 885 created hadron:

$$\mathcal{P} \propto \exp\left(-\frac{\sigma m_T^2}{\kappa}\right), \quad f(z) \propto \frac{(1-z)^a}{z} \exp\left(-\frac{bm_T^2}{z}\right). \quad (4.23)$$

886 The Lund string model is implemented in the PYTHIA 8 generator and the main
 887 parameters a, b, σ are determined by tuning to data. For the more complex case of
 888 baryons, the three quarks can be pictured in a quark-diquark frame. Finally, the gluons
 889 appear as kinks on strings. For more details and improvements to the model, see the
 890 PYTHIA manual [126].

891 4.3.2 The cluster hadronization model

892 Instead of building on color confinement, the cluster model [127, 128] makes the as-
 893 sumption that gluons can be viewed as carrying color and anticolor and behaving as a
 894 $q\bar{q}$ pair. Color singlets usually obey a mass spectrum that peaks at low mass due to
 895 the property of preconfinement of the parton shower [129], i.e. they are closer to one
 896 another in phase-space. The model then clusters these color singlets together and splits
 897 them per the following procedure: if a cluster of mass M , with parton constituents of
 898 masses m_1, m_2 , satisfies

$$M^{C_{\text{pow}}} > C_{\text{max}}^{C_{\text{pow}}} + (m_1 + m_2)^{C_{\text{pow}}}, \quad (4.24)$$

899 the algorithm splits it and the masses get redistributed. To split a cluster, the model
 900 pops a $q\bar{q}$ pair from the vacuum and forms two new clusters with one original parton
 901 each, and masses distributed according to

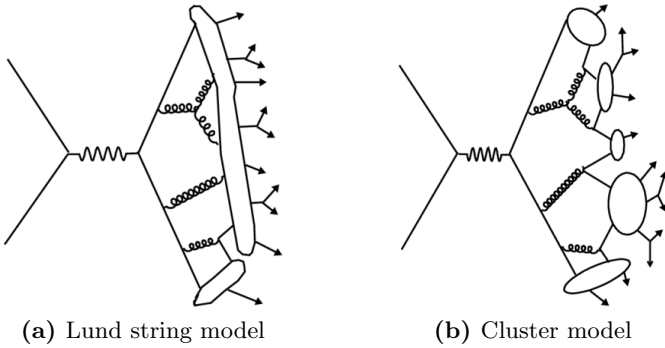


Figure 4.5: A pictorial representation of both hadronization models. (a) In the Lund model, the potential energy from the color field between two quarks increases linearly with the distance, like in a string. When a string breaks, a new quark-antiquark pair is created. (b) The cluster model groups color-connected partons together into clusters and lets them decay isotropically.

$$M_{1,2} = m_{1,2} + (M - m_{1,2} - m_q) \mathcal{R}_{1,2}^{P_{\text{split}}}, \quad (4.25)$$

with $\mathcal{R}_{1,2} \in [0, 1]$ two random numbers. Again, the parameters C_{pow} , C_{max} and P_{split} have to be tuned to data.

Notice that the cluster model does not propagate any spin information: the hadronized clusters therefore decay isotropically. Historically, the cluster model was implemented in the HERWIG event generator. Fig. 4.5 summarizes the conceptual differences between the Lund string and the cluster model.

As a concluding remark, the MC event generators represent the basis of a large fraction of experimental measurements. They are quite complex systems whose constituents are all inter-correlated: the different pieces interact and the matching between all appearing physical scales is not always explicit at the end of the simulation. Typically, the parton-shower output influences the hadronization tune, and it is in general difficult to disentangle their respective contributions. As such, variations in the MC setup are linked to large uncertainties which should, in principle, be taken into account with their full correlations.

916 5 The LHC and the ATLAS detector

917 The Large Hadron Collider (LHC) is currently the most powerful particle accelerator
 918 worldwide and is located at the Centre Européen pour la Recherche Nucléaire (CERN)
 919 on the French-Swiss border, near Geneva. Historically, it replaced the Large Electron-
 920 Positron (LEP) collider after it was decommissioned in 2000, and is being housed in
 921 the same tunnel. In this chapter, the main working parts of the accelerator complex
 922 are briefly reviewed, and the structure of the ATLAS detector presented in more de-
 923 tail. A short overview of the trigger and data acquisition system, as well as the object
 924 reconstruction and MC simulation, will close the subject.

925 5.1 The Large Hadron Collider

926 The LHC's main collider ring [130–132] is installed in a circular tunnel of ~ 27 km
 927 circumference and a depth varying between 45 m and 170 m under ground level. It is
 928 designed to accelerate protons up to an energy of 7 TeV, reaching a design center-of-
 929 mass energy of 14 TeV at a peak luminosity of 10^{34} cm $^{-2}$ s $^{-1}$. As a side note, the LHC
 930 can also accelerate heavy ions, and in the past a few runs of lead-lead, proton-lead and
 931 xenon-xenon collisions have also given interesting complementary physics results.

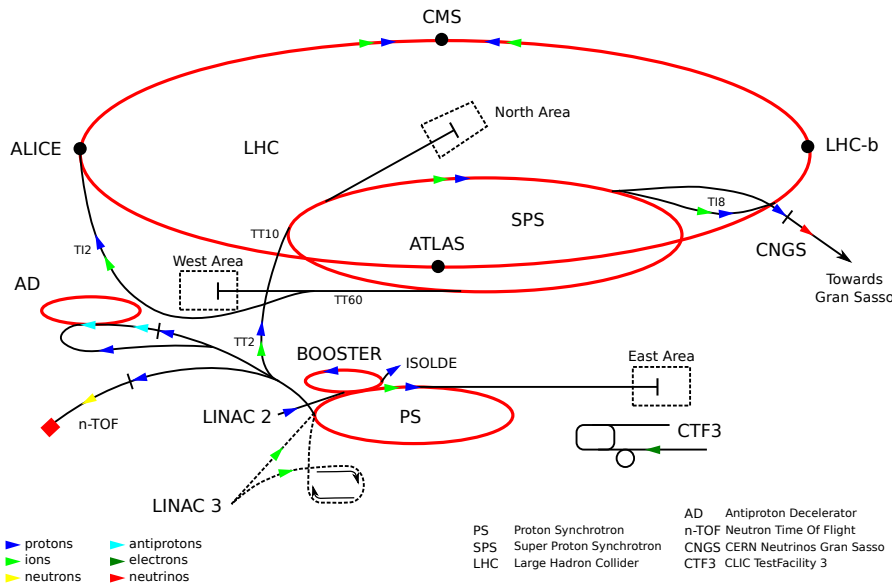


Figure 5.1: The LHC accelerator complex [133].

5 The LHC and the ATLAS detector

To accelerate protons to these high energies, a sequence of pre-accelerators boosts the proton beams before injecting them into the next link. A schematic of the full accelerator complex is presented in Fig. 5.1. Upon being produced and pre-collimated, the protons are accelerated to 50 MeV in the Linac2, then to 1.4 GeV in the Proton Synchrotron (PS) Booster, and to 26 GeV in the PS. Within the PS, the protons are collimated into 25 ns-spaced (7.5 m) bunches of around $1.15 \cdot 10^{11}$ protons per bunch. From there, the Super Proton Synchrotron (SPS) ramps up the energy to 450 GeV, and injects both beams in opposite directions into the LHC itself. After approximately 20 minutes of acceleration in the main LHC beampipe by 16 radiofrequency cavities, the proton bunches achieve the current energy of 6.5 TeV per beam.

Equipped with 1232 superconducting main dipole magnets, the LHC operates with magnetic fields of ~ 8.3 T to keep the proton bunches on their circular trajectory. The main dipole magnets are supplemented by higher-multipole magnets to correct for edge imperfections in the dipole field. Along the LHC beam path, 392 main quadrupole magnets are used to re-focus the proton beams.

Once at the nominal energy, the two circulating proton beams are brought to collision at four different interaction points, corresponding to the four biggest LHC experiments: ATLAS, CMS, ALICE and LHCb. Out of these, ATLAS and CMS are general-purpose detectors designed to discover higher-mass particles like the Higgs boson or possible supersymmetric resonances, as well as to produce high-precision measurements of particles like the top quark. On the other hand, ALICE is dedicated to studies of heavy-ion collisions and focuses on high-density QCD bound states, while LHCb is optimized to investigate heavy-flavor physics. From the start of Run II in 2015 until the Long Shutdown of December 2018, the LHC delivered a total integrated luminosity of 147 fb^{-1} at a maximal center-of-mass energy of 13 TeV and a peak luminosity of $2.1 \cdot 10^{34} \text{ cm}^{-2} \text{ s}^{-1}$, even surpassing the design value. The next section concentrates on the ATLAS detector substructure.

5.2 The ATLAS detector

A Toroidal LHC ApparatuS (ATLAS) [134] aims for high-energy precision measurements of the SM in all possible sectors: with the help of the enormous amount of data produced at LHC and the precision of the tracking detectors and calorimeters, it allows for measurements of particle masses, SM couplings or cross-section measurements, but also the observation of rare SM processes (like $t\bar{t}h$ production [135], light-by-light scattering [136] or $B_s^0 \rightarrow \mu^+ \mu^-$ decays [137]). These high-precision tests of the SM are intrinsically linked to searches for Beyond the SM (BSM) physics: higher-scale BSM particles participating in loop corrections to the SM can have an impact on the cross-sections or kinematic observables, and any observed deviation from the SM predictions would hint at New Physics at higher scales. In general, though, direct searches are employed to look for potential high-mass resonances.

The ATLAS detector, situated at the LHC beam interaction point 1 near Meyrin, Switzerland, has an onion-shell structure comprised of particle trackers, electromagnetic

and hadronic calorimeters, and a muon detector: from inner to outer radii, the produced particles encounter the Inner Detector (ID), the Liquid Argon (LAr) and the Tile Calorimeter (TileCal), and finally the Muon Spectrometer (MS). The detector itself is 44 m long and has a diameter of 25 m, and weighs more than 7000 tons. Fig. 5.2 shows a sketch of the ATLAS detector. To bend the charged-particle tracks for momentum measurement, ATLAS relies on four magnets: a 2 T central solenoid [138] close to the interaction point, an 8-coil barrel toroid [139] that is cylindrically placed around the detector generating a peak magnetic field of 4 T, and two other 8-coil toroid magnets at the detector endcaps [140] which provide a peak magnetic field of 4 T on the superconductor (0.2 – 3.5 T in the bore). The geometry of the magnet coils is shown in Fig. 5.3.

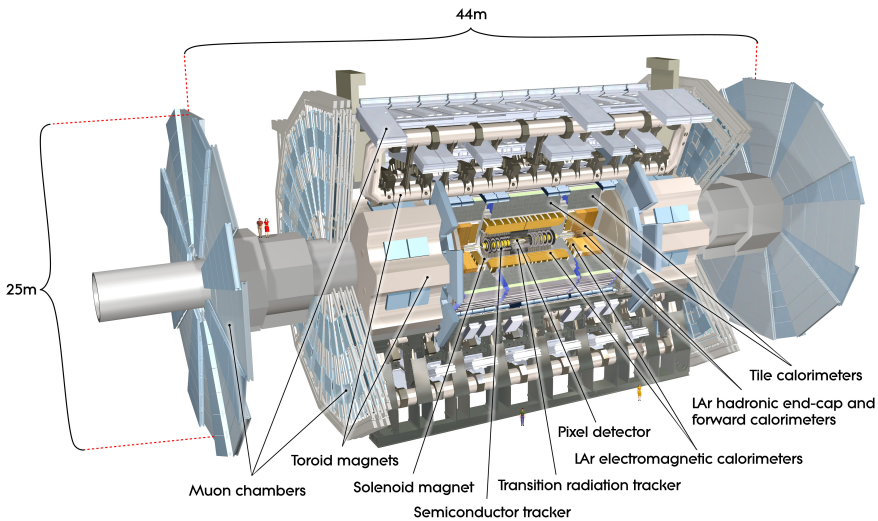


Figure 5.2: A cut-away view of the ATLAS detector. Figure from Ref. [134].

The ATLAS coordinate system is defined as right-handed and centered at the interaction point, with the beam axis chosen as the z -axis, the x -axis pointing towards the center of the LHC ring, and the y -axis pointing upwards.

5.2.1 The Inner Detector

Being the detector closest to the beampipe, the Inner Detector (ID) [141, 142] must fulfill several criteria for the reconstruction of charged-particles four-momenta, as well as for the identification of secondary vertices due to the decay of bottom-flavored hadrons or τ leptons, and for the measurement of the impact parameter. The ID is further divided into a silicon Pixel Detector [143], a Semiconductor Tracker (SCT) [144] and a Transition Radiation Tracker (TRT) [145, 146]. In Fig. 5.4, the structure of the ID is presented in a cut view along the beampipe (with the notable absence of the new insertable B -layer, or IBL [147, 148]).

The Pixel Detector has a total of $8.6 \cdot 10^7$ channels and is the device closest to the interaction point. Four concentric layers of silicon pixel detectors are laid out around the

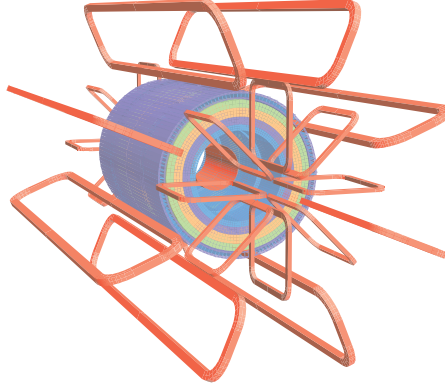


Figure 5.3: The geometry of the coils used to produce the magnetic field in the ATLAS detector. A solenoid magnet (2 T) is installed cylindrically around the beampipe, surrounded by a toroid magnet (4 T) and two endcap toroid magnets (4 T). Figure from Ref. [134].

beam axis in so-called barrel layers. The innermost layer is called the insertable B -layer (IBL) and was installed during the first Long Shutdown. It is only 3.3 cm away from the nominal interaction region and improves measurements of (secondary) vertex positions. It was designed to work in a high-radiation environment. Three other layers are disposed concentrically around the beampipe, and additionally three pixel disks are mounted on each endcap. The Pixel Detector reaches a resolution of $\sim 10 \mu\text{m} \times 75 \mu\text{m}$ [149, 150] in the transverse, respectively longitudinal ($R\phi, z$) directions.

At intermediate radius, the SCT is a silicon microstrip tracker and provides, using $6.2 \cdot 10^6$ readout channels, a measurement of the (R, ϕ, z) track points. Four SCT barrel layers are disposed at radii between 299 mm and 514 mm away from the beampipe, while 18 more planar discs are placed at the endcaps. The barrel modules have a resolution of $17 \mu\text{m} \times 570 \mu\text{m}$ [144, 151].

Finally, at the outer layer, the Transition Radiation Tracker is made of thin-walled straw tubes and gives information for distinguishing electrons from pions, as well as contributes to the transverse position measurement for a total of $3.5 \cdot 10^5$ readout channels. A straw tube is a 4 mm-diameter cylinder filled with gaseous xenon and a gold-plated tungsten wire strung through the center. The inner tube wall serves as cathode and the wire as an anode. A high voltage of 1.5 kV is applied, and charged particles passing through ionize the gas. The freed electrons then drift to the wire, and the drift time can be used to determine the distance of the particle from the anode. Moreover, electron identification succeeds by transition-radiation photons created between the straws and converted in the xenon gas. The probability of transition radiation is proportional to the relativistic γ -factor, which is usually highest for electrons and positrons. The TRT determines the transverse position at a resolution of $\sim 110 - 130 \mu\text{m}$ [152].

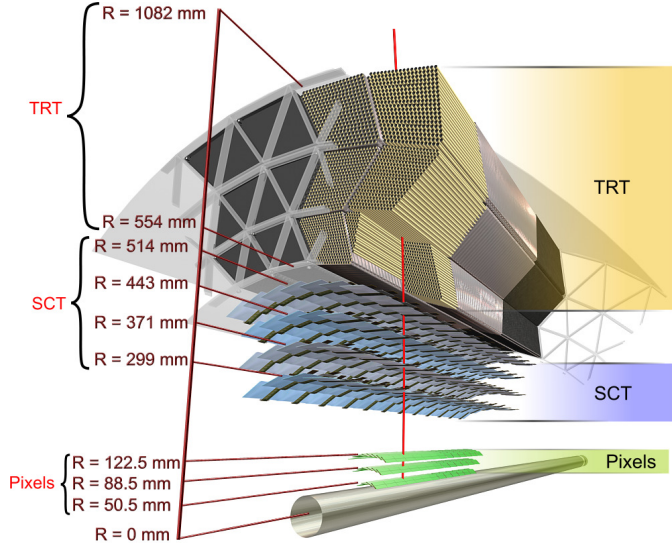


Figure 5.4: Cross-sectional view of the Inner Detector (ID). The ID particle tracker is made of the Pixel Detector, the microstrip Semiconductor Tracker (SCT), and the Transition Radiation Tracker (TRT). Figure from Ref. [134].

5.2.2 Calorimeters

The primary goal of calorimeters is to measure the energy deposited by the particles, but they also contribute to position measurements and particle identification as well as to the measurement of the missing transverse energy. ATLAS uses so-called sampling calorimeters with a *sandwich* structure. These detectors are made from alternating layers of high-density passive absorbers (Pb, Fe, Cu, ...) and active material (scintillating plastic, liquid argon, Si, ...) producing a detectable signal. The energy measurement is a destructive process: the incoming particle initiates secondary showers, and all produced particles deposit energy and radiate further until the total initial energy is absorbed. These energetic showers have different topologies depending on the type of incoming particle, namely whether they are leptonic (and photonic) or hadronic.

A passing electron/positron or a photon produces an electromagnetic (EM) shower in the absorber mainly through bremsstrahlung and electron-positron pair creation. EM showers are characterized by a rapid energy loss. A given detector material is described by the radiation length X_0 , which is the distance after which the incoming particle has deposited $1/e$ of its total energy.

In comparison, charged and neutral hadrons generate further hadronic activity by inelastic nuclear reactions through spallation and excitation. The secondary neutral mesons also generate additional EM shower activity. Furthermore, hadronic showers are generally wider than EM ones, and hadronic calorimeters are correspondingly much bulkier. They are characterized by the nuclear absorption length λ_a , for which 95% of the total energy is absorbed in a cylinder of radius λ_a . In ATLAS, both the EM and the hadronic calorimeters are found between the ID and the muon spectrometer.

1044 5.2.2.1 The Liquid Argon (LAr) Calorimeter

1045 Fig. 5.5 depicts the Liquid Argon (LAr) calorimeters [153] in yellow, which are closest
 1046 to the ID and enveloped by the Tile Calorimeter. The LAr calorimeters contain both
 1047 EM and hadronic detectors. The LAr calorimeters function as a system of alternating
 1048 lead/stainless steel absorbers and electrodes measuring the signal drift-time, with the
 1049 whole system immersed in liquid argon which plays the role of active medium.

1050 The electromagnetic barrel (EMB, $|\eta| < 1.475$) and endcap (EMEC, $1.375 < |\eta| <$
 1051 3.2) calorimeters use the same absorber material and geometry. In the forward region
 1052 (FCal) at rapidities $3.1 < |\eta| < 4.9$, a copper-based absorber covers EM activity while
 1053 a tungsten module provides measurement of hadronic energy deposition. Finally, a
 1054 hadronic LAr calorimeter is also placed at the endcaps (HEC) and complements readings
 1055 from the Tile Calorimeter. The EM calorimeters have an energy resolution of $\sigma_E/E =$
 1056 $10\%/\sqrt{E} + 0.7\%$, while the FCAL subdetector fares more poorly with a resolution of
 1057 $\sigma_E/E = 100\%/\sqrt{E} + 10\%$. Finally, the hadronic HEC subdetector reaches an energy
 1058 resolution of $\sigma_E/E = 50\%/\sqrt{E} + 3\%$ [154].

1059 5.2.2.2 The Tile Calorimeter (TileCal)

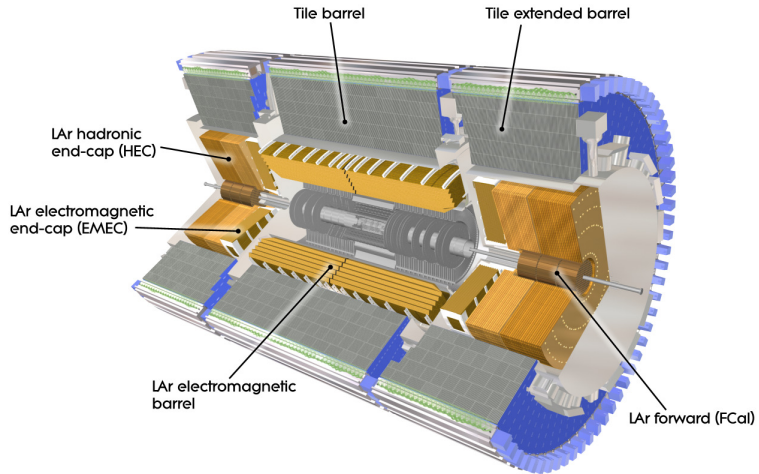


Figure 5.5: The ATLAS calorimetry system is composed of the inner Liquid Argon calorimeter (yellow) and the outer Tile Calorimeter (gray). Figure from Ref. [134].

1060 The central and two extended barrel regions are covered by the TileCal [155], which
 1061 is cylindrically disposed around the beampipe (see Fig. 5.5) and is made of iron plate
 1062 absorbers and plastic scintillators as the active medium. The scintillating light created
 1063 by hadronic energy deposition is wavelength-shifted and led to photomultiplier tubes that
 1064 amplify the signal. The TileCal has a total energy resolution of $\sigma_E/E = 50\%/\sqrt{E} + 3\%$
 1065 for single pions [156].

5.2.3 The Muon Spectrometer

At the outmost layer of the ATLAS detector, the MS [157] is designed to deliver high-precision measurements of the muon transverse momenta. It uses four different techniques to trigger and detect the produced muons: resistive-plate chambers (RPC) [158], cathode strip chambers (CSC) [159], monitored drift tubes (MDT) [160] and thin-gap chambers (TGC) [161], shown in Fig. 5.6. The muon tracks are bent by three air-core toroid magnets for a rapidity-dependent bending power between 1 – 7.5 Tm. This amounts to a resolution of $\sim 10\%$ in the transverse momentum of high-energy muons at around 1 TeV. Both the RPCs and the TGCs are used as a first-level trigger on well-resolved, high- p_T muons in the barrel region, respectively the endcaps. On the other hand, the MDTs which are laid out in the barrel and endcap regions, and the CSCs in the forward region, measure the position of the incoming muons in the bending plane.

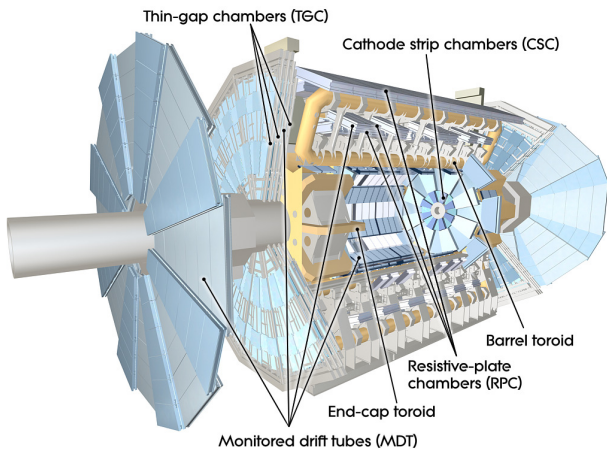


Figure 5.6: The ATLAS muon spectrometer. Figure from Ref. [134].

5.2.4 Trigger and Data acquisition

The collision rate at high-energy collider experiments like ATLAS poses enormous computing and storage requirements. At the LHC, the proton-bunch crossing-rate at the current luminosity towers at a monumental 40 MHz. With a data content of ~ 1.6 MB per event, the storage of all events would produce ~ 60 TB per second. Thus the event rate needs to be reduced to an affordable storage and readout rate. The ATLAS trigger and data acquisition system [162, 163] lowers the stored event rate using certain quality criteria from the detectors. The trigger system is organized in three sublevels:

- **Level 1:** The first layer triggers at the hardware level already, and uses both calorimetry information (cluster energy sum / isolation criteria) and data from the muon trigger chambers to reduce the event rate from 40 MHz to ~ 75 kHz. It also identifies regions-of-interest (ROI) characterized by specific signatures deemed physically relevant.

5 The LHC and the ATLAS detector

- 1091 • **Level 2:** At the software level, the Level 2 Trigger uses the ROIs identified by
1092 Level 1 and combines information from all subdetectors to focus on the physics
1093 objects. The event rate is then reduced from 75 kHz to ~ 1 kHz.
- 1094 • **Event Filter:** The full events are analyzed offline and the Level 2 selection is
1095 refined by the Event Filter (EF), which can also perform full event reconstruction
1096 at this stage. Accepted events are then stored permanently on disk at a rate of
1097 ~ 200 Hz for an acceptable total storage rate of around 300 MB per second.

1098 Since Run II, the ATLAS software trigger comprises a single high-level trigger (HLT)
1099 farm, instead of the separate Level 2 and EF trigger levels, reducing the Level 1 total
1100 event rate from 100 kHz to 1 – 1.5 kHz. The raw data is then stored first in the
1101 central CERN data center. These sites make up the so-called Tier-0 system. The LHC
1102 Computing Grid is composed of several levels (tiers). After the central CERN data
1103 center at Tier-0, the data is redistributed to 13 other computer storage and analysis
1104 sites forming the Tier-1, which store and process the raw data into refined formats
1105 and distributes it along to Tier-2 computer sites (university/institute clusters). Tier-3
1106 sites are composed of local computers for analysis purposes. Mostly, analysers use pre-
1107 processed data that simplifies the description of physics objects.

1108 5.2.4.1 Data formats

1109 From the raw data saved on-site to the final format available to analysts, several levels of
1110 data processing and reconstruction are implemented to derive a meaningful identification
1111 of physics objects that can be used as such in an analysis. Below are presented the
1112 successive file formats and their content:

- 1113 • **RAW:** The raw data from the trigger output are stored as primary information
1114 from the subdetectors: these complete events contain useless or redundant information
1115 and metadata for the final analyses.
- 1116 • **ESD:** The detector output present in the RAW events is fed to the reconstruction
1117 algorithm, and all the information needed for particle identification, track fitting,
1118 jet calibration is summarized in so-called Event Summary Data (ESD) files.
- 1119 • **xAOD:** More information is pruned away, and only the physics objects (electrons,
1120 muons, jets, MET, ...) are summarized in containers and saved as ROOT files
1121 called Analysis Object Data (xAOD).
- 1122 • **DxAOD:** The xAOD files are further reduced to analysis-dependent (Top, Higgs,
1123 SUSY ...) event subsets, the derived AODs (DxAOD). The goal is to reduce
1124 file size and analysis computing times. Derived AODs are produced by either
1125 removing uninteresting events (so-called *skimming*), eliminating entire variables
1126 or object collections from all events (*slimming*), or removing particular objects in
1127 some events (*thinning*). Analyses handle directly the derived xAOD files as input.

1128 **5.2.4.2 MC simulation in ATLAS**

1129 Common MC event generation was explained in Chapter 4. In the following, a *parton*
 1130 *level* event is defined as the set of particles (with their well-defined 4-momenta) produced
 1131 by the hard-scattering matrix-element or by the parton-shower algorithm applied to
 1132 the hard collision, but before hadronization. Both cases will be explicitly discerned
 1133 when necessary. Such parton-level events are unphysical since they do not obey color
 1134 confinement. The output of a full-fledged MC program after hadronization is a collection
 1135 of events at *particle level*: this is usually the point of comparison between theory and
 1136 experiment. Finally, accounting for the further evolution of particles in the magnetic
 1137 field of a specific experiment, as well as geometric acceptance and detection efficiencies,
 1138 defines measurable events at *detector level*. Fig. 5.7 illustrates the event level definitions.
 1139 The full process of producing sets of events at detector level from the theory input will
 1140 be referred to as MC simulation.

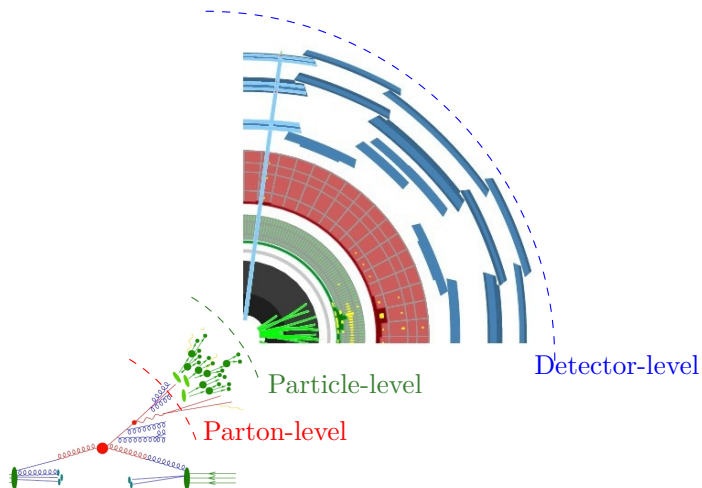


Figure 5.7: Definition of event levels: parton level after the hard collision (and including parton-showering), particle level after hadronization and detector level after the evolution in the ATLAS magnetic field, digitization and reconstruction.

1141 In the ATLAS experiment, this production chain is implemented in the **Athena** frame-
 1142 work, and comprises several steps outlined in Fig. 5.8. The event output at each stage
 1143 is identified by a tag. For a given process, the first step consists of basic MC produc-
 1144 tion using the programs available on the market (SHERPA, HERWIG7, PYTHIA8, and so
 1145 on). The **AthGeneration** subpackage handles the interfacing of public MC programs in
 1146 the ATLAS infrastructure, so as to ensure the use of common parameters, like particle
 1147 masses and decay widths, and to facilitate reproducibility. From job option scripts at
 1148 the user-level, the interface writes the standard input cards readable by the MC pro-
 1149 grams, and launches the event generation itself. The intermediate output at parton level
 1150 (from the hard ME) is saved as Les Houches Event (LHE) files, and the generation of
 1151 fully-showered and hadronized particle-level events (**EVNT/e-tag**) is referred to as **evgen**.

5 The LHC and the ATLAS detector

1152 Next, the simulation of events from particle to detector level happens in two phases:
 1153 **simul** (**s/a**-tags) and **reco** (**r**-tag). The actual simulation (the evolution of the particles
 1154 in the ATLAS magnetic field and the generation of the detector response) is handled
 1155 by the GEANT4 [164] program: it contains the whole detector geometry and reproduces
 1156 the particle hits in the subdetectors, accounting for detection efficiency. Because of
 1157 the enormous computing time needed to produce hits from the hundreds of particles
 1158 at play, an alternative is to parametrize the detector response without running a full
 1159 event simulation (so-called ATLFAST [165] simulation). The output of the **simul** step is
 1160 a HITS file. Then, as happens with the real data in the **reco** stage, signals simulated
 1161 in the subdetectors are digitized, and the physics objects reconstructed to produce the
 1162 xAOD format mentioned above. DxAODs derivations can be constructed for the latter
 1163 and serve as input to the analyses, like the MC event sets which will be introduced in
 1164 Chapter 9.

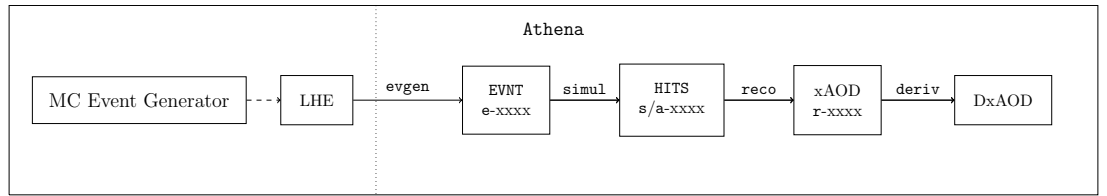


Figure 5.8: The **Athena** workflow for MC event generation and simulation.

1165

Part II

1166

Top-Quark Mass Determinations

6 Theoretical predictions for $t\bar{t}$ final-states

The top-quark pairs created e.g. at the LHC are not observable *per se*: the top quark has a short lifetime of $\sim 0.5 \cdot 10^{-24}$ s. Thus the only directly measurable quantities are the kinematic properties of their decay products. The top quark has a decay branching ratio of 99.8% for $t \rightarrow W^+ b$, $\bar{t} \rightarrow W^- \bar{b}$. So, the final-state contains two b -jets that can be experimentally tagged, and depends only on the decay mode of the W bosons. In the case of top-quark pair production, both W bosons can decay either hadronically or leptonically, with branching ratios $\Gamma(W \rightarrow q\bar{q}') = 0.67$, $\Gamma(W \rightarrow \ell\nu_\ell) = 0.33$: the final-state can either be dileptonic, monoleptonic (lepton+jets) or allhadronic, and the top-quark properties must then be reconstructed from the measured final-states. Fig. 6.1 depicts the topology of the three decay channels and Table 6.1 gives an overview of their respective cross-sections, advantages and disadvantages.

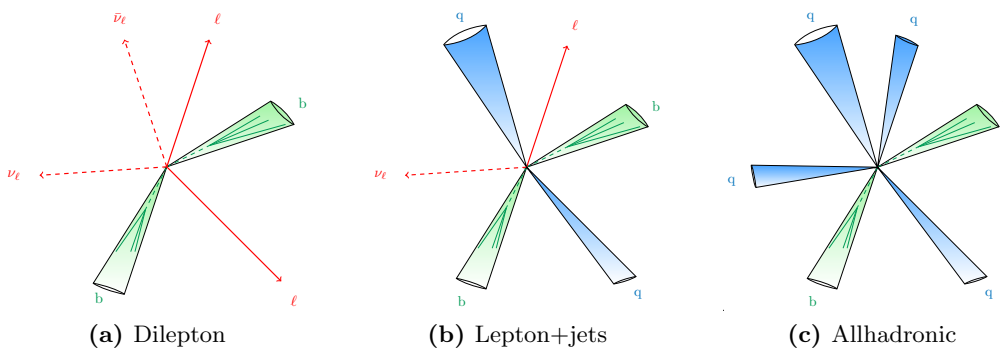


Figure 6.1: Topologies for $t\bar{t}$ events are stemming either from (a) dileptonic, (b) monoleptonic or (c) allhadronic decays.

A precise computation for the top-quark pair production cross-section and differential observables is paramount for the extraction of top-quark properties. Most theoretical systematic uncertainties are well under control and have been the subject of various studies in the last few years [175–178]. In this chapter, the different theoretical descriptions of $t\bar{t}$ final-states are first reviewed, the most important issues are summarized and their potential impact on the extraction of top-quark properties from data are discussed, with a special focus on the top-quark observables. To do so in a realistic and quantitative way, an analysis close to the ATLAS 8 TeV top-quark mass extraction in the dilepton channel [179] is set up. The dilepton channel is the cleanest decay mode for an experimental measurement of the top-quark mass with the possibility of requiring two well-reconstructed, high-momentum leptons. It has the advantage of a small background (coming mainly from fake leptons, diboson and Z +jets production) and a clean signa-

6 Theoretical predictions for $t\bar{t}$ final-states

| Final-state X | dilepton (w. $\tau^+\tau^-$) | $\ell+$ jets (w. $\tau+j$) | allhadronic | all channels |
|---------------------------------------|-------------------------------|-----------------------------|----------------|------------------------------|
| $\Gamma(t\bar{t} \rightarrow X) [\%]$ | 10.89 | 44.02 | 44.89 | 100.0 |
| $\sigma_{\text{NNLO}} [\text{pb}]$ | 27.42 | 110.82 | 113.02 | $251.76^{+2.54\%}_{-3.44\%}$ |
| Advantages | Clean signature | Full reconstruction | Largest BR | |
| Drawbacks | No full reconstruction | Jet-scale uncertainties | QCD background | |
| References | [166–168],[169, 170] | [167, 171],[5] | [172],[173] | |

Table 6.1: For the three decay channels in $t\bar{t}$ production, the branching ratios and inclusive theoretical cross-sections at QCD NNLO+NNLL were computed with the `Top++` program [174] for a top-quark mass of $m_t = 172.5$ GeV and the MSTW2008nnlo68cl PDF set. Advantages and drawbacks of (any) top-quark measurement in said channel are given. References for ATLAS measurements of the top-quark mass in particular are also laid out for each subchannel for the top-quark pole mass (in black), and for the MC mass (in blue) from template fits.

ture, but suffers from the small branching fraction ($\Gamma \sim 0.048$ for e/μ in the final-state). Cross-sections for all considered theoretical descriptions of $t\bar{t}$ final-states are given at the end of the chapter for the fiducial cuts employed in the analysis.

6.1 The narrow-width approximation (NWA)

Considering the intermediate state $W^+W^-b\bar{b}$, it makes sense at first to approximate it and examine only on-shell, doubly-resonant top-quark diagrams: the cross-section contribution stemming from non-resonant diagrams is expected to be of the order of $\mathcal{O}(\Gamma_t/m_t) \leq 1\%$, and usually neglecting other contributions is fine. This description is called the *narrow-width approximation* (NWA), and it builds on the limit $\Gamma_t \rightarrow 0$, where the top-quark propagator can then be written as

$$\lim_{\Gamma_t \rightarrow 0} \frac{1}{(p^2 - m_t^2) + m_t^2 \Gamma_t^2} = \frac{\pi}{m_t \Gamma_t} \delta(p^2 - m_t^2) + \mathcal{O}\left(\frac{\Gamma_t}{m_t}\right). \quad (6.1)$$

That is, top-quark production and decay entirely factorize, i.e.:

$$\begin{aligned} \mathcal{M}_{pp \rightarrow W^+W^-b\bar{b}} &= \mathcal{M}_{pp \rightarrow t\bar{t} \rightarrow W^+W^-b\bar{b}}^{\text{NWA}} + \mathcal{O}(\Gamma_t/m_t) \\ &= \mathcal{P}_{pp \rightarrow t\bar{t}} \otimes \mathcal{D}_{t \rightarrow W^+b} \otimes \mathcal{D}_{\bar{t} \rightarrow W^-\bar{b}} + \mathcal{O}(\Gamma_t/m_t), \end{aligned} \quad (6.2)$$

where \mathcal{P} denotes the $t\bar{t}$ production and \mathcal{D} the top-quark decay dynamics, and the spin correlations are correctly taken into account as indicated by the symbol \otimes . The corresponding three LO Feynman diagrams, as well as a few examples of one-loop diagrams for $gg \rightarrow t\bar{t}$ production, are shown in Fig. 6.2. Nowadays, most of the theoretical predictions used for the extraction of top-quark properties in experimental analyses rely on NLO matrix-elements for top-quark pair production only. The top-quark decay and all subsequent radiation is left to the MC generator, with the approximations it entails:

6.1 The narrow-width approximation (NWA)

particle decay predictions usually only have LO accuracy, spin correlations (in particular in the parton-shower) were only recently implemented, and resummation is as good as the shower algorithm's accuracy. Even so, there exists a number of more complete MC implementations for $t\bar{t}$ production in the NWA: the effects of NLO corrections to both production and decay were investigated in the POWHEG-BOX-v2 [17–19] framework called `ttb_NLO_dec` [180]. The HERWIG7.1 MC generator supports a new multijet merging algorithm adapted to $t\bar{t}$ production at NLO [181], and finally the SHERPA generator allows for the matching of the CS shower to production of $t\bar{t}$ associated with 1-, 2- and 3-jets at NLO [182, 183].

Furthermore, some dedicated calculations have appeared over the years. In particular, QCD NNLO corrections for $t\bar{t}$ production have been calculated for differential distributions [184–186], and combined with NLO EW corrections [187]. For a review of NLO EW effects, see Refs. [188–190]. Leaving corrections in top-quark pair production and considering now the top-quark decay, it was later shown that higher-order corrections to the top-quark decay have a measurable impact on differential distributions in certain regions of phase-space. NLO radiative corrections to the top-quark decays were computed [191–193] and completed by NNLO QCD corrections [194, 195], NNLL resummation and other improvements above higher-order corrections in α_s [196–201]. Within the NWA, the calculation of QCD NNLO + NNLL' (soft-gluon and small-mass resummation) corrections for differential distributions was combined with NLO EW corrections and is the most complete fixed-order calculation up-to-date [202].

For the results shown in Section 6.5 in the NWA, the top-quark pair production is described at NLO QCD and factorizes from the top-quark decay. Furthermore, only the $e\mu$ dilepton channel is considered, that is $pp \rightarrow (e^+\nu_e)(\mu^-\bar{\nu}_\mu)b\bar{b}$ production for the analysis presented in Chapter 7. The top-quark decay accuracy is handled in three different ways:

- (1) The top-quark decay at LO is realized in the fixed-order SHERPA setup, as in Ref. [203] (referred to as **NLO_{NWA}^{LOdec}** from now on).
- (2) The top-quark decay at NLO is computed in Ref. [192], and is shortly described below (**NLO_{NWA}^{NLOdec}**).
- (3) The top-quark decay is handled by the parton-shower, namely through the SHERPA CSS shower (**NLO_{PS}**).

Briefly, the **NLO_{NWA}^{LOdec}** calculation in the NWA is based on the formula from Ref. [192] where top-quark pair production and decay factorize. Taking the perturbative expansion of Eq. (6.2) to NLO gives

$$\begin{aligned} \mathcal{M}_{ij \rightarrow t\bar{t} \rightarrow b\bar{b}2\ell2\nu}^{\text{NWA, NLO}} = & \mathcal{P}_{ij \rightarrow t\bar{t}}^{\text{LO}} \otimes \mathcal{D}_{t \rightarrow b\ell^+ \nu}^{\text{LO}} \otimes \mathcal{D}_{\bar{t} \rightarrow \bar{b}\ell^- \bar{\nu}}^{\text{LO}} + \mathcal{P}_{ij \rightarrow t\bar{t}}^{\delta\text{NLO}} \otimes \mathcal{D}_{t \rightarrow b\ell^+ \nu}^{\text{LO}} \otimes \mathcal{D}_{\bar{t} \rightarrow \bar{b}\ell^- \bar{\nu}}^{\text{LO}} \\ & + \mathcal{P}_{ij \rightarrow t\bar{t}}^{\text{LO}} \otimes \left(\mathcal{D}_{t \rightarrow b\ell^+ \nu}^{\delta\text{NLO}} \otimes \mathcal{D}_{\bar{t} \rightarrow \bar{b}\ell^- \bar{\nu}}^{\text{LO}} + \mathcal{D}_{t \rightarrow b\ell^+ \nu}^{\text{LO}} \otimes \mathcal{D}_{\bar{t} \rightarrow \bar{b}\ell^- \bar{\nu}}^{\delta\text{NLO}} \right), \end{aligned} \quad (6.3)$$

where LO (δNLO) represent the LO (NLO) contributions to the $t\bar{t}$ production and top-quark decays, respectively.¹

¹The product $\mathcal{P}^{\delta\text{NLO}} \otimes \mathcal{D}^{\delta\text{NLO}}$ is formally of higher order.

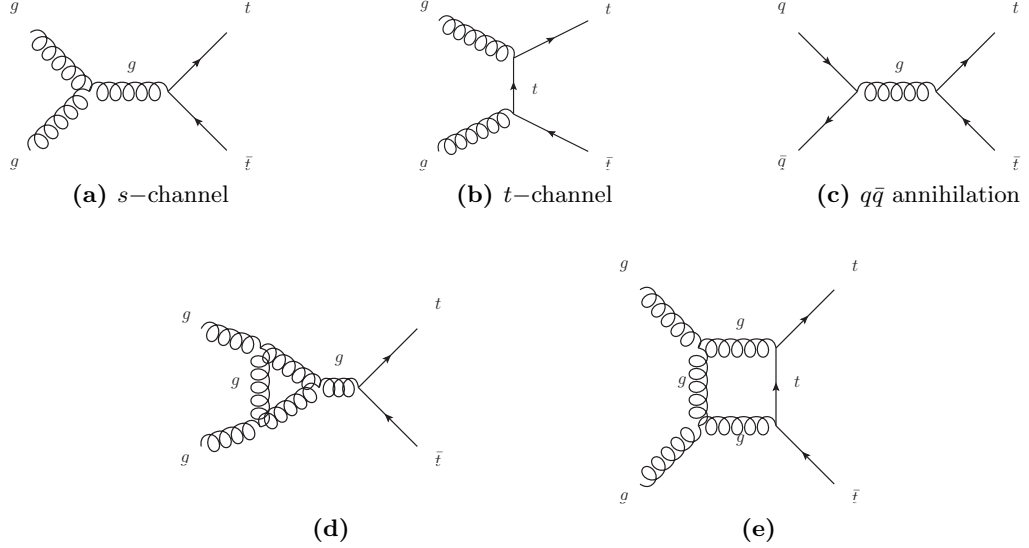


Figure 6.2: (a-c) Leading-order diagrams for $t\bar{t}$ production and (d-e) two examples of NLO QCD one-loop diagrams for $gg \rightarrow t\bar{t}$

As mentioned above, the NWA is expected to be precise enough for most calculations and yet, NLO and off-shell effects in the top-quark decay can have an important impact on sensitive regions of phase-space. In practice, experimental analyses do account for part of the non-doubly-resonant contributions: they include single-top quark production in the signal, since it contributes to the same final-state at NLO, or they subtract it consistently as background. To take care of the interference between $t\bar{t}$ and single-top diagrams, this is generally accomplished with the help of a diagram subtraction (DS) or diagram removal (DR) scheme [204]. This procedure is not entirely free of quirks and violates gauge-invariance. To get an entirely consistent theoretical prediction, it is therefore preferable to produce the full intermediate state $pp \rightarrow W^+W^-b\bar{b}$, which contains the complete set of Feynman diagrams at NLO.

6.2 $W^+W^-b\bar{b}$ production: review of existing calculations

The full calculation of $W^+W^-b\bar{b}$ at NLO in QCD contains all doubly-resonant top-quark diagrams, but also non-doubly resonant as well as non-factorizing contributions. Fig. 6.3 illustrates some of the additional Feynman diagrams.

At LO, the full $W^+W^-b\bar{b}$ final-state including the non-resonant diagrams has been computed in Refs. [203, 205–207]. In general, the calculation of NLO corrections poses some technical problems because of the existence of b -quarks in both initial- and final-state. In the 5-flavor scheme (5FNS), where b -quarks are treated as massless, collinear $g \rightarrow b\bar{b}$ splittings contribute to the final-state and the corresponding IR divergence has to be handled. Considering massive b -quarks (4FNS) has the advantage of allowing

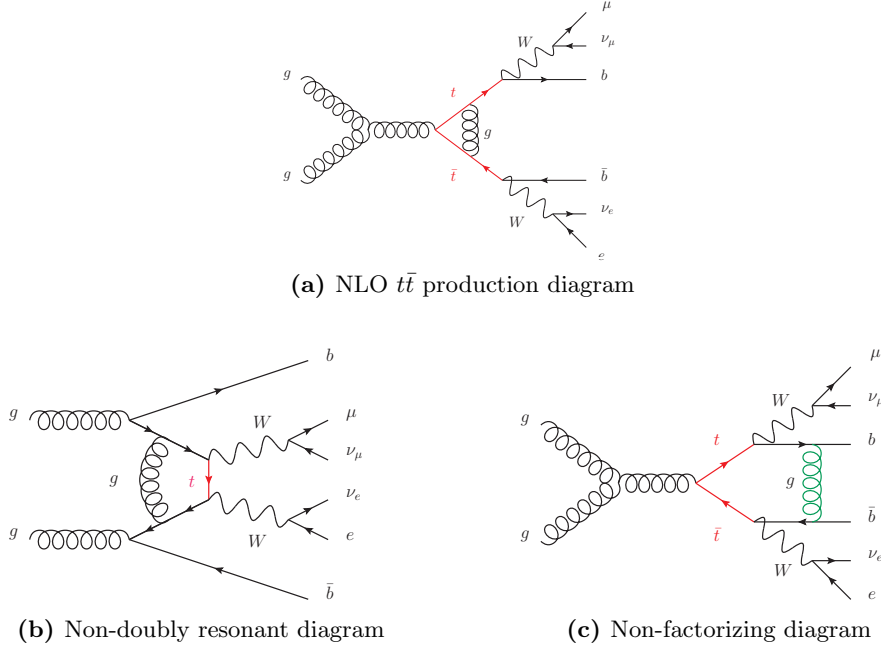


Figure 6.3: One-loop diagrams for $pp \rightarrow W^+W^-b\bar{b}$ production contain (a) NLO corrections to standard NWA $t\bar{t}$ production, but also (b) diagrams with one or no top-quark propagators and (c) resonant diagrams with non-factorizing legs

any phase space restrictions on the b -quarks without endangering infrared safety. It is therefore possible to consider exclusive 0-, 1- and 2-jet bins for $pp \rightarrow (e^+\nu_e)(\mu^-\bar{\nu}_\mu)b\bar{b}$ in the same setup. On the other hand, massive b -quarks are accompanied by an additional mass scale to the one-loop integrals and thus renders the integral evaluation less straightforward. In Refs. [208, 209], NLO calculations in the 4FNS have been performed.

Often, the $W^+W^-b\bar{b}$ prediction differs from the NWA in phase-space regions accessible only at NLO or sensitive to the top-quark decay kinematics. In Ref. [203], particular emphasis has been put on the impact of the non-factorizing contributions on the top-quark mass measurements in the dilepton channel. Recently the calculation of the NLO QCD corrections to $W^+W^-b\bar{b}$ production with full off-shell effects has also been achieved in the lepton+jets channel [210].

6.3 $W^+W^-b\bar{b}$ calculation setup at NLO QCD

Inclusive and differential cross-sections (along with results for top-quark mass determinations) were published in Ref. [211]. The calculation is analogous to the one described in Ref. [212]. The NLO QCD corrections to the $pp \rightarrow W^+W^-b\bar{b} \rightarrow (e^+\nu_e)(\mu^-\bar{\nu}_\mu)b\bar{b}$ process are computed, i.e. up to $\mathcal{O}(\alpha_s^2\alpha^2)$, in the 5FNS. This means that interference from (massless) b -quarks in the initial-state is taken into account. Top-quark finite width

6 Theoretical predictions for $t\bar{t}$ final-states

1284 effects are fully included. The complex mass scheme is used to incorporate the width in
 1285 a gauge-invariant way, where the top-quark mass is replaced by a complex number μ_t :

$$\mu_t^2 = m_t^2 - im_t\Gamma_t. \quad (6.4)$$

1286 The W and intermediate Z bosons also acquire a complex mass. Note that only
 1287 resonant W -boson diagrams are taken into account: non-resonant contributions and
 1288 finite- W -width effects were found to be small compared to top-quark effects [213]. The
 1289 calculation is realized at parton-level within the SHERPA v2.2.3 framework,² where
 1290 tree-level and real amplitudes are computed by the SHERPA matrix-element generators
 1291 COMIX [215–217] and AMEGIC [218]. The one-loop amplitudes are compiled by GoSAM
 1292 and linked to SHERPA via the BLHA2 interface. Finally, the IR divergences are sub-
 1293 tracted with the help of the Catani-Seymour dipole formalism as automated in SHERPA.

1294 There are 334 diagrams contributing to the $q\bar{q} \rightarrow W^+W^-bb$ virtual corrections, where
 1295 q are the light quarks (u, d, s, c), and 1068 diagrams contributing to $gg \rightarrow W^+W^-b\bar{b}$.
 1296 Additionally, because of the b -quarks present in the initial-state, 668 one-loop diagrams
 1297 contribute to $b\bar{b} \rightarrow W^+W^-b\bar{b}$.

1298 In the results presented in Chapters 7 and 8, the full $pp \rightarrow W^+W^-b\bar{b} \rightarrow (e^+\nu_e)(\mu^-\bar{\nu}_\mu)b\bar{b}$
 1299 QCD NLO prediction is compared with various $t\bar{t}$ predictions in the NWA. One of the
 1300 goals of this study is to disentangle the effects from production and decay corrections,
 1301 as well as from extra radiation in a parton-shower resummed approximation. The four
 1302 theoretical descriptions considered in the next chapter are summarized again for com-
 1303 pleteness:

1304 **NLO_{full}**: full NLO corrections to $pp \rightarrow W^+W^-b\bar{b}$ with leptonic W -decays,

1305 **NLO_{NWA}^{NLOdec}**: NLO $t\bar{t}$ production \otimes NLO decay,

1306 **NLO_{NWA}^{LOdec}**: NLO $t\bar{t}$ production \otimes LO decay,

1307 **NLO_{PS}**: NLO $t\bar{t}$ production+shower \otimes decay via parton showering.

1308 Note that the three first theoretical descriptions are not matched to a parton-shower.
 1309 The PDF4LHC15_nlo_30_pdfs sets [219] are interfaced to SHERPA via LHAPDF and events
 1310 are produced at a center-of-mass energy of $\sqrt{s} = 13$ TeV. The central top-quark mass
 1311 was set to $m_t = 172.5$ GeV and the G_μ —electroweak scheme was used with the following
 1312 numerical values:

$$G_\mu = 1.16637 \cdot 10^{-5} \text{ GeV}^{-2}, \quad M_W = 80.385 \text{ GeV}, \quad M_Z = 91.1876 \text{ GeV}, \quad (6.5)$$

$$\begin{aligned} \Gamma_t^{\text{LO}} &= 1.4806 \text{ GeV}, & \Gamma_t^{\text{NLO}} &= 1.3535 \text{ GeV}, \\ \Gamma_W^{\text{LO}} &= 2.0454 \text{ GeV}, & \Gamma_W^{\text{NLO}} &= 2.1155 \text{ GeV}, \\ \Gamma_Z &= 2.4952 \text{ GeV}, \end{aligned} \quad (6.6)$$

1313 where the LO (NLO) widths were used for the LO (NLO) decays, respectively.

²A patched version [214] was used for the CSS shower, with the correct eikonal expressions for radiating off massive top quarks (relevant only for the NLO_{PS} description).

¹³¹⁴ **6.4 Event requirements**

¹³¹⁵ To study the differences between these predictions and their impact on the top-quark
¹³¹⁶ mass determination, an analysis similar to the ATLAS top-quark mass measurement at
¹³¹⁷ 8 TeV in the dilepton channel [179] is performed. In this analysis, the trigger cuts on
¹³¹⁸ leptons and jets are adapted to the ATLAS 13 TeV standards. For details of the analysis,
¹³¹⁹ the reader is referred to Chapter 7. The following event requirements are applied:

- ¹³²⁰ • The number of b -jets $n_{b,\text{jets}} = 2$ with $p_T^{\text{jet}} > 25 \text{ GeV}$ and $|\eta^{\text{jet}}| < 2.5$. Jets are
¹³²¹ clustered with anti- k_T [220] as implemented in `FastJet` [221, 222] using a jet
¹³²² distance parameter of $R = 0.4$. In the analysis, a jet is considered a b -jet if it
¹³²³ contains a B -hadron (or its decay products).
- ¹³²⁴ • Exactly two oppositely charged leptons are required with $p_T^\mu > 28 \text{ GeV}$, $|\eta^\mu| < 2.5$
¹³²⁵ for muons and $p_T^e > 28 \text{ GeV}$, $|\eta^e| < 2.47$. For electrons, the crack region $1.37 <$
¹³²⁶ $|\eta^e| < 1.52$ between barrel and endcap EM calorimeters is excluded. For charged
¹³²⁷ leptons a separation of $\Delta R(\ell, \text{jet}) > 0.4$ to any jet is required: otherwise, the event
¹³²⁸ is vetoed entirely.
- ¹³²⁹ • $p_T^{\ell b} > 120 \text{ GeV}$. Using the same lepton- b -jet assignments as for $m_{\ell b}$, the value of
¹³³⁰ $p_T^{\ell b}$ is defined as the average transverse momentum of both lepton- b -jet systems.

¹³³¹ For the MC calculation, the central scales are set to $\mu_R = \mu_F = m_t$. The scale variation
¹³³² bands are obtained by varying $\mu_{R,F} = c_{R,F} m_t$, with $(c_R, c_F) \in \{(0.5, 0.5), (2, 2)\}$.³

In the NWA parton-shower results, the central scale was also compared to a dynamic scale called $\mu_{t\bar{t}}$. The latter is a “color-flow inspired” QCD scale suggested in Ref. [223]. For the Mandelstam invariants s , t and u , the dynamic scale is given by

$$\mu_{t\bar{t}}^2(q\bar{q} \rightarrow t\bar{t}) = 2 p_q p_t = m_t^2 - t , \quad (6.7)$$

$$\mu_{t\bar{t}}^2(\bar{q}q \rightarrow t\bar{t}) = 2 p_{\bar{q}} p_t = m_t^2 - u , \quad (6.8)$$

$$\mu_{t\bar{t}}^2(gg \rightarrow t\bar{t}) = \begin{cases} m_t^2 - t & \text{with weight } w_1 \propto \frac{u-m_t^2}{t-m_t^2} + \frac{m_t^2}{m_t^2-t} \left\{ \frac{4t}{t-m_t^2} + \frac{m_t^2}{s} \right\} \\ m_t^2 - u & \text{with weight } w_2 \propto \frac{t-m_t^2}{u-m_t^2} + \frac{m_t^2}{m_t^2-u} \left\{ \frac{4u}{u-m_t^2} + \frac{m_t^2}{s} \right\} , \end{cases} \quad (6.9)$$

¹³³³ the value of $\mu_{t\bar{t}}$ being chosen with a probability proportional to the two weights w_1 , w_2 .

³Also, 7-point variations were considered but the simultaneous variations are identical to their envelope.

1334 6.5 Total cross-section results

1335 The fiducial cross-sections after applying the aforementioned cuts are given in Table 6.2
 1336 for all considered predictions, where production at LO accuracy is also added for com-
 1337 pleteness. The renormalization and factorization scale uncertainties are given in percent.

| | X=LO [fb] | X=NLO [fb] |
|--|---------------------------------------|---------------------------------------|
| \mathbf{X}_{full} | $(739.5 \pm 0.3)^{+31.5\%}_{-22.4\%}$ | $(914 \pm 3)^{+2.1\%}_{-7.6\%}$ |
| $\mathbf{X}_{\text{NWA}}^{\text{LOdec}}$ | $(727.3 \pm 0.2)^{+31.4\%}_{-22.3\%}$ | $(1029 \pm 1)^{+10.4\%}_{-11.5\%}$ |
| $\mathbf{X}_{\text{NWA}}^{\text{NLOdec}}$ | - | $(905 \pm 1)^{+2.3\%}_{-7.7\%}$ |
| $\mathbf{X}_{\text{PS}}, \mu = m_t$ | $(637.7 \pm 0.9)^{+29.7\%}_{-21.0\%}$ | $(886 \pm 1)^{+8.5\%}_{-9.3\%}$ |
| $\mathbf{X}_{\text{PS}}, \mu = \mu_{t\bar{t}}$ | $(499.7 \pm 0.7)^{+27.6\%}_{-19.3\%}$ | $(805.2 \pm 0.9)^{+12.3\%}_{-10.9\%}$ |

Table 6.2: Cross-sections for all predictions at LO, respectively NLO in production, where the top-quark mass $m_t = 172.5$ GeV. The uncertainty stemming from MC integration is given in parentheses, and scale variation uncertainties are shown in percent.

1338 While the cross-sections for NLO_{full} and NLO_{NWA}^{NLOdec} agree with each other within
 1339 uncertainties, the NLO_{NWA}^{LOdec} cross-section is about 13% higher than the latter. The
 1340 NLO_{PS} cross-section, in comparison, is smaller because of the softening of b -jets in
 1341 the parton-shower which leads to a higher rejection rate when taking jet requirements
 1342 into account. The $\mu_{t\bar{t}}$ scale is larger than the central scale m_t , thus the even smaller
 1343 cross-section for this scale choice. Notice also the reduction in the renormalization
 1344 and factorization scale uncertainties when including NLO corrections to the top-quark
 1345 decay. Usually, rather than total inclusive cross-sections, the most sensitive top-quark
 1346 mass measurements rely on differential distributions, where mostly the distributions
 1347 for $t\bar{t}$ final-states are MC-generated and *fitted* to extract the top-quark mass (see the
 1348 full explanation of the method in Chapter 7). One caveat of considering differential
 1349 distributions is that the measured top-quark mass is rather represented by the MC
 1350 input top-quark mass parameter m_t^{MC} , instead of the top-quark pole mass measured in
 1351 inclusive $t\bar{t}$ measurements.

1352 Leaving the difference between heavy-quark mass schemes aside, the exact procedure
 1353 used in current ATLAS analyses for measuring the MC top-quark mass is explained
 1354 in the next chapter, along with quantitative comparisons of the theoretical predictions
 1355 outlined above.

7 NWA versus $W^+W^-b\bar{b}$: Top-quark mass uncertainties at parton level

This chapter shall investigate quantitatively the effect of using the different theoretical predictions presented above in a top-quark mass extraction. The measurement method is based on the ATLAS 8 TeV analysis in the dilepton channel [179], where the ATLAS cuts are adapted to the 13 TeV center-of-mass energy. This chapter first introduces the template fit method that was used in the experimental measurement. After a short discussion of important features of the considered observables, the results for the fit of the top-quark mass and its dependence on the different theoretical descriptions of the $t\bar{t}$ dilepton final-state are laid out.

7.1 The template fit method

In the dilepton channel, the top-quark momenta cannot be fully reconstructed in the experiment because of the two-particle spectrum spread given by the neutrinos from both W decays. One successful method is to use a differential distribution that is sensitive to the top-quark mass instead and which can be defined without having to properly reconstruct the top-quark intermediate states. The procedure is the following:

- Choose a distribution that is sensitive to the theoretical top-quark mass: for example, the average invariant mass of the lepton- b -jet system $m_{\ell b}$ (which consists of the visible top-quark decay products) is chosen as a function of the top-quark mass set in the MC event generator.
- Generate distributions for different input top-quark masses m_t^{in} . These are called *template* distributions.
- Individually fit the template distributions simulated for the input masses m_t^{in} with an appropriate function. Considering the simple example of a Gaussian fit, this gives:

$$\mathcal{G}(A, \mu, \sigma; m_t^{\text{in}}) = A(m_t^{\text{in}}) \exp \left(-\frac{(\mu(m_t^{\text{in}}) - m_t^{\text{in}})^2}{2\sigma^2(m_t^{\text{in}})} \right), \quad (7.1)$$

where the parameters A , μ , σ are fitted to the distributions generated for each input mass.

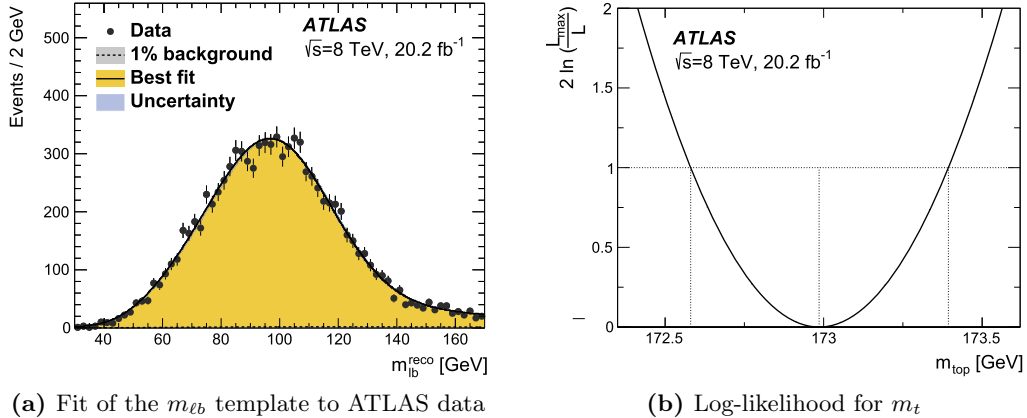


Figure 7.1: (a) The ATLAS 8 TeV analysis generates template distributions for m_{lb} for different input top-quark masses. These are fitted by a suitable function. (b) The likelihood function for m_t is then maximized in an fit to the measured m_{lb} distribution to extract the top-quark mass (Figures from Ref. [179]).

1383 This step is called *calibration* in the following paragraphs, and the functions for each
 1384 of the input top-quark masses are called calibration functions. The dependence of the
 1385 parameters on m_t^{in} is assumed to be linear, a fact that is checked against the MC
 1386 prediction. Once it is confirmed, the linear dependence is imposed (in this example,
 1387 $A(m_t^{\text{in}}) = a + b \cdot m_t^{\text{in}}$ with a and b fixed, and analogously for $\mu(m_t^{\text{in}})$, $\sigma(m_t^{\text{in}})$). The
 1388 underlying linear parameters are then kept constant, and the only free parameter is the
 1389 extracted top-quark mass $m_t = m_t^{\text{out}}$ to be measured. This function can then be used
 1390 directly in an unbinned likelihood fit to the distribution measured in experimental data,
 1391 as shown in Fig. 7.1 as an illustration from the ATLAS 8 TeV measurement.

1392 For a satisfying modeling of the m_{lb} distribution, the sum of a Gaussian and a Landau
 1393 distribution is used in the analysis. In practice, the overall normalization factor is fixed
 1394 to the measured data. In the rest of this chapter, the extraction is repeated from a
 1395 custom analysis implemented in Rivet [224] similar to the one performed by ATLAS,
 1396 for the four different theoretical setups presented in Chapter 6 at parton level (with
 1397 the full MC final-state for the parton-showered results). Different observables are also
 1398 compared in addition to m_{lb} .

1399 7.2 Definition of the observables

1400 The results presented in the rest of this chapter were published in Ref. [211]. The reader
 1401 is referred to the latter for details that are omitted in the following. A list of observables
 1402 is studied that should in principle be maximally sensitive to the top-quark mass while
 1403 minimally sensitive to theoretical systematic uncertainties (that is, including differences
 1404 between NWA and full $W^+W^-b\bar{b}$ predictions):

- 1405 • m_{lb} – the invariant mass of the two lepton- and b -jet systems

$$m_{\ell b}^2 = (p_\ell + p_b)^2 . \quad (7.2)$$

Since both top quarks decay leptonically and there is no possibility to determine the charge of the b -jets experimentally, there is an ambiguity in the assignment of the lepton and b -jet to the two top quarks. Here, the same criterion is used as in the ATLAS analysis: the two possible pairs for the lepton- b -jet system $(\ell^+ b_1, \ell^- b_2)$ are tried out, and the pairing that minimizes the sum of the two $m_{\ell b}$ values per event is chosen. The final value is set to the average of both $m_{\ell b}$ values.

- m_{T2} – following Refs. [225, 226] in the case of the final-state $(e^+\nu_e)(\mu^-\bar{\nu}_\mu)b\bar{b}$, the definition of this variable is given by

$$m_{T2}^2 = \min_{p_T^{\nu_1} + p_T^{\nu_2} = p_T^{\text{miss}}} \left[\max \left\{ m_T^2 \left(p_T^{(\ell^+ b_1)}, p_T^{\nu_1} \right), m_T^2 \left(p_T^{(\ell^- b_2)}, p_T^{\nu_2} \right) \right\} \right] . \quad (7.3)$$

The same pairing as for $m_{\ell b}$ is chosen for the lepton and b -jet systems, and the transverse mass is defined as

$$m_T^2 \left(p_T^{(\ell b_i)}, p_T^{\nu_i} \right) = m_{(\ell b_i)}^2 + 2 \left(E_T^{(\ell b_i)} E_T^{\nu_i} - p_T^{(\ell b_i)} p_T^{\nu_i} \right) , \quad (7.4)$$

with $E_T = \sqrt{|p_T|^2 + m^2}$ and $m_{\nu_i} = 0$.

- $E_T^{\Delta R}$ – the lepton transverse energy weighted by the angular distance to the corresponding b -jet

$$E_T^{\Delta R} = \frac{1}{2} \left(E_T^{l_1} \Delta R(l_1, b_1) + E_T^{l_2} \Delta R(l_2, b_2) \right) , \quad (7.5)$$

where again the above $m_{\ell b}$ criterion is used.

- $m_{\ell\ell}$ – the invariant mass of the two-lepton system.

For the $\text{NLO}_{\text{NWA}}^{\text{LOdec}}$, $\text{NLO}_{\text{NWA}}^{\text{NLQdec}}$ and NLO_{full} calculations, only the parton level is considered, including the decay products from the W bosons. The b -jets are identified with the b -quarks in that case. For the NLOps prediction, the cuts and observables are defined on the parton-level output of the shower algorithm, before any hadronization but with the full-particle final-state. Sets of MC samples were produced for the input top-quark masses

$$m_t \in \{165.0, 172.5, 180.0\} [\text{GeV}] . \quad (7.6)$$

The dependence on the input top-quark mass m_t is shown for all four observables in Fig. 7.2. Whereas $m_{\ell b}$ and m_{T2} are the most sensitive to the input m_t with a ratio to the central choice of the order $\mathcal{O}(2-3)$, the dependence of the $E_T^{\Delta R}$ and $m_{\ell\ell}$ observables on the top-quark mass is rather weak.

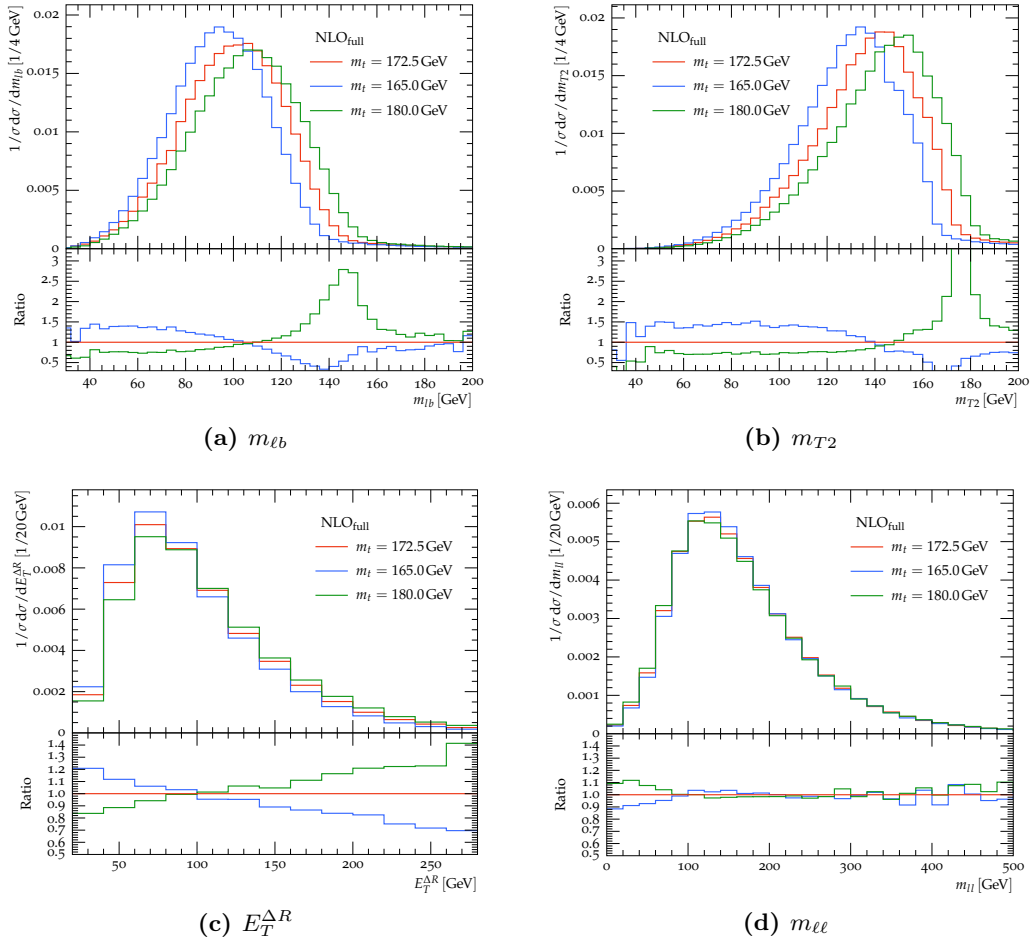


Figure 7.2: Differential observables are shown for three different top-mass points chosen symmetrically around $m_t = 172.5 \text{ GeV}$ for the full $W^+W^-b\bar{b}$ NLO prediction. While the (a) m_{llb} and the (b) m_{T2} observables show the highest top-mass dependence, the observables (c) $E_T^{\Delta R}$ and (d) m_{lll} are not sensitive enough to the top-mass to be considered for the template fit.

1431 7.3 Comparison of the different theoretical descriptions

1432 The normalized differential cross-section for the m_{llb} observable is outlined in Fig. 7.3
 1433 for the four theoretical predictions presented in Chapter 6. The ratio to the complete
 1434 $W^+W^-b\bar{b}$ NLO_{full} calculation is shown, where the latter's scale uncertainties are
 1435 represented by gray bands in the plot. Note that the m_{llb} distribution has a sharp kinematic
 1436 edge at $m_{llb}^{\text{edge}} = \sqrt{m_t^2 - m_W^2} \sim 153 \text{ GeV}$. Beyond the kinematic edge, the bins
 1437 are only populated by wrong lepton- b -jet pairing, additional radiation from the initial-
 1438 state clustered along the lepton- b -jet system, and non-resonant contributions. The LO
 1439 cross-section for $t\bar{t}$ production vanishes in this phase-space region. Thus, because NLO

7.3 Comparison of the different theoretical descriptions

corrections represent the first non-trivial order contributing to this region, differences between the theoretical descriptions considered here are expected to be sizeable around and above this kinematic edge. On the other hand, as seen in Fig. 7.2, this region also displays the highest sensitivity to the top-quark mass.

In Fig. 7.3, all predictions for $m_{\ell b}$ agree within a few percent in the bulk of the distribution, $40 \text{ GeV} \leq m_{\ell b} \leq 140 \text{ GeV}$, except for $\text{NLO}_{\text{NWA}}^{\text{LOdec}}$. The latter introduces a positive slope around and above the peak with differences of $\mathcal{O}(-10\%)$ at small masses up to $+20\%$ at $\sim 140 \text{ GeV}$, effectively shifting the peak to higher values of $m_{\ell b}$. This translates into an artificially higher extracted mass for the top quark when using LO decay predictions. In contrast, $\text{NLO}_{\text{NWA}}^{\text{NLOdec}}$ is found within 4% of the NLO_{full} prediction for the bulk of the distribution, starting to differ above the kinematic edge and stagnating at -50% of the full prediction in the tail, as expected. Finally, for the NLO_{PS} case, the tail at high $m_{\ell b}$ -values is populated by the additional radiation from the parton-shower, and is driven closer to NLO_{full} while it mostly lies between $\text{NLO}_{\text{NWA}}^{\text{LOdec}}$ and $\text{NLO}_{\text{NWA}}^{\text{NLOdec}}$ in the rest of the distribution.

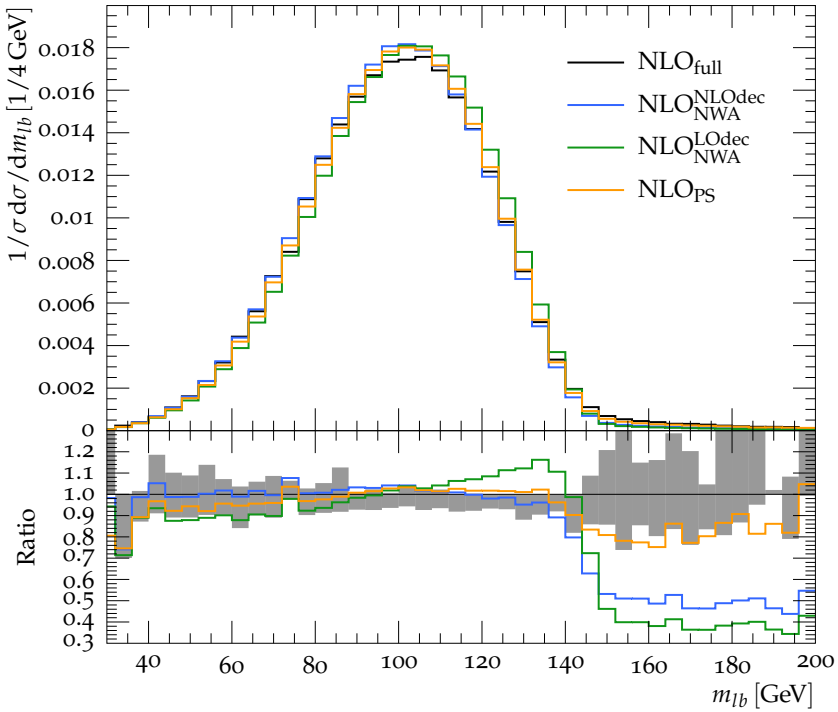


Figure 7.3: The normalized differential lepton- b -jet system invariant mass $m_{\ell b}$ is shown for all four theoretical predictions considered at 13 TeV, with their ratio to the NLO_{full} prediction. The gray band represents the latter's scale variation uncertainty.

Similar features can be observed for the normalized distribution of m_{T2} in Fig. 7.4 on a larger range up to the kinematic edge at $m_{T2}^{\text{edge}} = m_t$. In Figs. 7.5a and 7.5b, the normalized $E_T^{\Delta R}$ and $m_{\ell\ell}$ distributions show smaller differences between the theoretical predictions, with maximal deviations of $\mathcal{O}(10 - 12\%)$ in the regions of lowest cross-section. Since they are much less sensitive to the top-quark mass, though, they are not considered for the template fitting procedure in the results below.

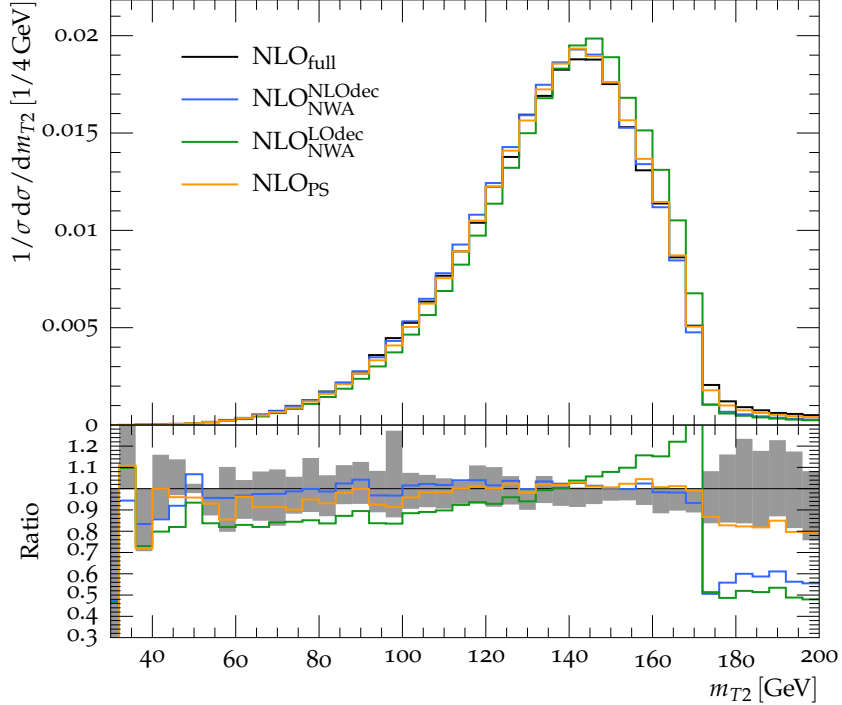


Figure 7.4: The normalized m_{T2} distribution is depicted for the four theoretical predictions, and shows a behavior similar to $m_{\ell b}$.

It is also enlightening to look at the scale dependence of the four theoretical descriptions for LO and NLO production. In Fig. 7.6a, the ratio of the $W^+W^-b\bar{b}$ prediction NLO_{full} to LO_{full} is shown for the $m_{\ell b}$ observable. Although large corrections are expected above the kinematic edge when going from LO to NLO in production, one finds unexpectedly important corrections in the low-mass region as well, where differences between both orders of accuracy in production are not covered by the scale uncertainties. In the NWA case shown in Fig. 7.6b, the NLO corrections to the top-quark decay also push the prediction out of the NLO_{NWA}^{NLOdec} scale uncertainties. The differences between the NLO_{NWA}^{LOdec} and NLO_{NWA}^{NLOdec}, respectively NLO_{PS} are also not covered around the kinematic edge. In general, scale uncertainties in the NWA are shown to be misguidedly small in the tails of the $m_{\ell b}$ and m_{T2} distributions. The behavior of scale-varied predictions is depicted for m_{T2} , $E_T^{\Delta R}$ and $m_{\ell\ell}$ in Figs. 7.7–7.9.

Taking into account the mass sensitivity (Fig. 7.2a) and the systematic differences between predictions (Fig. 7.6a), the template fit strategy should be optimized to maximize

7.3 Comparison of the different theoretical descriptions

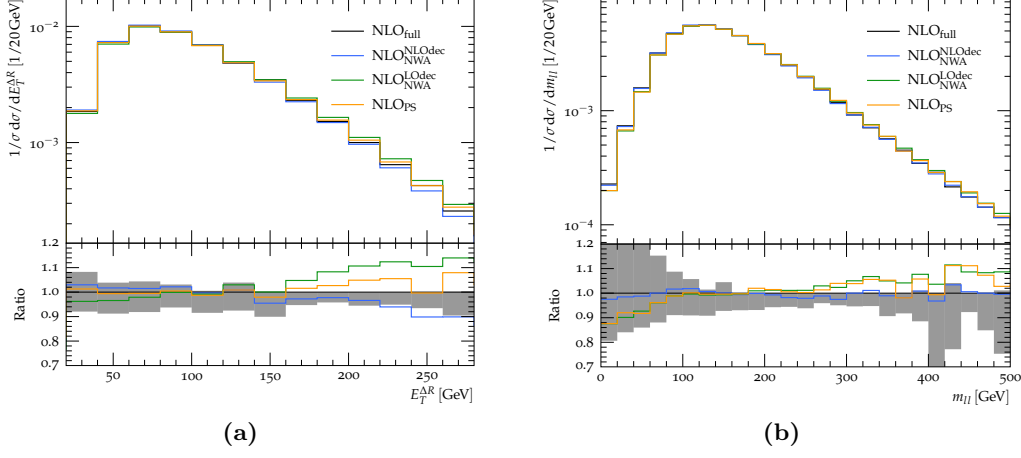


Figure 7.5: The normalized differential cross-sections for the (a) $E_T^{\Delta R}$ and (b) $m_{\ell\ell}$ distributions with all four theoretical predictions.

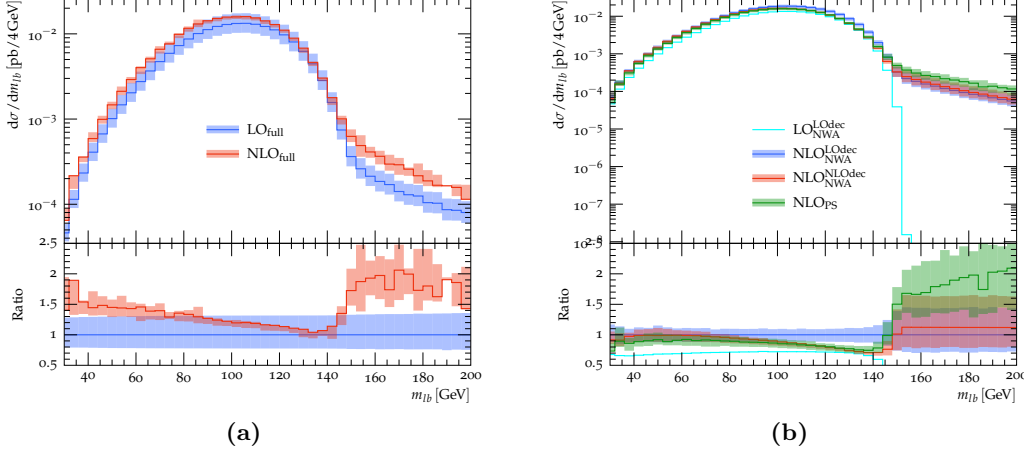


Figure 7.6: Results including scale variation bands for m_{tb} , for (a) the LO^{full} and NLO^{full} calculations, (b) the calculations based on the NWA. The ratios with respect to (a) LO^{full} and (b) NLO^{LOdec} are also shown.

the top-quark mass sensitivity while keeping the systematic uncertainty associated to the theoretical predictions to a minimum. The fit range is chosen to be

$$40 \text{ GeV} \leq m_{\ell b} \leq 160 \text{ GeV}, \quad (7.7)$$

$$80 \text{ GeV} \leq m_{T2} \leq 180 \text{ GeV}.$$

The exact dependence on the fit range was investigated, where the results were reproduced with a restricted range of $m_{\ell b} \leq 140 \text{ GeV}$, and numerical values were found to be stable.

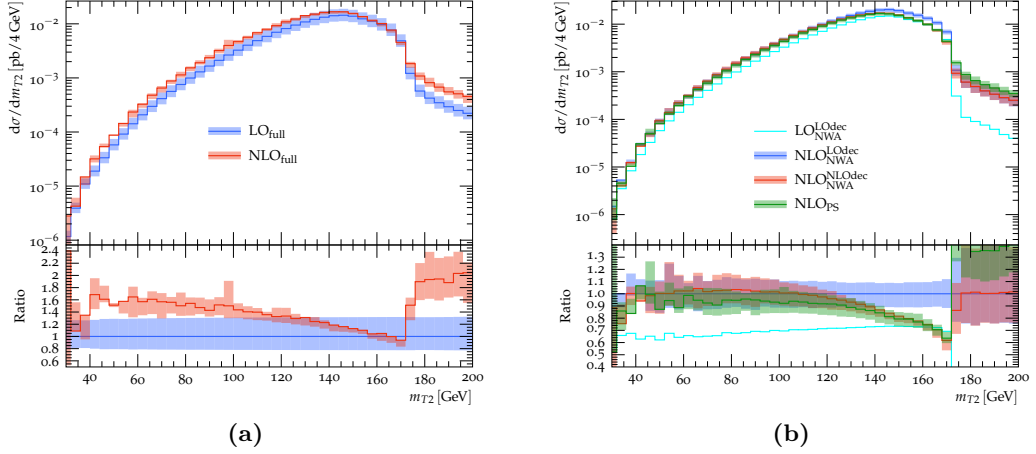


Figure 7.7: Results including scale variation bands for m_{T2} , for (a) the LO_{full} and NLO_{full} calculations, and (b) the calculations based on the NWA. The ratios are defined as in Fig. 7.6.

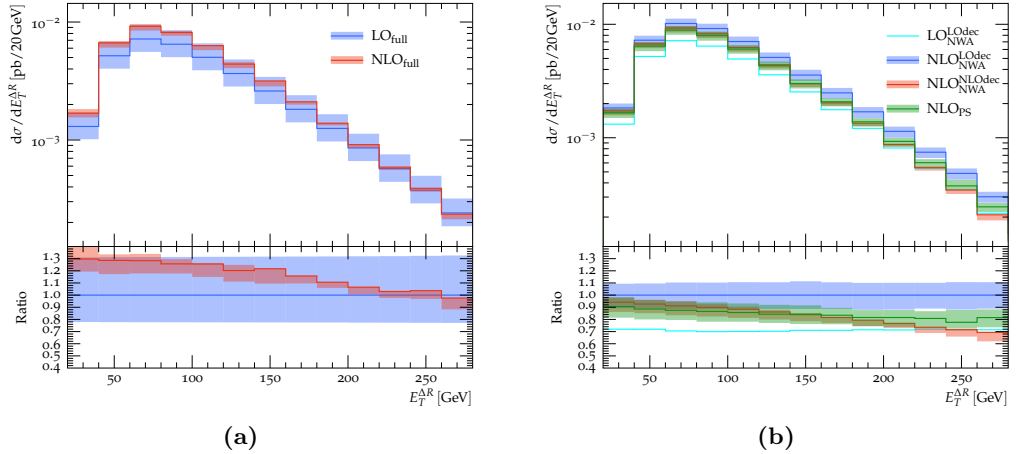


Figure 7.8: Results including scale variation bands for $E_T^{\Delta R}$ for (a) the LO_{full} and NLO_{full} calculations, and (b) the calculations based on the NWA. The ratios are defined as in Fig. 7.6.

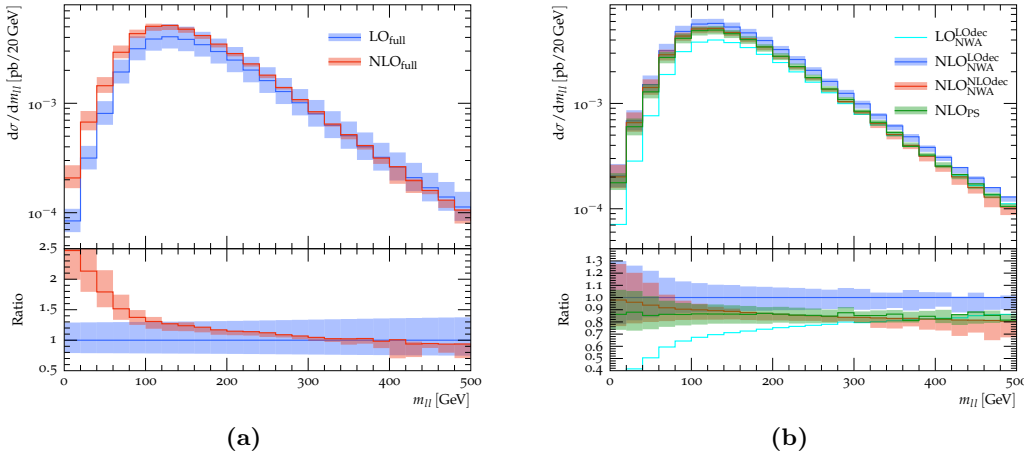


Figure 7.9: Results including scale variation bands for $m_{\ell\ell}$, for (a) the LO_{full} and NLO_{full} calculations, and (b) the calculations based on the NWA. The ratios are defined as in Fig. 7.6.

7.4 Template fit results

After the qualitative discussion of differential results in the last section, results from the template fitting procedure are shown and numerical values compared for the extracted top-quark mass from the different theoretical descriptions. To this effect, since no data was available to compare to, the procedure outlined in Section 7.1 is adapted and the following approach is applied to produce plots like the one displayed in Fig. 7.10:

- **Simulation** : The distributions for $m_{\ell b}$ and m_{T2} are produced at parton level with the three input top-quark masses m_t^{in} for all theoretical descriptions.
 - **Template calibration**: The template distributions produced in the first step are individually fitted to the sum of a Gaussian and a Landau function. The theoretical description used as a basis for the distribution is called the *calibration set*. In the example of Fig. 7.10a, the two calibration sets are described by the red/blue reference points in the legend.
 - **Pseudo-data**: From the different theoretical descriptions, a subset of events is drawn and labeled as *pseudo-data*. This sample corresponds to a luminosity of 50 fb^{-1} . In Fig. 7.10a, the theoretical description used for producing pseudo-data is given at the top of the plot. In general, the pseudo-data set is drawn from the more complete of the two predictions, which should be closer to real data. For a given theory prediction, pseudo-experiments are performed by repeating the random drawing of the pseudo-data 1000 times from the subset of all events.
 - **m_t extraction**: For each of the input top-quark masses m_t^{in} , an unbinned likelihood fit is applied to the pseudo-data, using the corresponding calibration set, to determine the extracted value of the top-quark mass m_t^{out} .

The normalization of the histograms is chosen to reproduce the pseudo-data cross-section in the fit range, so that the result of template fits depends only on differences in the distribution shape. Taking again Fig. 7.10a as reference, the red/blue points indicate the offset of the extracted top-quark mass with respect to the MC input mass $\Delta m_t^{\text{MC}} = m_t^{\text{out}} - m_t^{\text{in}}$. When using the calibration function generated from the same theoretical prediction as used to produce the pseudo-data, the offset Δm_t should be close to zero and serves as a cross-check that no systematic bias exists in the fitting procedure. The error bars indicate the statistical uncertainty associated with the finite size of the pseudo-data sample. The numerical offset Δm_t given in the legend is calculated as the average of the offsets from the three mass points. Finally, the systematic uncertainty bands are provided by fitting the calibration set to the scale-varied pseudo-data.

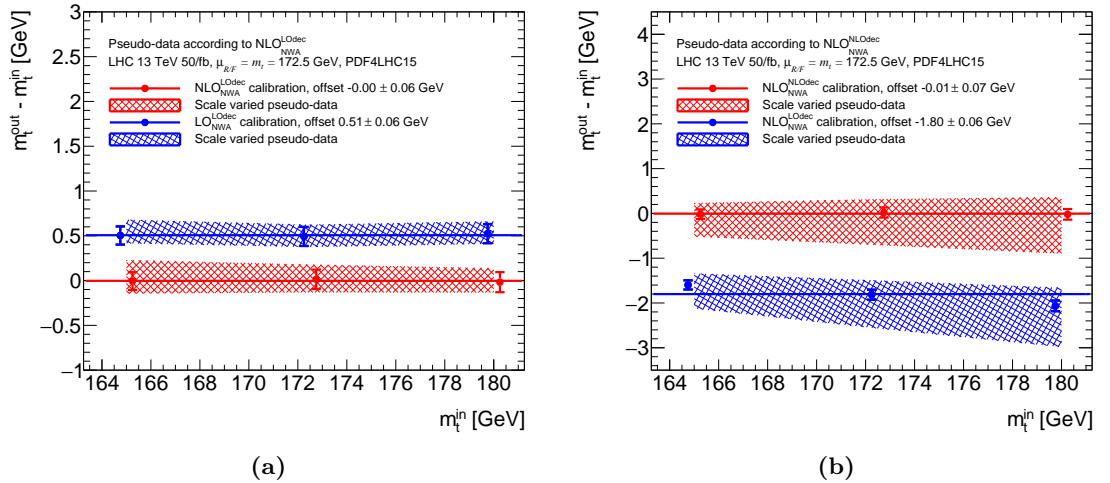


Figure 7.10: Pseudo-data is drawn from (a) $\text{NLO}_{\text{NWA}}^{\text{LOdec}}$ and (b) $\text{NLO}_{\text{NWA}}^{\text{NLOdec}}$ samples, and the difference between the input mass and the fit output is shown for each mass point. The calibration set from the same prediction (red) is used to show the absence of systematic bias in the template fit. The calibration set from (a) $\text{LO}_{\text{NWA}}^{\text{LOdec}}$ and (b) $\text{NLO}_{\text{NWA}}^{\text{LOdec}}$ yields an offset (blue) in the top-quark mass extracted from the theoretically more complete respective pseudo-data.

The predictions are considered in order of increasing complexity. Fig. 7.10a shows the offset between extracted and input top-quark masses when generating pseudo-data according to the $\text{NLO}_{\text{NWA}}^{\text{LOdec}}$ prediction, and using the calibration function fitted from $\text{LO}_{\text{NWA}}^{\text{LOdec}}$ MC templates in blue. The offset in m_t produced by going from LO to NLO in $t\bar{t}$ production amounts to 0.51 GeV. For comparison, Fig. 7.10b gives the offset from fitting the $\text{NLO}_{\text{NWA}}^{\text{NLOdec}}$ pseudo-data with the $\text{NLO}_{\text{NWA}}^{\text{LOdec}}$ calibration function: higher-order corrections in the top-quark decay lead to an offset of -1.80 GeV. Moreover, the NLO decay corrections in Fig. 7.10b lead to larger uncertainty bands, because the scale variations produce non-uniform shape differences. These results already highlight the importance of higher-order corrections to the top-quark decay in mass measurements based on $m_{\ell b}$.

Considering higher-order corrections in both production and decay simultaneously, the offsets in the extracted top-quark masses are given in Fig. 7.11a for the NWA case, and in Fig. 7.11b for the full $W^+W^-b\bar{b}$ case. The factorization of production and decay in the NWA approximation yields an offset of -1.38 GeV , corresponding to the sum of the offsets in NLO production and in NLO decay separately shown in Fig. 7.10a, respectively Fig. 7.10b.

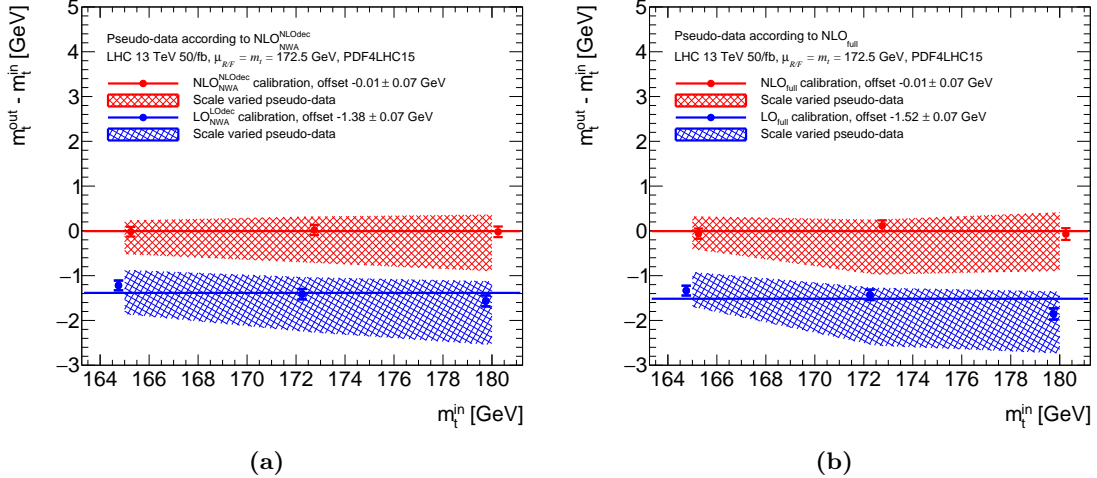


Figure 7.11: From fitting the $m_{t\ell b}$ distribution, the offset for the extracted top-quark mass based on (a) $\text{NLO}_{\text{NWA}}^{\text{NLOdec}}$ and (b) NLO_{full} pseudo-data underlines the effect of taking NLO contributions for production and decay into account.

After these basic considerations, the top-quark mass offsets stemming from the most complete predictions are discussed. The offsets in m_t produced when fitting the NLO_{full} pseudo-data set with the calibration from the $\text{NLO}_{\text{NWA}}^{\text{NLOdec}}$ and the NLO_{PS} predictions are shown in Fig. 7.12a, respectively Fig. 7.12b. While $\text{NLO}_{\text{NWA}}^{\text{NLOdec}}$ still yields a sizeable offset of 0.83 GeV , the uncertainty bands now overlap. In the case of the NLO_{PS} calibration, the offset with respect to NLO_{full} pseudo-data is compatible with zero within statistical uncertainties. Although the NLO_{PS} prediction does not describe the top-quark decay at NLO accuracy beyond the soft limit, it still largely reproduces the full $W^+W^-b\bar{b}$ description for the most part of the $m_{t\ell b}$ fit range, as can be seen in Fig. 7.3. Further studies were performed to understand if the discrepancy between $\text{NLO}_{\text{NWA}}^{\text{NLOdec}}$ and NLO_{PS} originates in the genuine NLO-accurate description of the decay. More details are given in Appendix A, where the parton-shower number of emissions in both production and decay is gradually restricted, and offsets in m_t are compared to the $\text{NLO}_{\text{NWA}}^{\text{NLOdec}}$ prediction. Reducing the number of emissions to one in both production and decay showers moves the NLO_{PS} fitted m_t -value close to the $\text{NLO}_{\text{NWA}}^{\text{NLOdec}}$ prediction. It is the general softening of $m_{t\ell b}$ around the kinematic edge, originating in the successive emissions from the parton-shower, that drives the top-quark mass fitted from the NLO_{PS} prediction towards the NLO_{full} value.

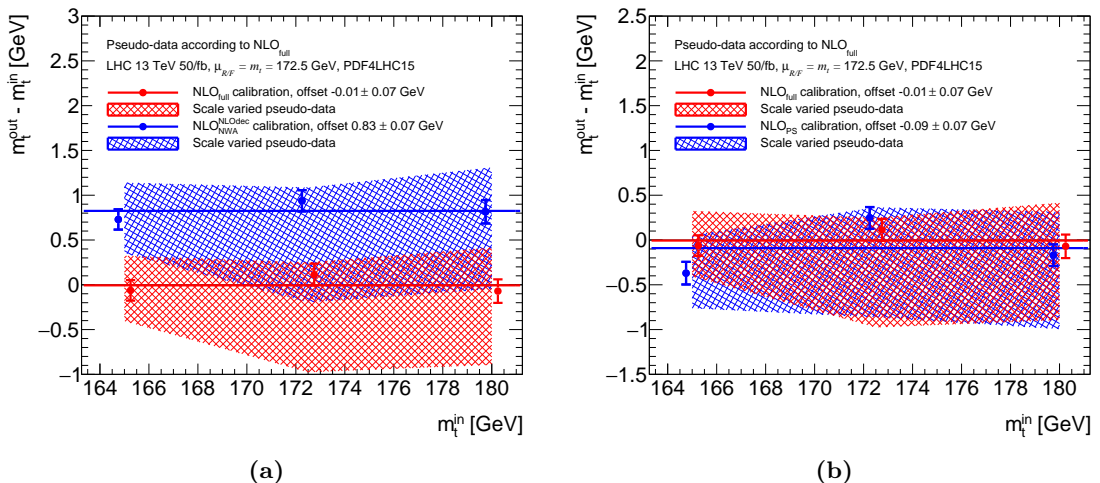


Figure 7.12: Top-quark mass offsets from $m_{\ell\ell}$ for pseudo-data generated from the NLO_{full} prediction are reduced when considering the case of (a) NLO_{NWA}^{NLOdec} and (b) NLO_{PS} calibration functions.

Similar results are also shown for the m_{T2} distribution in Appendix A. The numerical offsets for all comparisons are summarized in Table 7.1, together with a combined χ^2 computed from both $m_{\ell b}$ and m_{T2} offsets for the same theoretical predictions. The value of χ^2 is defined as $\chi^2 = (o_1 - o_2)^2 / (u_1^2 + u_2^2)$, with $i = 1, 2 = m_{\ell b}, m_{T2}$ and $o_i \pm u_i$ are the corresponding offsets and their (uncorrelated) uncertainties. While almost all χ^2 values are consistent with zero, the comparison between NLO_{NWA}^{NLOdec} and NLO_{PS} differs significantly: therefore, the m_{T2} estimator for the top-quark mass is concluded to be less sensitive to differences between the two latter predictions.

In conclusion, this study shows that higher-order corrections to the top-quark decay are at least as important as corrections to $t\bar{t}$ production, considering a top-quark mass extraction based on the $m_{\ell b}$ distribution. Moreover, the theoretical scale uncertainties in the NWA with LO top-quark decay seem to be underestimated. Yet, even the inclusion of the NLO corrections to the top-quark decay falls short of describing the full final-state. The comparisons presented above suffer from a few shortcomings: in particular, further showering and hadronization effects, as well as detector efficiencies are expected to partly wash out the differences observed in the extracted top-quark mass at detector level. This is the subject of Chapter 9, which treats the topic in an even closer experimental setup with the help of a folding procedure in the ATLAS framework.

| Pseudo-data | Calibration | Offset [GeV] | | Figure | | χ^2 |
|--------------------------------------|--------------------------------------|--------------|--------------|--------------|----------|----------|
| | | $m_{\ell b}$ | m_{T2} | $m_{\ell b}$ | m_{T2} | |
| NLO _{NWA} ^{LOdec} | LO _{NWA} ^{LOdec} | +0.51 ± 0.06 | +0.48 ± 0.04 | 7.10a | A.4a | 0.17 |
| NLO _{NWA} ^{NLOdec} | NLO _{NWA} ^{LOdec} | -1.80 ± 0.06 | -1.67 ± 0.04 | 7.10b | A.4b | 3.25 |
| NLO _{NWA} ^{NLOdec} | LO _{NWA} ^{LOdec} | -1.38 ± 0.07 | -1.24 ± 0.05 | 7.11a | A.4c | 2.65 |
| NLOfull | LOfull | -1.52 ± 0.07 | -1.62 ± 0.05 | 7.11b | A.4d | 1.35 |
| NLOfull | NLO _{NWA} ^{NLOdec} | +0.83 ± 0.07 | +0.60 ± 0.06 | 7.12a | A.4e | 6.22 |
| NLOfull | NLO _{PS} | -0.09 ± 0.07 | -0.07 ± 0.06 | 7.12b | A.4f | 0.05 |
| NLO _{PS} | NLO _{NWA} ^{LOdec} | -0.92 ± 0.07 | -1.17 ± 0.05 | A.3a | A.4g | 8.45 |
| NLO _{PS} | NLO _{NWA} ^{NLOdec} | +0.96 ± 0.07 | +0.68 ± 0.05 | A.3b | A.4h | 10.59 |
| NLO _{PS} | NLO _{PS} (μ_{tt}) | -0.03 ± 0.07 | +0.02 ± 0.05 | A.5b | A.5d | 0.34 |

Table 7.1: The offsets from the top-quark mass extraction are given in GeV for pairs of the considered theoretical descriptions, from which the pseudo-data is generated, respectively the calibration function produced. The results are given for both the $m_{\ell b}$ and m_{T2} distributions, along with the corresponding plot references (see also Appendix A). A χ^2 -value is computed between the offsets procured from fits of $m_{\ell b}$ and m_{T2} .

¹⁵⁶⁷ 8 Folding of predictions to detector level

¹⁵⁶⁸ In the following chapter, the results outlined in Chapter 7 are reproduced with full
¹⁵⁶⁹ particle-level predictions and the NLO_{full} calculation is compared to $t\bar{t}$ results in the
¹⁵⁷⁰ ATLAS framework at detector level. To study the extracted values of the top-quark
¹⁵⁷¹ mass from reconstructed events in a fast-simulation style, all distributions are folded
¹⁵⁷² from particle level to detector level in a custom implementation. Top-quark mass deter-
¹⁵⁷³ minations focus entirely on the dilepton channel in this chapter, but the folding setup
¹⁵⁷⁴ can be used in all decay channels.

¹⁵⁷⁵ 8.1 Inverse problems

¹⁵⁷⁶ Usually, when performing a measurement, background contributions are first subtracted
¹⁵⁷⁷ from data, and the corresponding signal distributions are unfolded to particle level [227]
¹⁵⁷⁸ so that available measurements can be directly compared by theorists to their own pre-
¹⁵⁷⁹ dictions. The unfolding procedure is a particular example of so-called inverse problems:
¹⁵⁸⁰ having a true distribution $f(x)$ for some observable Ω , $x \in [\Omega_{\min}, \Omega_{\max}]$, the measured
¹⁵⁸¹ distribution $g(y)$ is given by the Fredholm integral equation:

$$g(y) = \int_{\Omega_{\min}}^{\Omega_{\max}} K(x, y) f(x) dx , \quad (8.1)$$

¹⁵⁸² where the kernel $K(x, y)$ is a continuous function. For binned results, discretizing
¹⁵⁸³ Eq. (8.1) gives a linear equation for \mathbf{x} , \mathbf{y} the n -, respectively m -bin histograms corre-
¹⁵⁸⁴ sponding to the true, respectively the measured distribution:

$$y_j = \sum_{i=1}^n A_{ij} x_i, \quad j \in \{1, \dots, m\} , \quad (8.2)$$

¹⁵⁸⁵ where \mathbf{A} is the bin migration matrix. The problem of inverting Eq. (8.2), that is to
¹⁵⁸⁶ uncover the true distribution \mathbf{x} of an observable Ω from the measured signal distribution
¹⁵⁸⁷ \mathbf{y} , is the foundation of unfolding procedures. Because noise in the measured function
¹⁵⁸⁸ can lead to instabilities in the inversion of the response matrix \mathbf{A} , the procedure has
¹⁵⁸⁹ to be regularized. There are two distinct unfolding methods: direct unfolding proce-
¹⁵⁹⁰ dures, which usually implement some regularization parameter for a smooth inversion
¹⁵⁹¹ of Eq. (8.2), and iterative methods. For a short review of unfolding methods in particle
¹⁵⁹² physics, see Refs. [228, 229].

Conversely, instead of unfolding the data to particle level, the chosen strategy for the 13 TeV ATLAS top-quark mass analysis in both lepton+jets and dilepton channels is to produce the distribution templates and perform the likelihood fit only at detector level. This is for several reasons: in particular, the top-quark mass extraction in the lepton+jets channel [5] simultaneously fits three parameters, namely the top-quark mass, the jet- and the b -jet energy scale factors (see Section 8.4). It is therefore simpler to simulate all samples up to detector level, and directly perform the fit of all three parameters without having to handle a 3D-unfolding. The full simulation also avoids numerical instabilities inherent to the chosen unfolding algorithm. The main disadvantage of the direct method lies in the computing time: indeed, all MC samples (m_t -varied central predictions, systematics-varied samples, and background) have to be simulated up to detector level. Instead, a complementary approach is proposed with the use of direct folding, as in Eq. (8.2), to provide distributions at detector level from the samples generated at particle level. Thus, the costly ATLAS simulation is avoided and one can quickly quantify effects of systematic uncertainties on e.g. the extracted top-quark mass.

8.2 Folding setup in ATLAS

Considering the results of Chapter 7, the goal is to use the folding setup in ATLAS to estimate the uncertainty in using the incomplete $t\bar{t}$ prediction instead of a full parton-showered $W^+W^-b\bar{b}$ event set. It is clear that simulating all MC samples from particle to detector level is time-consuming: with one theoretical central prediction (for example POWHEG+PYTHIA8) and one parameter for the template fit (e.g. the top-quark mass m_t), one has to produce and simulate as many samples as top-quark mass points.

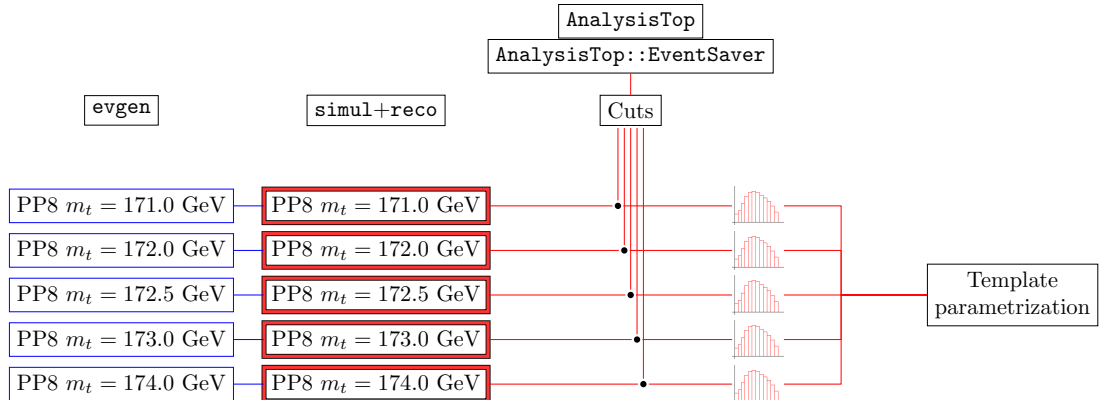


Figure 8.1: The workflow for a template fit of the central prediction POWHEG+PYTHIA8 (PP8) and five top-quark mass points.

Fig. 8.1 illustrates the current analysis workflow for five top-quark mass points. Each of the samples is produced at particle level first (`evgen` in blue on the far left) and has to be simulated and reconstructed (`simul+reco` in red). In the ATLAS 13 TeV analysis, all samples entering the template fit parametrization are fast-simulated with

the ATLFAST [165] package. A custom event saver from the `AnalysisTop` package applies the cuts outlined later in Section 8.5 and saves histograms for control purposes, as well as the final observables entering the top-quark mass fit. Histograms of the $m_{\ell b}$ distribution for all individual mass points are then fed to the template parametrization.

To estimate systematic uncertainties, MC variation samples currently go through the same routine. For example, MC samples with variations of radiative parameters (e.g. `hdamp` in POWHEG, or a variation of the shower and hadronization algorithm) are also simulated and parametrized, and the result of the template fit is taken as a systematic uncertainty on the central sample for the extracted top-quark mass. In the following, for a swifter evaluation of the associated systematics, histograms of variation samples are directly folded from particle to detector level, and the output in the template fit is used to estimate the systematic uncertainty on the extracted top-quark mass.

A simple version of Eq. (8.2) is introduced, where pure bin migration is implemented by a right stochastic matrix \mathbf{A} , and the detector efficiencies are represented by two bin-by-bin probability vectors ϵ^{eff} and f^{acc} :

$$\mathcal{R}_i = \frac{1}{f_i^{\text{acc}}} A_{ij} \times \left(\mathcal{P}_j \epsilon_j^{\text{eff}} \right), \quad (8.3)$$

where \mathcal{R}_i is the number of events at detector level in bin i (for an arbitrary differential distribution), and \mathcal{P}_j is the number of events at particle level in bin j . The migration matrix entry A_{ij} is the probability for an event in bin j at particle level to move to bin i at detector level, provided the event is reconstructed. Finally, the efficiency ϵ_j^{eff} is the probability for an event in bin j at particle level to be reconstructed in the detector, and $1/f_i^{\text{acc}}$ the probability of an event in bin i at detector level to stem from a fake signal (i.e. it has no existing counterpart at particle level). The migration matrices and detector efficiencies only encode the experimental resolution simulated by ATLFAST.

This alternative procedure is depicted in Fig. 8.2. The central POWHEG+PYTHIA8 (PP8) sample is simulated once: histograms at both detector level (in red) and particle level (in blue) are fed to the custom folding package (green nodes). From the distributions at both levels, a script produces the migration matrices and detector efficiencies defined above. In principle, for a given top-quark mass, pure theoretical uncertainties can then be estimated by applying the migration matrices and efficiencies from the central sample to variation samples, since detector effects do not depend on the MC theory variations themselves. A folding script implements Eq. (8.3) and generates folded detector-level histograms from the particle-level MC-varied samples. They are also saved for future use in the template fit. Moreover, consistency and statistical cross-checks can be performed separately. In principle, this procedure can be applied to all **theoretical** uncertainties. Now, in addition to the usual systematic variations, an estimate is computed for the uncertainty stemming from the non-resonant and non-factorizing diagrams in the full $W^+W^-b\bar{b}$ calculation.

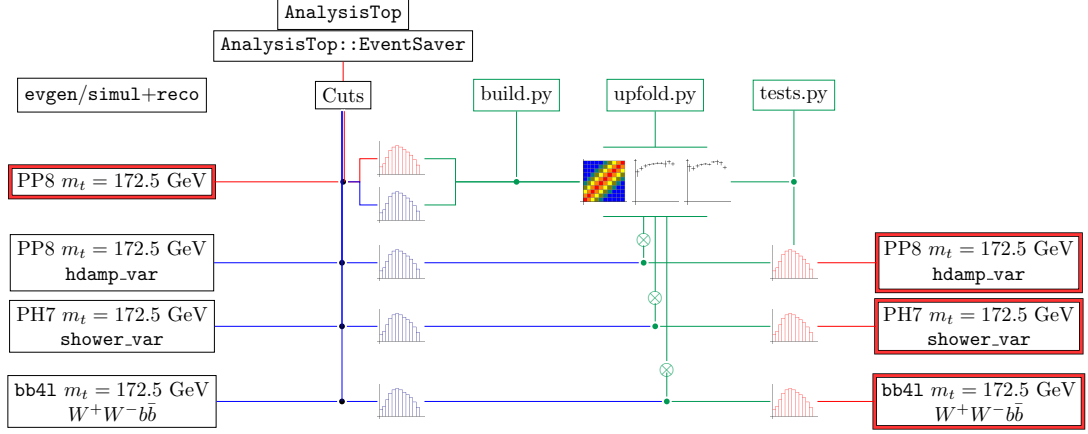


Figure 8.2: The folding package builds migration matrices and efficiency histograms from the simulated detector- and the particle level of a central sample, for example POWHEG + PYTHIA8 with $m_t = 172.5$ GeV. They are used to fold particle-level histograms from MC-varied samples to detector level.

1656 8.3 Theoretical descriptions of the signal

1657 The MC derivation samples (DxAOD) used for all subsequent studies were produced
 1658 officially by ATLAS during the MC16a campaign (optimized to describe the 2015/2016
 1659 data) and are summarized in Appendix B. The nominal samples for NLO $t\bar{t}$ in the
 1660 NWA are generated by POWHEG (for the matrix-element) and parton-showered with
 1661 PYTHIA8 for five different mass points.¹ These samples are simulated to detector level
 1662 with the ATLFast algorithm, but a cross-check is done with respect to the full GEANT4
 1663 simulation for one mass point. For a fairer comparison of the full $W^+W^-b\bar{b}$ prediction to
 1664 the $t\bar{t}$ NWA description, the single-top Wt channel (with diagram-removal) is added to
 1665 the $t\bar{t}$ sample. In order to generate $W^+W^-b\bar{b}$ predictions at particle level, the following
 1666 setup is used:

- 1667
- 1668 • **Parton-level production:** The full dilepton final-state $(e^+\nu_e)(\mu^-\bar{\nu}_\mu)b\bar{b}$ events
 1669 are produced at parton level with a local installation of the `bb4l` generator in
 1670 POWHEG-BOX-RES [230]. They are generated outside of the ATLAS framework
 1671 since the implementation of the `bb4l` program has not been validated yet. LHE
 files are written out by POWHEG for later showering.

1672

 - 1673 • **Particle-level production:** The PYTHIA8 parton-shower is applied in the AT-
 1674 LAS framework to the parton-level events produced with `bb4l`. Hadronization is
 1675 also handled in PYTHIA by the Lund model.

¹Samples with nine top-quark mass points were officially produced, but only the same mass points as for $W^+W^-b\bar{b}$ samples are used in this study.

- 1675 • **Analysis pre-step:** The MC simulation step in ATLAS produces a so-called event
 1676 (EVNT) file containing the particle information and kinematics. To be able to run
 1677 the `AnalysisTop` routine on the sample, one needs to transform it to a DxAOD
 1678 derivation format. The truth information is propagated to the derivation level,
 1679 which contains thinned MC truth information.

1680 For first studies, predictions for five mass points are generated for the $t\bar{t}$ NWA and
 1681 the $W^+W^-b\bar{b}$ configurations (as well as for single-top Wt samples), with:

$$m_t \in \{171, 172, 172.5, 173, 174\} [\text{ GeV}] . \quad (8.4)$$

1682 8.4 Object definition

1683 In ATLAS, the measured data and the MC simulation output are fed to reconstruction
 1684 algorithms. These algorithms rely on well-defined physics objects at detector level. The
 1685 Level-1 trigger identifies well-resolved candidate physics objects, like electrons, photons,
 1686 muons and jets. The Level-2 trigger cuts are then designed to refine this selection. With-
 1687 out entering into much detail, trigger and reconstruction algorithms for electrons and
 1688 photons [231], muons [232], jets [233], taus [234] and MET [156, 235] mostly use infor-
 1689 mation from calorimeter energy clusters matched to one or several tracks identified in
 1690 the Inner Detector. More about the exact trigger cut definitions and object selection can
 1691 be found in Ref. [236]. The identification and reconstruction requirements for electrons,
 1692 muons and jets are briefly reviewed.

1693 8.4.1 Electrons

1694 Electron reconstruction matches energy deposits in the EM calorimeter to tracks identi-
 1695 fied in the Inner Detector. For electrons and photons at the Level-1 trigger, a minimal
 1696 transverse energy requirement $E_{T,\min}$ is used. In order to distinguish possible fake sig-
 1697 nals, a veto can be applied on the activity in the hadronic calorimeter behind the iden-
 1698 tified cluster in the EM calorimeter. To originate from the primary interaction vertex,
 1699 electrons have to fulfill $|z_0| \cdot \sin(\theta) < 0.5 \text{ mm}$ and $|d_0|/\sigma_{d_0} < 5$. Here, z_0 and d_0 are the
 1700 longitudinal and transverse impact parameters, θ is the azimuthal angle, and σ_{d_0} is the
 1701 transverse impact parameter resolution.

1702 At the Level-2 trigger, precision tracks from the Inner Detector are extrapolated to the
 1703 EM calorimeter and have to match an identified cluster within $(\Delta\eta, \Delta\phi) = (0.05, 0.05)$.
 1704 A multivariate algorithm [237] is used for calibrating the measured cluster energy. Then,
 1705 electrons are identified with a likelihood (LH) discriminant that defines three working
 1706 points: `Loose`, `Medium` and `Tight`. This multivariate likelihood depends on variables
 1707 characterizing the topologies of EM showers in the calorimeter.

1708 **8.4.2 Muons**

1709 Muon reconstruction happens in two steps: a so-called fast reconstruction, and a pre-
 1710 cision stage. In the fast step, information from the MDT detectors in the Muon Spec-
 1711 trometer is used to fit the track of the muon candidate: these identified muons are called
 1712 *MS-only* muons. The track of the muon candidate is then extrapolated back to the
 1713 interaction vertex and combined with tracks identified in the Inner Detector. If such
 1714 a track is found, the identified object is called *combined* muon. In the precision stage,
 1715 the same procedure is applied: if no corresponding track is found in the Inner Detector,
 1716 tracks are extrapolated from the interaction point out to the Muon Spectrometer. To
 1717 be assigned to the primary vertex, the muon tracks need to fulfill $|z_0| \cdot \sin(\theta) < 0.5$ mm
 1718 and $|d_0|/\sigma_{d_0} < 3$.

1719 Quality requirements are also applied to muon selection and offer different degrees
 1720 of background rejection, mainly from pion and kaon decays. Muons are reconstructed
 1721 with a minimal requirement on the transverse momentum. Depending on whether the
 1722 candidate objects are MS-only or combined muons, as well as on their kinematics, they
 1723 are classified in **Loose**, **Medium**, **Tight** or **High- p_T** . Additionally, an optional isolation
 1724 criterion for low- p_T muons can be applied.

1725 **8.4.3 Jets**

1726 The anti- k_T jet algorithm [220] is applied (with a distance parameter $R = 0.4$ for small-
 1727 R jets) to topological clusters identified in the calorimeter. These topo-clusters are
 1728 reconstructed from the full set of calorimeter clusters. The identified jets have to be
 1729 calibrated, and correction factors are applied to retrieve their correct 4-momentum and
 1730 origin vertex. In particular, the determination of jet energy scale (JES) factors and
 1731 uncertainties comprises several steps, and usually includes comparisons between MC and
 1732 data. In the ATLAS jet calibration, a MC-based comparison is followed by an *in situ*
 1733 energy calibration step.² Especially for the case of the ATLAS top-quark mass analysis in
 1734 the lepton+jets channel (which is not covered in this work), the jet- and b -jet energy scale
 1735 systematics dominate the total measurement uncertainty. For a comprehensive study of
 1736 jet reconstruction and associated uncertainties, the reader is referred to Ref. [238].

1737 Finally, jets stemming from b -quarks can be discriminated against light-quark jets.
 1738 This feature is crucial in several analyses, including the measurement of the top-quark
 1739 mass. Mostly, the identification of a b -jet (so-called b -tagging) relies on the observation
 1740 of a displaced vertex from which the jet originates. There exist multiple b -tagging
 1741 algorithms: impact-based (IP2D and IP3D [239, 240]), secondary vertex identification
 1742 (SV [241]) and decay chain multi-vertex (JetFitter [242]). In ATLAS, the output from
 1743 all three procedures are combined in a multivariate likelihood algorithm (MV2 [235]). A
 1744 point in the likelihood discriminant can be chosen and defines the tagging efficiency (in
 1745 the following chapter, a 70% b -tagging efficiency is chosen).

²This type of energy calibration uses events where a well-known reference object recoils against one measured jet, e.g. $Z(\rightarrow \ell\ell) + j$ or $\gamma + j$.

8.5 Event requirements

The AnalysisTop package in the ATLAS framework contains all the subpackages that are useful for general top-quark measurements. In this case, AnalysisTop version 21.2.61 is used. As mentioned earlier, the code executes both lepton+jets and dilepton routines simultaneously, albeit with different cutflows and orthogonal channel selections. The various MC samples were presented above, and the following requirements are applied on the events in the $e\mu$ dilepton channel:

- Two oppositely charged leptons with exactly one electron and one muon which fulfill $p_T^\ell > 28$ GeV. For reconstructed events, the lepton criteria for passing the high-level trigger (HLT) requirements are taken from the Top Trigger Group recommendation. These depend on the luminosity and are different for 2015 and 2016 data. They are set to the following values for 2015, respectively 2016 data:

| Trigger cut | Object | Min. [GeV] | LH | Isolation | L-1 |
|--------------------------------|-----------|-------------|--------|--|-------|
| HLT_e24_lhmedium_L1EM20VH | e^\pm | $E_T > 24$ | Medium | — | VH |
| | e^\pm | $E_T > 60$ | Medium | — | — |
| | e^\pm | $E_T > 120$ | Loose | — | — |
| | μ^\pm | $p_T > 20$ | — | $\sum p_T^{\text{track}}/p_T^e < 0.1(R = 0.2)$ | — |
| | μ^\pm | $p_T > 50$ | — | — | — |
| HLT_e26_lhtight_nod0_ivarloose | e^\pm | $E_T > 26$ | Tight | $\sum p_T^{\text{track}}/p_T^e < 0.1$ | d_0 |
| | e^\pm | $E_T > 60$ | Medium | — | d_0 |
| | e^\pm | $E_T > 140$ | Loose | — | d_0 |
| | μ^\pm | $p_T > 26$ | — | $\sum p_T^{\text{track}}/p_T^\mu < 0.07$ | — |
| | μ^\pm | $p_T > 50$ | — | — | — |

The electrons are designated by their likelihood discriminant (LH). An isolation cut can be applied, where a maximum is set on the scalar sum of the transverse momentum in a cone around an object track (with variable size for the 2016 Run). Finally, an additional Level-1 trigger veto can be applied on the hadronic activity behind the EM clusters (VH). For 2016 data, no impact parameter requirement is set on the electron tracks.

- $H_T = \sum_i p_{T,i} > 120$ GeV, the scalar transverse momentum sum of all particles.
- $n_{\text{jets}} \geq 2$ for the total number of jets with $p_T^{\text{jet}} > 25$ GeV.
- Exactly two b -jets with $p_T^{\text{jet}} > 25$ GeV. For reconstructed events, a 70% b -tagging working point is chosen for the MV2c10 [239, 243] b -tagging algorithm. A b -jet is defined within particle-level events using the JET_N_GHOST criterion (so-called ghost association [244]), for which a jet is b -tagged if it contains a B -hadron.
- $m_{\ell\ell} > 15$ GeV for the invariant mass of the two-lepton system.

9 Determination of the top-quark mass at detector level

The simulated $t\bar{t}$ NWA predictions are compared at particle and detector level for control distributions, as well as for the $m_{\ell b}$ histogram which enters the template fit for the top-quark mass determination. Migration matrices and detector efficiencies derived from those samples are also plotted. After some simple cross-checks of the setup, the $W^+W^-b\bar{b}$ folded results and template parametrization are presented, along with numerical comparisons of both theoretical descriptions for the extraction of the top-quark mass. All results shown here are preliminary and should be taken with a grain of salt.

9.1 Differential results at particle and detector level

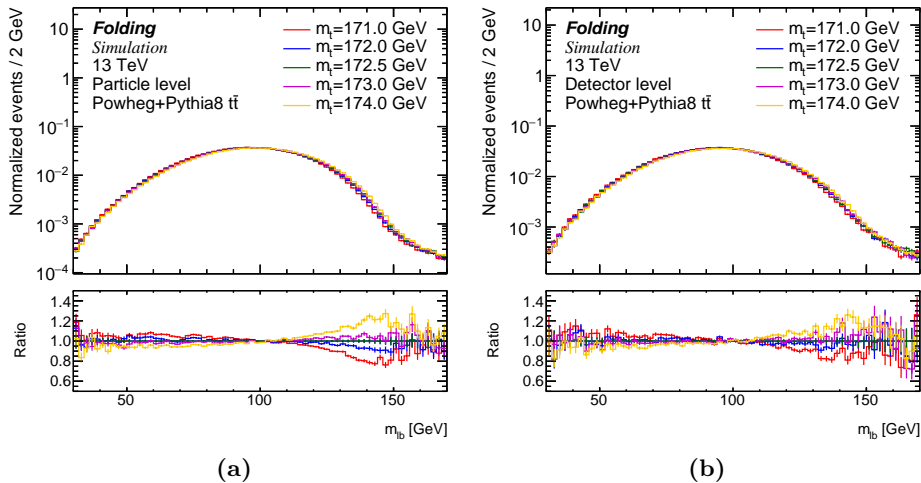


Figure 9.1: The normalized $m_{\ell b}$ distribution from the PP8 $t\bar{t}$ NWA predictions is shown for five top-quark mass points at (a) particle level and (b) detector level.

In Fig. 9.1, distributions of the $m_{\ell b}$ observable are shown for the five different MC top-quark mass points generated from the $t\bar{t}$ NWA predictions produced by POWHEG matched to PYTHIA8 (PP8). In all plots, the distributions are normalized to unity since, as in Chapter 7, only shape differences matter in the template fit. The ratio is shown to the prediction with the central top-quark mass, and error bars indicate MC statistical uncertainties. The predictions are shown at particle level in Fig. 9.1a and

9 Determination of the top-quark mass at detector level

at detector level in Fig. 9.1b. Already, the sensitivity to the input top-quark mass decreases visibly when comparing the particle and detector levels. Fig. 9.2a gives the particle-level $m_{\ell b}$ distribution for the full $W^+W^-b\bar{b}$ prediction at NLO QCD matched to the PYTHIA8 parton-shower, again as a function of the five input top-quark masses. Finally, Fig. 9.2b underlines the difference between the $t\bar{t}$ and $W^+W^-b\bar{b}$ computations for an input top-quark mass of $m_t = 172.5$ GeV. In general, the $m_{\ell b}$ distribution from the parton-showered $W^+W^-b\bar{b}$ sample is shifted towards higher top-quark masses.

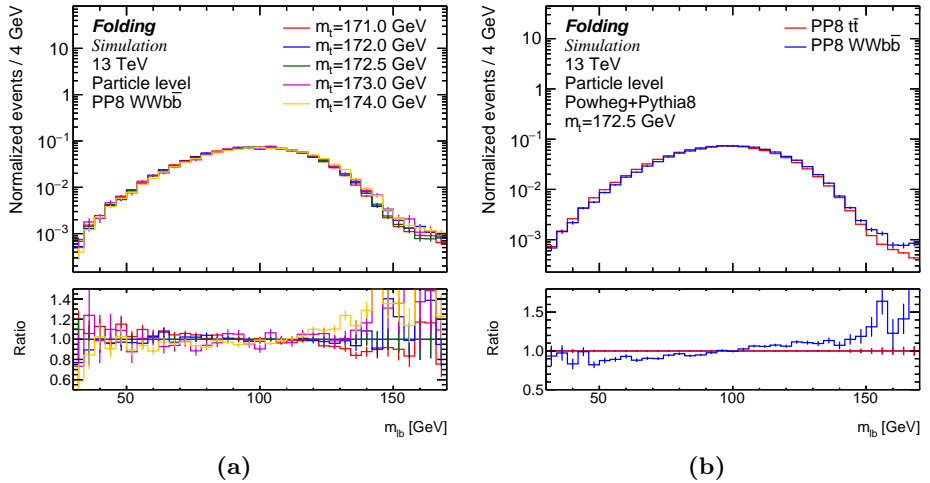


Figure 9.2: The normalized $m_{\ell b}$ distribution is given for the generated $W^+W^-b\bar{b}$ events (a) for the five different input top-quark masses and (b) for $m_t = 172.5$ GeV and compared to $t\bar{t}$ at the same mass point.

Now, as stated above, the $W^+W^-b\bar{b}$ predictions are to be folded from particle to detector level using the $t\bar{t}$ migration matrices. Before jumping to the final results, a few control observables are used to reconstruct the migration matrices and efficiencies. Histograms are pictured at particle and detector level for the $t\bar{t}$ sample at $m_t = 172.5$ GeV. In Fig. 9.3a, the distribution of the angular separation between both leptons $\Delta R_{\ell\ell}$ is shown. The total number of events corresponds to the full MC sample. The migration matrix \mathbf{A}_{ij} is pictured in Fig. 9.3b. In each case, the migration matrix rows are normalized to unity. For distributions relying on well-reconstructed objects, like $\Delta R_{\ell\ell}$, the migration matrix is very diagonal. The efficiency ϵ^{eff} and inverse fake rate f^{acc} are displayed in Fig. 9.3c and Fig. 9.3d, respectively. The overall efficiency is small with an average of $\sim 26\%$ due to the reconstruction trigger cuts at detector level, which do not exist at particle level.

9.1 Differential results at particle and detector level

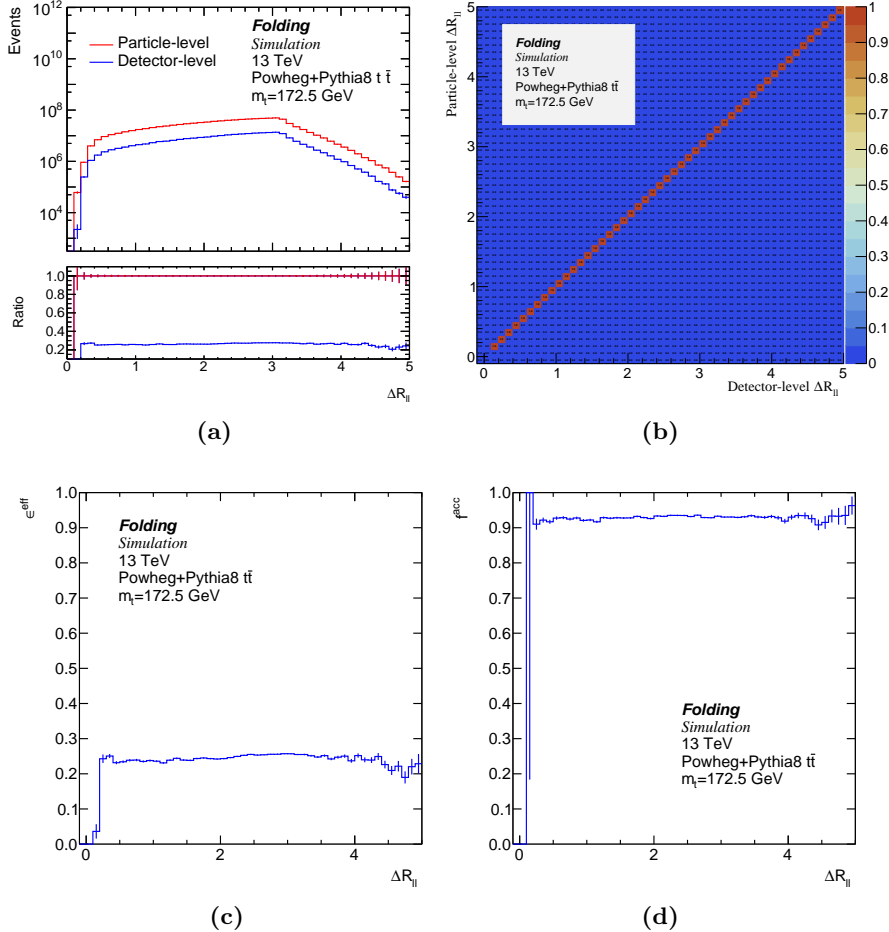


Figure 9.3: The angular separation between both leptons $\Delta R_{\ell\ell}$ for the PP8 $t\bar{t}$ sample at $m_t = 172.5$ GeV (a) Differential distributions at particle and detector level (b) Migration matrix \mathbf{A}_{ij} (c) Efficiency ϵ_{eff} (d) Inverse fake rate f^{acc} as defined in Eq. (8.3).

9 Determination of the top-quark mass at detector level

Jets are generally harder to reconstruct. Fig. 9.4 gives histograms, migration matrices and detector efficiencies for the number of jets n_{jets} . Some migration to the next bins (and next-to-next bins for higher jet multiplicities) can be observed. While for $\Delta R_{\ell\ell}$ both the efficiency and the fake rate were almost constant, Fig. 9.4d underlines some bin-dependence of the fake rate for the number of reconstructed jets.

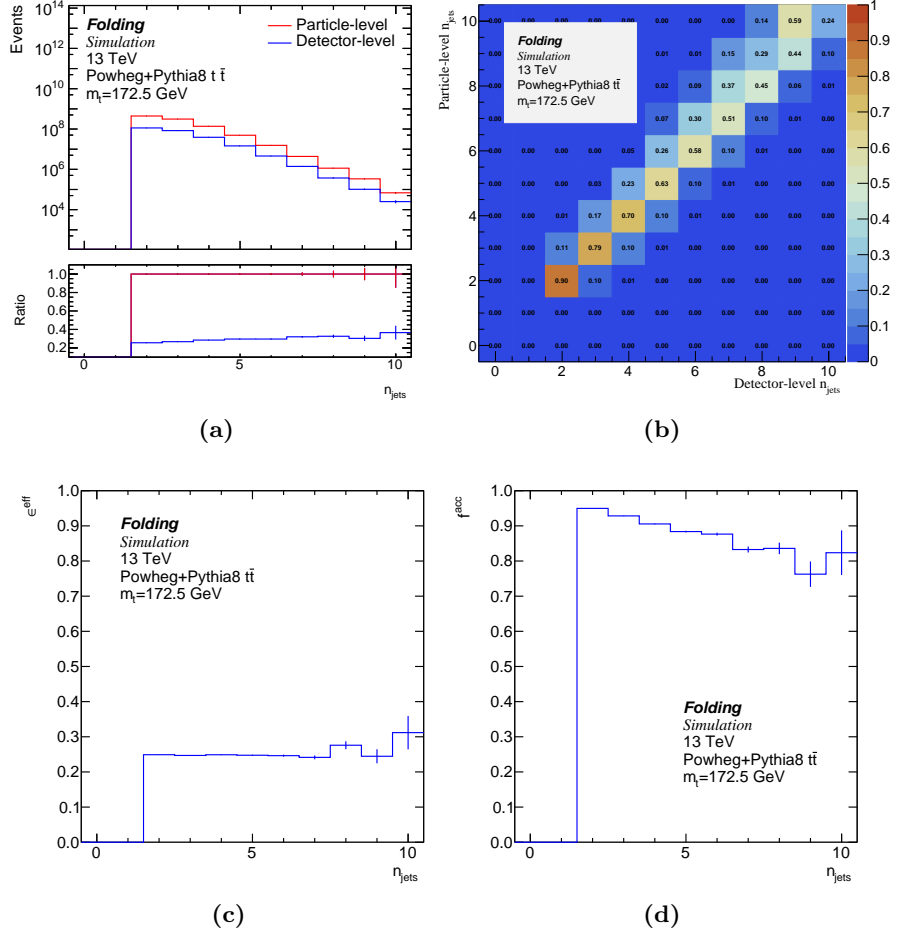


Figure 9.4: The number of jets n_{jets} for the PP8 $t\bar{t}$ sample at $m_t = 172.5 \text{ GeV}$ (a) Differential distributions at particle and detector level (b) Migration matrix \mathbf{A}_{ij} (c) Efficiency ϵ_{eff} (d) Inverse fake rate f_{acc} as defined in Eq. (8.3).

Finally, for the $m_{\ell b}$ distribution, the same quantities are shown in Fig. 9.5. The definition of the $m_{\ell b}$ observable is identical to the one given in Chapter 6. Here, the migration matrices were rebinned for better visibility. Correct reconstruction is harder, and mostly depends on the pairing of the lepton- and b -jet systems, which might not be the same at particle than at detector level. The efficiency is highest below the kinematic edge, which corresponds to well-separated, on-shell top-quark pairs.

9.1 Differential results at particle and detector level

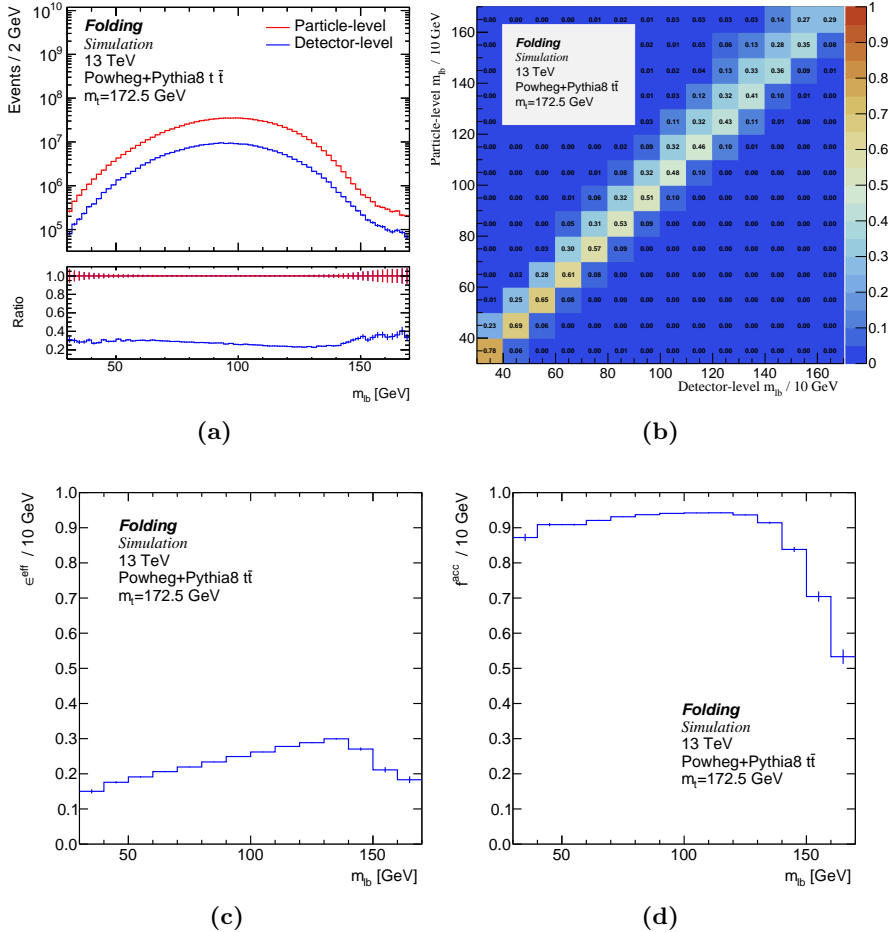
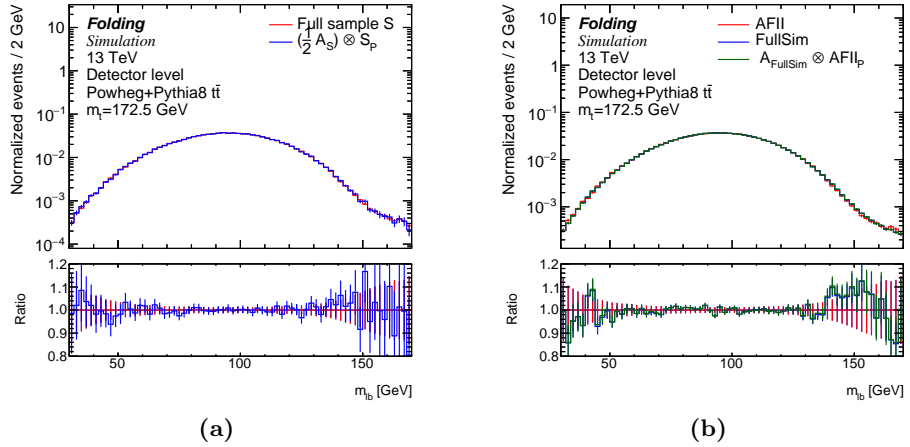


Figure 9.5: The lepton- b -jet invariant mass $m_{\ell b}$ for the PP8 $t\bar{t}$ sample at $m_t = 172.5$ GeV (a) Differential distributions at particle and detector level (b) Migration matrix \mathbf{A}_{ij} (c) Efficiency ϵ^{eff} (d) Inverse fake rate f^{acc} as defined in Eq. (8.3).

1817 9.2 Statistical and systematic cross-checks

1818 Several cross-checks are performed with respect to statistical and systematic biases that
 1819 could appear in the folding procedure. To ensure that statistical uncertainties are prop-
 1820 agated correctly, only half of the sample for the $t\bar{t}$ prediction at $m_t = 172.5$ GeV is used
 1821 to derive migration matrices and efficiencies. The folding matrices from this reduced
 1822 sample, called symbolically $\frac{1}{2}A_S$, are then applied to the particle-level sample S_P with
 1823 full statistics. The $m_{\ell b}$ distribution obtained at detector level (folded from the subset
 1824 sample) is compared to the simulated detector-level distribution with full statistics S in
 1825 Fig. 9.6a. The differences between both are covered by the statistical uncertainties with
 1826 no significant bias. In Fig. 9.6b, the $m_{\ell b}$ distribution is compared at detector level for
 1827 the GEANT4 (FullSim) and the ATLFAST (AFII) algorithms. Although some structure
 1828 in the distribution tail seems to indicate a softer spectrum for ATLFAST than for the full
 1829 simulation, both distributions still agree within statistical uncertainties.



1830 **Figure 9.6:** Migration matrices from one sample are used to fold another sample's particle-level
 1831 mass distribution for statistical and systematic cross-checks. (a) A statistical subset
 1832 is used to derive migration matrices $\frac{1}{2}A_S$ and fold the full sample S_P . (b) Same for
 1833 the GEANT4 (SIM) and ATLFAST (AFII) simulated samples.

1834 In the following, migration matrices are consistently chosen to use the same input top-
 1835 quark mass as the sample to be folded. Still, the input top-quark mass does not produce
 1836 any systematic bias in the folded distributions: in Fig. 9.7a, the migration matrices from
 1837 the $m_t = 174$ GeV sample are used to fold the $m_t = 171$ GeV prediction to detector
 1838 level. The folded and simulated distributions for $m_t = 171$ GeV agree perfectly. The
 1839 same should be true of any theoretical MC variation. Usually, the h_{damp} parameter in
 1840 POWHEG, which regulates the amount of hard radiation, is taken as such a variation.
 The central value is chosen as $h_{\text{damp}} = 1.5 \cdot m_t =: h_1$. The variation sample uses
 $h_{\text{damp}} = 3 \cdot m_t =: h_2$. Folding the varied sample at particle level $h_{2,P}$ with the migration
 1841 matrices A_{h_1} from the central sample leads to good agreement at detector level, as shown
 1842 in Fig. 9.7b.

9.2 Statistical and systematic cross-checks

Finally, a comparison is made between the PYTHIA8 and HERWIG7 parton-showers at particle level in Fig. 9.8a. The fact that PYTHIA8 produces harder radiation than HERWIG7 is well-known (see Chapter 11 for the case of Higgs pair production). The effect on the top-quark mass was investigated in the POWHEG-BOX-RES framework recently [245], where offsets in the position of the peak of the W - b -jet system of up to 1 GeV were underlined. In the dilepton case, the parton-shower differences do lead to important offsets at particle level. Once detector effects are taken into account, though, the discrepancy is much less pronounced, as shown in Fig. 9.8b.

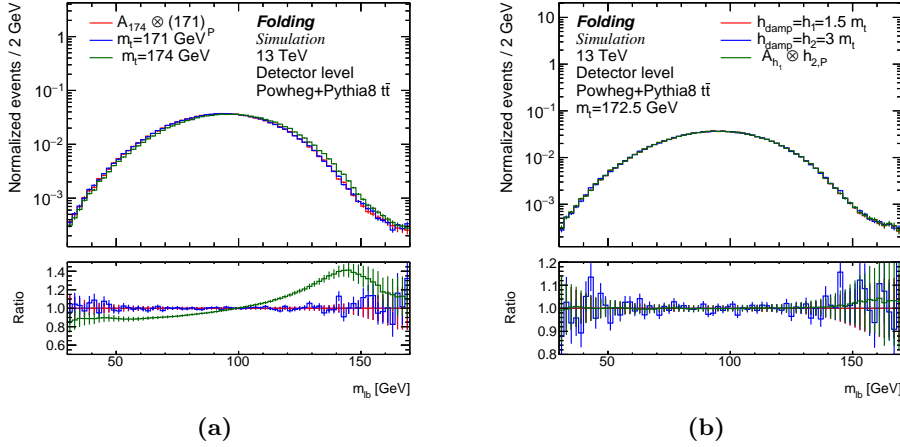


Figure 9.7: (a) Same as Fig. 9.6 for the $m_t = 174$ GeV sample folding of the $m_t = 171$ GeV prediction, and (b) for the central and varied values of the h_{damp} parameter.

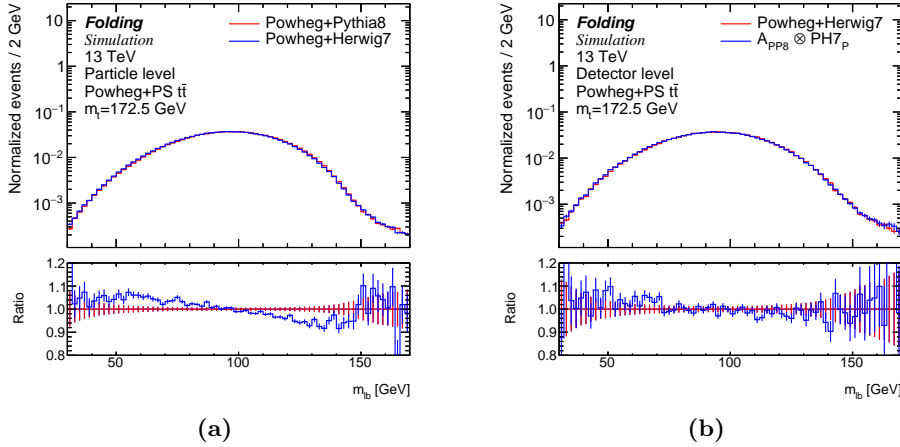


Figure 9.8: (a) The PYTHIA8 (PP8) and HERWIG7 (PH7) parton>Showered samples are compared at particle level for a fixed top-quark mass $m_t = 172.5$ GeV. (b) Same as Fig. 9.6 for the PP8 and PH7 samples.

1849 9.3 Folded results and template parametrization

1850 In Fig. 9.9, the normalized $m_{\ell b}$ distribution is shown for the signal ($t\bar{t}$ and single-top in
 1851 the Wt channel) and the $W^+W^-b\bar{b}$ predictions at detector level for an input top-quark
 1852 mass $m_t = 172.5$ GeV. The single-top contribution starts populating the region above
 1853 the kinematic edge $m_{\ell b}^{\text{edge}} \sim 153$ GeV. The migration matrices \mathbf{A}_{ij} , efficiencies ϵ^{eff} and
 1854 inverse fake rates f^{acc} from the central $t\bar{t}$ sample are used to fold the $W^+W^-b\bar{b}$ particle-
 1855 level prediction. The same samples are then compared to 2015/2016 data from ATLAS
 1856 at $\sqrt{s} = 13$ TeV. As a matter of fact, the $t\bar{t}$ +single-top prediction at $m_t = 172.5$ GeV
 1857 agrees very well with data.¹ The $m_{\ell b}$ distribution from the corresponding $W^+W^-b\bar{b}$
 1858 sample introduces a bias (in green), which shall be quantified in the top-quark mass
 1859 extraction.

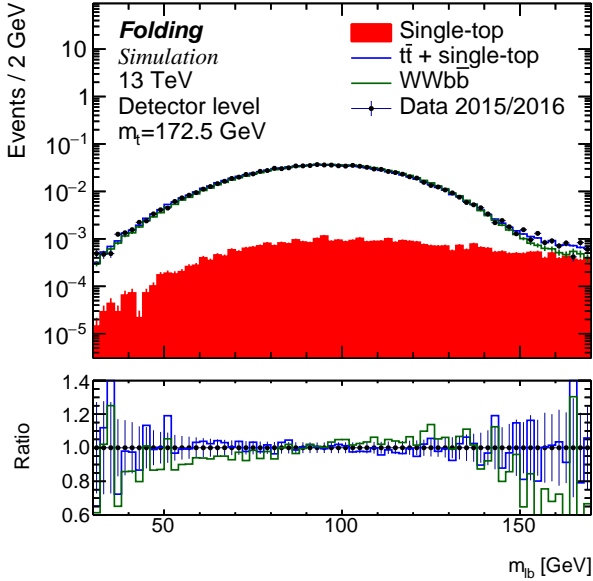


Figure 9.9: The normalized $m_{\ell b}$ distribution at an input top-quark mass of $m_t = 172.5$ GeV is shown for the $t\bar{t}$ and single-top sample, as well as for the $W^+W^-b\bar{b}$ prediction folded to detector level. Additionally, ATLAS 2015/2016 data points are given for a qualitative comparison. The data amounts to 36.2 fb^{-1} . The lower plot shows the ratio to data (with statistical uncertainties as error bars).

1860 The $m_{\ell b}$ template distributions for all five input top-quark masses are parametrized
 1861 separately. In this case, a sum of three Gaussian distributions is used for a total of
 1862 18 parameters (9 functional parameters \times 2 linear parametrizations as a function of
 1863 m_t). Fig. 9.10 shows the $m_{\ell b}$ distribution from the central MC sample and the fitted
 1864 functions. The fit is performed with MINUIT [246] within the `AnalysisTop` framework.
 1865 The fit range is set to $m_{\ell b} \in [40 \text{ GeV}, 148 \text{ GeV}]$, and the chosen functions satisfactorily
 1866 describe the distribution in the fit range.

¹Note that no background is simulated, but the fiducial contribution is expected to be of $\mathcal{O}(1\%)$.

9.4 Numerical results for top-quark mass uncertainties

1867 The linear dependence of the functional parameters on the top-quark mass is then
 1868 fixed, and the mass itself is left as the only free parameter. The linear dependence of the
 1869 different functional parameters on the input top-quark mass is shown in Appendix C.

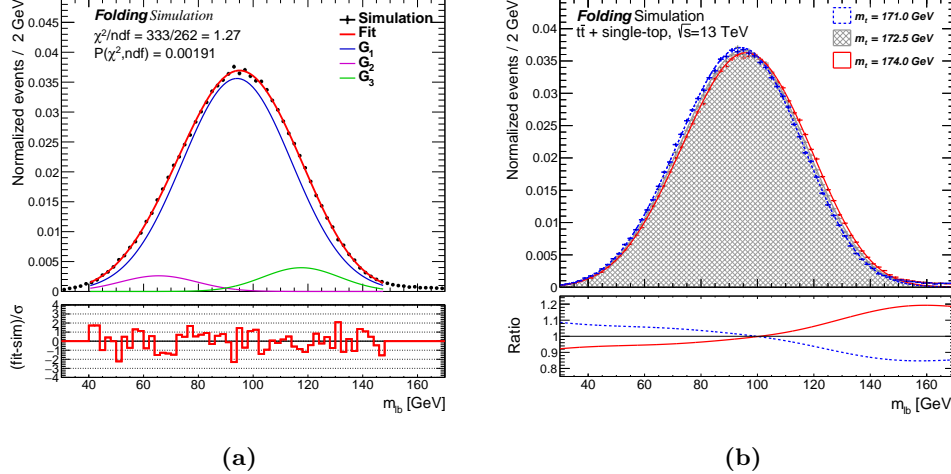


Figure 9.10: (a) The m_{tb} distribution and the three Gaussian fit functions are shown for $m_t = 172.5$ GeV. (b) The template histograms and the fit functions are shown for $m_t = 171$ GeV, $m_t = 172.5$ GeV and $m_t = 174$ GeV.

1870 9.4 Numerical results for top-quark mass uncertainties

1871 Similarly to Chapter 7, the calibration functions determined from the $W^+W^-b\bar{b}$ are used
 1872 to fit pseudo-data drawn from the $t\bar{t}$ +single-top samples with 1000 pseudo-experiments
 1873 (PE). The template fit to pseudo-data gives an offset in the extracted top-quark mass,
 1874 $\Delta m_t = m_t^{\text{out}} - m_t^{\text{in}}$. This offset can then be assigned as a systematic uncertainty com-
 1875 ponent, quantifying the difference between the incomplete $t\bar{t}$ +single-top and the full
 1876 $W^+W^-b\bar{b}$ prediction.

1877 Fig. 9.11 displays the result of the fitting procedure. The offsets between the extracted
 1878 top-quark mass and the input MC mass are given for each mass point. Again, the use
 1879 of $t\bar{t}$ calibration functions yields an offset close to zero (in red), serving as a cross-check
 1880 that no bias exists in the fitting procedure. The result from using $W^+W^-b\bar{b}$ calibration
 1881 functions (in red) yields an average value for $\Delta m_t = -0.330 \pm 0.022$ GeV. The second
 1882 uncertainty is the statistical uncertainty on the systematic offset Δm_t .

1883 Other systematic uncertainties are computed analogously to the scale variations in
 1884 Chapter 7. Instead of producing as many calibration functions as systematic samples,
 1885 the same calibration function generated from $t\bar{t}$ +single-top is fitted to pseudo-data drawn
 1886 from the systematic variation samples. The exact definition of the variations is presented
 1887 in Ref. [247].

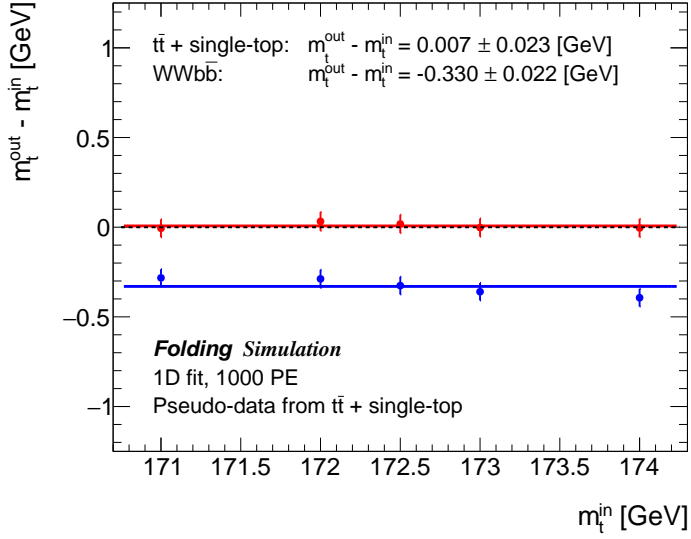


Figure 9.11: A comparison similar to the ones performed in Chapter 7 is presented at detector level. The folded $W^+W^-b\bar{b}$ prediction is used to fit pseudo-data drawn from $t\bar{t}+\text{single-top}$ samples. This introduces an average offset of $\Delta m_t = -0.330 \pm 0.022$ GeV in the top-quark mass extraction.

1888 The matrix-element MC generator is currently the dominating source of systematic
 1889 uncertainty, with $\Delta m_t = 1.28$ GeV. The signal MC generator uncertainty is estimated in
 1890 a 2-point variation, by comparing the MC@NLO [119] matrix-element generator parton-
 1891 showered with PYTHIA8 to the central prediction. Finally, the inherent uncertainty
 1892 accompanying the folding procedure was estimated by the following provision: all the
 1893 $W^+W^-b\bar{b}$ samples were folded with migration matrices from the most extreme mass
 1894 points, $m_t = 171$ GeV and $m_t = 174$ GeV. The resulting offset in the extracted top-
 1895 quark mass is negligibly small.

1896 Although the uncertainty in comparing $W^+W^-b\bar{b}$ to $t\bar{t}+\text{single-top}$ predictions is still
 1897 largely inferior to the other dominant systematics, two points can be emphasized. First,
 1898 there is a built-in uncertainty in describing the $t\bar{t}$ and single-top Wt contribution sepa-
 1899 rately. One has to account for the interference between the $t\bar{t}$ and single-top Wt sam-
 1900 ples: usually, this is estimated by comparing predictions using diagram removal (DR)
 1901 and diagram subtraction (DS) [204]. By describing the full $W^+W^-b\bar{b}$ final-state, this
 1902 uncertainty naturally vanishes. Second, as mentioned above, the W - b -jet system (and
 1903 by extension the $m_{\ell b}$ distribution) is sensitive to the details of the parton-shower algo-
 1904 rithm. It would be interesting to estimate those uncertainties at detector level also for
 1905 the $W^+W^-b\bar{b}$ final-state. There is indeed a fine interplay between initial-state radiation
 1906 populating the tail of the $m_{\ell b}$ distribution, and the sensitivity of the kinematic edge to
 1907 final-state radiation. Further studies of the different matching prescriptions and vetoing
 1908 possibilities [245] in `bb4l` could help better understanding these parton-shower related
 1909 uncertainties.

9.4 Numerical results for top-quark mass uncertainties

| Uncertainty | $ \Delta m_t $ |
|--|-----------------|
| Theory | |
| Non-factorizing / non doubly-resonant | 0.33 GeV |
| Signal MC Generator | 1.28 GeV |
| Hadronization | 0.71 GeV |
| ISR/FSR | 0.16 GeV |
| Experiment | |
| Jet energy scale (light jets) | 0.72 GeV |
| <i>b</i> -jet energy scale | 0.43 GeV |
| Jet energy resolution | 0.42 GeV |
| <i>b</i> -tagging | 0.13 GeV |

Table 9.1: A partial list of systematic uncertainties is given for the top-quark mass extraction. It is to be compared to the offset in the top-quark mass given by using the calibration from $W^+W^-b\bar{b}$ to fit the $t\bar{t}$ +single-top pseudo-data.

1910

Part III

1911

Top-Quark Mass Effects in Higgs Pair Production

1912

1913 10 Top-mass dependence in Higgs pair production at NLO

1915 The top-quark mass has substantial effects in the Higgs sector. After the discovery of
 1916 the Higgs boson by both ATLAS [248] and CMS [249] experiments in 2012, which was
 1917 the crowning completion of one of LHC's foremost goals, the experimental community
 1918 set to measure its properties to further test if it was compatible with the SM predicted
 1919 Higgs boson. As of today, some of the Higgs boson properties are very well-measured (as
 1920 for the example of its mass, spin, or couplings to heavier fermions and gauge bosons).
 1921 Still, because of lower branching ratios and irreducible backgrounds, the measurement
 1922 of the Higgs boson couplings to light fermions, as well as the Higgs self-coupling, is
 1923 still accompanied by large uncertainties of the order of $\mathcal{O}(100\%)$ in the case of the
 1924 trilinear self-coupling. This leaves room for New Physics to appear. The latest ATLAS
 1925 constraint on the Higgs boson self-coupling, in ratio to its predicted value from the
 1926 SM $c_{hhh} = \lambda/\lambda_{SM}$, is $-5.0 \leq c_{hhh} \leq 12.1$ [16] at 95% confidence level (CL), from a
 1927 combination of three searches for the hh final-states $b\bar{b}b\bar{b}$, $b\bar{b}\tau^+\tau^-$ and $b\bar{b}\gamma\gamma$. These limits
 1928 assume the other Higgs couplings to be SM-like. In the future, with the accumulation of
 1929 data at high-luminosity (HL)-LHC, the experimental bounds are expected to improve,
 1930 and the measurement of differential distributions (with a small number of total events) is
 1931 even conceivable. In the rest of this chapter, the theoretical standpoint of hh production
 1932 is reviewed, and the way New Physics can strongly affect this process is presented in the
 1933 framework of a non-linear EFT.

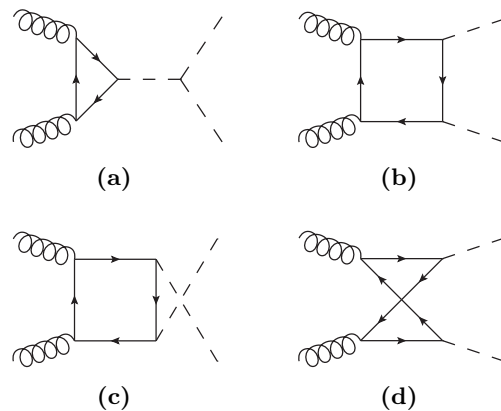


Figure 10.1: (a-d) LO Feynman diagrams for hh production by gluon-fusion.

10.1 Theoretical descriptions of hh production

At the LHC, Higgs bosons (and in particular Higgs boson pairs, which are considered in the next chapters) are produced mainly via a top-quark loop. Fig. 10.1 displays the LO Feynman diagrams for di-Higgs production in gluon-fusion: diagrams that contain the Higgs self-coupling λ are called *triangle-like* (as in Fig. 10.1a), and diagrams that do not *box-like* (as in Figs 10.1b–10.1d).¹ Because $gg \rightarrow hh$ production is loop-induced, NLO corrections start at two-loop order already and pose a challenge to compute. The matrix-element for $g(p_1, \mu, a) + g(p_2, \nu, b) \rightarrow h(p_3) + h(p_4)$ production decomposes into two form factors (with p_i the 4-momenta, Greek letters for the Lorentz indices and roman letters for the color indices):

$$\mathcal{M}_{ab}^{\mu\nu} = \frac{\alpha_s}{8\pi v^2} \delta_{ab} \epsilon_\mu \epsilon_\nu (F_1(\hat{s}, \hat{t}, m_h^2, m_t^2, d) T_1^{\mu\nu} + F_2(\hat{s}, \hat{t}, m_h^2, m_t^2, d) T_2^{\mu\nu}), \quad (10.1)$$

where the Lorentz structure is contained in the tensors T_1 , T_2 and the functions F_1 , F_2 depend on four physical scales altogether (two kinematic invariants and both particle mass scales, as well as on the analytically-continued dimension d). Finally, the first form factor can be further split into a contribution stemming only from triangle-like diagrams, respectively only box-like diagrams:

$$F_1 = F_\Delta + F_\square, \quad (10.2)$$

and the box diagrams contribute to both F_\square and F_2 . Historically, the LO one-loop total cross-section has been known analytically for a long time [250], and the triangular form factor given in Eq. (10.2), for $\tau = 4m_t^2/\hat{s}$, takes the form

$$F_\Delta = \frac{6m_h^2 \lambda \hat{s}}{\hat{s} - m_h^2} \tau (1 + (1 - \tau)f(\tau)), \quad (10.3)$$

$$f(\tau) := \begin{cases} \arcsin^2(\frac{1}{\sqrt{\tau}}) & \tau \geq 1 \\ -\frac{1}{4} \left(\log\left(\frac{1+\sqrt{1-\tau}}{1-\sqrt{1-\tau}}\right) - i\pi \right)^2 & \tau < 1. \end{cases}$$

The triangle diagrams can be reduced to single Higgs production and subsequent attachment of the triple Higgs vertex, where all the NLO integrals (massive two-loop up to three-point) have been computed with the full top-mass dependence [251–253]. The two-loop massive four-point integrals to $gg \rightarrow hh$ are known analytically only partly [254–256]. Some computations exist with expansions in given kinematic limits (large top-quark mass [254], top-quark threshold [257], small Higgs transverse momentum [258], and high-energy expansion [259, 260]). In the following, only the heavy-top limit $m_t \rightarrow \infty$ is considered, without any expansion in $1/m_t^{2n}$, as well as several approximations that include part of the full-theory result at NLO QCD.

¹At two-loop level, some diagrams do not contain the coupling λ but have triangular topologies, see e.g. the last diagram in Fig. 10.4.

1961 10.1.1 Approximations in the heavy-top limit ($m_t \rightarrow \infty$)

1962 To circumvent the direct computation of the difficult NLO QCD corrections to $gg \rightarrow hh$,
 1963 one neat approach that was applied successfully in Higgs production (as well as in a
 1964 whole collection of other processes) is to collapse one top-quark loop to an effective
 1965 coupling between gluons and Higgs bosons within a so-called Effective Field Theory
 1966 (EFT). This is the so-called heavy-top limit (HTL). EFTs are usually employed to
 1967 describe physics entering at a higher-scale than the typical scales of the process at
 1968 hand. In an agnostic approach, one assumes nothing about new particles and instead
 1969 computes effective couplings between known particles, that are only indirectly affected
 1970 by more massive particles. Their exact degrees of freedom are thus integrated out of
 1971 the calculation. This was for example the basic framework of the Fermi theory before
 1972 W and Z bosons were discovered, where one assumes a 4-particle interaction vertex
 1973 between fermions coupling with strength G_F . In the case of di-Higgs production, the
 1974 top-quark degrees of freedom are integrated out and an effective coupling between gluons
 1975 and Higgs bosons is introduced. There exist different consistent formulations of a theory
 1976 with effective coupling vertices between gluons and Higgs bosons: usually, one introduces
 1977 higher-dimension contact operators into the SM Lagrangian, with an EFT expansion in
 1978 the New Physics scale $1/\Lambda$.² Another EFT formulation will be introduced in Section 10.2.

1979 In the next Sections, comparisons are shown between predictions for the full theory
 1980 at QCD NLO and various approximations based on the heavy-top limit for variations of
 1981 the Higgs couplings.³ In order of increasing accuracy, these are:

- 1982 • **Pure HTL:** all top-quark loops are shrunk to an effective vertex between gluons
 1983 and Higgs bosons. At LO, the form factors given in Eqs. (10.1), (10.3), for $\tau \rightarrow \infty$,
 1984 reduce to

$$F_{\Delta} \rightarrow \frac{3m_h^2 \lambda}{\hat{s} - m_h^2} \left(\frac{4}{3} \hat{s} \right) , \quad (10.5)$$

$$F_{\square} \rightarrow -\frac{4}{3} \hat{s} , \quad (10.6)$$

$$F_2 \rightarrow 0 . \quad (10.7)$$

1985 At NLO, they are at most given by one-loop diagrams.

- 1986 • **Born-improved HTL:** the virtual and real contributions are calculated within
 1987 HTL, but reweighted on an event-by-event basis with the ratio of the full-theory
 1988 Born to the HTL Born contribution,

$$d\sigma_{V,R}^{B,i} = d\sigma_{V,R}^{\text{HTL}} \frac{d\sigma_B^{\text{FT}}}{d\sigma_B^{\text{HTL}}} . \quad (10.8)$$

²Mostly, nowadays, analyses consider only dimension-6 operators, because the only dimension-5 operator violates lepton number conservation.

³In the SM case, there are already important differences between the considered approximations [261].

- 1989 • **FT_{approx}** : the same prescription as given in Eq. (10.8) is applied for the virtual
 1990 contribution, but the real-emission matrix-element is computed in the full theory
 1991 (these are at most one-loop diagrams).
- 1992 • **Full theory:** the real and two-loop virtual contributions are computed with full
 1993 m_t -dependence.

1994 **10.1.2 Two-loop contribution in the SM**

1995 The first full computation of NLO QCD corrections to $gg \rightarrow hh$ production in the SM
 1996 was presented in Ref. [261]. All BSM results shown in Sections 10.3 and 11.2 are based
 1997 on two-loop amplitudes calculated numerically for the SM.

1998 As a brief description of the calculation, the two-loop contribution to the SM amplitude
 1999 was generated by an extended version of GoSAM called GoSAM-2LOOP. The reduction
 2000 to master integrals was operated with REDUZE 2 [262] as far as possible, and the integral
 2001 evaluation performed with the help of sector decomposition in SECDEC 3 [263–265]. In
 2002 particular, the integration itself was implemented within a rank-one lattice quasi-Monte-
 2003 Carlo rule (QMC) that is described in more detail in Refs. [266, 267]. The Higgs and
 2004 the top-quark mass are fixed, so that the integrals depend only on the two kinematic
 2005 invariants \hat{s} and \hat{t} .⁴

2006 Examples of the SM two-loop Feynman diagrams are given in the first, third and last
 2007 rows of Fig. 10.4. The amplitude was calculated for a pre-sampled set of 5372 phase-space
 2008 points in (\hat{s}, \hat{t}) at 14 TeV and 1343 points at 100 TeV. IR subtraction was performed
 2009 within the CS dipole formalism, where for the gg channel, the insertion operator **I** is
 2010 given by

$$\mathbf{I}_{gg} = \frac{\alpha_s}{2\pi} \frac{(4\pi)^\epsilon}{\Gamma(1-\epsilon)} \left(\frac{\mu_R^2}{2p_1 \cdot p_2} \right)^\epsilon \cdot 2 \left(\frac{C_A}{\epsilon^2} + \frac{\beta_0}{2\epsilon} - C_A \frac{\pi^2}{3} + \frac{\beta_0}{2} + K_g \right), \quad (10.9)$$

2011 with $\beta_0 = \frac{11}{6}C_A - \frac{2}{3}T_R N_f$ and $K_g = \left(\frac{67}{18} - \frac{\pi^2}{6} \right) C_A - \frac{10}{9}T_R N_f$. As a side note, the IR
 2012 singular pattern is the same between the SM and the BSM case presented below. When
 2013 inserting the CS operator into the Born term, see Eq. (4.8), the poles from the virtual
 2014 contribution should cancel. To get the correct finite terms, thus, the Born has to be
 2015 expanded up to $\mathcal{O}(\epsilon^2)$. The explicit cancellation of poles in ϵ is checked numerically.

2016 **10.2 The Electroweak Chiral Lagrangian**

2017 Regarding variations of the Higgs couplings, one class of extensions of the SM called the
 2018 Electroweak Chiral Lagrangian (EWChL) [269, 270] is considered, which is a non-linear
 2019 realization of an EFT. The EWChL, to leading-order, is given as

⁴The top-quark mass is renormalized on-shell. Dependence of the numerical results on the top-mass scheme are investigated in Ref. [268].

$$\begin{aligned}
 \mathcal{L}_2 = & -\frac{1}{2}\langle G_{\mu\nu}G^{\mu\nu}\rangle - \frac{1}{2}\langle W_{\mu\nu}W^{\mu\nu}\rangle - \frac{1}{4}B_{\mu\nu}B^{\mu\nu} + \sum_{\psi=q_L,l_L,u_R,d_R,e_R} \bar{\psi}iD\psi \\
 & + \frac{v^2}{4} \langle D_\mu U^\dagger D^\mu U \rangle (1 + F_U(h)) + \frac{1}{2}\partial_\mu h \partial^\mu h - V(h) \\
 & - v \left[\bar{q}_L \left(Y_u + \sum_{n=1}^{\infty} Y_u^{(n)} \left(\frac{h}{v} \right)^n \right) UP_+ q_R + \bar{q}_L \left(Y_d + \sum_{n=1}^{\infty} Y_d^{(n)} \left(\frac{h}{v} \right)^n \right) UP_- q_R \right. \\
 & \left. + \bar{l}_L \left(Y_e + \sum_{n=1}^{\infty} Y_e^{(n)} \left(\frac{h}{v} \right)^n \right) UP_- l_R + \text{h.c.} \right], \tag{10.10}
 \end{aligned}$$

2020 where $U = \exp(2i\phi^a T^a/v)$ is the Goldstone matrix and contains the electroweak
 2021 Goldstone fields ϕ^a , and T^a are the generators of $SU(2)_L$. Here, $P_\pm = 1/2 \pm T_3$ are the
 2022 chiral projection operators, and the Higgs sector is characterized by an order-by-order
 2023 expansion in the Higgs EW singlet h , given by the functions

$$F_U(h) = \sum_{n=1}^{\infty} f_{U,n} \left(\frac{h}{v} \right)^n, \quad V(h) = v^4 \sum_{n=2}^{\infty} f_{V,n} \left(\frac{h}{v} \right)^n. \tag{10.11}$$

2024 The coefficients $f_{U,n}$, $V_{U,n}$ and $Y_{u,d,e}^{(n)}$ are in principle free parameters and can be of
 2025 $\mathcal{O}(1)$. The SM case is retrieved when

$$f_{U,1} = 2, \quad f_{U,2} = 1, \quad f_{V,2} = f_{V,3} = \frac{m_h^2}{2v^2}, \quad f_{V,4} = \frac{m_h^2}{8v^2}, \quad Y_f^{(1)} = Y_f. \tag{10.12}$$

2026 Now, this Lagrangian is structured not in terms of canonical dimensions for the quantum
 2027 fields and couplings, but rather in terms of *chiral* dimensions (as in the case of the
 2028 chiral EFT of pions in QCD). The chiral dimension assigned to fields, derivatives and
 2029 couplings are

$$d_\chi(A_\mu, \varphi, h) = 0, \quad d_\chi(\partial, \bar{\psi}\psi, g, y) = 1, \tag{10.13}$$

2030 with A_μ being any gauge field, g representing any of the SM gauge couplings, and y
 2031 any weak coupling (like the Yukawa couplings). The ordering in the chiral dimension d_χ
 2032 is equivalent to counting the number of loops L , $d_\chi = 2L + 2$. In summary, the NLO
 2033 (in α_s) QCD corrections to hh production stem from one-loop diagrams in the leading
 2034 (in d_χ) EWChL \mathcal{L}_2 and from tree diagrams in the next-to leading part \mathcal{L}_4 . All of these
 2035 contributions are of chiral dimension $d_\chi = 4$. Then, in the Higgs sector, the effective
 2036 Lagrangian reduces to

$$\mathcal{L} \supset \underbrace{-m_t \left(c_t \frac{h}{v} + c_{tt} \frac{h^2}{v^2} \right) \bar{t}t}_{\mathcal{L}_2} - c_{hhh} \frac{m_h^2}{2v} h^3 + \underbrace{\frac{\alpha_s}{8\pi} \left(c_{ggh} \frac{h}{v} + c_{gggh} \frac{h^2}{v^2} \right) G_{\mu\nu}^a G^{a,\mu\nu}}_{\mathcal{L}_4}. \tag{10.14}$$

2037 The EWChL introduces five anomalous couplings to the SM and the corresponding
 2038 LO Feynman diagrams are given in Fig. 10.2.

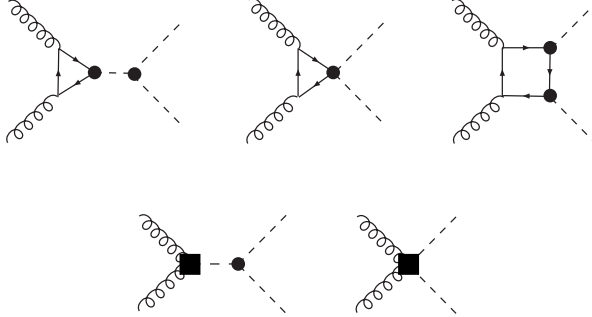


Figure 10.2: LO diagrams for the various terms from the EWChL Lagrangian. Both vertices from \mathcal{L}_2 (black dots) and local contact terms from \mathcal{L}_4 (black squares) contribute.

2039 Diagrams that are of higher chiral dimension (or do not belong to $\mathcal{O}(\alpha_s^4 \alpha^2)$) are sys-
 2040 tematically neglected, like the ones given in Fig. 10.3. The full virtual amplitude is then
 2041 given by two-loop contributions (Fig. 10.4), one-loop diagrams that contain one effective
 2042 coupling from \mathcal{L}_4 (Fig. 10.5), and one tree-diagram containing exactly two effective
 2043 vertices between gluons and Higgs bosons (Fig. 10.6). Note that all two-loop diagrams
 2044 with non-SM values of the Higgs couplings can be retrieved from their SM counterparts
 2045 by rescaling at amplitude-level:

$$\begin{aligned} \mathcal{M}_V(\Delta_1) &\rightarrow \mathcal{M}_V^{\text{SM}}(\Delta_1) \cdot c_t c_{hh} && (1^{\text{st}} \text{ row in Fig. 10.4}) \\ \mathcal{M}_V(\Delta_2) &\rightarrow \mathcal{M}_V^{\text{SM}}(\Delta_1) \cdot \frac{\hat{s} - m_h^2}{3m_h^2} c_{tt} && (2^{\text{nd}} \text{ row in Fig. 10.4}) \\ \mathcal{M}_V(\square) &\rightarrow \mathcal{M}_V^{\text{SM}}(\square) \cdot c_t^2 && (3^{\text{rd}}, 4^{\text{th}} \text{ rows in Fig. 10.4}), \end{aligned}$$

2046 where $\mathcal{M}_V(\Delta_1)$ are the triangle diagrams from the 1st row of Fig. 10.4, $\mathcal{M}_V(\Delta_2)$ from
 2047 the 2nd row (given by the corresponding diagrams from the 1st row where the s -channel
 2048 Higgs propagator gets pinched), and $\mathcal{M}_V(\square)$ are the box-diagrams from the 3rd row.
 2049 Accordingly, the amplitudes computed in Ref. [261] are used for the pre-sampled set of
 2050 phase-space points and are simply rescaled.

2051 Finally, real-emission diagrams contain five-point one-loop diagrams with SM-like
 2052 topologies, as well as tree diagrams carrying one effective coupling between gluons and
 2053 Higgs bosons from \mathcal{L}_4 (Fig. 10.7).

2054 10.3 Total cross-sections for BSM benchmark points

2055 All results for total and differential cross-sections presented in this chapter can be found
 2056 in Ref. [271]. To summarize, all HTL contributions were computed analytically with

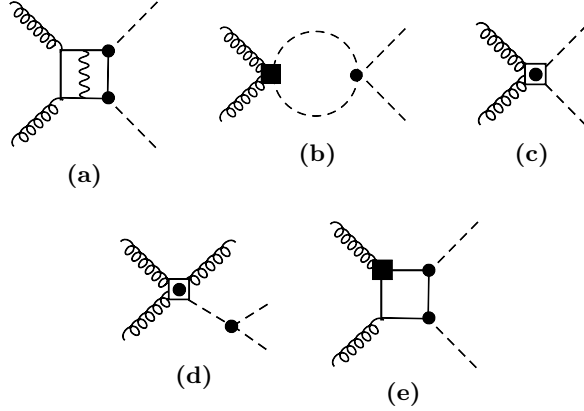


Figure 10.3: (a-d) Diagrams that do not scale like α_s^4 are consistently neglected. (e) The chromomagnetic operator $Q_{ttG} = c_t g_s \bar{t}_L \sigma_{\mu\nu} G^{\mu\nu} t_R$ only contributes at two-loop order at least ($d_\chi = 6$).

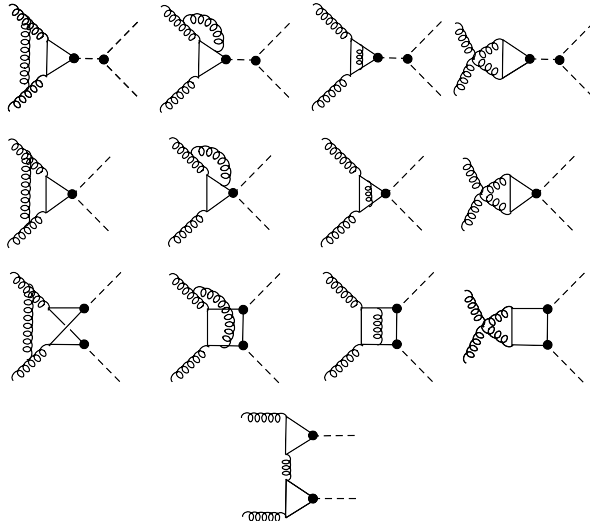


Figure 10.4: Two-loop diagrams generated by the EWChL at NLO QCD. They can all be computed by rescaling from the corresponding SM diagrams (see text).

2057 FORM. In FT_{approx} and in the full theory predictions, the real radiation is provided by
 2058 GoSAM. A Universal FeynRules Output (UFO) model [272] for the EWChL was pro-
 2059 duced with FEYNRULES [273, 274] and interfaced to GoSAM to produce all tree and
 2060 one-loop diagrams. The various parts are assembled into a C++ code which performs the
 2061 phase-space integration with VEGAS as interfaced through the CUBA package.

2062 The results shown below are produced at a center-of-mass energy of $\sqrt{s} = 14$ TeV,
 2063 where the PDF4LHC15_nlo_100_pdfs is used and interfaced through LHAPDF. The cor-
 2064 responding value of $\alpha_s(\mu)$, with $\alpha_s(m_Z) = 0.118$, is consistently employed throughout

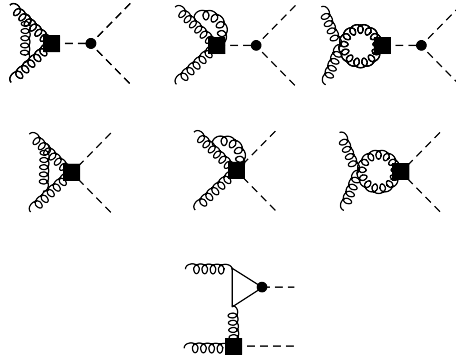


Figure 10.5: One-loop virtual contributions at NLO QCD: these diagrams contain exactly one effective contact coupling from \mathcal{L}_4 .

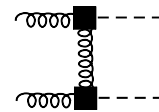


Figure 10.6: Tree diagram at NLO QCD containing exactly two effective couplings from \mathcal{L}_4 .

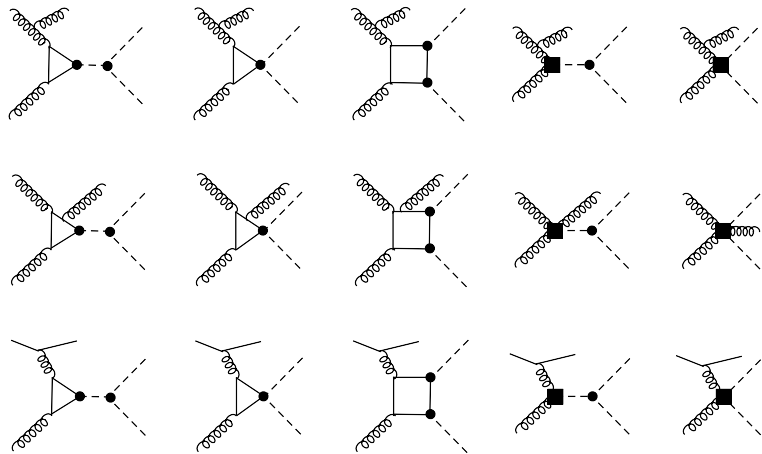


Figure 10.7: Real-emission contributions that are either one-loop diagrams without effective contact coupling, or tree diagrams with exactly one such coupling.

2065 the calculation. The Higgs boson and top-quark masses are set to $m_h = 125$ GeV and
 2066 $m_t = 173$ GeV, as the two-loop amplitudes were computed with these values, and both
 2067 their widths are set to zero. Finally, the renormalization and factorization scales are set
 2068 to $\mu_R = \mu_F = \mu_0 = m_{hh}/2$ and uncertainties are estimated according to 7-point scale
 2069 variations $\mu_{R,F} = c_{R,F}\mu_0$ with $(c_R, c_F) \in \{0.5, 1, 2\} \times \{0.5, 1, 2\} \setminus \{(0.5, 2), (2, 0.5)\}$.

To characterize the 5-dimensional BSM space, the set of Higgs coupling variations used in the following part is based mostly on the definition of benchmark (BM) points presented in Ref. [275]. There, the BSM space is scanned for different values of the Higgs anomalous couplings and clustered into blocks that manifest a similar behavior in differential distributions. The set of BM points is defined in Table 10.1, and the total cross-sections, K -factors and uncertainties are shown in Table 10.2.

First, looking at Table 10.2, the NLO cross-sections can become quite sizeable depending on the BM point considered (of $\mathcal{O}(100)$ times the SM cross-section), and some are even excluded considering recent bounds on hh production from experimental limits. With the ATLAS current limit [16] on the observed non-resonant hh production cross-section of 220 fb at 95% CL, several BM points would indeed be excluded already. Second, the full m_t -dependent NLO corrections are important, with K -factors between 1.66 and 2.34, and are accompanied by large scale uncertainties of $\mathcal{O}(15 - 20\%)$ (similarly to single Higgs production at NLO QCD [276, 277]). Finally, the K -factors themselves depend substantially on the considered BSM point. This is also illustrated in Fig. 10.8, where only one parameter is varied at a time. In fact, studies realized in the heavy-top limit suggest the K -factors's dependence on the different couplings to be quite small [278] (of $\mathcal{O}(5\%)$ or less for all considered coupling variations). Once full top-quark loop corrections are taken into account, though, the K -factors for c_{hhh} , c_{tt} and c_t vary by more than 30% (55% for c_{tt}). Later on, in Section 10.4, it will be shown that this feature is especially prominent around the top-quark pair $2m_t$ threshold when considering differential distributions.

| BM | c_{hhh} | c_t | c_{tt} | c_{ggh} | c_{gggh} |
|----|-----------|-------|----------|------------------|-----------------|
| 1 | 7.5 | 1.0 | -1.0 | 0.0 | 0.0 |
| 2 | 1.0 | 1.0 | 0.5 | $-\frac{1.6}{3}$ | -0.2 |
| 3 | 1.0 | 1.0 | -1.5 | 0.0 | $\frac{0.8}{3}$ |
| 4 | -3.5 | 1.5 | -3.0 | 0.0 | 0.0 |
| 5 | 1.0 | 1.0 | 0.0 | $\frac{1.6}{3}$ | $\frac{1.0}{3}$ |
| 6 | 2.4 | 1.0 | 0.0 | $\frac{0.4}{3}$ | $\frac{0.2}{3}$ |
| 7 | 5.0 | 1.0 | 0.0 | $\frac{0.4}{3}$ | $\frac{0.2}{3}$ |
| 8a | 1.0 | 1.0 | 0.5 | $\frac{0.8}{3}$ | 0.0 |
| 9 | 1.0 | 1.0 | 1.0 | -0.4 | -0.2 |
| 10 | 10.0 | 1.5 | -1.0 | 0.0 | 0.0 |
| 11 | 2.4 | 1.0 | 0.0 | $\frac{2.0}{3}$ | $\frac{1.0}{3}$ |
| 12 | 15.0 | 1.0 | 1.0 | 0.0 | 0.0 |
| SM | 1.0 | 1.0 | 0.0 | 0.0 | 0.0 |

Table 10.1: Different BM points in the 5-dimensional Higgs coupling space are analyzed below at inclusive, respectively differential cross-section level.

Furthermore, the ratio of the cross-section to the SM can be parametrized [275, 279] in terms of the anomalous Higgs couplings: the cross-section ratio is expressed as a polynomial whose coefficients correspond to all squared/interference terms from the various diagrams. At LO, this gives 15 possible combinations:

| BM | $\sigma_{\text{NLO}} [\text{fb}]$ | K-factor | scale uncertainties [%] | stat. uncertainties [%] | $\frac{\sigma_{\text{NLO}}}{\sigma_{\text{NLO,SM}}}$ |
|----------|-----------------------------------|----------|-------------------------|-------------------------|--|
| B_1 | 194.89 | 1.88 | $^{+19}_{-15}$ | 1.6 | 5.915 |
| B_2 | 14.55 | 1.88 | $^{+5}_{-13}$ | 0.56 | 0.4416 |
| B_3 | 1047.37 | 1.98 | $^{+21}_{-16}$ | 0.15 | 31.79 |
| B_4 | 8922.75 | 1.98 | $^{+19}_{-16}$ | 0.39 | 270.8 |
| B_5 | 59.325 | 1.83 | $^{+4}_{-15}$ | 0.36 | 1.801 |
| B_6 | 24.69 | 1.89 | $^{+2}_{-11}$ | 2.1 | 0.7495 |
| B_7 | 169.41 | 2.07 | $^{+9}_{-12}$ | 2.2 | 5.142 |
| B_{8a} | 41.70 | 2.34 | $^{+6}_{-9}$ | 0.63 | 1.266 |
| B_9 | 146.00 | 2.30 | $^{+22}_{-16}$ | 0.31 | 4.431 |
| B_{10} | 575.86 | 2.00 | $^{+17}_{-14}$ | 3.2 | 17.48 |
| B_{11} | 174.70 | 1.92 | $^{+24}_{-8}$ | 1.2 | 5.303 |
| B_{12} | 3618.53 | 2.07 | $^{+16}_{-15}$ | 1.2 | 109.83 |
| SM | 32.95 | 1.66 | $^{+14}_{-13}$ | 0.1 | 1 |

Table 10.2: The total cross-sections for the considered BSM BM points, with their respective K-factors, scale and (MC) statistical uncertainties, as well as the ratio to the SM cross-section $\sigma_{\text{NLO,SM}} = 32.95 \text{ fb}$.

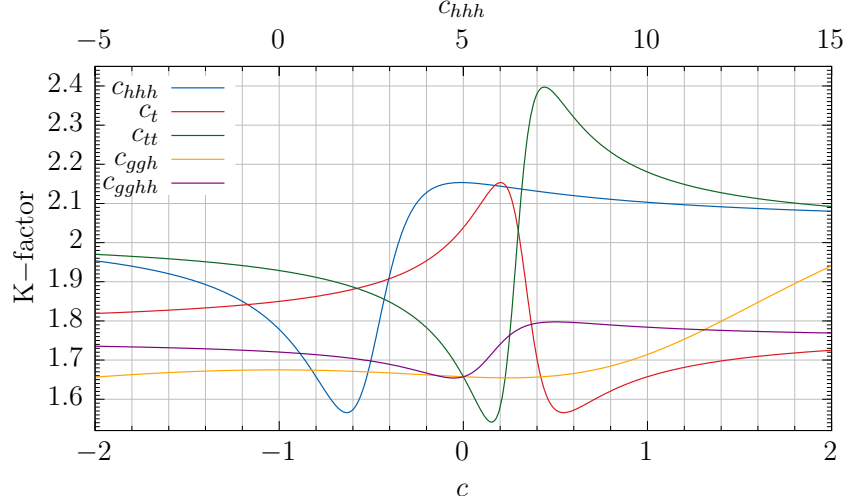


Figure 10.8: The K -factor is shown as a function of c_{hhh} on the top axis, and of the other couplings on the lower axis.

$$\begin{aligned}
 \sigma/\sigma_{SM} = & A_1 c_t^4 + A_2 c_{tt}^2 + A_3 c_t^2 c_{hhh}^2 + A_4 c_{ggh}^2 c_{hhh}^2 + A_5 c_{gghh}^2 + A_6 c_{tt} c_t^2 \\
 & + A_7 c_t^3 c_{hhh} + A_8 c_{tt} c_t c_{hhh} + A_9 c_{tt} c_{ggh} c_{hhh} + A_{10} c_{tt} c_{gghh} \\
 & + A_{11} c_t^2 c_{ggh} c_{hhh} + A_{12} c_t^2 c_{gghh} + A_{13} c_t c_{hhh}^2 c_{ggh} \\
 & + A_{14} c_t c_{hhh} c_{gghh} + A_{15} c_{ggh} c_{hhh} c_{gghh}. \tag{10.15}
 \end{aligned}$$

10.3 Total cross-sections for BSM benchmark points

2096 The coefficients A_1 to A_{15} are corrected at NLO, and 8 new coefficients appear from
 2097 genuine NLO diagrams:

$$\Delta\sigma/\sigma_{SM} = A_{16} c_t^3 c_{ggh} + A_{17} c_t c_{tt} c_{ggh} + A_{18} c_t c_{ggh}^2 c_{hhh} + A_{19} c_t c_{ggh} c_{gghh} \\ + A_{20} c_t^2 c_{ggh}^2 + A_{21} c_{tt} c_{ggh}^2 + A_{22} c_{ggh}^3 c_{hhh} + A_{23} c_{ggh}^2 c_{gghh}. \quad (10.16)$$

2098 These coefficients can be determined by dedicated event generation runs for a set of
 2099 the 5-dimensional parameter space, and by projecting out a system of equations, or
 2100 by a simple fit of the polynomial in Eq. (10.16) to the calculated set of cross-sections.
 2101 The results for the NLO coefficients A_1 to A_{23} at $\sqrt{s} = 14$ TeV are given in Table D.1.
 2102 Interestingly, once the cross-section coefficients are computed, the parametrization given
 2103 in Eqs. (10.15), (10.16) yields the cross-section for any point of the BSM space. This
 2104 for example allows to produce iso-contour plots where curves represent configurations in
 2105 the BSM space which lead to the same cross-section, see Figs. 10.9, 10.10, 10.11. In the
 2106 latter, two BSM couplings are simultaneously varied (within bounds still approximately
 2107 allowed by experimental measurements), and iso-curves for the ratio to the SM cross-
 2108 section at LO (red), respectively NLO (black), are shown.

2109 The cross-section iso-curves are given for c_{tt} against c_{gghh} in Fig. 10.9a, respectively
 2110 against c_{ggh} in Fig. 10.9b. In both cases, the cross-section varies sizeably with respect
 2111 to the SM value, and is generally more sensitive to changes in c_{tt} . The NLO corrections
 2112 to hh introduce important shifts in the iso-curves (reflected by the large K -factors).
 2113 Fig. 10.10 shows iso-contours for variations of c_{hhh} versus c_{ggh} , respectively c_{tt} . Again,
 2114 the curves are much more dependent on c_{hhh} than on the Higgs contact coupling, as
 2115 exhibited by Fig. 10.10a. In comparison, the dependence of the cross-section on c_{hhh}
 2116 and c_{tt} is large, with ratios to the SM cross-section going up to a factor $\mathcal{O}(\sim 100)$.
 2117 Finally, iso-contours are also plotted for simultaneous variations of c_t versus c_{tt} and c_{hhh}
 2118 in Fig. 10.11.

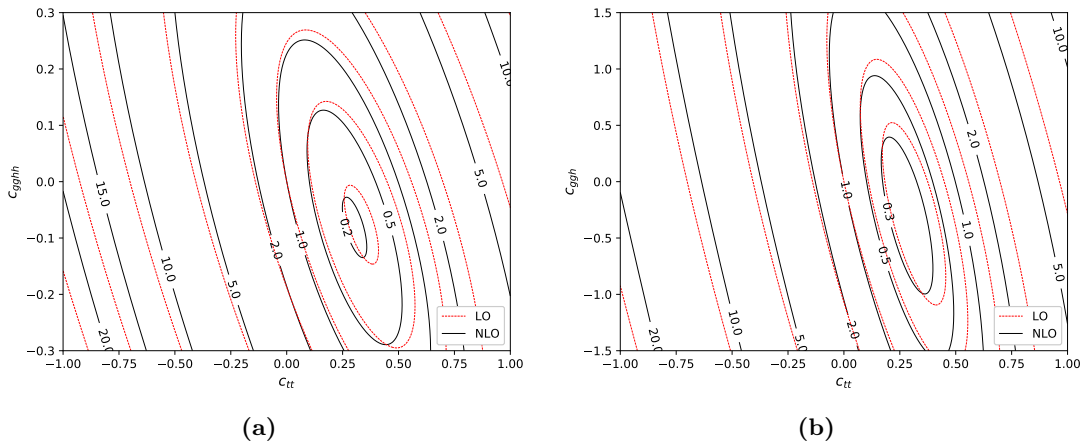


Figure 10.9: Iso-contours of σ/σ_{SM} : (a) c_{gghh} and (b) c_{ggh} versus c_{tt} .

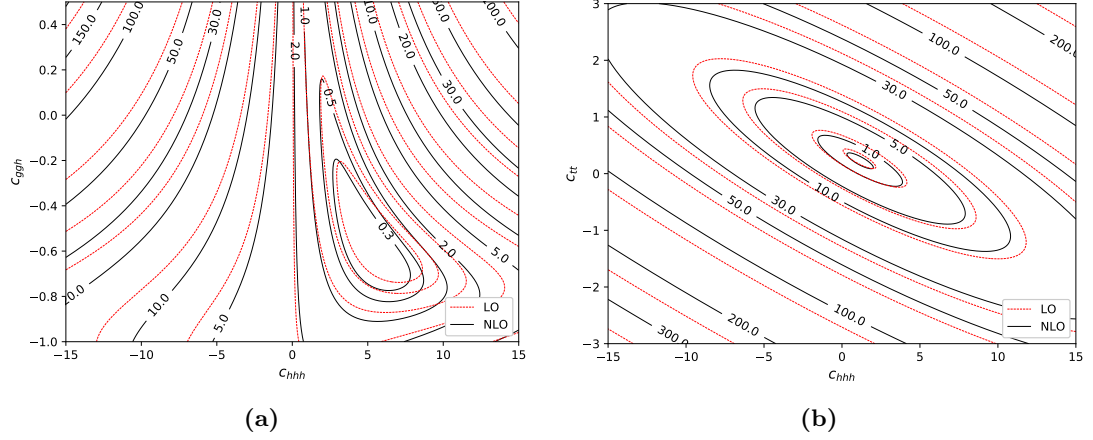


Figure 10.10: Iso-contours of σ/σ_{SM} : (a) c_{gg} and (b) c_{tt} versus c_{hh} .

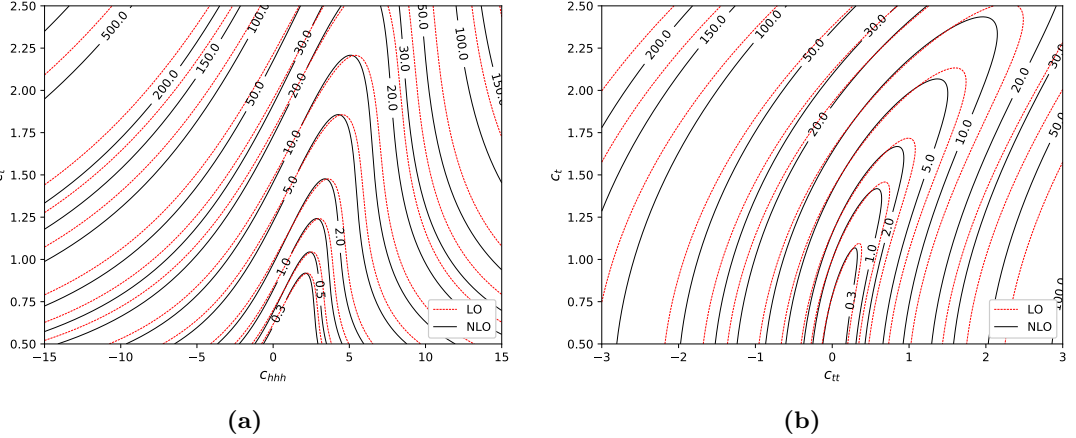


Figure 10.11: Iso-contours of σ/σ_{SM} : (a) c_t versus c_{hh} and (b) c_t versus c_{tt} .

10.4 Differential cross-sections and HTL approximations

Next, differential cross-sections are compared for the various approximations laid out in Section 10.1.1. Distributions are shown for the invariant mass of the Higgs boson pair system m_{hh} and the transverse momentum of one (any) Higgs $p_{T,h}$, for a subset of the BM points defined in Table 10.2.

In Fig. 10.12, both distributions are displayed for the BM point 6: the SM distributions are plotted against the the BSM Born-improved, FT_{approx} and full predictions, respectively, both at LO and NLO. While the B_6 total cross-section is similar to the SM value for all considered NLO approximations, the interference pattern between triangle- and box-like diagrams is very different. The m_{hh} observable in Fig. 10.12a manifests a

dip around $m_{hh} = 370$ GeV,⁵ which would be a characteristic sign of BSM physics at the differential level. As a matter of fact, the chosen value of $c_{hhh} = 2.4$ corresponds approximately to a maximal destructive interference between triangle- and box-like contributions when the other couplings are kept fixed at their SM values. Secondly, the differential K -factor shown in the first ratio plot (in red), which is found to be relatively flat in the usual HTL approximations, varies by more than 70% for the full m_t -dependent NLO prediction. Finally, while both the Born-improved and FT_{approx} descriptions show the largest difference to the full NLO calculation around the top-quark pair threshold (see the purple and green curves in the second ratio plot), they describe the tail of the m_{hh} distribution rather well. The same considerations apply to the $p_{T,h}$ distribution plotted in Fig. 10.12b.

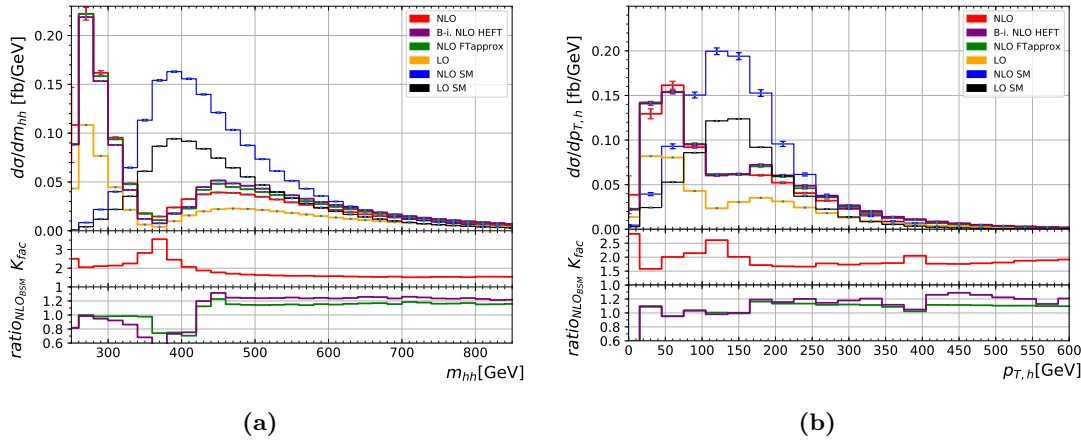


Figure 10.12: (a) Higgs boson pair invariant mass and (b) Higgs transverse momentum for BM point 6 ($c_{hhh} = 2.4, c_t = 1, c_{tt} = 0, c_{ggh} = 2/15, c_{gghh} = 1/15$) with all considered hh production approximations.

The same differential distributions are plotted for the BM point 9 in Fig. 10.13, which is characterized by SM values for c_{hhh}, c_t and non-zero values of c_{tt} and gluon-Higgs couplings c_{ggh}, c_{gghh} . In this case, the cross-section is much larger than the SM value. The anomalous gluon-Higgs coupling values also enhance the tail of both distributions (the dependence of the c_{gghh} term grows proportionally to the invariant \hat{s} in the limit $\hat{s} \rightarrow \infty$). Both NLO approximations fall short of describing the full prediction around the top-quark pair threshold and in the middle-range part of the m_{hh} distribution.

Renormalization and factorization scale uncertainties are given along the central prediction for the BM point 5 in Fig. 10.14. This BM point is one example where, contrary to the SM case, the envelope is not given by the two most extreme scale variations $c_{R,F} \in \{(0.5, 0.5), (2, 2)\}$, which both give downwards deviations. As for the SM point, the NLO BM prediction is not covered by the LO scale uncertainties. All BM points not shown here are given in Appendix D for completeness.

⁵The LO pure HTL amplitude vanishes at $m_{hh} = 429$ GeV.

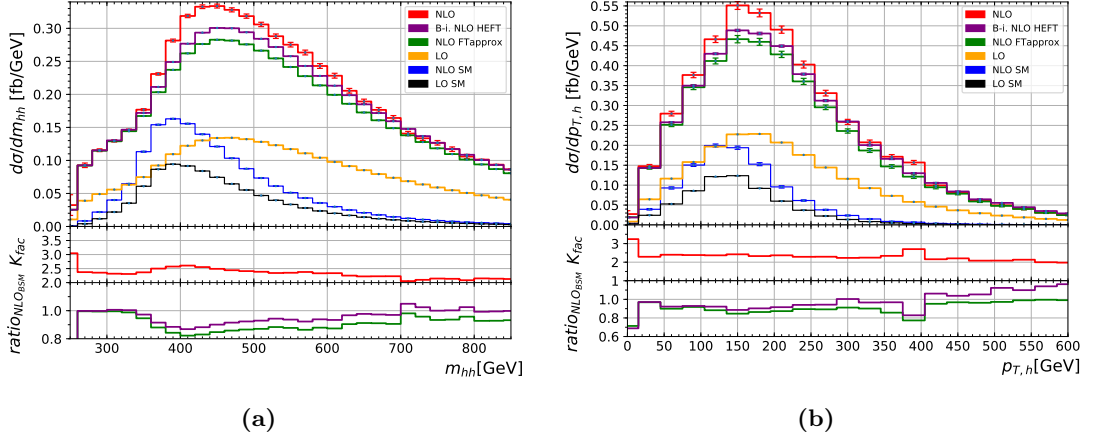


Figure 10.13: (a) Higgs boson pair invariant mass and (b) Higgs transverse momentum for BM point 9 ($c_{hhh} = 1, c_t = 1, c_{tt} = 1, c_{ggh} = -0.4, c_{gggh} = -0.2$).

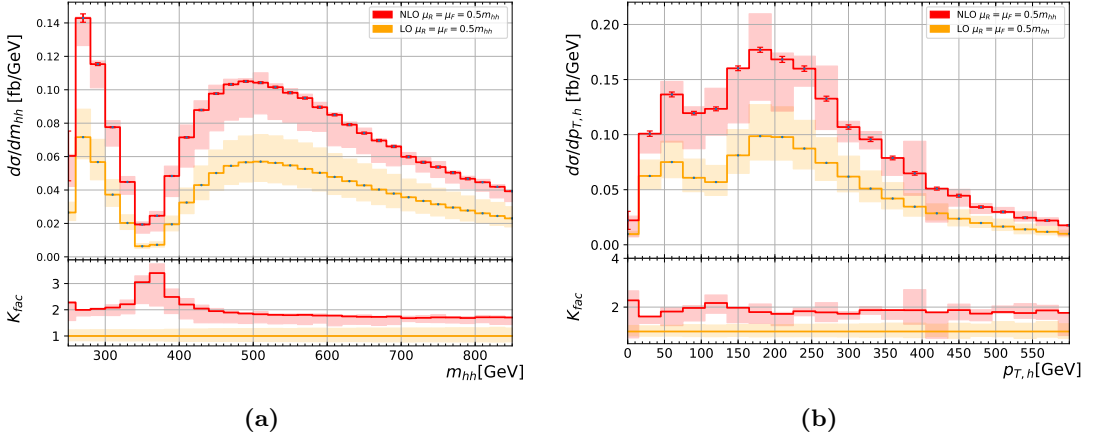


Figure 10.14: The (a) m_{hh} and (b) $p_{T,h}$ distributions for BM point 5 ($c_{hhh} = 1, c_t = 1, c_{tt} = 0, c_{ggh} = 8/15, c_{gggh} = 1/3$), along with μ_R/μ_F scale uncertainties.

2153 Note that both BM points 5 and 9 assume values of c_{ggh} that are already excluded
 2154 by CMS for $c_t = 1$ [280]. Generally, the full m_t -dependent NLO prediction introduces a
 2155 high dependence of the K -factor on both the anomalous Higgs couplings and at the dif-
 2156 ferential level in distribution bins. For some BM points, the Born-improved and FT approx-
 2157 imations fare rather poorly and should be replaced by the full theory prediction
 2158 when comparing to experimentally measured cross-sections, for maximal exclusion limits
 2159 on anomalous couplings. In particular, it should help identify updated BM points in the
 2160 BSM space of anomalous Higgs couplings. In this prospect, part of the EWChL setup
 2161 presented above is incorporated into a MC event generator available to experimentalists.

2162 11 Variations of the triple Higgs coupling 2163 and parton-shower effects

2164 Having considered the extension of the SM through the EWChL and the effects of the
 2165 full NLO QCD corrections due to the top-quark loops in hh production, its implementa-
 2166 tion in a full-fledged MC event generator is presented. Numerical results and differential
 2167 distributions are given in more detail in Ref. [281]. A version of the m_t -dependent predic-
 2168 tion at NLO was already implemented in the case of the SM in the POWHEG-BOX-V2
 2169 package `UserProcesses-V2/ggHH`. It is extended to allow for variations of both the Higgs
 2170 boson trilinear self-coupling λ and the top-Higgs Yukawa coupling y_t : the result is a pub-
 2171 lic MC generator that permits full particle-level production. In particular, Higgs bosons
 2172 are allowed to decay, and the fixed-order calculation can be matched to a parton-shower
 2173 and hadronization package. In this chapter, the working mode of the POWHEG-BOX
 2174 MC generator is briefly presented. The interfacing of the two-loop contribution to hh
 2175 production (including the aforementioned coupling variations) is explained, and NLO
 2176 cross-sections at $\sqrt{s} = 13, 14, 27$ TeV, as well as differential distributions at $\sqrt{s} = 14$ TeV
 2177 are shown. Finally, the matching of the fixed-order NLO calculation to a parton-shower
 2178 is studied in more depth, and shower-related systematic uncertainties are estimated.

2179 11.1 The Powheg-BOX framework

2180 The POWHEG-BOX framework [17–19] is a `fortran` MC event generator skeleton that
 2181 handles MC integration and event production for any arbitrary NLO process, suppos-
 2182 ing the user grants the few necessary input ingredients for the calculation, namely a
 2183 parametrization of phase-space and the different contributions to the amplitude. The
 2184 POWHEG-BOX also constitutes a repository of previously calculated processes which are
 2185 made publicly available. In the following, the second version of the program POWHEG-
 2186 BOX-V2 is used. The POWHEG formalism is based on the following formula for the
 2187 hardest emission:

$$d\sigma_{\text{NLO}} = d\Phi_m \bar{B}(\Phi_m) \left(\Delta(p_{T,\min}, \mu^2) + \int_{p_{T,\min}} d\Phi_1 \Delta(p_T, \mu^2) \frac{R(\Phi_{m+1})}{B(\Phi_m)} \Theta(\mu^2 - p_T) \right), \quad (11.1)$$

2188 where $p_{T,\min}$ is the parton-shower IR cutoff, μ^2 is the shower starting scale, B and R are
 2189 the Born and the real-emission matrix-elements, and \bar{B} represents the Born underlying
 2190 configuration. Note that in general, the transverse momentum could be replaced by
 2191 any other shower evolution variable. The function Δ is the Sudakov form factor (see

11 Variations of the triple Higgs coupling and parton-shower effects

2192 Section 4.2.2) yielding the probability of no-emission above a given scale. In the POWHEG
 2193 notation, it is written as:

$$\Delta(t_0, t) = \exp \left(- \int d\Phi_1 \frac{R(\Phi_{m+1}) \Theta(t - t_0)}{B(\Phi_m)} \right). \quad (11.2)$$

2194 For more details, the reader is referred to Ref. [18]. The workflow is quite simple and
 2195 separates into four stages:

- 2196 • An importance sampling grid for the integration is determined: if run in parallel
 2197 mode, POWHEG generates importance sampling grids for each seed and subse-
 2198 quently combines them into one and stores the result in a `pwgxgrid.dat` file.
- 2199 • The integration is performed, and an upper bounding envelope is determined for
 2200 the underlying Born kinematics cross-section \bar{B} and stored into a `pwggrid.dat`
 2201 file.
- 2202 • The upper bound for the normalization of the radiation function $R(\Phi_{m+1})/B(\Phi_m)$
 2203 is found, and stored into a `pwgubound.dat` file.
- 2204 • Events can be generated in the LHE format, and run in parallel. Files `pwgevents.lhe`
 2205 are produced and can then be fed to a parton-shower algorithm later on.

2206 11.2 Interfacing two-loop contributions

2207 The grid of the amplitude at pre-sampled PS points used for producing the results of
 2208 Chapter 10 is stored and has to be interfaced to POWHEG. First, the program has
 2209 to be able to call the virtual amplitude at any phase-space point (without having to
 2210 recompute the expensive two-loop integrals for any possible kinematics (\hat{s}, \hat{t})). In the
 2211 SM `ggHH` program [282], this is handled by setting up a Python interface that interpolates
 2212 the 2-dimensional grid: first, the (\hat{s}, \hat{t}) phase-space is re-parametrized into new variables
 2213 (x, c_θ) to produce an almost uniform distribution of phase-space points. This is achieved
 2214 by choosing

$$x = f(\beta(\hat{s})), \quad c_\theta = |\cos(\theta)| = \left| \frac{\hat{s} + 2\hat{t} - 2m_h^2}{\hat{s}\beta(\hat{s})} \right|, \quad \beta = \sqrt{1 - \frac{4m_h^2}{\hat{s}}} \quad (11.3)$$

2215 with f any monotonic function. In this case, $f(\beta(\hat{s}))$ is chosen to be the cumulative
 2216 distribution function of the phase-space points generated in Ref. [261]. A uniform grid in
 2217 the (x, c_θ) space is generated, and the result at each point is set by linearly interpolating
 2218 the amplitude using the neighboring points computed by `SECDEC`. The amplitude at
 2219 any phase-space points is then interpolated using the Clough-Tougher scheme in `SciPy`,
 2220 which allows for a high numerical stability. For details on the grid performance and
 2221 caveats, the reader is referred to Ref. [281, 282].

11.3 Total and differential cross-sections at fixed-order

The implementation of variations of the Higgs trilinear self-coupling λ bases on a simple observation: at all orders (in QCD), the squared amplitude for di-Higgs production is a second-order polynomial in λ ,

$$M_\lambda \equiv |\mathcal{M}_\lambda|^2 = A + B\lambda + C\lambda^2. \quad (11.4)$$

Thus knowing the amplitude for three values of λ allows to interpolate the matrix-element to any other arbitrary value. In this case, grids of the virtual amplitudes are produced for $\lambda \in \{-1, 0, 1\}$. Before starting the POWHEG run, the three grids are combined to a new grid containing the virtual amplitude for the user-given value of the Higgs self-coupling by simple Lagrange interpolation,

$$M_\lambda = M_{\lambda=0} (1 - \lambda^2) + \frac{M_{\lambda=1}}{2} (\lambda + \lambda^2) + \frac{M_{\lambda=-1}}{2} (-\lambda + \lambda^2), \quad (11.5)$$

where the uncertainties on the three amplitudes are added in quadrature. This grid is then further propagated to the Clough-Tougher interpolation routine. Note that in the BSM case, points at 100 TeV are also included in the grid to further improve statistics at higher center-of-mass energies, and by extension, in the tails of the distributions. On the other hand, because BSM distributions differ in shape from the SM case (for example, see Fig. 11.2), phase-space regions that could well be populated for certain values of the anomalous couplings are not always well-sampled by the SM grid.

11.3 Total and differential cross-sections at fixed-order

The PDF4LHC15_nlo_30_pdfas set is used and interfaced to POWHEG-BOX-V2 through LHAPDF. Jets are clustered by the anti- k_T algorithm [220] as implemented in `FastJet`, with a jet distance parameter of $R = 0.4$ and a minimum transverse momentum $p_{T,\min}^{\text{jet}} = 20 \text{ GeV}$. Otherwise, the same setup presented in Section 10.3 is used for the next results. Note that the nomenclature is different, with respect to Chapter 10, for variations of the Higgs trilinear coupling and the top-Higgs Yukawa coupling: the Higgs self-coupling ratio to the SM value, formerly called c_{hh} , is replaced by κ_λ (in reference to the widely-used experimental κ framework), and the top-Higgs Yukawa coupling ratio c_t is now named y_t .

Total cross-sections for various values of $\kappa_\lambda = \lambda/\lambda_{\text{SM}}$ were computed for $\sqrt{s} = 13, 14$ and 27 TeV and are displayed in Table 11.1. Note again that the cross-section has a minimum around $\kappa_\lambda \sim 2.4$, for which the interference between triangle- and box-like diagrams is at its most destructive. The K -factor is plotted in Fig. 11.1 as a function of the Higgs self-coupling, this time ranging over the full, not yet excluded region for κ_λ .

The distribution of the invariant mass of the Higgs boson pair hh is shown for the considered values of κ_λ in Fig. 11.2 with their respective scale uncertainties. For values of κ_λ that lead to minimal cross-section, the interference pattern is well-recognizable with a dip around $m_{hh} \sim 350 \text{ GeV}$, near the top-pair threshold. For greater values of

11 Variations of the triple Higgs coupling and parton-shower effects

| $\lambda_{\text{BSM}}/\lambda_{\text{SM}}$ | $\sigma_{\text{NLO}}@13\text{TeV} [\text{fb}]$ | $\sigma_{\text{NLO}}@14\text{TeV} [\text{fb}]$ | $\sigma_{\text{NLO}}@27\text{TeV} [\text{fb}]$ | K-factor@14TeV |
|--|--|--|--|----------------|
| -1 | $116.71^{+16.4\%}_{-14.3\%}$ | $136.91^{+16.4\%}_{-13.9\%}$ | 504.9 | 1.86 |
| 0 | $62.51^{+15.8\%}_{-13.7\%}$ | $73.64^{+15.4\%}_{-13.4\%}$ | 275.29 | 1.79 |
| 1 | $27.84^{+11.6\%}_{-12.9\%}$ | $32.88^{+13.5\%}_{-12.5\%}$ | $127.7^{+11.5\%}_{-10.4\%}$ | 1.66 |
| 2 | $12.42^{+13.1\%}_{-12.0\%}$ | $14.75^{+12.0\%}_{-11.8\%}$ | 59.10 | 1.56 |
| 2.4 | $11.65^{+13.9\%}_{-12.7\%}$ | $13.79^{+13.5\%}_{-12.5\%}$ | 53.67 | 1.65 |
| 3 | $16.28^{+16.2\%}_{-15.3\%}$ | $19.07^{+17.1\%}_{-14.1\%}$ | 69.84 | 1.90 |
| 5 | $81.74^{+20.0\%}_{-15.6\%}$ | $95.22^{+19.7\%}_{-11.5\%}$ | 330.61 | 2.14 |

Table 11.1: The cross-sections for di-Higgs production at full NLO QCD are given for $\sqrt{s} = 13, 14$ and 27 TeV with scale uncertainties for several values of $\kappa_\lambda = \lambda/\lambda_{\text{SM}}$.

2256 $|\kappa_\lambda|$, this dip completely disappears and the enhanced triangle-like contribution tends
 2257 to populate the lower m_{hh} -region. A similar behavior is observed for the transverse
 2258 momentum of one (any) Higgs boson, as presented in Fig. 11.3, although the effect is
 2259 partly washed out.

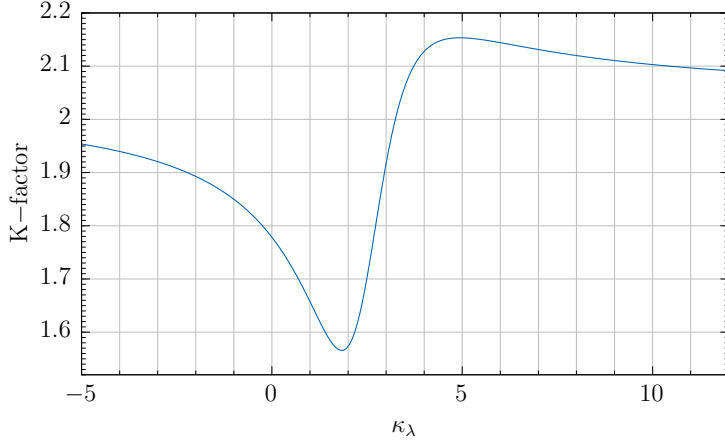


Figure 11.1: The full-theory NLO QCD K -factor is plotted as a function of the trilinear Higgs self-coupling κ_λ .

2260 Furthermore, variations of the top-Higgs Yukawa coupling y_t can be recovered by a
 2261 trick: allowing for y_t variations changes Eq. (11.4) into

$$|\mathcal{M}|^2 = y_t^4 \left[\mathcal{M}_B \mathcal{M}_B^* + \frac{\lambda}{y_t} (\mathcal{M}_B \mathcal{M}_T^* + \mathcal{M}_T \mathcal{M}_B^*) + \frac{\lambda^2}{y_t^2} \mathcal{M}_T \mathcal{M}_T^* \right], \quad (11.6)$$

2262 where \mathcal{M}_B is the box- and \mathcal{M}_T is the triangle contribution, and only the ratio $\frac{\lambda}{y_t}$
 2263 appears up to an overall factor. So, it suffices to generate events with the value of λ

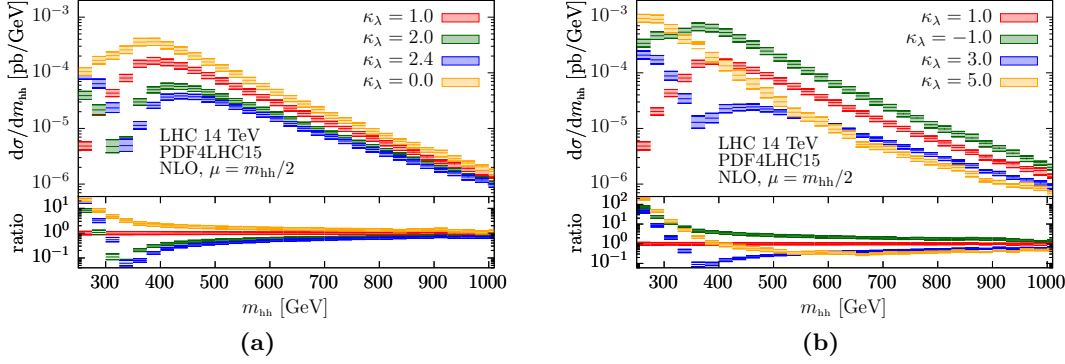


Figure 11.2: The Higgs boson pair invariant mass distributions for different values of κ_λ are given at $\sqrt{s} = 14$ TeV.

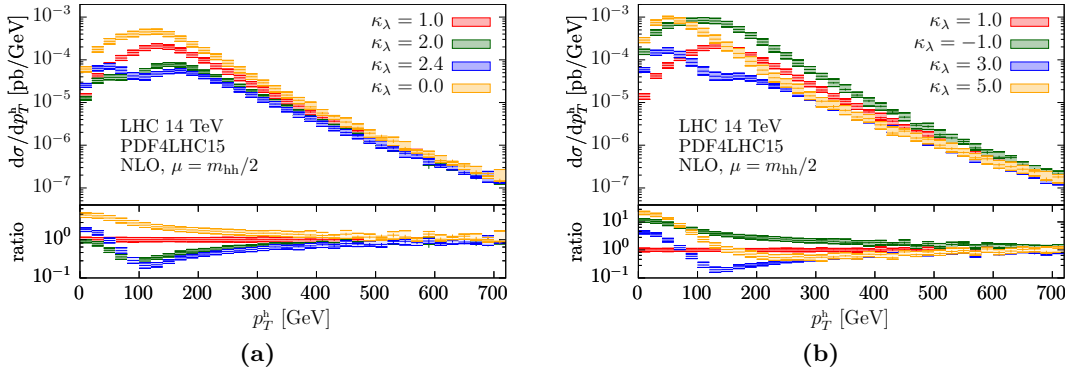


Figure 11.3: The transverse momentum of one (any) Higgs boson is shown for several values of κ_λ at $\sqrt{s} = 14$ TeV.

2264 corresponding to the desired value of the ratio $\frac{\lambda}{y_t}$, and finally rescale all results by y_t^4 .
 2265 For example, to produce results for $\kappa_\lambda = 1$, $y_t = 0.8$, the cross-section is given by

$$d\sigma_{\text{NLO}}(\kappa_\lambda = 1, y_t = 0.8) = (0.8)^4 \cdot d\sigma_{\text{NLO}}\left(y_t = 1, \kappa_\lambda = \frac{1}{0.8} = 1.25\right). \quad (11.7)$$

2266 Both m_{hh} and p_T^h distributions are displayed for y_t -values close to the currently ex-
 2267 cluded region in Fig. 11.4.

2268 11.4 Parton-shower matched predictions at NLO

2269 For use by experimentalists in a full simulation, the fixed-order calculation is matched to
 2270 a parton-shower (whose final-state can also be hadronized later on) within POWHEG. In
 2271 the fourth generation stage presented above, POWHEG generates full parton-level events

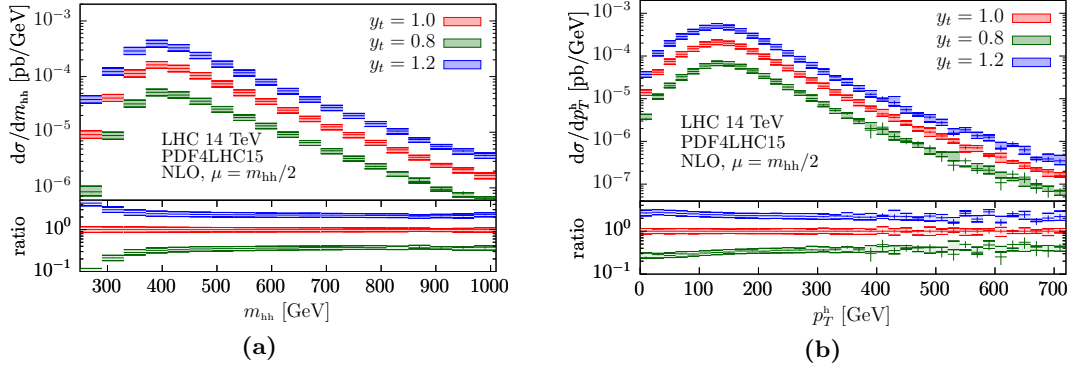


Figure 11.4: (a) The invariant mass of the Higgs boson pair system and (b) the transverse momentum of one Higgs boson are shown for three values of y_t . The procedure for generating y_t -varied events is explained in the text.

and stores them in LHE files. These events can then be used as input to most modern parton-shower programs. For this purpose, two different parton-shower programs are employed, namely PYTHIA 8.235 and HERWIG7.1.4. Additionally, both the angular-ordered (so called \tilde{q}) and the dipole shower algorithms present in HERWIG are applied. The interfacing of both programs to POWHEG is mostly automatized: the standard `UserHooks` based on the `main31` LHE showering routine from PYTHIA are used to set the shower p_T definitions and vetoes (see Appendix E). For HERWIG7, a process-independent interface library is present since revision `r3591` of the POWHEG-BOX-V2 which sets the `LHEReader` class and handles the HERWIG output for the event analysis. Finally, in both showers, the tunes are left to their default values. Note that the Sudakov form factor is automatically included by POWHEG when producing LHE files. The POWHEG h_{damp} parameter is kept fixed throughout the next section and set to $h_{\text{damp}} = 250$ GeV.

In Fig. 11.5a, the transverse momentum of one (any) Higgs boson p_T^h is shown for the fixed-order NLO prediction, as well as the matched predictions to the three different shower algorithms: PYTHIA 8 (PP8), and both the angular-ordered \tilde{q} shower (PH7- \tilde{q}) and the dipole shower (PH7-dipole) from HERWIG. For variables that are inclusive in the additional radiation, like p_T^h , all predictions are largely identical. In the case of variables that are sensitive to real emission, like the angular distance of both Higgs bosons $\Delta R^{hh} = \sqrt{(\eta_1 - \eta_2)^2 + (\phi_1 - \phi_2)^2}$ shown in Fig. 11.5b, the showered predictions differ from the NLO calculation. There, the Sudakov exponent effectively resums radiation around $\Delta R^{hh} = \pi$, where the Higgs bosons are close to a back-to-back configuration. In addition, the parton-shower starts populating the region $\Delta R^{hh} < \pi$. Also, differences between the PYTHIA and HERWIG parton-showers are already visible: while both HERWIG showers produce very similar results, PYTHIA overshoots their prediction by $\sim 50\%$.

The differences between both parton-shower programs become more obvious when considering the transverse momentum of the Higgs boson pair system p_T^{hh} , displayed in Fig. 11.6 for two values of the Higgs trilinear coupling $\kappa_\lambda = 1$, $\kappa_\lambda = 2.4$. In that case, both PYTHIA and HERWIG agree at low transverse momentum, until they start to deviate

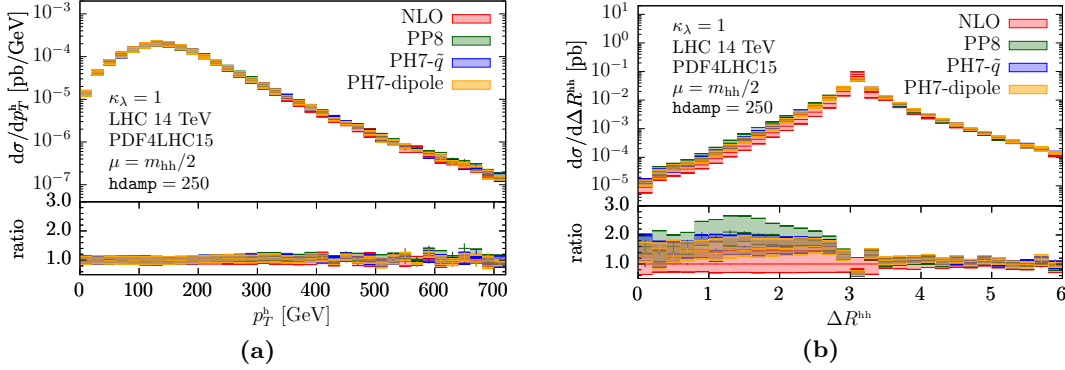


Figure 11.5: For the SM case $\kappa_\lambda = 1$, (a) the transverse momentum of one Higgs boson, and (b) the angular distance between both Higgs bosons are shown for the fixed-order NLO case, as well as for the three different parton-shower algorithms. The parton-level events from POWHEG are matched to PYTHIA 8 (PP8), and to both the angular-ordered \tilde{q} -shower (PH7- \tilde{q}) and the dipole shower (PH7-dipole) from HERWIG7.

at $p_T^{hh} \sim 100$ GeV already. Then, while both HERWIG showers correctly reproduce the hard NLO emission in the high- p_T^{hh} region, the PYTHIA parton-shower produces much harder radiation and its ratio to the fixed-order prediction stagnates at ~ 2 over the remaining range. In di-Higgs production, the harder spectrum from PYTHIA was found to be due to too hard sub-leading jets produced solely in the shower [283] as compared to the older PYTHIA 6 parton-shower. In other processes, like $t\bar{t}$ production, sizeable differences between PYTHIA and HERWIG had also already been observed [284].

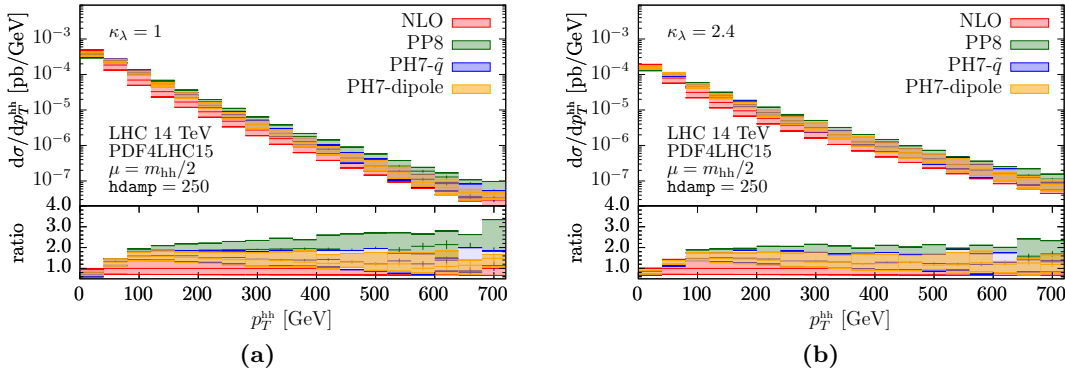


Figure 11.6: The NLO fixed-order prediction is compared to results from the three parton-shower algorithms with respect to the transverse momentum of the Higgs boson pair system p_T^{hh} for (a) $\kappa_\lambda = 1$ and (b) $\kappa_\lambda = 2.4$.

As a way to estimate shower-matching uncertainties, the maximal transverse momentum allowed for shower emissions can be set in HERWIG by varying the so-called hard

11 Variations of the triple Higgs coupling and parton-shower effects

scale μ_Q . The parameter `HardScaleFactor` is varied to $c_Q = 0.5$, $c_Q = 2$ and applied on the central hard shower scale separately for the up- and down-variations of the renormalization and factorization scales $\mu_{R,F}$. In Fig. 11.7, the result is presented for the di-Higgs transverse momentum p_T^{hh} and the angular separation between the Higgs bosons ΔR^{hh} . The shower scale variations add to the renormalization/factorizations scale uncertainties, bringing their common envelope to a corresponding 50% – 100% overall systematic uncertainty in the far- p_T^{hh} region of the distribution. The differences between the central PYTHIA and HERWIG predictions are then partly covered by the hard shower scale variations.

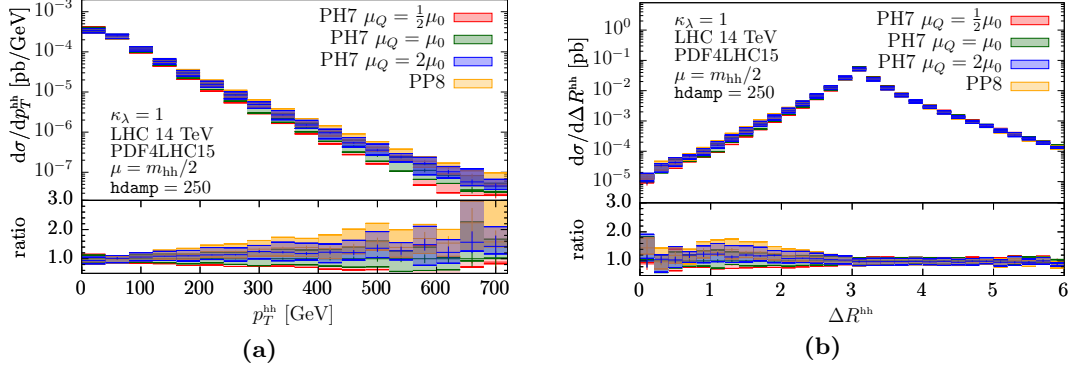


Figure 11.7: (a) The di-Higgs transverse momentum p_T^{hh} and (b) the angular separation ΔR^{hh} between the Higgs bosons are shown for variations of the HERWIG hard shower scale, which regulates the maximal allowed transverse momentum of shower emissions. The hard scale $\mu_Q = c_Q\mu_0$ is varied by $c_Q \in \{\frac{1}{2}, 2\}$ with respect to the default scale μ_0 .

All in all, considering both scale and parton-shower uncertainties, the Higgs pair process underlines the necessity of computing higher-order corrections in both fixed-order and logarithmic accuracy. In the future, it will be informative to study parton-shower (as well as other non-perturbative, e.g. hadronization) modeling effects in loop-induced color singlet production and try to reduce the sizeable associated uncertainties.

2323 12 Conclusion and Outlook

2324 A precise determination of the top-quark mass is important for several reason. Experi-
2325 mentally, its value is used in global electroweak fits, which are one of the most stringent
2326 tests of the SM. Theoretically, it largely affects the running of the Higgs quartic coupling
2327 and thus the stability of the SM vacuum. Nowadays, experimental measurements have
2328 reduced the top-quark mass uncertainty to the point where new questions have to be
2329 asked. In particular:

- 2330 • Are the theoretical descriptions of the $t\bar{t}$ final-state used in MC simulations for
2331 experimental analyses good enough?
- 2332 • Do the uncertainties correctly cover the unknown higher-order corrections and
2333 other neglected contributions?
- 2334 • What is the exact nature of the measured MC top-quark mass, and how does it
2335 relate to other mass schemes?

2336 The answer to these questions requires a lot of effort from both the experimental
2337 and theoretical sides. One specific assumption made in most $t\bar{t}$ analyses relies on the
2338 factorization of top-quark pair production and decay: such a treatment is called the
2339 narrow-width approximation (NWA). In automatized particle-level MC event generators,
2340 this description usually contains NLO QCD production of a $t\bar{t}$ pair and LO decay of the
2341 top quarks. The full parton-level final-state is then handed over to the parton-shower
2342 and hadronization algorithms. It was shown that for certain observables, higher-order
2343 and off-shell effects can lead to important differences. Specifically, NLO QCD corrections
2344 to the top-quark decay can have sizeable effects on the kinematics of its decay products.

2345 To reach a quantifiable answer to the first and second questions stated above, the
2346 determination of the top-quark mass in the dilepton channel is taken as an example.
2347 Experimentally, the template fit method provides an extraction of the MC top-quark
2348 mass. Following the same procedure, template distributions for $pp \rightarrow (e^+\nu_e)(\mu^-\bar{\nu}_\mu)b\bar{b}$
2349 are produced at $\sqrt{s} = 13$ TeV using four different theoretical descriptions of the final-
2350 state at parton level. Starting from top-quark pair production at NLO QCD, three
2351 different levels of accuracy for the top-quark decay are investigated: LO, respectively
2352 NLO QCD, as well as decay by a parton-shower. Finally, these three NWA predictions
2353 are compared to a $W^+W^-b\bar{b}$ calculation at parton level. The latter contains Feynman
2354 diagrams that are not present in the NWA, namely diagrams with top-quark legs that
2355 do not factorize, and diagrams with zero or one top-quark propagator only.

12 Conclusion and Outlook

2356 In an implementation similar to the ATLAS analysis, distributions of the lepton and
2357 b -jet invariant mass $m_{\ell b}$ are parametrized separately for a set of MC input top-quark
2358 masses. Once the parameters are fixed, only the top-quark mass is left as a free quantity
2359 to be determined by a fit to data. To compare the different calculations two-by-two,
2360 the parametrization from one theoretical prediction is used in an unbinned likelihood
2361 fit to pseudo-data drawn from another prediction. The offsets outlined in the extracted
2362 top-quark mass represent the systematic uncertainty accompanying the use of the in-
2363 complete set of diagrams. It is shown that NLO corrections to the top-quark decay in
2364 the NWA have an important effect on the extracted top-quark mass. In fact, the offset
2365 in the top-quark mass is opposite in sign and higher in absolute value than from NLO
2366 corrections to $t\bar{t}$ production. When comparing the NLO top-quark decay to the full
2367 $W^+W^-b\bar{b}$ computation, the offset is reduced to (0.83 ± 0.07) GeV. More importantly,
2368 the offset in the extracted top-quark mass stemming from renormalization/factorization
2369 scale variations now overlap. These comparisons suggest that the scale uncertainties in
2370 $t\bar{t}$ production with LO top-quark decay are underestimated. While the NLO corrections
2371 to the top-quark decay describe correctly the emission of a hard jet from the final-state,
2372 the parton-shower is formally of LO accuracy in QCD. Yet, because it produces addi-
2373 tional radiation as the parton level is fully showered down to hadronization scales, it
2374 comes close to the top-quark mass extracted from $W^+W^-b\bar{b}$ samples, with an offset of
2375 (-0.09 ± 0.07) GeV.

2376 The studies presented above suffer from two complications: first, they were realized at
2377 parton level, and it is unclear if the bias in the extracted top-quark mass is as important
2378 at detector level. Second, they only compared pure $t\bar{t}$ predictions to the full $W^+W^-b\bar{b}$
2379 computation, while usually single-top production in the Wt channel is also included in
2380 the signal. As a first attempt at curing both issues, a setup implemented in the ATLAS
2381 framework is presented, where particle-level distributions can be folded up to detector
2382 level. Bin migration matrices and detector efficiencies are derived from simulated $t\bar{t}$
2383 samples produced at five different top-quark mass points. In parallel, $W^+W^-b\bar{b}$ samples
2384 are generated using the `bb41` MC generator present in the POWHEG-BOX-RES frame-
2385 work, and matched to the PYTHIA8 parton-shower. This time, the folding matrices from
2386 the $t\bar{t}$ prediction are used to bring the $W^+W^-b\bar{b}$ distribution of $m_{\ell b}$ to detector level.
2387 The same procedure of template parametrization and fit to pseudo-data is repeated at
2388 detector level, and the templates from $t\bar{t}$ and single-top Wt are compared to the full
2389 $W^+W^-b\bar{b}$ calculation. This procedure is fast, and avoids the need to simulate all MC
2390 variation samples. The offset in the extracted top-quark mass between $W^+W^-b\bar{b}$ and
2391 $t\bar{t}$ +single-top predictions amounts to (-0.330 ± 0.022) GeV. In relation to the third
2392 question given above, the folding setup might be useful to estimate the top-quark mass
2393 IR-dependence on e.g. the shower cutoff scale Q_0 in HERWIG: in turn, this would help
2394 shed some light on the controversial relations between different mass definitions.

2395 The top-quark mass also has sizeable theoretical effects in the computation of Higgs
2396 boson pair production in gluon-gluon fusion at the LHC. This process is important since
2397 it is the golden channel to experimentally constrain the trilinear Higgs self-coupling. At
2398 LO, Higgs pair production takes place via an intermediate top-quark loop. At NLO, the
2399 virtual contributions are thus of two-loop order and the Feynman integrals contain up

2400 to four mass scales. Only part of the master integrals are known analytically at this
2401 point. Nevertheless, these integrals were evaluated numerically with the full top-quark
2402 mass dependence using sector decomposition. To allow for variations of the Higgs boson
2403 couplings to the QCD sector, a non-linear EFT framework is introduced in the form of
2404 the Electroweak Chiral Lagrangian (EWChL). At NLO in QCD, this class of extensions
2405 contains five couplings parametrizing variations from the SM: the Higgs-top Yukawa
2406 coupling c_t and the trilinear Higgs self-coupling c_{hhh} , as well as effective couplings for
2407 two-top-two-Higgs c_{tt} , gluon-gluon-Higgs c_{ggh} and two-gluons-two-Higgs c_{gghh} vertices.
2408

The setup is based on a grid of virtual two-loop amplitudes for pre-sampled phase-space points in the SM. Cross-section results are then presented for Higgs pair production at NLO QCD with full top-quark mass dependence in the EWChL framework. Both inclusive and differential cross-sections are produced at $\sqrt{s} = 14$ TeV for several benchmark points characterizing the BSM parameter space. Inclusive cross-sections exhibit large K -factors up to ~ 2.34 depending on the considered benchmark point. In particular, once the full top-quark loops are taken into account, a sizeable dependence of the K -factors on the top-quark couplings c_t and c_{tt} is found, as well as on the trilinear coupling c_{hhh} .

Finally, a MC event generator is put forward for use by experimentalists in Higgs pair searches. Within the POWHEG-BOX-V2 framework, the MC generator ggHH for Higgs pair production in the SM at NLO QCD is extended with the possibility of varying the trilinear Higgs self-coupling and the Higgs-top Yukawa coupling. In this program, the hard NLO matrix-element can be matched to both PYTHIA8 and HERWIG7 parton-showers. Some first studies suggest that there are considerable uncertainties associated to the parton-shower.

Challenging prospects are still awaiting in future top-quark and Higgs-boson physics. In consideration of the major advances and successes met in the last years, the question arises whether there is still hope to unveil New Physics at the LHC. While the LHC started as a discovery machine, it is now, perhaps surprisingly, well-suited to precision measurements. With the advent of the HL-LHC, the sheer amount of expected data will drive down statistical uncertainties. Increasingly, all questions examined in this work will gain in importance. Further approximations used in theoretical descriptions will need improving, and more fundamental issues need closer scrutiny – like the heavy-quark mass definition problem. Yet, smaller statistical uncertainties will assuredly be accompanied by better systematics, as detectors improve and new methods are developed to keep all sources of uncertainty under control. These refinements will prove of extreme use in the measurement of the properties of the Higgs boson, especially of the true form of its potential. Finally, new generations of colliders will hopefully see the light sooner or later, and keep the physics community hard at work for years to come. As *Star Trek* character Captain Jean-Luc Picard said, "Our mission is to go forward. [...] There's still much to do; still so much to learn."

2440 Bibliography

- 2441 [1] PARTICLE DATA GROUP collaboration, *Review of Particle Physics*, *Phys. Rev. D*
2442 **98** (2018) 030001.
- 2443 [2] CDF collaboration, *Observation of Top Quark Production in $\bar{p}p$ Collisions with*
2444 *the Collider Detector at Fermilab*, *Phys. Rev. Lett.* **74** (1995) 2626–2631.
- 2445 [3] D0 collaboration, *Observation of the top quark*, *Phys. Rev. Lett.* **74** (1995)
2446 2632–2637.
- 2447 [4] “LHC Top Working Group.”
2448 <https://twiki.cern.ch/twiki/bin/view/LHCPhysics/LHCTopWG>.
- 2449 [5] ATLAS collaboration, *Measurement of the top quark mass in the $t\bar{t} \rightarrow$*
- 2450 *lepton+jets channel from $\sqrt{s} = 8$ TeV ATLAS data and combination with*
2451 *previous results*, *Submitted to: Eur. Phys. J.* (2018) [arXiv:1810.01772].
- 2452 [6] CMS collaboration, *Measurement of the top quark mass using proton-proton data*
2453 *at $\sqrt{s} = 7$ and 8 TeV*, *Phys. Rev.* **D93** (2016) 072004 [arXiv:1509.04044].
- 2454 [7] P. Marquard, A.V. Smirnov, V.A. Smirnov et al., *Quark Mass Relations to*
2455 *Four-Loop Order in Perturbative QCD*, *Phys. Rev. Lett.* **114** (2015) 142002
2456 [arXiv:1502.01030].
- 2457 [8] M. Beneke and V.M. Braun, *Heavy quark effective theory beyond perturbation*
2458 *theory: Renormalons, the pole mass and the residual mass term*, *Nucl. Phys.*
2459 **B426** (1994) 301–343 [arXiv:hep-ph/9402364].
- 2460 [9] I.I.Y. Bigi, M.A. Shifman, N.G. Uraltsev et al., *The Pole mass of the heavy*
2461 *quark. Perturbation theory and beyond*, *Phys. Rev.* **D50** (1994) 2234–2246
2462 [arXiv:hep-ph/9402360].
- 2463 [10] M. Beneke, *More on ambiguities in the pole mass*, *Phys. Lett.* **B344** (1995)
2464 341–347 [arXiv:hep-ph/9408380].
- 2465 [11] A.H. Hoang, C. Lepenik and M. Preisser, *On the Light Massive Flavor*
2466 *Dependence of the Large Order Asymptotic Behavior and the Ambiguity of the*
2467 *Pole Mass*, *JHEP* **09** (2017) 099 [arXiv:1706.08526].
- 2468 [12] A.H. Hoang and I.W. Stewart, *Top Mass Measurements from Jets and the*
2469 *Tevatron Top-Quark Mass*, *Nucl. Phys. Proc. Suppl.* **185** (2008) 220–226
2470 [arXiv:0808.0222].

Bibliography

- 2471 [13] A.H. Hoang, S. Plätzer and D. Samitz, *On the Cutoff Dependence of the Quark
2472 Mass Parameter in Angular Ordered Parton Showers*, *JHEP* **10** (2018) 200
2473 [arXiv:1807.06617].
- 2474 [14] ATLAS collaboration, *Combined measurements of Higgs boson production and
2475 decay using up to 80 fb^{-1} of proton-proton collision data at $\sqrt{s} = 13 \text{ TeV}$
2476 collected with the ATLAS experiment*, Tech. Rep. ATLAS-CONF-2018-031,
2477 CERN, Geneva, Jul 2018.
- 2478 [15] CMS collaboration, *Combined measurements of the Higgs boson's couplings at
2479 $\sqrt{s} = 13 \text{ TeV}$* , Tech. Rep. CMS-PAS-HIG-17-031, CERN, Geneva, 2018.
- 2480 [16] ATLAS collaboration, *Combination of searches for Higgs boson pairs in pp
2481 collisions at 13 TeV with the ATLAS experiment.*, Tech. Rep.
2482 ATLAS-CONF-2018-043, CERN, Geneva, Sep 2018.
- 2483 [17] P. Nason, *A New method for combining NLO QCD with shower Monte Carlo
2484 algorithms*, *JHEP* **11** (2004) 040 [arXiv:hep-ph/0409146].
- 2485 [18] S. Frixione, P. Nason and C. Oleari, *Matching NLO QCD computations with
2486 Parton Shower simulations: the POWHEG method*, *JHEP* **11** (2007) 070
2487 [arXiv:0709.2092].
- 2488 [19] S. Alioli, P. Nason, C. Oleari et al., *A general framework for implementing NLO
2489 calculations in shower Monte Carlo programs: the POWHEG BOX*, *JHEP* **06**
2490 (2010) 043 [arXiv:1002.2581].
- 2491 [20] SUPER-KAMIOKANDE collaboration, *Evidence for oscillation of atmospheric
2492 neutrinos*, *Phys. Rev. Lett.* **81** (1998) 1562–1567.
- 2493 [21] S.L. Glashow, *The renormalizability of vector meson interactions*, *Nuclear
2494 Physics* **10** (1959) 107 – 117.
- 2495 [22] S. Weinberg, *A model of leptons*, *Phys. Rev. Lett.* **19** (1967) 1264–1266.
- 2496 [23] A. Salam and J.C. Ward, *Weak and electromagnetic interactions*, *Il Nuovo
2497 Cimento* **11** (1959) 568–577.
- 2498 [24] D.J. Gross and F. Wilczek, *Ultraviolet behavior of non-abelian gauge theories*,
2499 *Phys. Rev. Lett.* **30** (1973) 1343–1346.
- 2500 [25] H.D. Politzer, *Reliable perturbative results for strong interactions?*, *Phys. Rev.
2501 Lett.* **30** (1973) 1346–1349.
- 2502 [26] ATLAS collaboration, *Standard Model Summary Plots Spring 2019*, Tech. Rep.
2503 ATL-PHYS-PUB-2019-010, CERN, Geneva, Mar 2019.
- 2504 [27] F. Englert and R. Brout, *Broken symmetry and the mass of gauge vector mesons*,
2505 *Phys. Rev. Lett.* **13** (1964) 321–323.

- 2506 [28] P.W. Higgs, *Broken symmetries and the masses of gauge bosons*, *Phys. Rev. Lett.*
2507 **13** (1964) 508–509.
- 2508 [29] G.S. Guralnik, C.R. Hagen and T.W.B. Kibble, *Global conservation laws and*
2509 *massless particles*, *Phys. Rev. Lett.* **13** (1964) 585–587.
- 2510 [30] J. Bardeen, L.N. Cooper and J.R. Schrieffer, *Theory of superconductivity*, *Phys.*
2511 *Rev.* **108** (1957) 1175–1204.
- 2512 [31] T.D. Lee, *A Theory of Spontaneous T Violation*, *Phys. Rev. D* **8** (1973)
2513 1226–1239.
- 2514 [32] S. Dimopoulos and H. Georgi, *Softly Broken Supersymmetry and SU(5)*, *Nucl.*
2515 *Phys.* **B193** (1981) 150–162.
- 2516 [33] LHC HIGGS CROSS SECTION WORKING GROUP collaboration, *Handbook of*
2517 *LHC Higgs Cross Sections: 4. Deciphering the Nature of the Higgs Sector*,
2518 [[arXiv:1610.07922](#)].
- 2519 [34] K.G. Chetyrkin and M.F. Zoller, *Three-loop β -functions for top-Yukawa and the*
2520 *Higgs self-interaction in the standard model*, *JHEP* **2012** (2012) 33.
- 2521 [35] S. Chigusa, T. Moroi and Y. Shoji, *State-of-the-Art Calculation of the Decay*
2522 *Rate of Electroweak Vacuum in the Standard Model*, *Phys. Rev. Lett.* **119** (2017)
2523 211801.
- 2524 [36] G. Degrassi, S. Di Vita, J. Elias-Miró et al., *Higgs mass and vacuum stability in*
2525 *the Standard Model at NNLO*, *JHEP* **2012** (2012) 98.
- 2526 [37] A.V. Bednyakov, B.A. Kniehl, A.F. Pikelner et al., *Stability of the electroweak*
2527 *vacuum: Gauge independence and advanced precision*, *Phys. Rev. Lett.* **115**
2528 (2015) 201802.
- 2529 [38] J. Schechter and J.W.F. Valle, *Neutrino masses in $SU(2) \otimes U(1)$ theories*, *Phys.*
2530 *Rev. D* **22** (1980) 2227–2235.
- 2531 [39] T. Yanagida, *Horizontal Symmetry and Masses of Neutrinos*, *Progress of*
2532 *Theoretical Physics* **64** (1980) 1103–1105.
- 2533 [40] R.N. Mohapatra and G. Senjanovic, *Neutrino Mass and Spontaneous Parity*
2534 *Nonconservation*, *Phys. Rev. Lett.* **44** (1980) 912.
- 2535 [41] F. Borzumati, Y. Grossman, E. Nardi et al., *Neutrino masses and mixing in*
2536 *supersymmetric models without R parity*, *Phys. Lett.* **B384** (1996) 123–130
2537 [[arXiv:hep-ph/9606251](#)].
- 2538 [42] N. Haba, M. Matsuda and M. Tanimoto, *Large neutrino flavor mixings and*
2539 *gauge mediated supersymmetry breaking scenario*, *Phys. Lett.* **B478** (2000)
2540 351–357 [[arXiv:hep-ph/9911511](#)].

Bibliography

- 2541 [43] B.S. DeWitt, *Quantum Theory of Gravity. I. The Canonical Theory*, *Phys. Rev.*
2542 **160** (1967) 1113–1148.
- 2543 [44] B.S. DeWitt, *Quantum Theory of Gravity. II. The Manifestly Covariant Theory*,
2544 *Phys. Rev.* **162** (1967) 1195–1239.
- 2545 [45] B.S. DeWitt, *Quantum Theory of Gravity. III. Applications of the Covariant
2546 Theory*, *Phys. Rev.* **162** (1967) 1239–1256.
- 2547 [46] F. Zwicky, *Die Rotverschiebung von extragalaktischen Nebeln*, *Helvetica Physica
2548 Acta* **6** (1933) 110–127.
- 2549 [47] H.W. Babcock, *The rotation of the Andromeda Nebula*, *Lick Observatory Bulletin*
2550 **19** (1939) 41–51.
- 2551 [48] K.C. Freeman, *On the Disks of Spiral and S0 Galaxies*, **160** (1970) 811.
- 2552 [49] V.C. Rubin and W.K. Ford, Jr., *Rotation of the Andromeda Nebula from a
2553 Spectroscopic Survey of Emission Regions*, **159** (1970) 379.
- 2554 [50] K.G. Begeman, A.H. Broeils and R.H. Sanders, *Extended rotation curves of
2555 spiral galaxies - Dark haloes and modified dynamics*, **249** (1991) 523–537.
- 2556 [51] A.D. Sakharov, *Violation of CP Invariance, C asymmetry, and baryon
2557 asymmetry of the universe*, *Pisma Zh. Eksp. Teor. Fiz.* **5** (1967) 32–35.
- 2558 [52] PLANCK collaboration, *Planck 2013 results. XVI. Cosmological parameters*,
2559 *Astron. Astrophys.* **571** (2014) A16 [[arXiv:1303.5076](#)].
- 2560 [53] S. Weinberg, *Gauge Hierarchies*, *Phys. Lett.* **82B** (1979) 387–391.
- 2561 [54] M.D. Schwartz, *Quantum Field Theory and the Standard Model*. Cambridge
2562 University Press, 2014.
- 2563 [55] M.E. Peskin and D.V. Schroeder, *An Introduction to Quantum Field Theory*.
2564 Addison-Wesley, Reading, USA, 1995.
- 2565 [56] G. Isidori, *Lecture notes in Quantum Field Theory II*, Frühjahrsemester 2015.
- 2566 [57] G. Buchalla, *Lecture notes for Introduction to the SM*, Wintersemester 2008.
- 2567 [58] G. Heinrich, *Lecture notes for Colorful Loops: Introduction to Quantum
2568 Chromodynamics and Loop Calculations*, Sommersemester 2018.
- 2569 [59] H.B.G. Casimir, *On the Attraction Between Two Perfectly Conducting Plates*,
2570 *Indag. Math.* **10** (1948) 261–263.
- 2571 [60] G. 't Hooft and M. Veltman, *Regularization and renormalization of gauge fields*,
2572 *Nuclear Physics B* **44** (1972) 189 – 213.

- [61] G. Passarino and M. Veltman, *One-loop corrections for e^+e^- annihilation into $\mu^+\mu^-$ in the Weinberg model*, *Nuclear Physics B* **160** (1979) 151 – 207.
- [62] A. Denner and S. Dittmaier, *Reduction schemes for one-loop tensor integrals*, *Nucl. Phys.* **B734** (2006) 62–115 [arXiv:hep-ph/0509141].
- [63] T. Binoth, J.P. Guillet, G. Heinrich et al., *An algebraic/numerical formalism for one-loop multi-leg amplitudes*, *JHEP* **10** (2005) 015 [arXiv:hep-ph/0504267].
- [64] J.M. Campbell, E.W.N. Glover and D.J. Miller, *One loop tensor integrals in dimensional regularization*, *Nucl. Phys.* **B498** (1997) 397–442 [arXiv:hep-ph/9612413].
- [65] J. Fleischer, F. Jegerlehner and O.V. Tarasov, *Algebraic reduction of one loop Feynman graph amplitudes*, *Nucl. Phys.* **B566** (2000) 423–440 [arXiv:hep-ph/9907327].
- [66] A.I. Davydychev, *A Simple formula for reducing Feynman diagrams to scalar integrals*, *Phys. Lett.* **B263** (1991) 107–111.
- [67] Z. Bern, L.J. Dixon and D.A. Kosower, *Dimensionally regulated one loop integrals*, *Phys. Lett.* **B302** (1993) 299–308 [arXiv:hep-ph/9212308].
- [68] C.G. Callan, *Broken scale invariance in scalar field theory*, *Phys. Rev. D* **2** (1970) 1541–1547.
- [69] K. Symanzik, *Small distance behaviour in field theory and power counting*, *Communications in Mathematical Physics* **18** (1970) 227–246.
- [70] K. Symanzik, *Small-distance-behaviour analysis and Wilson expansions*, *Communications in Mathematical Physics* **23** (1971) 49–86.
- [71] J.C. Ward, *An identity in quantum electrodynamics*, *Phys. Rev.* **78** (1950) 182–182.
- [72] Y. Takahashi, *On the generalized ward identity*, *Il Nuovo Cimento (1955-1965)* **6** (1957) 371–375.
- [73] A.D. Martin, W.J. Stirling, R.S. Thorne et al., *Parton distributions for the LHC*, *The European Physical Journal C* **63** (2009) 189–285.
- [74] S. Hoeche, “SLAC Theoretical Physics, Monte-Carlo Simulations.” <https://theory.slac.stanford.edu/our-research/simulations>.
- [75] T. Hahn, *Cuba—a library for multidimensional numerical integration*, *Computer Physics Communications* **168** (2005) 78 – 95.
- [76] G.P. Lepage, *A new algorithm for adaptive multidimensional integration*, *Journal of Computational Physics* **27** (1978) 192 – 203.

Bibliography

- 2607 [77] J.H. Friedman and M.H. Wright, *A nested partitioning procedure for numerical*
2608 *multiple integration*, *ACM Trans. Math. Softw.* **7** (1981) 76–92.
- 2609 [78] W.H. Press and G.R. Farrar, *Recursive Stratified Sampling for Multidimensional*
2610 *Monte Carlo Integration*, *Computers in Physics* **4** (1990) 190–195.
- 2611 [79] J. Berntsen, T.O. Espelid and A. Genz, *An Adaptive Algorithm for the*
2612 *Approximate Calculation of Multiple Integrals*, *ACM Trans. Math. Softw.* **17**
2613 (1991) 437–451.
- 2614 [80] A. Buckley, J. Ferrando, S. Lloyd et al., *LHAPDF6: parton density access in the*
2615 *LHC precision era*, *The European Physical Journal C* **75** (2015) 132.
- 2616 [81] J.M. Campbell, R.K. Ellis and W.T. Giele, *A multi-threaded version of MCFM*,
2617 *The European Physical Journal C* **75** (2015) 246.
- 2618 [82] K. Arnold, M. Bähr, G. Bozzi et al., *VBFNLO: A parton level Monte Carlo for*
2619 *processes with electroweak bosons*, *Computer Physics Communications* **180**
2620 (2009) 1661 – 1670.
- 2621 [83] J. Baglio et al., *VBFNLO: A Parton Level Monte Carlo for Processes with*
2622 *Electroweak Bosons - Manual for Version 2.7.0*, [arXiv:1107.4038].
- 2623 [84] J. Baglio et al., *Release Note - VBFNLO 2.7.0*, [arXiv:1404.3940].
- 2624 [85] Z. Bern, L.J. Dixon, F. Febres Cordero et al., *The BlackHat Library for*
2625 *One-Loop Amplitudes*, *J. Phys. Conf. Ser.* **523** (2014) 012051 [arXiv:1310.2808].
- 2626 [86] V. Hirschi, R. Frederix, S. Frixione et al., *Automation of one-loop QCD*
2627 *corrections*, *JHEP* **05** (2011) 044 [arXiv:1103.0621].
- 2628 [87] V. Hirschi, *New developments in MadLoop*, [arXiv:1111.2708].
- 2629 [88] R. Pittau, *Status of MadLoop/aMC@NLO*, in *International Workshop on Future*
2630 *Linear Colliders (LCWS11) Granada, Spain, September 26-30, 2011*, 2012,
2631 [arXiv:1202.5781].
- 2632 [89] J. Alwall, R. Frederix, S. Frixione et al., *The automated computation of tree-level*
2633 *and next-to-leading order differential cross sections, and their matching to parton*
2634 *shower simulations*, *JHEP* **2014** (2014) 79.
- 2635 [90] F. Caccioli, P. Maierhöfer and S. Pozzorini, *Scattering amplitudes with open*
2636 *loops*, *Phys. Rev. Lett.* **108** (2012) 111601.
- 2637 [91] F. Buccioni, S. Pozzorini and M. Zoller, *On-the-fly reduction of open loops*, *The*
2638 *European Physical Journal C* **78** (2018) 70.
- 2639 [92] G. Cullen, N. Greiner, G. Heinrich et al., *Automated one-loop calculations with*
2640 *GoSam*, *The European Physical Journal C* **72** (2012) 1889.

- [93] G. Cullen, H. van Deurzen, N. Greiner et al., *GoSam-2.0: a tool for automated one-loop calculations within the Standard Model and beyond*, *The European Physical Journal C* **74** (2014) 3001.
- [94] S. Actis, A. Denner, L. Hofer et al., *Recursive generation of one-loop amplitudes in the Standard Model*, *JHEP* **04** (2013) 037 [[arXiv:1211.6316](#)].
- [95] S. Actis, A. Denner, L. Hofer et al., *RECOLA: REcursive Computation of One-Loop Amplitudes*, *Comput. Phys. Commun.* **214** (2017) 140–173 [[arXiv:1605.01090](#)].
- [96] G. Bevilacqua, M. Czakon, M.V. Garzelli et al., *HELAC-NLO*, *Comput. Phys. Commun.* **184** (2013) 986–997 [[arXiv:1110.1499](#)].
- [97] S. Badger, B. Biedermann, P. Uwer et al., *Numerical evaluation of virtual corrections to multi-jet production in massless QCD*, *Computer Physics Communications* **184** (2013) 1981 – 1998.
- [98] F. Campanario, T.M. Figy, S. Plätzer et al., *Electroweak Higgs Boson Plus Three Jet Production at Next-to-Leading-Order QCD*, *Phys. Rev. Lett.* **111** (2013) 211802.
- [99] T. Binoth, F. Boudjema, G. Dissertori et al., *A proposal for a standard interface between Monte Carlo tools and one-loop programs*, *Computer Physics Communications* **181** (2010) 1612 – 1622.
- [100] S. Alioli, S. Badger, J. Bellm et al., *Update of the Binoth Les Houches Accord for a standard interface between Monte Carlo tools and one-loop programs*, *Computer Physics Communications* **185** (2014) 560 – 571.
- [101] P. Nogueira, *Automatic Feynman Graph Generation*, *Journal of Computational Physics* **105** (1993) 279 – 289.
- [102] J.A.M. Vermaasen, *New features of FORM*, [[arXiv:math-ph/0010025](#)].
- [103] T. Peraro, *Ninja: Automated integrand reduction via Laurent expansion for one-loop amplitudes*, *Computer Physics Communications* **185** (2014) 2771 – 2797.
- [104] G. Cullen, J.P. Guillet, G. Heinrich et al., *Golem95C: A library for one-loop integrals with complex masses*, *Computer Physics Communications* **182** (2011) 2276 – 2284.
- [105] J.P. Guillet, G. Heinrich and J.F. von Soden-Fraunhofen, *Tools for NLO automation: extension of the Golem95C integral library*, *Comput. Phys. Commun.* **185** (2014) 1828–1834 [[arXiv:1312.3887](#)].
- [106] P. Mastrolia, G. Ossola, T. Reiter et al., *Scattering Amplitudes from Unitarity-based Reduction Algorithm at the Integrand-level*, *JHEP* **08** (2010) 080 [[arXiv:1006.0710](#)].

Bibliography

- 2677 [107] R.K. Ellis and G. Zanderighi, *Scalar one-loop integrals for QCD*, *JHEP* **02**
2678 (2008) 002 [[arXiv:0712.1851](#)].
- 2679 [108] A. van Hameren, *Oneloop: For the evaluation of one-loop scalar functions*,
2680 *Computer Physics Communications* **182** (2011) 2427 – 2438.
- 2681 [109] S. Catani and M.H. Seymour, *A General algorithm for calculating jet*
2682 *cross-sections in NLO QCD*, *Nucl. Phys.* **B485** (1997) 291–419
2683 [[arXiv:hep-ph/9605323](#)].
- 2684 [110] S. Frixione, Z. Kunszt and A. Signer, *Three jet cross-sections to next-to-leading*
2685 *order*, *Nucl. Phys.* **B467** (1996) 399–442 [[arXiv:hep-ph/9512328](#)].
- 2686 [111] S. Frixione, *A General approach to jet cross-sections in QCD*, *Nucl. Phys.* **B507**
2687 (1997) 295–314 [[arXiv:hep-ph/9706545](#)].
- 2688 [112] G. Salam, *ICTP-SAIFR School on QCD and LHC physics, Sao Paulo, Brazil*,
2689 July 2015.
- 2690 [113] G. Altarelli and G. Parisi, *Asymptotic Freedom in Parton Language*, *Nucl. Phys.*
2691 **B126** (1977) 298–318.
- 2692 [114] Y.L. Dokshitzer, *Calculation of the Structure Functions for Deep Inelastic*
2693 *Scattering and e^+e^- Annihilation by Perturbation Theory in Quantum*
2694 *Chromodynamics.*, *Sov. Phys. JETP* **46** (1977) 641–653.
- 2695 [115] V.N. Gribov and L.N. Lipatov, *Deep inelastic ep scattering in perturbation*
2696 *theory*, *Sov. J. Nucl. Phys.* **15** (1972) 438–450.
- 2697 [116] M. Dasgupta, F.A. Dreyer, K. Hamilton et al., *Logarithmic accuracy of parton*
2698 *showers: a fixed-order study*, *JHEP* **09** (2018) 033 [[arXiv:1805.09327](#)].
- 2699 [117] M. Bahr et al., *Herwig++ Physics and Manual*, *Eur. Phys. J.* **C58** (2008)
2700 639–707 [[arXiv:0803.0883](#)].
- 2701 [118] J. Bellm et al., *Herwig 7.0/Herwig++ 3.0 release note*, *Eur. Phys. J.* **C76** (2016)
2702 196 [[arXiv:1512.01178](#)].
- 2703 [119] S. Frixione and B.R. Webber, *Matching NLO QCD computations and parton*
2704 *shower simulations*, *JHEP* **2002** (2002) 029–029.
- 2705 [120] S. Frixione, P. Nason and C. Oleari, *Matching NLO QCD computations with*
2706 *parton shower simulations: the POWHEG method*, *JHEP* **2007** (2007) 070–070.
- 2707 [121] S. Gieseke, P. Stephens and B. Webber, *New formalism for QCD parton showers*,
2708 *JHEP* **12** (2003) 045 [[arXiv:hep-ph/0310083](#)].
- 2709 [122] T. Sjostrand, S. Mrenna and P.Z. Skands, *PYTHIA 6.4 Physics and Manual*,
2710 *JHEP* **05** (2006) 026 [[arXiv:hep-ph/0603175](#)].

- 2711 [123] T. Sjostrand, S. Mrenna and P.Z. Skands, *A Brief Introduction to PYTHIA 8.1*,
 2712 *Comput. Phys. Commun.* **178** (2008) 852–867 [arXiv:0710.3820].
- 2713 [124] T. Gleisberg, S. Hoeche, F. Krauss et al., *Event generation with SHERPA 1.1*,
 2714 *JHEP* **02** (2009) 007 [arXiv:0811.4622].
- 2715 [125] B. Andersson, G. Gustafson, G. Ingelman et al., *Parton fragmentation and string*
 2716 *dynamics*, *Physics Reports* **97** (1983) 31 – 145.
- 2717 [126] T. Sjöstrand, S. Ask, J.R. Christiansen et al., *An introduction to PYTHIA 8.2*,
 2718 *Computer Physics Communications* **191** (2015) 159 – 177.
- 2719 [127] A. Kupco, *Cluster hadronization in HERWIG 5.9*, in *Monte Carlo generators for*
 2720 *HERA physics. Proceedings, Workshop, Hamburg, Germany, 1998-1999*,
 2721 292–300, 1998, [arXiv:hep-ph/9906412].
- 2722 [128] S. Gieseke, F. Loshaj and P. Kirchgässner, *Soft and diffractive scattering with the*
 2723 *cluster model in Herwig*, *The European Physical Journal C* **77** (2017) 156.
- 2724 [129] D. Amati and G. Veneziano, *Preconfinement as a property of perturbative QCD*,
 2725 *Physics Letters B* **83** (1979) 87–92.
- 2726 [130] O.S. Brüning, P. Collier, P. Lebrun et al., *LHC Design Report*, CERN Yellow
 2727 Reports: Monographs. CERN, Geneva, 2004.
- 2728 [131] O. Buning, P. Collier, P. Lebrun et al., *LHC Design Report. 2. The LHC*
 2729 *infrastructure and general services*. 2004.
- 2730 [132] M. Benedikt, P. Collier, V. Mertens et al., *LHC Design Report. 3. The LHC*
 2731 *injector chain*. 2004.
- 2732 [133] “CERN Official Website.”
 2733 <http://public.web.cern.ch/public/en/research/AccelComplex-en.html>.
- 2734 [134] ATLAS collaboration, *The ATLAS Experiment at the CERN Large Hadron*
 2735 *Collider*, *JINST* **3** (2008) S08003.
- 2736 [135] ATLAS collaboration, *Observation of Higgs boson production in association with*
 2737 *a top quark pair at the LHC with the ATLAS detector*, *Phys. Lett.* **B784** (2018)
 2738 173–191 [arXiv:1806.00425].
- 2739 [136] ATLAS collaboration, *Observation of light-by-light scattering in ultraperipheral*
 2740 *Pb+Pb collisions with the ATLAS detector*, .
- 2741 [137] ATLAS collaboration, *Study of the rare decays of B_s^0 and B^0 mesons into muon*
 2742 *pairs using data collected during 2015 and 2016 with the ATLAS detector*,
 2743 *Submitted to: JHEP* (2018) [arXiv:1812.03017].
- 2744 [138] M. Aleksa, F. Bergsma, P.A. Giudici et al., *Measurement of the ATLAS solenoid*
 2745 *magnetic field*. Dec 2007.

Bibliography

- 2746 [139] ATLAS collaboration, *ATLAS barrel toroid: Technical design report*, Technical
2747 Design Report ATLAS. CERN, Geneva, 1997.
- 2748 [140] ATLAS collaboration, *ATLAS end-cap toroids: Technical Design Report*,
2749 Technical Design Report ATLAS. CERN, Geneva, 1997.
- 2750 [141] ATLAS collaboration, *ATLAS inner detector: Technical design report. Vol. 2*.
2751 1997.
- 2752 [142] ATLAS collaboration, *ATLAS inner detector: Technical design report. Vol. 1*.
2753 1997.
- 2754 [143] ATLAS collaboration, M.S. Alam et al., *ATLAS pixel detector: Technical design
2755 report*. 1998.
- 2756 [144] ATLAS collaboration, *Operation and performance of the ATLAS semiconductor
2757 tracker*, *JINST* **9** (2014) P08009 [[arXiv:1404.7473](#)].
- 2758 [145] ATLAS TRT collaboration, *The ATLAS transition radiation tracker*, in
2759 *Astroparticle, particle and space physics, detectors and medical physics
2760 applications. Proceedings, 8th Conference, ICATPP 2003, Como, Italy, October
2761 6-10, 2003*, 497–501, 2003, [[arXiv:hep-ex/0311058](#)], DOI.
- 2762 [146] A.S. Boldyrev et al., *The ATLAS transition radiation tracker*, *Instrum. Exp.
2763 Tech.* **55** (2012) 323–334.
- 2764 [147] F. Hügging, *The ATLAS Pixel Insertable B-layer (IBL)*, *Nuclear Instruments
2765 and Methods in Physics Research Section A: Accelerators, Spectrometers,
2766 Detectors and Associated Equipment* **650** (2011) 45 – 49.
- 2767 [148] A. La Rosa, *The ATLAS Insertable B-Layer: from construction to operation*,
2768 *JINST* **11** (2016) C12036 [[arXiv:1610.01994](#)].
- 2769 [149] H. Pernegger, *The Pixel Detector of the ATLAS Experiment for LHC Run-2*,
2770 *Tech. Rep. ATL-INDET-PROC-2015-001. 06*, CERN, Geneva, Feb 2015.
- 2771 [150] ATLAS collaboration, *The Upgraded Pixel Detector of the ATLAS Experiment
2772 for Run-2 at the LHC*, *Tech. Rep. ATL-INDET-PROC-2016-009*, CERN,
2773 Geneva, Nov 2016.
- 2774 [151] S. Viel et al., *Performance of silicon pixel detectors at small track incidence
2775 angles for the ATLAS Inner Tracker Upgrade*, *Nucl. Instrum. Meth.* **A831**
2776 (2016) 254–259.
- 2777 [152] ATLAS collaboration, *Performance of the ATLAS Transition Radiation Tracker
2778 in Run 1 of the LHC: tracker properties*, *JINST* **12** (2017) P05002
2779 [[arXiv:1702.06473](#)].

- 2780 [153] ATLAS collaboration, *ATLAS liquid-argon calorimeter: Technical Design*
 2781 *Report*, Technical Design Report ATLAS. CERN, Geneva, 1996.
- 2782 [154] P. Strizenec, *Performance of the ATLAS liquid argon calorimeter after three*
 2783 *years of LHC operation and plans for a future upgrade*, *Journal of*
 2784 *Instrumentation* **9** (2014) C09007–C09007.
- 2785 [155] ATLAS collaboration, *ATLAS tile calorimeter: Technical Design Report*,
 2786 *Technical Design Report ATLAS*. CERN, Geneva, 1996.
- 2787 [156] A. Hrynevich, *Performance of the ATLAS tile calorimeter*, *Journal of*
 2788 *Instrumentation* **12** (2017) C06021–C06021.
- 2789 [157] ATLAS collaboration, *ATLAS muon spectrometer: Technical Design Report*,
 2790 *Technical Design Report ATLAS*. CERN, Geneva, 1997.
- 2791 [158] D. Boscherini, *Performance and operation of the ATLAS Resistive Plate*
 2792 *Chamber system in LHC Run-1*, *JINST* **9** (2014) C12039.
- 2793 [159] K. Nikolopoulos et al., *Cathode strip chambers in ATLAS : Installation,*
 2794 *commissioning and in situ performance*, in *Proceedings, 2008 IEEE Nuclear*
 2795 *Science Symposium*, 2819–2824, 2008.
- 2796 [160] M. Livan, *Monitored drift tubes in ATLAS*, *Nuclear Instruments and Methods in*
 2797 *Physics Research Section A: Accelerators, Spectrometers, Detectors and*
 2798 *Associated Equipment* **384** (1996) 214 – 218.
- 2799 [161] K. Nagai, *Thin gap chambers in ATLAS*, *Nuclear Instruments and Methods in*
 2800 *Physics Research Section A: Accelerators, Spectrometers, Detectors and*
 2801 *Associated Equipment* **384** (1996) 219 – 221.
- 2802 [162] ATLAS collaboration, *Performance of the ATLAS Trigger System in 2010*, *The*
 2803 *European Physical Journal C* **72** (2012) 1849.
- 2804 [163] ATLAS collaboration, *The Run-2 ATLAS Trigger System*, *J. Phys. Conf. Ser.*
 2805 **762** (2016) 012003.
- 2806 [164] GEANT4 collaboration, *GEANT4: A Simulation toolkit*, *Nucl. Instrum. Meth.*
 2807 **A506** (2003) 250–303.
- 2808 [165] E. Richter-Was, D. Froidevaux and L. Poggioli, *ATLFAST 2.0 a fast simulation*
 2809 *package for ATLAS*, .
- 2810 [166] ATLAS collaboration, *Measurement of the top quark mass with the template*
 2811 *method in the $t\bar{t} \rightarrow$ lepton + jets channel using ATLAS data*, *The European*
 2812 *Physical Journal C* **72** (2012) 2046.
- 2813 [167] ATLAS collaboration, *Measurement of the top quark mass in the $t\bar{t} \rightarrow$*
 2814 *lepton+jets and $t\bar{t} \rightarrow$ dilepton channels using $\sqrt{s} = 7$ TeV ATLAS data*, *The*
 2815 *European Physical Journal C* **75** (2015) 330.

Bibliography

- 2816 [168] ATLAS collaboration, *Measurement of the $t\bar{t}$ production cross-section using $e\mu$*
2817 *events with b-tagged jets in pp collisions at $\sqrt{s} = 7$ and 8 TeV with the ATLAS*
2818 *detector*, *The European Physical Journal C* **74** (2014) 3109.
- 2819 [169] ATLAS collaboration, *Measurement of the top quark mass in the $t\bar{t}$ dilepton*
2820 *channel from $\sqrt{s} = 8$ TeV ATLAS data*, *Physics Letters B* **761** (2016) 350 – 371.
- 2821 [170] ATLAS collaboration, *Measurement of lepton differential distributions and the*
2822 *top quark mass in $t\bar{t}$ production in pp collisions at $\sqrt{s} = 8$ TeV with the ATLAS*
2823 *detector*, *The European Physical Journal C* **77** (2017) 804.
- 2824 [171] ATLAS collaboration, *Determination of the top-quark pole mass using $t\bar{t} + 1$ -jet*
2825 *events collected with the ATLAS experiment in 7 TeV pp collisions*, *JHEP* **2015**
2826 (2015) 121.
- 2827 [172] ATLAS collaboration, *Measurement of the top-quark mass in the fully hadronic*
2828 *decay channel from ATLAS data at $\sqrt{s} = 7$ TeV*, *The European Physical Journal*
2829 *C* **75** (2015) 158.
- 2830 [173] ATLAS collaboration, *Top-quark mass measurement in the all-hadronic $t\bar{t}$ decay*
2831 *channel at $\sqrt{s} = 8$ TeV with the ATLAS detector*, *JHEP* **2017** (2017) 118.
- 2832 [174] M. Czakon and A. Mitov, *Top++: A Program for the Calculation of the*
2833 *Top-Pair Cross-Section at Hadron Colliders*, *Comput. Phys. Commun.* **185**
2834 (2014) 2930 [[arXiv:1112.5675](#)].
- 2835 [175] ATLAS collaboration, *Studies on top-quark Monte Carlo modelling for Top2016*,
2836 Tech. Rep. ATL-PHYS-PUB-2016-020, CERN, Geneva, Sep 2016.
- 2837 [176] ATLAS collaboration, *Studies on top-quark Monte Carlo modelling with Sherpa*
2838 *and MG5_aMC@NLO*, Tech. Rep. ATL-PHYS-PUB-2017-007, CERN, Geneva,
2839 May 2017.
- 2840 [177] ATLAS collaboration, *Investigation of systematic uncertainties on the*
2841 *measurement of the top-quark mass using lepton transverse momenta*, Tech. Rep.
2842 ATL-PHYS-PUB-2018-001, CERN, Geneva, Feb 2018.
- 2843 [178] ATLAS collaboration, *Improvements in $t\bar{t}$ modelling using NLO+PS Monte*
2844 *Carlo generators for Run2*, Tech. Rep. ATL-PHYS-PUB-2018-009, CERN,
2845 Geneva, Jul 2018.
- 2846 [179] ATLAS collaboration, *Measurement of the top quark mass in the $t\bar{t} \rightarrow$ dilepton*
2847 *channel from $\sqrt{s} = 8$ TeV ATLAS data*, *Phys. Lett.* **B761** (2016) 350–371
2848 [[arXiv:1606.02179](#)].
- 2849 [180] J.M. Campbell, R.K. Ellis, P. Nason et al., *Top-pair production and decay at*
2850 *NLO matched with parton showers*, *JHEP* **04** (2015) 114 [[arXiv:1412.1828](#)].

- 2851 [181] J. Bellm, S. Gieseke and S. Plätzer, *Merging NLO Multi-jet Calculations with*
 2852 *Improved Unitarization*, *Eur. Phys. J.* **C78** (2018) 244 [[arXiv:1705.06700](#)].
- 2853 [182] S. Hoeche, F. Krauss, P. Maierhoefer et al., *Next-to-leading order QCD*
 2854 *predictions for top-quark pair production with up to two jets merged with a parton*
 2855 *shower*, *Phys. Lett.* **B748** (2015) 74–78 [[arXiv:1402.6293](#)].
- 2856 [183] S. Höche, P. Maierhöfer, N. Moretti et al., *Next-to-leading order QCD predictions*
 2857 *for top-quark pair production with up to three jets*, *Eur. Phys. J.* **C77** (2017) 145
 2858 [[arXiv:1607.06934](#)].
- 2859 [184] M. Czakon, D. Heymes and A. Mitov, *High-precision differential predictions for*
 2860 *top-quark pairs at the LHC*, *Phys. Rev. Lett.* **116** (2016) 082003
 2861 [[arXiv:1511.00549](#)].
- 2862 [185] M. Czakon, D. Heymes and A. Mitov, *Dynamical scales for multi-TeV top-pair*
 2863 *production at the LHC*, *JHEP* **04** (2017) 071 [[arXiv:1606.03350](#)].
- 2864 [186] M. Czakon, D. Heymes and A. Mitov, *fastNLO tables for NNLO top-quark pair*
 2865 *differential distributions*, [[arXiv:1704.08551](#)].
- 2866 [187] M. Czakon, D. Heymes, A. Mitov et al., *Top-pair production at the LHC through*
 2867 *NNLO QCD and NLO EW*, *JHEP* **10** (2017) 186 [[arXiv:1705.04105](#)].
- 2868 [188] W. Hollik and D. Pagani, *The electroweak contribution to the top quark*
 2869 *forward-backward asymmetry at the Tevatron*, *Phys. Rev.* **D84** (2011) 093003
 2870 [[arXiv:1107.2606](#)].
- 2871 [189] J.H. Kühn, A. Scharf and P. Uwer, *Weak Interactions in Top-Quark Pair*
 2872 *Production at Hadron Colliders: An Update*, *Phys. Rev.* **D91** (2015) 014020
 2873 [[arXiv:1305.5773](#)].
- 2874 [190] D. Pagani, I. Tsinikos and M. Zaro, *The impact of the photon PDF and*
 2875 *electroweak corrections on $t\bar{t}$ distributions*, *Eur. Phys. J.* **C76** (2016) 479
 2876 [[arXiv:1606.01915](#)].
- 2877 [191] W. Bernreuther, A. Brandenburg, Z.G. Si et al., *Top quark pair production and*
 2878 *decay at hadron colliders*, *Nucl. Phys.* **B690** (2004) 81–137
 2879 [[arXiv:hep-ph/0403035](#)].
- 2880 [192] K. Melnikov and M. Schulze, *NLO QCD corrections to top quark pair production*
 2881 *and decay at hadron colliders*, *JHEP* **0908** (2009) 049 [[arXiv:0907.3090](#)].
- 2882 [193] J.M. Campbell and R.K. Ellis, *Top-quark processes at NLO in production and*
 2883 *decay*, *J. Phys.* **G42** (2015) 015005 [[arXiv:1204.1513](#)].
- 2884 [194] M. Brucherseifer, F. Caola and K. Melnikov, $\mathcal{O}(\alpha_s^2)$ *corrections to*
 2885 *fully-differential top quark decays*, *JHEP* **04** (2013) 059 [[arXiv:1301.7133](#)].

Bibliography

- 2886 [195] J. Gao and A.S. Papanastasiou, *Top-quark pair-production and decay at high*
2887 *precision*, *Phys. Rev.* **D96** (2017) 051501 [[arXiv:1705.08903](#)].
- 2888 [196] M. Beneke, P. Falgari, S. Klein et al., *Hadronic top-quark pair production with*
2889 *NNLL threshold resummation*, *Nucl. Phys.* **B855** (2012) 695–741
2890 [[arXiv:1109.1536](#)].
- 2891 [197] M. Cacciari, M. Czakon, M. Mangano et al., *Top-pair production at hadron*
2892 *colliders with next-to-next-to-leading logarithmic soft-gluon resummation*, *Phys.*
2893 *Lett.* **B710** (2012) 612–622 [[arXiv:1111.5869](#)].
- 2894 [198] A. Ferroglio, S. Marzani, B.D. Pecjak et al., *Boosted top production: factorization*
2895 *and resummation for single-particle inclusive distributions*, *JHEP* **01** (2014) 028
2896 [[arXiv:1310.3836](#)].
- 2897 [199] A. Broggio, A.S. Papanastasiou and A. Signer, *Renormalization-group improved*
2898 *fully differential cross sections for top pair production*, *JHEP* **10** (2014) 98
2899 [[arXiv:1407.2532](#)].
- 2900 [200] N. Kidonakis, *High-order threshold corrections for top-pair and single-top*
2901 *production*, in *Proceedings, Meeting of the APS Division of Particles and Fields*
2902 (*DPF 2015*): *Ann Arbor, Michigan, USA, 4-8 Aug 2015*, 2015,
2903 [[arXiv:1509.07848](#)].
- 2904 [201] B.D. Pecjak, D.J. Scott, X. Wang et al., *Resummed differential cross sections for*
2905 *top-quark pairs at the LHC*, *Phys. Rev. Lett.* **116** (2016) 202001
2906 [[arXiv:1601.07020](#)].
- 2907 [202] M.L. Czakon et al., *Top quark pair production at NNLO+NNLL' in QCD*
2908 *combined with electroweak corrections*, in *11th International Workshop on Top*
2909 *Quark Physics (TOP2018) Bad Neuenahr, Germany, September 16-21, 2018*,
2910 2019, [[arXiv:1901.08281](#)].
- 2911 [203] G. Heinrich, A. Maier, R. Nisius et al., *NLO QCD corrections to W^+W^-bb*
2912 *production with leptonic decays in the light of top quark mass and asymmetry*
2913 *measurements*, *JHEP* **1406** (2014) 158 [[arXiv:1312.6659](#)].
- 2914 [204] S. Frixione, E. Laenen, P. Motylinski et al., *Single-top hadroproduction in*
2915 *association with a W boson*, *JHEP* **07** (2008) 029 [[arXiv:0805.3067](#)].
- 2916 [205] A. Denner, S. Dittmaier, S. Kallweit et al., *NLO QCD corrections to $WWbb$*
2917 *production at hadron colliders*, *Phys. Rev. Lett.* **106** (2011) 052001
2918 [[arXiv:1012.3975](#)].
- 2919 [206] A. Denner, S. Dittmaier, S. Kallweit et al., *NLO QCD corrections to off-shell*
2920 *top-antitop production with leptonic decays at hadron colliders*, *JHEP* **10** (2012)
2921 110 [[arXiv:1207.5018](#)].

- 2922 [207] G. Bevilacqua, M. Czakon, A. van Hameren et al., *Complete off-shell effects in*
 2923 *top quark pair hadroproduction with leptonic decay at next-to-leading order,*
 2924 *JHEP* **02** (2011) 083 [[arXiv:1012.4230](#)].
- 2925 [208] R. Frederix, *Top Quark Induced Backgrounds to Higgs Production in the*
 2926 *$WW^{(*)} \rightarrow ll\nu\nu$ Decay Channel at Next-to-Leading-Order in QCD*, *Phys. Rev.*
 2927 *Lett.* **112** (2014) 082002 [[arXiv:1311.4893](#)].
- 2928 [209] F. Cascioli, S. Kallweit, P. Maierhöfer et al., *A unified NLO description of*
 2929 *top-pair and associated Wt production*, *Eur. Phys. J.* **C74** (2014) 2783
 2930 [[arXiv:1312.0546](#)].
- 2931 [210] A. Denner and M. Pellen, *Off-shell production of top-antitop pairs in the*
 2932 *lepton+jets channel at NLO QCD*, *JHEP* **02** (2018) 013 [[arXiv:1711.10359](#)].
- 2933 [211] G. Heinrich, A. Maier, R. Nisius et al., *NLO and off-shell effects in top quark*
 2934 *mass determinations*, *JHEP* **07** (2018) 129 [[arXiv:1709.08615](#)].
- 2935 [212] G. Heinrich, A. Maier, R. Nisius et al., *NLO QCD corrections to $WWbb$*
 2936 *production with leptonic decays in the light of top quark mass and asymmetry*
 2937 *measurements*, *JHEP* **2014** (2014) 158.
- 2938 [213] A. Denner, S. Dittmaier, S. Kallweit et al., *NLO QCD corrections to off-shell*
 2939 *top-antitop production with leptonic decays at hadron colliders*, *JHEP* **2012**
 2940 (2012) 110.
- 2941 [214] S. Höche and J.C. Winter. Private communication.
- 2942 [215] C. Duhr, S. Hoeche and F. Maltoni, *Color-dressed recursive relations for*
 2943 *multi-parton amplitudes*, *JHEP* **08** (2006) 062 [[arXiv:hep-ph/0607057](#)].
- 2944 [216] T. Gleisberg and S. Hoeche, *Comix, a new matrix element generator*, *JHEP* **12**
 2945 (2008) 039 [[arXiv:0808.3674](#)].
- 2946 [217] T. Gleisberg, S. Hoeche, F. Krauss et al., *How to calculate colourful cross*
 2947 *sections efficiently*, [[arXiv:0808.3672](#)].
- 2948 [218] F. Krauss, R. Kuhn and G. Soff, *AMEGIC++ 1.0: A Matrix element generator*
 2949 *in C++*, *JHEP* **02** (2002) 044 [[arXiv:hep-ph/0109036](#)].
- 2950 [219] J. Butterworth et al., *PDF4LHC recommendations for LHC Run II*, *J. Phys.*
 2951 **G43** (2016) 023001 [[arXiv:1510.03865](#)].
- 2952 [220] M. Cacciari, G.P. Salam and G. Soyez, *The Anti- $k(t)$ jet clustering algorithm*,
 2953 *JHEP* **04** (2008) 063 [[arXiv:0802.1189](#)].
- 2954 [221] M. Cacciari and G.P. Salam, *Dispelling the N^3 myth for the k_t jet-finder*, *Phys.*
 2955 *Lett.* **B641** (2006) 57–61 [[arXiv:hep-ph/0512210](#)].

Bibliography

- 2956 [222] M. Cacciari, G.P. Salam and G. Soyez, *FastJet User Manual*, *Eur. Phys. J.* **C72**
2957 (2012) 1896 [arXiv:1111.6097].
- 2958 [223] S. Höche, J. Huang, G. Luisoni et al., *Zero and one jet combined next-to-leading*
2959 *order analysis of the top quark forward-backward asymmetry*, *Phys. Rev.* **D88**
2960 (2013) 014040 [arXiv:1306.2703].
- 2961 [224] A. Buckley, J. Butterworth, L. Lönnblad et al., *Rivet user manual*, *Comput.*
2962 *Phys. Commun.* **184** (2013) 2803–2819 [arXiv:1003.0694].
- 2963 [225] C.G. Lester and D.J. Summers, *Measuring masses of semiinvisibly decaying*
2964 *particles pair produced at hadron colliders*, *Phys. Lett.* **B463** (1999) 99–103
2965 [arXiv:hep-ph/9906349].
- 2966 [226] A. Barr, C. Lester and P. Stephens, *m(T2): The Truth behind the glamour*, *J.*
2967 *Phys.* **G29** (2003) 2343–2363 [arXiv:hep-ph/0304226].
- 2968 [227] C. Buttar, J. D’Hondt, M. Kramer et al., *Standard Model Handles and Candles*
2969 *Working Group: Tools and Jets Summary Report*, 03 2008.
- 2970 [228] V. Blobel, *An Unfolding method for high-energy physics experiments*, in *Advanced*
2971 *Statistical Techniques in Particle Physics. Proceedings, Conference, Durham,*
2972 *UK, March 18-22, 2002*, 258–267, 2002, [arXiv:hep-ex/0208022],
2973 <http://www.ippp.dur.ac.uk/Workshops/02/statistics/proceedings//blobel2.pdf>.
- 2974 [229] S. Schmitt, *Data Unfolding Methods in High Energy Physics*, *EPJ Web Conf.*
2975 **137** (2017) 11008 [arXiv:1611.01927].
- 2976 [230] T. Ježo and P. Nason, *On the Treatment of Resonances in Next-to-Leading Order*
2977 *Calculations Matched to a Parton Shower*, *JHEP* **12** (2015) 065
2978 [arXiv:1509.09071].
- 2979 [231] ATLAS collaboration, *Electron reconstruction and identification in the ATLAS*
2980 *experiment using the 2015 and 2016 LHC proton-proton collision data at $\sqrt{s} =$*
2981 *13 TeV*, *Submitted to: Eur. Phys. J.* (2019) [arXiv:1902.04655].
- 2982 [232] ATLAS collaboration, *Muon reconstruction performance of the ATLAS detector*
2983 *in proton–proton collision data at $\sqrt{s} = 13$ TeV*, *Eur. Phys. J.* **C76** (2016) 292
2984 [arXiv:1603.05598].
- 2985 [233] ATLAS collaboration, *ATLAS jet and missing energy reconstruction, calibration*
2986 *and performance in LHC Run-2*, Tech. Rep. ATL-PHYS-PROC-2017-045. 06,
2987 CERN, Geneva, May 2017.
- 2988 [234] ATLAS collaboration, *The ATLAS Tau Trigger in Run 2*, Tech. Rep.
2989 ATLAS-CONF-2017-061, CERN, Geneva, Jul 2017.
- 2990 [235] ATLAS collaboration, *Performance of b-Jet Identification in the ATLAS*
2991 *Experiment*, *JINST* **11** (2016) P04008 [arXiv:1512.01094].

- 2992 [236] ATLAS collaboration, *Performance of the ATLAS Trigger System in 2015*, *Eur. Phys. J.* **C77** (2017) 317 [arXiv:1611.09661].
- 2993
- 2994 [237] ATLAS collaboration, *Electron and photon energy calibration with the ATLAS detector using data collected in 2015 at $\sqrt{s} = 13$ TeV*, Tech. Rep.
- 2995
- 2996 ATL-PHYS-PUB-2016-015, CERN, Geneva, Aug 2016.
- 2997 [238] ATLAS collaboration, *Jet energy measurement and its systematic uncertainty in proton-proton collisions at $\sqrt{s} = 7$ TeV with the ATLAS detector*, *Eur. Phys. J.* **C75** (2015) 17 [arXiv:1406.0076].
- 2998
- 2999
- 3000 [239] ATLAS collaboration, A. Calandri, *Flavour tagging algorithms and performance at the ATLAS experiment*, no. ATL-PHYS-PROC-2016-105. Geneva, Aug 2016.
- 3001
- 3002 [240] M. Lehmacher, *b-Tagging Algorithms and their Performance at ATLAS*, in *Proceedings, 34th International Conference on High Energy Physics (ICHEP 2008): Philadelphia, Pennsylvania, July 30-August 5, 2008*, 2008,
- 3003
- 3004
- 3005 [arXiv:0809.4896], <http://weblib.cern.ch/abstract?ATL-PHYS-PROC-2008-052>.
- 3006 [241] ATLAS collaboration, *Secondary vertex finding for jet flavour identification with the ATLAS detector*, no. ATL-PHYS-PUB-2017-011. Geneva, Jun 2017.
- 3007
- 3008 [242] G. Piacquadio and C. Weiser, *A new inclusive secondary vertex algorithm for b-jet tagging in ATLAS*, *Journal of Physics: Conference Series* **119** (2008)
- 3009
- 3010 032032.
- 3011 [243] ATLAS collaboration, *Optimisation of the ATLAS b-tagging performance for the 2016 LHC Run*, Tech. Rep. ATL-PHYS-PUB-2016-012, CERN, Geneva, Jun
- 3012
- 3013 2016.
- 3014 [244] M. Cacciari and G.P. Salam, *Pileup subtraction using jet areas*, *Phys. Lett.* **B659**
- 3015 (2008) 119–126 [arXiv:0707.1378].
- 3016 [245] P. Nason, *The Top Quark Mass at the LHC*, in *Proceedings, Old and New Strong Interactions from LHC to Future Colliders (LFC17): Trento, Italy, September 11-15, 2017*, 65–70, 2017, [arXiv:1801.04826].
- 3017
- 3018
- 3019 [246] F. James, *MINUIT Function Minimization and Error Analysis: Reference Manual Version 94.1*, .
- 3020
- 3021 [247] ATLAS collaboration, *Measurement of the top quark mass in the $t\bar{t} \rightarrow \text{lepton+jets}$ and $t\bar{t} \rightarrow \text{dilepton}$ channels using $\sqrt{s} = 7$ TeV ATLAS data*,
- 3022
- 3023 *Eur. Phys. J.* **C75** (2015) 330 [arXiv:1503.05427].
- 3024 [248] ATLAS collaboration, *Observation of a new particle in the search for the Standard Model Higgs boson with the ATLAS detector at the LHC*, *Phys. Lett.*
- 3025
- 3026 **B716** (2012) 1–29 [arXiv:1207.7214].

Bibliography

- 3027 [249] CMS collaboration, *Observation of a new boson at a mass of 125 GeV with the*
3028 *CMS experiment at the LHC*, *Phys. Lett.* **B716** (2012) 30–61 [[arXiv:1207.7235](#)].
- 3029 [250] E.W.N. Glover and J.J. van der Bij, *Higgs Boson Pair Production via Gluon*
3030 *Fusion*, *Nucl. Phys.* **B309** (1988) 282.
- 3031 [251] M. Spira, A. Djouadi, D. Graudenz et al., *Higgs boson production at the LHC*,
3032 *Nucl. Phys.* **B453** (1995) 17–82 [[arXiv:hep-ph/9504378](#)].
- 3033 [252] R. Bonciani, A. Ferroglio, P. Mastrolia et al., *Two-loop $N(F)=1$ QED Bhabha*
3034 *scattering differential cross section*, *Nucl. Phys.* **B701** (2004) 121–179
3035 [[arXiv:hep-ph/0405275](#)].
- 3036 [253] C. Anastasiou, S. Beerli, S. Bucherer et al., *Two-loop amplitudes and master*
3037 *integrals for the production of a Higgs boson via a massive quark and a*
3038 *scalar-quark loop*, *JHEP* **01** (2007) 082 [[arXiv:hep-ph/0611236](#)].
- 3039 [254] G. Degrassi, P.P. Giardino and R. Gröber, *On the two-loop virtual QCD*
3040 *corrections to Higgs boson pair production in the Standard Model*, *Eur. Phys. J.*
3041 **C76** (2016) 411 [[arXiv:1603.00385](#)].
- 3042 [255] R. Bonciani, V. Del Duca, H. Frellesvig et al., *Next-to-leading order QCD*
3043 *corrections to the decay width $H \rightarrow Z\gamma$* , *JHEP* **08** (2015) 108 [[arXiv:1505.00567](#)].
- 3044 [256] T. Gehrmann, S. Guns and D. Kara, *The rare decay $H \rightarrow Z\gamma$ in perturbative*
3045 *QCD*, *JHEP* **09** (2015) 038 [[arXiv:1505.00561](#)].
- 3046 [257] R. Gröber, A. Maier and T. Rauh, *Reconstruction of top-quark mass effects in*
3047 *Higgs pair production and other gluon-fusion processes*, *JHEP* **03** (2018) 020
3048 [[arXiv:1709.07799](#)].
- 3049 [258] R. Bonciani, G. Degrassi, P.P. Giardino et al., *Analytical Method for*
3050 *Next-to-Leading-Order QCD Corrections to Double-Higgs Production*, *Phys. Rev.*
3051 *Lett.* **121** (2018) 162003 [[arXiv:1806.11564](#)].
- 3052 [259] G. Mishima, *High-Energy Expansion of Two-Loop Massive Four-Point Diagrams*,
3053 *JHEP* **02** (2019) 080 [[arXiv:1812.04373](#)].
- 3054 [260] J. Davies, G. Mishima, M. Steinhauser et al., *Double Higgs boson production at*
3055 *NLO in the high-energy limit: complete analytic results*, *JHEP* **01** (2019) 176
3056 [[arXiv:1811.05489](#)].
- 3057 [261] S. Borowka, N. Greiner, G. Heinrich et al., *Full top quark mass dependence in*
3058 *Higgs boson pair production at NLO*, *JHEP* **10** (2016) 107 [[arXiv:1608.04798](#)].
- 3059 [262] A. von Manteuffel and C. Studerus, *Reduze 2 - Distributed Feynman Integral*
3060 *Reduction*, [[arXiv:1201.4330](#)].

- 3061 [263] J. Carter and G. Heinrich, *SecDec: A general program for sector decomposition*,
 3062 *Comput. Phys. Commun.* **182** (2011) 1566–1581 [[arXiv:1011.5493](#)].
- 3063 [264] S. Borowka, J. Carter and G. Heinrich, *Numerical Evaluation of Multi-Loop*
 3064 *Integrals for Arbitrary Kinematics with SecDec 2.0*, *Comput. Phys. Commun.*
 3065 **184** (2013) 396–408 [[arXiv:1204.4152](#)].
- 3066 [265] S. Borowka, G. Heinrich, S.P. Jones et al., *SecDec-3.0: numerical evaluation of*
 3067 *multi-scale integrals beyond one loop*, *Comput. Phys. Commun.* **196** (2015)
 3068 470–491 [[arXiv:1502.06595](#)].
- 3069 [266] S.P. Jones, *Automation of 2-loop Amplitude Calculations*, *PoS LL2016* (2016)
 3070 069 [[arXiv:1608.03846](#)].
- 3071 [267] S. Borowka, G. Heinrich, S. Jahn et al., *A GPU compatible quasi-Monte Carlo*
 3072 *integrator interfaced to pySecDec*, *Comp. Phys. Comm.* (2018)
 3073 [[arXiv:1811.11720](#)].
- 3074 [268] J. Baglio, F. Campanario, S. Glaus et al., *Gluon fusion into Higgs pairs at NLO*
 3075 *QCD and the top mass scheme*, [[arXiv:1811.05692](#)].
- 3076 [269] G. Buchalla, O. Catà and C. Krause, *Complete Electroweak Chiral Lagrangian*
 3077 *with a Light Higgs at NLO*, *Nucl. Phys.* **B880** (2014) 552–573 [[arXiv:1307.5017](#)].
- 3078 [270] G. Buchalla, O. Catá and C. Krause, *On the Power Counting in Effective Field*
 3079 *Theories*, *Phys. Lett.* **B731** (2014) 80–86 [[arXiv:1312.5624](#)].
- 3080 [271] G. Buchalla, M. Capozi, A. Celis et al., *Higgs boson pair production in non-linear*
 3081 *Effective Field Theory with full m_t -dependence at NLO QCD*, *JHEP* **09** (2018)
 3082 057 [[arXiv:1806.05162](#)].
- 3083 [272] C. Degrande, C. Duhr, B. Fuks et al., *UFO - The Universal FeynRules Output*,
 3084 *Comput. Phys. Commun.* **183** (2012) 1201–1214 [[arXiv:1108.2040](#)].
- 3085 [273] A. Alloul, N.D. Christensen, C. Degrande et al., *FeynRules 2.0 - A complete*
 3086 *toolbox for tree-level phenomenology*, *Comput. Phys. Commun.* **185** (2014)
 3087 2250–2300 [[arXiv:1310.1921](#)].
- 3088 [274] N.D. Christensen and C. Duhr, *FeynRules - Feynman rules made easy*, *Comput.*
 3089 *Phys. Commun.* **180** (2009) 1614–1641 [[arXiv:0806.4194](#)].
- 3090 [275] A. Carvalho, M. Dall’Osso, T. Dorigo et al., *Higgs Pair Production: Choosing*
 3091 *Benchmarks With Cluster Analysis*, *JHEP* **04** (2016) 126 [[arXiv:1507.02245](#)].
- 3092 [276] A. Djouadi, M. Spira and P. Zerwas, *Production of Higgs bosons in proton*
 3093 *colliders. QCD corrections*, *Physics Letters B* **264** (1991) 440 – 446.
- 3094 [277] S. Dawson, *Radiative corrections to Higgs boson production*, *Nucl. Phys.* **B359**
 3095 (1991) 283–300.

Bibliography

- 3096 [278] R. Grober, M. Muhlleitner, M. Spira et al., *NLO QCD Corrections to Higgs Pair*
3097 *Production including Dimension-6 Operators*, *JHEP* **09** (2015) 092
3098 [[arXiv:1504.06577](#)].
- 3099 [279] A. Azatov, R. Contino, G. Panico et al., *Effective field theory analysis of double*
3100 *Higgs boson production via gluon fusion*, *Phys. Rev.* **D92** (2015) 035001
3101 [[arXiv:1502.00539](#)].
- 3102 [280] CMS collaboration, *Measurement and interpretation of differential cross sections*
3103 *for Higgs boson production at $\sqrt{s} = 13$ TeV*, *Phys. Lett.* **B792** (2019) 369
3104 [[arXiv:1812.06504](#)].
- 3105 [281] G. Heinrich, S.P. Jones, M. Kerner et al., *Probing the trilinear Higgs boson*
3106 *coupling in di-Higgs production at NLO QCD including parton shower effects*,
3107 [[arXiv:1903.08137](#)].
- 3108 [282] G. Heinrich, S.P. Jones, M. Kerner et al., *NLO predictions for Higgs boson pair*
3109 *production with full top quark mass dependence matched to parton showers*,
3110 *JHEP* **08** (2017) 088 [[arXiv:1703.09252](#)].
- 3111 [283] *Les Houches 2017: Physics at TeV Colliders Standard Model Working Group*
3112 *Report*, 2018.
- 3113 [284] S. Ferrario Ravasio, T. Jezo, P. Nason et al., *A Theoretical Study of Top-Mass*
3114 *Measurements at the LHC Using NLO+PS Generators of Increasing Accuracy*,
3115 [[arXiv:1801.03944](#)].

3116 A Further template fit plots

3117 A better understanding of the discrepancy between the NLO_{full} prediction and the
 3118 $\text{NLO}_{\text{NWA}}^{\text{NLOdec}}$, respectively NLO_{PS} calculations is needed. Compared to the NLO_{full} pseudo-
 3119 data, the $\text{NLO}_{\text{NWA}}^{\text{NLOdec}}$ prediction leads to a rather large offset in the top-quark mass of
 3120 (0.83 ± 0.07) GeV. On the other hand, the NLO_{PS} prediction gives an offset to the
 3121 $W^+W^-b\bar{b}$ pseudo-data of only (-0.09 ± 0.07) GeV. New parton-showered predictions
 3122 ($n_{\max}^{\text{prod}}, n_{\max}^{\text{dec}}$) are produced where the shower is terminated after a certain number of
 3123 emissions n_{\max} in the $t\bar{t}$ production and decay showers. In Fig. A.1, the pseudo-data
 3124 from these predictions are compared to the full parton-shower and the $\text{NLO}_{\text{NWA}}^{\text{NLOdec}}$ cali-
 3125 bration function and pseudo-data. For each of the samples, the offset in m_t is given as
 3126 a colored bar (in blue for the $\text{NLO}_{\text{NWA}}^{\text{NLOdec}}$ calibration function, respectively in red when
 3127 using the NLO_{PS} calibration). Then, for only one allowed emission in both production
 3128 and decay showers, the top-quark mass offset between $\text{NLO}_{\text{PS}}^{(1,1)}$ and $\text{NLO}_{\text{NWA}}^{\text{NLOdec}}$ is re-
 3129 duced to (-0.11 ± 0.06) GeV. Thus, the additional radiation accounts for the observed
 3130 discrepancy in the offsets.

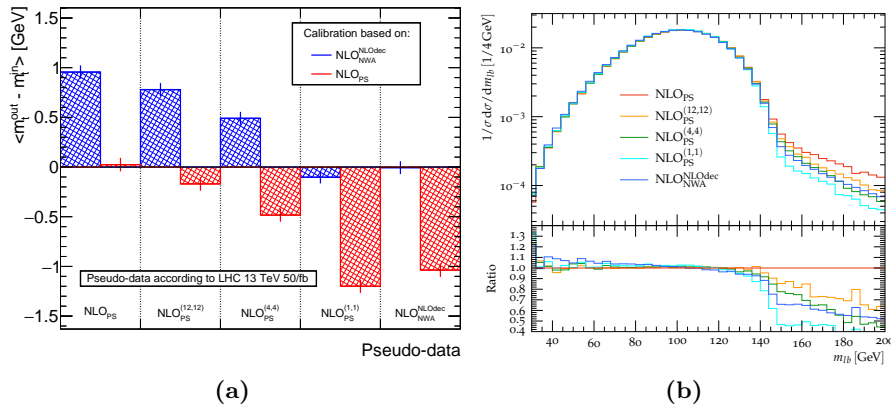


Figure A.1: (a) The offsets fitted from the $m_{t\bar{t}}$ distribution are shown for $\text{NLO}_{\text{PS}}^{(n_{\max}^{\text{prod}}, n_{\max}^{\text{dec}})}$ restricted-shower pseudo-data samples. (b) The normalized $m_{t\bar{t}}$ distribution is plotted for the mentioned predictions at $m_t = 172.5$ GeV.

A Further template fit plots

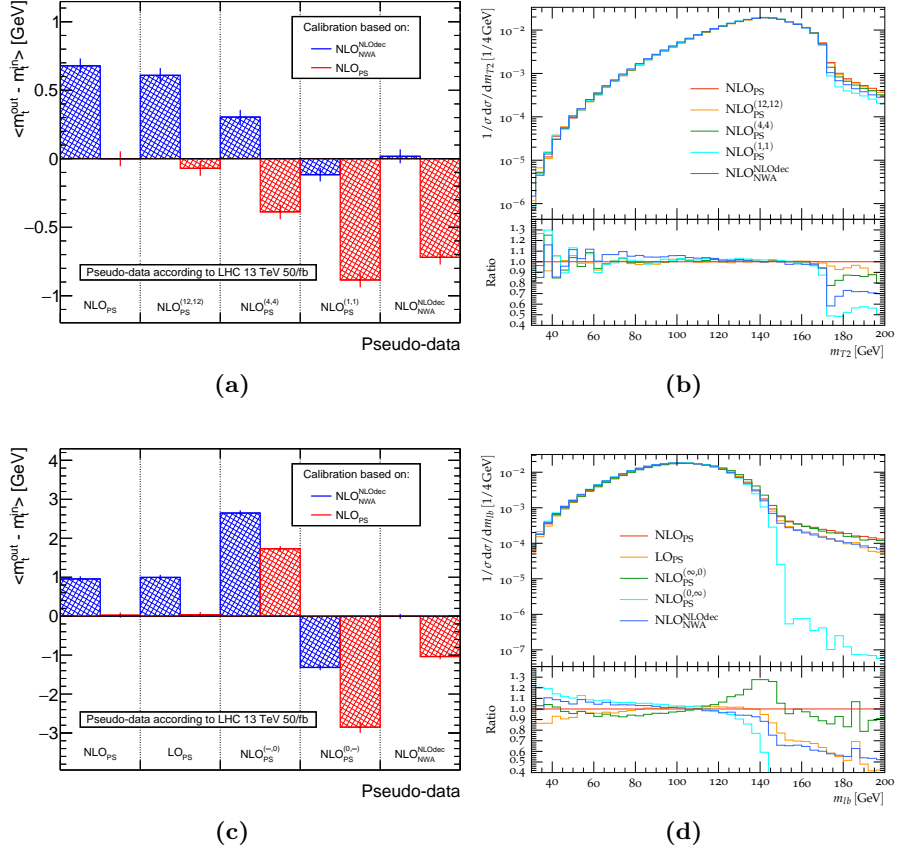


Figure A.2: (a-b) Same as A.1 for m_{T2} . (c-d) Same as Fig. A.1, but for the NLO_{PS} and LO_{PS} cases, as well as for pseudo-data sets generated by predictions where the decay shower, respectively the production shower are entirely deactivated.

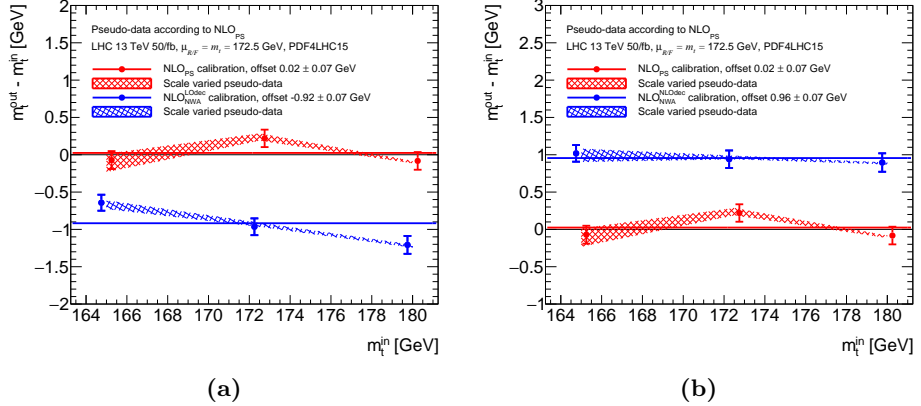


Figure A.3: Further band plots from $m_{\ell b}$ fitted pseudo-data sets.

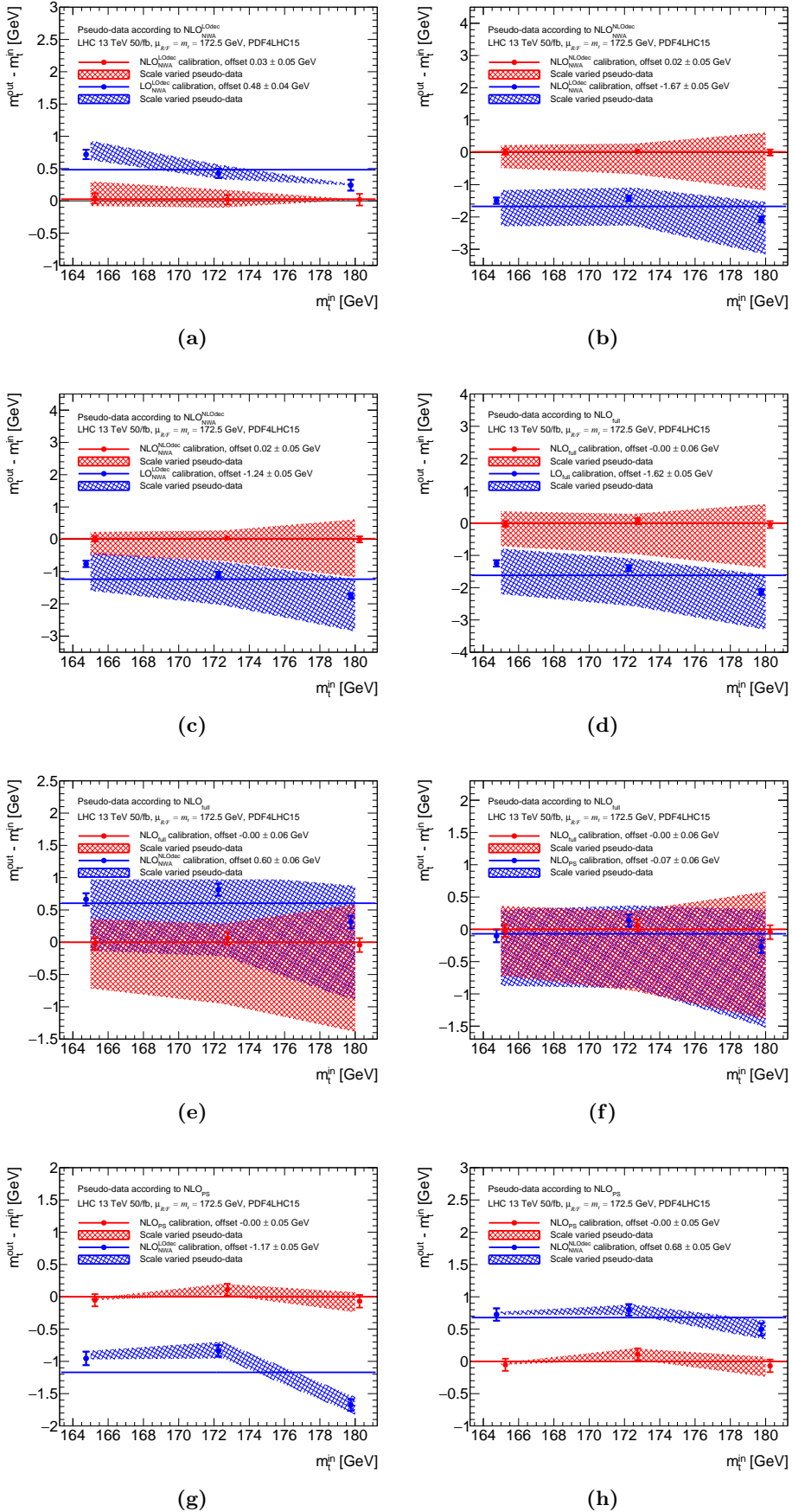


Figure A.4: Further band plots from m_{T2} fitted pseudo-data sets.

A Further template fit plots

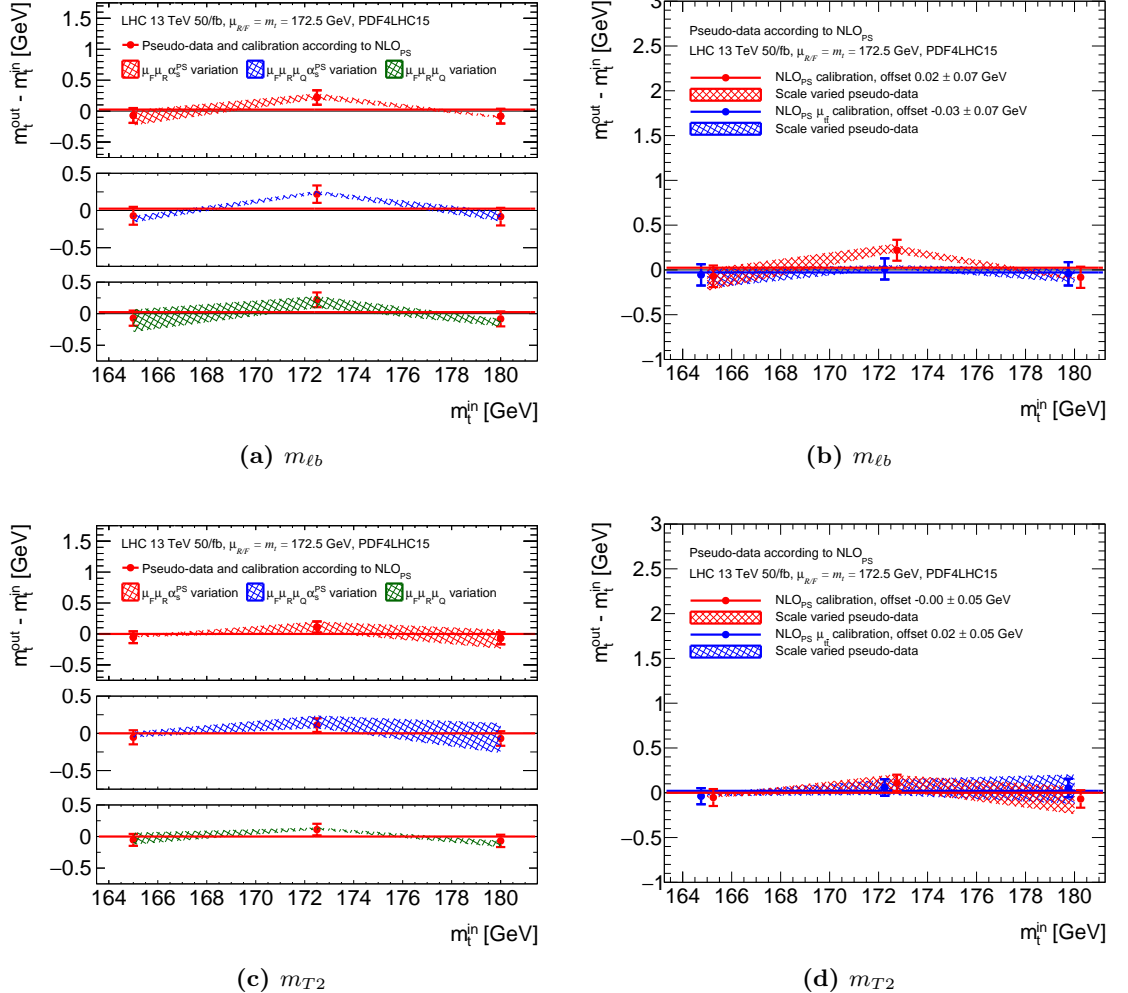


Figure A.5: Offsets from NLO_{PS} predictions comparing (a) different prescriptions for evaluating the shower scale uncertainties and (b) the two different central scale choices described in the text.

B Monte-Carlo samples at detector level

| Sample DSID | Generator (ME + PS/Had) | m_t [GeV] | Simulation tags |
|--|--|-------------|-------------------------|
| NLO $t\bar{t}$ (NWA) | | | |
| 411053 | POWHEG+PYTHIA8 | 171 | E6696_A875_R9364_P3629 |
| 411054 | POWHEG+PYTHIA8 | 172 | E6696_A875_R9364_P3629 |
| 410472 | POWHEG+PYTHIA8 | 172.5 | E6348_A875_R9364_P3629 |
| 411057 | POWHEG+PYTHIA8 | 173 | E6696_A875_R9364_P3629 |
| 411058 | POWHEG+PYTHIA8 | 174 | E6696_A875_R9364_P3629 |
| NLO $W^+W^-b\bar{b}$ | | | |
| 999991 | BB4L+HERWIG7 | 171 | — |
| 999992 | BB4L+HERWIG7 | 172 | — |
| 999995 | BB4L+HERWIG7 | 172.5 | — |
| 999993 | BB4L+HERWIG7 | 173 | — |
| 999994 | BB4L+HERWIG7 | 174 | — |
| NLO single-top W^-t (DR) | | | |
| 411109 | POWHEG+PYTHIA8 | 171 | E6852_A875_R9364_P3629 |
| 411111 | POWHEG+PYTHIA8 | 172 | E6852_A875_R9364_P3629 |
| 410646 | POWHEG+PYTHIA8 | 172.5 | E6552_A875_R9364_P3629 |
| 411117 | POWHEG+PYTHIA8 | 173 | E6852_A875_R9364_P3629 |
| 411119 | POWHEG+PYTHIA8 | 174 | E6852_A875_R9364_P3629 |
| NLO single-top $W^+\bar{t}$ (DR) | | | |
| 411110 | POWHEG+PYTHIA8 | 171 | E6852_A875_R9364_P3629 |
| 411112 | POWHEG+PYTHIA8 | 172 | E6852_A875_R9364_P3629 |
| 410647 | POWHEG+PYTHIA8 | 172.5 | E6552_A875_R9364_P3629 |
| 411118 | POWHEG+PYTHIA8 | 173 | E6852_A875_R9364_P3629 |
| 411120 | POWHEG+PYTHIA8 | 174 | E6852_A875_R9364_P3629 |
| $t\bar{t}$ variation samples | | | |
| 410472 | POWHEG+PYTHIA8 | 172.5 | E6348_S3126_R9364_P3629 |
| 410482 | POWHEG+PYTHIA8 $h_{\text{damp}}^{\text{up}}$ | 172.5 | E6454_A875_R9364_P3629 |
| 410558 | POWHEG+HERWIG7.0.4 | 172.5 | E6366_A875_R9364_P3629 |

Table B.1: Summary of the MC derivations used as input to the top-quark mass analysis presented in Chapter 8-9.

3132 C Template fit parameters at detector level

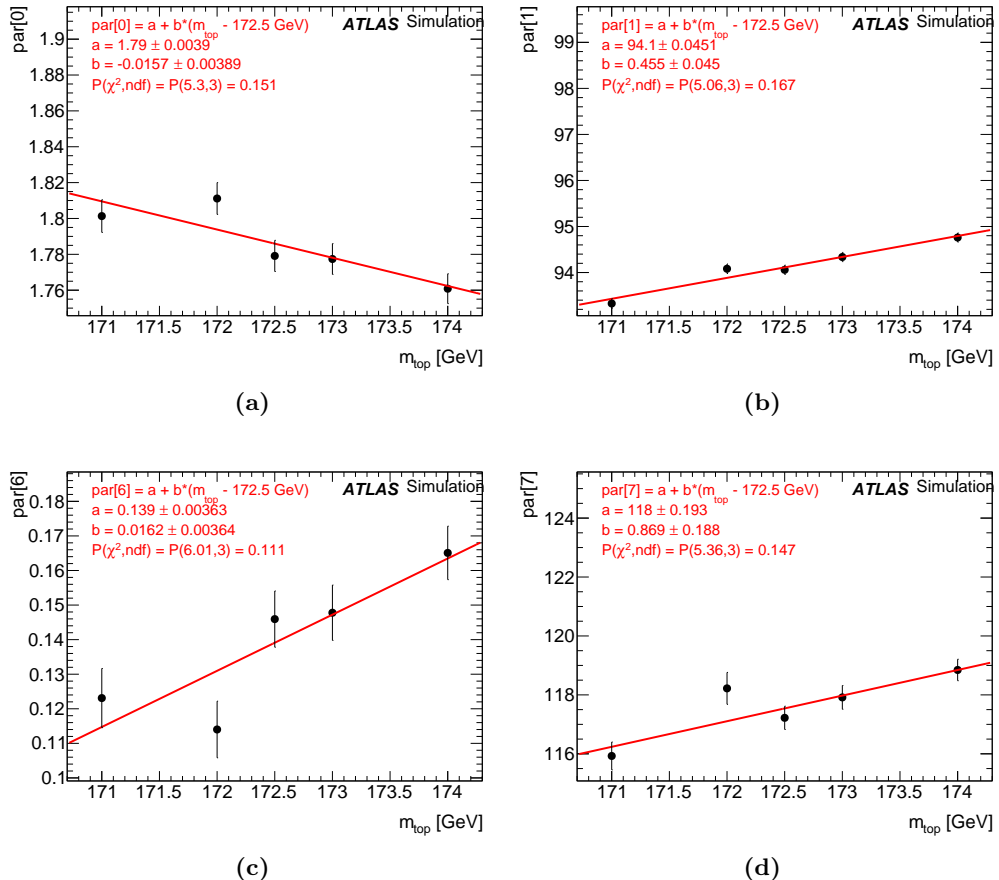


Figure C.1: The linear dependence of the four free functional fit parameters on the MC input top-quark mass, for the $t\bar{t}$ +single-top samples at detector level. From the nine original parameters from the three Gaussian functions, four are left floating and five are fixed.

3133 D BSM benchmark points in hh production

3134 The coefficients A_i , $i = 1, \dots, 23$ (15) defined for the general expression of the NLO
 3135 (LO) cross-section as a function of the anomalous Higgs couplings in Eq. (10.16) are
 3136 shown in Table D.1, at 13 TeV at LHC. To compute these, the cross-section was calcu-
 3137 lated for different values of the couplings that were replaced in Eq. (10.16), thus giving
 3138 a system of equations that one can project out to extract the values of the coefficients
 3139 A_i .

3140 The LO and NLO coefficients for $\sqrt{s} = 13, 14$ and 27 TeV are available on the ARXIV
 3141 e-print of Ref. [271], as well as a Mathematica file explaining how to use them. These
 3142 can also be derived differentially for a fixed bin width. The differential coefficients can
 3143 be downloaded for the m_{hh} distribution, with the binning shown in the histograms.

| A_i | A_i^{LO} | ΔA_i^{LO} | A_i^{NLO} | ΔA_i^{NLO} |
|----------|-------------------|--------------------------|--------------------|---------------------------|
| A_1 | 2.0806 | 0.0016 | 2.2339 | 0.0101 |
| A_2 | 10.2011 | 0.0081 | 12.4598 | 0.0424 |
| A_3 | 0.2781 | 0.0019 | 0.3422 | 0.0154 |
| A_4 | 0.3140 | 0.0003 | 0.3468 | 0.0033 |
| A_5 | 12.2731 | 0.0101 | 13.0087 | 0.0962 |
| A_6 | -8.4931 | 0.0089 | -9.6455 | 0.0504 |
| A_7 | -1.3587 | 0.0015 | -1.5755 | 0.0136 |
| A_8 | 2.8025 | 0.0131 | 3.4385 | 0.0772 |
| A_9 | 2.4802 | 0.0128 | 2.8669 | 0.0772 |
| A_{10} | 14.6908 | 0.0311 | 16.6912 | 0.1785 |
| A_{11} | -1.1592 | 0.0031 | -1.2529 | 0.0291 |
| A_{12} | -5.5118 | 0.0131 | -5.8122 | 0.1340 |
| A_{13} | 0.5605 | 0.0034 | 0.6497 | 0.0287 |
| A_{14} | 2.4798 | 0.0190 | 2.8593 | 0.1930 |
| A_{15} | 2.8943 | 0.0158 | 3.1448 | 0.1487 |
| A_{16} | | | -0.008162 | 0.000225 |
| A_{17} | | | 0.020865 | 0.000399 |
| A_{18} | | | 0.016816 | 0.000783 |
| A_{19} | | | 0.029858 | 0.000829 |
| A_{20} | | | -0.027025 | 0.000702 |
| A_{21} | | | 0.072692 | 0.001288 |
| A_{22} | | | 0.014523 | 0.000704 |
| A_{23} | | | 0.123291 | 0.006506 |

Table D.1: The coefficients defined in Eqs. (10.15), (10.16) are determined by computing cross-sections for a subset of parameters, and projecting out equations for the A_i 's. Statistical uncertainties are propagated from the cross-section level to the coefficient result, without correlations.

D BSM benchmark points in hh production

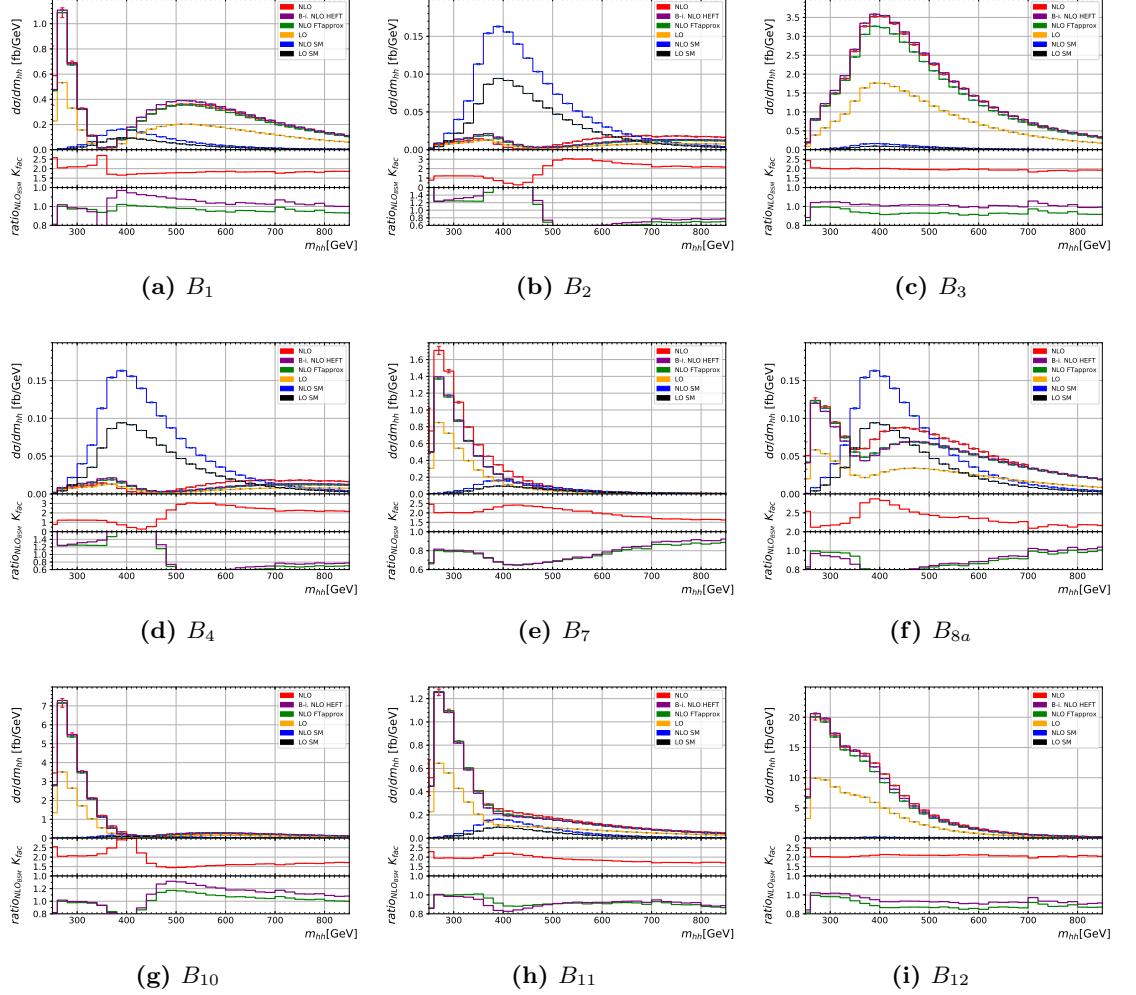


Figure D.1: The invariant mass of the Higgs boson pair m_{hh} is shown for the different benchmark points B_i , $i = 1, \dots, 12$ defined in Table 10.1 and not already shown in Chapter 10.

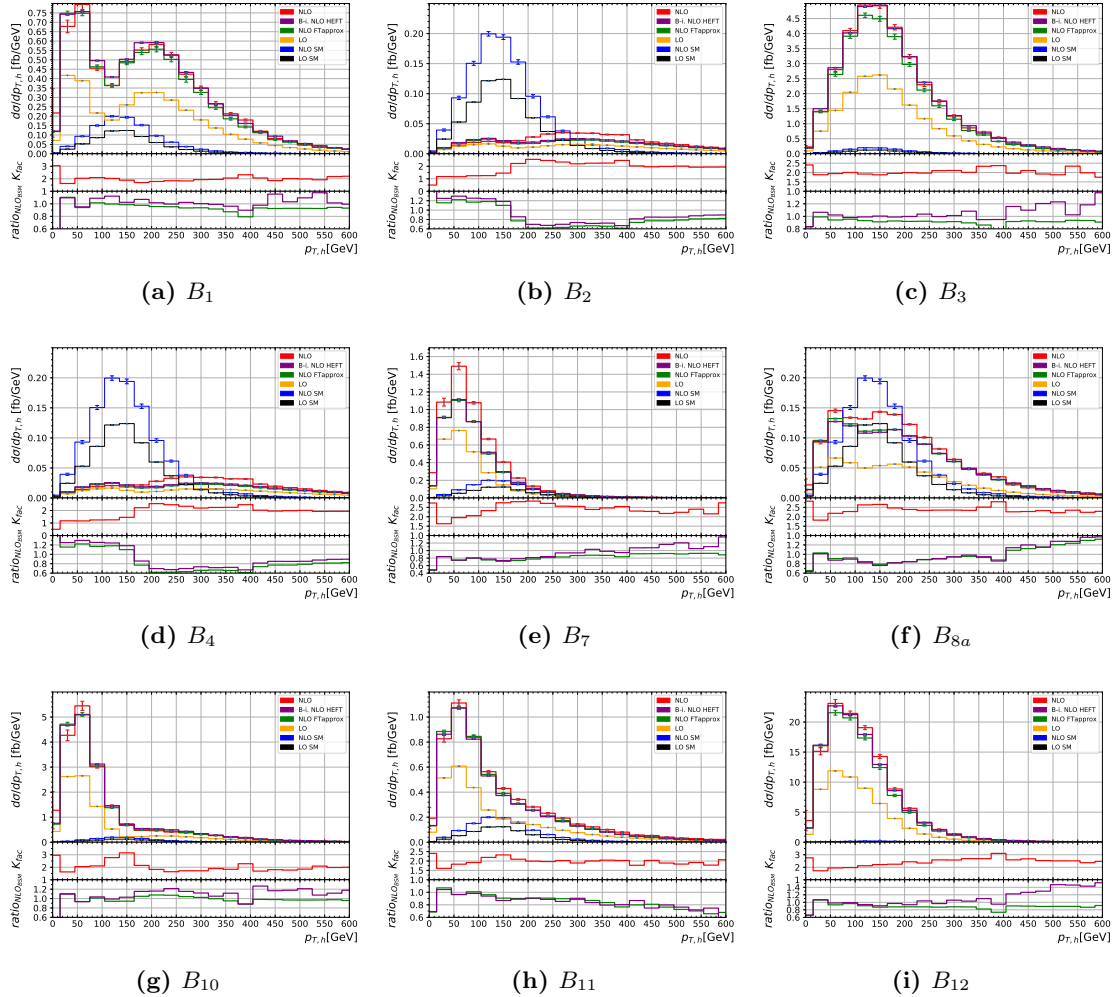


Figure D.2: The transverse momentum $p_{T,h}$ of one (any) Higgs boson is shown for the different benchmark points B_i , $i = 1, \dots, 12$ defined in Table 10.1 and not already shown in Chapter 10.

E Hardness definitions in parton-shower matching

3144 **E Hardness definitions in parton-shower
3145 matching**

3146 The technical parameters for matching the PYTHIA8 parton-shower to LHE files pro-
3147 duced by POWHEG are defined in a file called `main31.cmnd`, which bases on the LHE
3148 showering example from PYTHIA. There, several definitions for the additional radia-
3149 tion have to be set in order for the parton-shower to avoid double-counting regions of
3150 phase-space already covered by POWHEG. The following definitions are set:

- 3151 • The number of final-state particles in the Born process $gg \rightarrow hh$.

3152 `POWHEG:nFinal = 2`

- 3153 • The parton-shower vetoes emissions that have a transverse momentum higher than
3154 the hardest POWHEG emission, and checks the first three. A veto is applied if
3155 `pTemt > pThard` (see below).

3156 `POWHEG:veto = 1`

3157 `POWHEG:vetoCount = 3`

- 3158 • The `pTemt` and `pThard` scale definition is set: `pTemt` is set to the transverse mo-
3159 mentum of the radiated particle with respect to the emitting parton, and `pThard` is
3160 set to the `SCALUP` value read in the LHE event, and set by POWHEG. The definition
3161 of the emitted parton is chosen by PYTHIA for the final-state radiation.

3162 `POWHEG:pTemt = 0`

3163 `POWHEG:pThard = 0`

3164 `POWHEG:emitted = 0`

3165 `POWHEG:pTdef = 1`

3166 The hardness `pTdef` is defined by the transverse momentum p_T for initial-state
3167 radiation, and with the distance between radiator and emitted partons d_{ij} for
3168 final-state radiation corresponding to the POWHEG definition given by:

$$d_{ij} = \frac{m_{ij}^2 E_i E_j}{(E_i + E_j)^2}. \quad (\text{E.1})$$

3169 Acknowledgments

3170 First and foremost, I am infinitely grateful to both my supervisors, Stefan Kluth on the
3171 ATLAS computing side, and Gudrun Heinrich in the phenomenology group, for actively
3172 following my progress and keeping me on the right track with always astute advice. I
3173 could not have done it without their considerate help and encouragement.

3174 I am much obliged to all my publication collaborators, past and present, for their
3175 hard work, spontaneity and for maintaining an ever enjoyable working atmosphere: G.
3176 Buchalla, A. Celis, M. Capozi, G. Heinrich, S. Jones, M. Kerner, G. Luisoni, R. Mah-
3177 bubani, A. Maier, R. Nisius, H. Rzehak, J. Schlenk, M. Schulze and J. Winter. I would
3178 also like to thank A. Knue and B. Pearson for their incredible understanding of all
3179 the tiny details of the ATLAS analysis. They are responsible for making the interface
3180 comprehensible, which probably saved me a lot of nightmarish headaches.

3181 Of course, there is no office without officemates: my appreciation goes to A. Knue, A.
3182 Verbytskyi, D. Britzger, F. Klimpel and S. Schulte from the ATLAS computing group,
3183 for the lively discussions and the enormous pleasure I had working with you.

3184 Much valued was the time spent with the people from Gudrun's phenomenology group:
3185 it is not always easy to move to a new city or meet entirely new people, and for the casual
3186 climate and the few Oktoberfest visits together, I am most grateful. Thanks to H. Bahl,
3187 M. Capozi, L. Chen, S. Hessenberger, S. Jahn, V. Papara, C. Pietsch, J. Schlenk, T.
3188 Zirke for making especially my first few months in Munich brighter.

3189 I am eternally indebted to all the excellent friends that made the time at the Institute
3190 seem relativistically short, in particular those living permanently in, or sporadically
3191 passing by Connollystrasse: E. Bertoldo, M. Capozi, N. Ferreiro, M. Mancuso and F.
3192 Putzolu, E. Vitagliano, F. Guescini.

3193 I cannot stress enough how much friends were important to my mental sanity: after
3194 the long hours and weekends of work, it was always good to know whom to count on for
3195 releasing the pressure. This also applies to all the people whose visits from Switzerland
3196 rekindled the spark during a weekend of partying. Lots and lots of thanks in particular
3197 to A. Arbet-Engels, C. Crusem, B. Despond, I. El Mais, M. Predikaka and K. Novoselc,
3198 A. Du Cos, A. Lichtlé, G. Mathys, C. Traveletti and all my friends from Zurich.

3199 To my girlfriend at the time, Marthe, I want to say how grateful I am for the moments
3200 we enjoyed together. The past two years were beautiful, and I am profoundly glad to
3201 have walked part of the path with you.

3202 Finally, I offer my last resounding thanks to my whole family, in particular to my
3203 parents and my siblings. Without my parents, I would never have a life nearly as
3204 exciting and vibrant as this one. Thank you for what I know sometimes amounted to
3205 difficult sacrifices and for your unfaltering support. To my brother and sister, thanks
3206 for the frequent calls, the fun times in Gruyère, Munich or wherever halfway was, and
3207 generally for keeping me anchored in the normal world.